UNIVERSITÉ DU QUÉBEC À CHICOUTIMI

Dissertation presented to the
University of Quebec at Chicoutimi
in partial fulfillment of
the requirement for the degree of
Doctor of Philosophy in Engineering

by
ZHEYUAN MA

EFFECT OF Fe-INTERMETALLICS AND POROSITY ON TENSILE AND IMPACT PROPERTIES OF Al-Si-Cu AND Al-Si-Mg CAST ALLOYS

August 2002

Bibliothèque
Paul-Émile-Boulet

UQAC
Université du Québec
à Chicoutimi

Mise en garde/Advice

Afin de rendre accessible au plus grand nombre le résultat des travaux de recherche menés par ses étudiants gradués et dans l'esprit des règles qui régissent le dépôt et la diffusion des mémoires et thèses produits dans cette Institution, **l'Université du Québec à Chicoutimi (UQAC)** est fière de rendre accessible une version complète et gratuite de cette œuvre.

Motivated by a desire to make the results of its graduate students' research accessible to all, and in accordance with the rules governing the acceptation and diffusion of dissertations and theses in this Institution, the **Université du Québec à Chicoutimi (UQAC)** is proud to make a complete version of this work available at no cost to the reader.

L'auteur conserve néanmoins la propriété du droit d'auteur qui protège ce mémoire ou cette thèse. Ni le mémoire ou la thèse ni des extraits substantiels de ceux-ci ne peuvent être imprimés ou autrement reproduits sans son autorisation.

The author retains ownership of the copyright of this dissertation or thesis. Neither the dissertation or thesis, nor substantial extracts from it, may be printed or otherwise reproduced without the author's permission.

UNIVERSITÉ DU QUÉBEC À CHICOUTIMI

THÈSE PRÉSENTÉE À
L'UNIVERSITÉ DU QUÉBEC À CHICOUTIMI
COMME EXIGENCE PARTIELLE
DU DOCTORAT EN INGÉNIERIE

ZHEYUAN MA

EFFETS DES INTERMÉTALLIQUES DE FER ET DES POROSITÉS SUR LES PROPRIÉTÉS DE TRACTION ET D'IMPACT SUR LES ALLIAGES DE COULÉE Al-Si-Cu ET Al-Si-Mg

AOÛT 2002

Dedicated to my parents

谨以此献给我的父母

RÉSUMÉ

Les alliages aluminium-silicium (Al-Si) sont une importante classe de matériaux qui constituent la majorité des pièces d'aluminium coulées produites, dû à leurs propriétés supérieures et leurs excellentes caractéristiques de coulées. À l'intérieur de cette famille d'alliages, les alliages de fonderie Al-Si-Cu et Al-Si-Mg sont fréquemment employés dans les applications automobiles. Les alliages commercialement populaires 319 et 356, représentant ces deux systèmes d'alliages, furent sélectionnés pour étude dans le présent travail, avec pour but d'investiguer l'effet des intermétalliques du fer et des porosités sur la performance de l'alliage. Ceci fut exécuté à travers une étude des propriétés de traction et d'impact, celles-ci étant deux propriétés mécaniques importantes utilisées dans les calculs de conception. Le fer, à travers la précipitation des constituants intermétalliques de seconde phase, en particulier la phase en forme de plaquettes β-Al_5FeSi, est nuisible aux propriétés des alliages. De même les porosités dues au gaz ou aux retassures dans les coulées sont nuisibles aux propriétés mécaniques. Par la détermination des éléments d'alliage, du processus de fonderie et des paramètres de solidification optimaux (*viz.*, le contenu en Fe, la modification au Sr et le taux de refroidissement) requis pour minimiser les effets nuisibles des porosités et des intermétalliques du fer, et par l'étude de leur rôle sur le comportement des fractures, le mécanisme de fracture dans les alliages a pu être déterminé.

Des coulées furent préparées à partir des fontes d'alliages industriels et commerciaux 319.2, B319.2 et A356.2, contenant des niveaux de Fe de 0.2-1.0 wt%. Des fontes modifiées au Sr (~200 ppm) furent aussi préparées pour chaque niveau de Fe. Les moules réfractaires refroidis aux extrémités utilisés ont donné une solidification directionnelle et une plage de taux de refroidissement (ou espace interdendritique) à l'intérieur de la même coulée. Des échantillons de traction et d'impact, machinés à partir de spécimens provenant des coulées, et sectionnés à diverses hauteurs au-dessus de l'extrémité refroidie, ont donné des espaces interdendritiques de ~23 à ~85 μm. Tous les échantillons furent soumis à un traitement thermique T6 avant les essais. Les essais furent exécutés en employant les machines d'essais Instron Universal et Instrumented Charpy. Les techniques de microscopie optique, d'analyse d'image, de SEM et de EPMA furent utilisées dans les analyses microstructurales et de fracture.

Les résultats ont démontré que le taux de refroidissement le plus élevé (23 μm d'espace interdendritique) est le paramètre le plus significatif contrôlant la dimension et la distribution de la phase β-Al_5FeSi et des porosités, dans les alliages non modifiés 319.2 et A356.2. La modification au Sr est plus efficace dans la réduction de la dimension des

plaquettes de phase β, à des bas niveaux de Fe, mais celle-ci augmente à la fois la fraction volumique des porosités et la dimension des pores de façon significative. L'alliage B319.2 contenant du Mg montre une réduction de la dimension des plaquettes de β due à sa transformation partielle en particules de script chinois $Al_8FeMg_3Si_6$. Dans les alliages modifiés au Sr, une augmentation de la dimension des plaquettes β est encore observée à certains taux de refroidissement. La fraction volumique des porosités et la dimension des pores diminuent aussi avec l'addition de Mg.

La ductilité des alliages est améliorée par l'augmentation simultanée du taux de refroidissement et de la réduction du contenu en Fe. La ductilité de l'alliage B319.2 est inférieure à celle de l'alliage 319.2 dû à la précipitation du Mg_2Si, à la transformation partielle de β-Al_5FeSi en $Al_8FeMg_3Si_6$, et à l'interaction Sr-Mg qui diminue l'efficacité de la modification au Sr. L'alliage A356.2 affiche une ductilité beaucoup plus élevée que les alliages 319 pour un même niveau de Fe, dû à l'absence de la phase intermétallique $CuAl_2$ dans le premier alliage. La modification au Sr améliore aussi à la fois la ductilité et la résistance en traction, et est utile dans le maintien d'une limite ultime cohérente dans les alliages 319, puisqu'une dispersion beaucoup moindre des valeurs de limite ultime est observée, peu importe leur source (expérimentale ou industrielle). Aucun effet apparent sur la limite élastique n'est observé.

Le fer détériore la limite ultime dans les alliages expérimentaux non modifiés et les alliages industriels modifiés 319.2, B319.2 et A356.2. Des corrélations polynomiales du second degré sont obtenues entre la limite ultime et le contenu en Fe à tous les taux de refroidissement (R^2 >0.8) pour la plupart des alliages; les alliages expérimentaux modifiés et les alliages industriels non modifiés 319.2, cependant ont montré une dispersion considérable de la limite ultime. La corrélation entre la contrainte et le contenu en Fe ou le taux de refroidissement est plus complexe: en général, la limite élastique augmente à la fois avec le taux de refroidissement et le contenu en Fe dans les alliages 319.2 (R^2 >0.8). Dans les alliages B319.2, l'effet du taux de refroidissement n'est pas très apparent: Fe augmente la limite élastique dans les alliages expérimentaux mais diminue celle-ci dans les alliages industriels. Dans les alliages A356.2, les valeurs de la limite élastique sont distribuées à l'intérieur d'une plage étroite montrant une tendance à la baisse dans les alliages non modifiés et une tendance à la hausse dans les alliages modifiés.

La dimension des plaquettes de β-Al_5FeSi affecte la ductilité et la résistance en traction des alliages, les changements étant très perceptibles jusqu'à des longueurs (ou surfaces) de plaquettes β de ~100 μm (400 μm^2) dans les alliages 319 et de ~70 μm (300 μm^2) dans les alliages A356.2. Des corrélations de puissance et logarithmiques sont obtenues entre la ductilité et la dimension des plaquettes β (R^2 >0.8). Dans les alliages A356.2, seules de faibles variations dans la dimension de la phase β peut être tolérée afin de maintenir des niveaux de ductilité satisfaisants. La diminution de la limite ultime avec la dimension des plaquettes β est plus prononcée dans les alliages 319.2 que dans les alliages B319.2 et A356.2. Aucune relation définie entre la dimension des plaquettes β et la limite élastique n'a pu être établie.

La porosité est nuisible à la résistance en traction et à la ductilité des alliages. Bien que le paramètre de dimension maximum des pores caractérise le mieux les relations entre la porosité et les propriétés de traction, les valeurs de R^2 obtenues montrent que cela n'est pas le facteur primaire contrôlant la ductilité et la résistance en traction. Aucune corrélation définie n'a pu être établie entre la porosité et la limite élastique. Des corrélations linéaires assez bonnes ont été obtenues entre le log de la limite ultime et le log de la déformation (%) pour tous les alliages, expérimentaux ou industriels, sous toutes les conditions (R^2 : 0.6-0.93). L'utilisation de cette relation est recommandée au lieu de la relation entre la limite ultime et le log de la déformation (%) basée sur le concept d'index de qualité proposé par Drouzy *et al.*[136] pour interpréter les propriétés de traction des deux systèmes d'alliages.

Les propriétés d'impact sont aussi améliorées avec l'augmentation du taux de refroidissement et la réduction du contenu en Fe. Les alliages modifiés 319.2 montrent des relations de puissances et linéaires (à des bas/hauts taux de refroidissement), alors que les alliages non modifiés 319.2 et A356.2 montrent des corrélations linéaires, tous les alliages B319.2 montrent de corrélations de puissance, et les alliages modifiés A356.2 montrent des corrélations logarithmiques à tous les taux de refroidissement (R^2 >0.95 dans tous les cas). Les propriétés d'impact obtenues au plus haut taux de refroidissement sont de loin supérieures à celles obtenues à des taux de refroidissement autres (*cf.* 12.4 J à 23 μm d'espace interdendritique avec 4.88 J à 85 μm d'espace interdendritique dans les alliages non modifiés 319.2). L'intermétallique β-Al_5FeSi détériore les propriétés d'impact de façon significative, l'effet étant le plus apparent pour des dimensions des plaquettes β se situant à l'intérieur de la plage 30-150 μm dans les alliages 319, et 10-50 μm dans les alliages A356.2. Des corrélations assez bonnes ont été obtenues entre les porosités et les propriétés d'impact. En présence de Mg, l'alliage non modifié B319.2 montre une augmentation de l'énergie d'impact, particulièrement à des niveaux faibles (0.4%) en Fe et à des taux de refroidissement élevés (espace interdendritique 23-47 μm). Le strontium est efficace dans l'amélioration de l'énergie d'impact, même à des niveaux élevés en Fe. L'amélioration est moins apparente dans les alliages B319.2, et très sensible au changement du taux de refroidissement dans les alliages 319.2. Les alliages A356.2 modifiés au Sr montrent des énergies d'impact du double de celles des alliages 319 soumis aux mêmes conditions dû à l'absence de la phase $CuAl_2$ dans les premiers alliages. Une bonne relation inverse est obtenue entre la vitesse moyenne de fissuration et l'énergie d'impact, les plus hautes vitesses de fissuration étant observées dans les échantillons non modifiés obtenus à des contenus en Fe les plus élevés et aux taux de refroidissement les plus bas. Les essais d'impact sont plus sensibles aux variations dans la microstructure ou aux défauts de coulée que ne le sont les essais de traction. Les courbes d'énergie d'impact en fonction de la limite ultime montrent des relations exponentielles, tandis que les courbes d'énergie d'impact en fonction de la déformation (%) affichent des relations linéaires pour tous les d'alliages, modifiés ou non, et peu importe la composition de l'alliage.

À de faibles niveaux de Fe et à des taux de refroidissement élevés (0.4% Fe, espace interdendritique de 23 μm), l'initiation et la propagation des fissures dans les alliages non

modifiés 319, se produisent par le clivage des plaquettes de β-Al_5FeSi (au lieu de leur décohésion de la matrice). La morphologie des plaquettes (individuelles ou embranchées) est importante pour déterminer la direction de propagation de la fissure. Les fissures se propagent aussi par la fracture du $CuAl_2$ non dissous ou d'autres intermétalliques de cuivre, aussi bien que par les particules de Si fragmentées. Dans les alliages 319 modifiés au Sr, les fissures sont majoritairement initiées par la fragmentation ou le clivage des plaquettes perforées de la phase β, en addition à celles des particules grossières de Si et des intermétalliques de cuivre non dissous. Dans les alliages A356.2, les fissures sont initiées principalement par la fracture des particules de Si ou leur détachement de la matrice de Al, alors que la propagation des fissures a lieu par coalescence des particules de Si fracturées, excepté quand les intermétalliques de β-Al_5FeSi sont présents, auquel cas ce dernier a préséance. Dans le cas de modification au Sr, les fissures se propagent par la liaison des particules de Si fracturées / détachées, aussi bien que par les intermétalliques β-fer fragmentés. Dans les échantillons exhibant de basses énergies d'impact, l'initiation et la propagation des fissures se produisent principalement par le clivage des intermétalliques de β-fer.

ABSTRACT

Aluminum-silicon (Al-Si) alloys are an important class of materials that constitute the majority of aluminum cast parts produced, due to their superior properties and excellent casting characteristics. Within this family of alloys, Al-Si-Cu and Al-Si-Mg cast alloys are frequently employed in automotive applications. The commercially popular 319 and 356 alloys, representing these two alloy systems, were selected for study in the present work, with the aim of investigating the effect of iron intermetallics and porosity on the alloy performance. This was carried out through a study of the tensile and impact properties, these being two of the important mechanical properties used in design calculations. Iron, through the precipitation of second phase intermetallic constituents, in particular the plate-like β-Al_5FeSi phase, is harmful to the alloy properties. Likewise, gas- or shrinkage porosity in castings is also detrimental to the mechanical properties. By determining the optimum alloying, melt processing and solidification parameters (*viz.*, Fe content, Sr modification and cooling rate) required to minimize the harmful effects of porosity and iron intermetallics, and studying their role on the fracture behavior, the fracture mechanism in the alloys could be determined.

Castings were prepared from both industrial and experimental 319.2, B319.2 and A356.2 alloy melts, containing Fe levels of 0.2-1.0 wt%. Sr-modified (~200 ppm) melts were also prepared for each alloy Fe level. The end-chilled refractory mold used provided directional solidification and a range of cooling rates (or dendrite arm spacings, DAS) within the same casting. Tensile and impact test samples machined from specimen blanks sectioned from the castings at various heights above the chill end provided DASs of 23-85μm. All samples were T6-heat-treated before testing. Tests were carried out employing Instron Universal and Instrumented Charpy testing machines. Optical microscopy, image analysis, SEM and EPMA techniques were used for microstructural and fracture analysis.

The results show that the highest cooling rate (23 μm DAS) is the most significant parameter controlling the size and distribution of the β-Al_5FeSi phase and porosity in the unmodified 319.2 and A356.2 alloys. Sr modification is more effective in reducing the β-platelet size at low Fe levels, but increases both porosity volume fraction and pore size significantly. The Mg-containing B319.2 alloy shows reduction in the β-platelet size due to its partial transformation into $Al_8FeMg_3Si_6$ Chinese script particles. In the Sr-modified alloys, increase in the β-platelet size is still observed at some cooling rates. Porosity volume fraction and pore size also decrease with Mg addition.

Alloy ductility is improved by simultaneous increase in cooling rate and decrease in Fe content. Ductility of B319.2 alloy is lower than that of 319.2, due to precipitation of Mg_2Si, partial transformation of β-Al_5FeSi into $Al_8FeMg_3Si_6$, and an Sr-Mg interaction that diminishes the effectiveness of Sr modification. The A356.2 alloy displays much higher ductilities than the 319 alloys for the same Fe level, due to absence of the $CuAl_2$ intermetallic phase in the former. Modification with Sr also improves both ductility and tensile strength, and is useful in maintaining a consistent UTS level in 319 alloys, in that much less dispersion of UTS values is observed, regardless of their source (experimental or industrial). No apparent effect on YS is observed.

Iron deteriorates UTS in unmodified-experimental and modified-industrial 319.2 alloys, B319.2 and A356.2 alloys. Second-degree polynomial correlations are obtained between UTS and Fe content at all cooling rates (R^2 >0.8) for most alloys; the modified-experimental and unmodified-industrial 319.2 alloys, however, show considerable dispersion in UTS. Correlation between yield strength and Fe content or cooling rate is more complex: in general, YS increases with both cooling rate and Fe content in 319.2 alloys (R^2 >0.8). In B319.2 alloys, effect of cooling rate is not very apparent: Fe increases YS in the experimental alloys, but decreases it in the industrial alloys. In A356.2 alloys, YS values are distributed within a narrow band that shows a decreasing trend in the unmodified alloys, and an increasing trend in the modified alloys.

The β-Al_5FeSi platelet size is deleterious to alloy ductility and tensile strength, the changes being very noticeable up to β-platelet lengths (areas) of ~100 μm (400 μm^2) in the 319 alloys and ~70 μm (300 μm^2) in the A356.2 alloys. Power or logarithmic correlations are obtained between ductility and β-platelet size (R^2 >0.8). In the A356.2 alloys, only small variations in β-size can be tolerated to maintain satisfactory ductility levels. Decrease in UTS with β-platelet size is sharper in the 319.2 alloys than in B319.2 and A356.2 alloys. No definite relation between β-platelet size and YS was established.

Porosity is harmful to alloy strength and ductility. Although the maximum pore size parameter best characterizes the porosity-tensile property relationships, the R^2 values obtained show that it is not the primary factor controlling ductility and tensile strength. No definite correlation between porosity and YS was established. Fairly good linear correlations are obtained between log UTS and log El% for all alloys, experimental or industrial, under all conditions. (R^2 : 0.6-0.93). The use of this relation is recommended in place of the UTS vs. log El% plots of the quality index concept proposed by Drouzy *et al.*[136] to interpret the tensile properties of the two alloy systems.

Impact properties also improve with increase in cooling rate and decrease in Fe content. Modified 319.2 alloys show linear/power relations (at low/high cooling rates), while unmodified 319.2 and A356.2 alloys show linear correlations, all B319.2 alloys show power correlations, and modified A356.2 alloys show logarithmic correlations at all cooling rates (R^2 >0.95 in all cases). Impact properties obtained at the highest cooling rate are far superior to those obtained at other cooling rates (*cf.* 12.4 J at 23 μm DAS with 4.88 J at

85 μm DAS in unmodified 319.2 alloy). The β-Al_5FeSi intermetallic deteriorates impact properties significantly, the effect being most apparent within 30-150 μm β-platelet sizes in 319 alloys, and 10-50 μm β-platelet sizes in A356.2 alloy. Fairly good correlations between porosity and impact properties are obtained. In the presence of Mg, unmodified B319.2 alloys show an increase in impact energy, particularly at low Fe levels (0.4%) and high cooling rates (23-47 μm DAS). Strontium is effective in improving impact energy, even at high Fe levels. The improvement is less apparent in B319.2 alloys, and very sensitive to change in cooling rate in 319.2 alloys. Sr-modified A356.2 alloys show impact energies double those of 319 alloys under the same conditions, due to the absence of the $CuAl_2$ phase in the former. A good inverse relation is obtained between average crack speed and impact energy, highest crack speeds being observed in unmodified samples obtained at highest Fe contents and lowest cooling rates. Impact testing is more sensitive to variations in microstructure or casting defects than tensile testing. Impact energy-UTS plots show exponential relationships, whereas impact energy-El% plots display linear relationships for all alloys, modified or not, and regardless of the alloy composition.

At low Fe levels and high cooling rates (0.4% Fe, 23 μm DAS), crack initiation and propagation in unmodified 319 alloys occurs through the cleavage of β-Al_5FeSi platelets (rather than by their decohesion from the matrix). The morphology of the platelets (individual or branched) is important in determining the direction of crack propagation. Cracks also propagate through the fracture of undissolved $CuAl_2$ or other Cu-intermetallics, as well as through fragmented Si particles. In Sr-modified 319 alloys, cracks are mostly initiated by the fragmentation or cleavage of perforated β-phase platelets, in addition to that of coarse Si particles and undissolved Cu-intermetallics. In A356.2 alloys, cracks initiate mainly through the fracture of Si particles or their debonding from the Al matrix, while crack propagation occurs through the coalescence of fractured Si particles, except when β-Al_5FeSi intermetallics are present, in which case the latter take precedence. In the Sr-modified case, cracks propagate through the linkage of fractured/debonded Si particles, as well as fragmented β-iron intermetallics. In samples exhibiting low impact energies, crack initiation and propagation occur mainly through cleavage of the β-iron intermetallics.

ACKNOWLEDGEMENTS

It is a great pleasure to finally have the chance to acknowledge all those who were involved directly or indirectly in making this work a success. I take it a pleasure to convey my sincere thanks to my supervisors Professors F. H. Samuel and A. M. Samuel for their invaluable guidance in each stage of my study.

Financial assistance (scholarships) and in-kind support received from the Natural Sciences and Engineering Research Council of Canada (NSERC), General Motors Powertrain Group (U.S.A.), Corporativo Nemak (Mexico), and the Centre québécois de recherche et de développement de l'aluminium (CQRDA) is gratefully acknowledged.

I would like to express my appreciation to several colleagues, particularly Mr. André Bouchard and Mr. Alain Bérubé, for their help and for creating an enjoyable working atmosphere. I wish to acknowledge Mrs. Li Liu for the courtesy of providing a major part of the β-iron intermetallic and porosity data, and Mr. Carl Lepage for his valuable assistance with the French abstract. Many thanks go to Dr. Jijin Yang who motivated me to join UQAC and who has been a constant source of encourgement.

Finally, I would like to record my deep gratitude to the members of my family, especially my parents. Without their encouragement and support, I would not have enough strength to finish my work.

TABLE OF CONTENTS

LIST OF TABLES

LIST OF FIGURES

Chapter 2

Chapter 3

Chapter 4

Chapter 5

Chapter 6

CHAPTER 1

DEFINITION OF THE PROBLEM

CHAPTER 1

DEFINITION OF THE PROBLEM

1.1 INTRODUCTION

Aluminum cast alloys are the most versatile of all foundry alloys and generally have high castability ratings. Among them, Al-Si alloys are by far the most important commercial cast alloys (constituting 85% to 90% of the total aluminum cast parts produced[1]), on account of their superiority to other alloy systems in casting characteristics.

In the present work, Al-Si-Cu and Al-Si-Mg cast alloys, belonging to the Al-Si alloy system and represented respectively by 319 and 356 alloys, were selected for study, due to the high demand of these alloys in the automobile industry, which is the largest consumer of Al-Si cast alloys.

Iron is the most deleterious impurity element normally present in such alloys. The high difference in the solubility of iron in molten and solid aluminum makes most of the iron appear as an intermetallic second phase (in combination with Al or other elements), which deteriorates the mechanical properties. Iron also plays an important role in porosity formation in Al-Si casting alloys. Common sources of iron pick-up in foundry processing are from melting equipment and from remelted scrap castings. Increased activity in the recycling of spent automobiles in order to cut down alloy production costs has caused iron

levels to soar as high as 1.5-2.0%. Iron cannot be readily removed from molten aluminum by conventional foundry treatments.

Porosity in castings is always detrimental to mechanical properties, especially ductility, fracture toughness, fatigue life and in some cases, the surface finish.[2] It also reduces the casting size, depreciates corrosion stability and has a particularly bad influence on dynamic strength.[3] Two types of porosity are observed in Al-Si cast alloys: (a) gas porosity, mainly caused by the evolution of dissolved hydrogen due to the difference in its solubility in solid and liquid aluminum, or reactions in the liquid, and (b) shrinkage porosity created by the density difference between liquid and solid metals and inadequate liquid mobility (limited feeding).[4-8]

Tensile and impact properties are two of the important mechanical properties that are routinely determined and used in design calculations. Tensile testing is one of the most common methods used to measure the static mechanical properties of a metallic material. From a complete record of tensile testing data, a lot of important information can be obtained, such as the properties and degrees of elastic and plastic deformations, yield strength, ultimate tensile strength, the energy needed for tensile fracture, *etc.*

Impact behavior, namely impact toughness, is usually defined by the total energy absorbed by a specimen in fracturing it. This fracture occurs under an impact test at a high strain rate or rapid rate of loading which causes a brittle fracture. Castings which have identical properties when tested in tension or torsion at slow strain rates can show pronounced differences in their tendency for brittle fracture when tested in an impact test. Both the tensile and impact properties can be correlated to the microstructure and the

formation of iron intermetallics and porosity. In general, with the increase of the volume fraction and size of intermetallics and porosity, the tensile and impact properties decrease.

1.2 OBJECTIVES

In the present work, the 319 and 356 alloys were selected to study the effect of iron intermetallics and porosity on the tensile and impact properties. Both experimental and industrial alloys were employed, to obtain an estimation of the scatter in properties expected with the use of industrial alloys. The main goals of the study were as follows.

1. To determine the effect of iron intermetallics and porosity on alloy performance through a study of the tensile and impact behavior in the 319 and 356 alloys.
2. To determine the optimum alloying and melt processing parameters in order to minimize the harmful effects of said porosity and intermetallics in relation to these properties.
3. To study the role played by iron intermetallics, as well as porosity, on fracture behavior, and hence determine the fracture mechanism of these alloys.

CHAPTER 2

LITERATURE REVIEW

CHAPTER 2

LITERATURE REVIEW

2.1 INTRODUCTION

Aluminum alloys containing silicon as the major alloying element offer excellent castability, high wear and corrosion resistance, good weldability, low specific gravity, high thermal conductivity, reduction of the coefficient of thermal expansion (due to the added silicon), and good retention of physical and mechanical properties at elevated temperatures.[9,10] It is for this reason that aluminum-silicon (Al-Si) alloy castings constitute 85 to 90% of the total aluminum cast parts produced.

Due to their excellent strength-to-weight ratio, Al-Si castings obtain extensive applications in the automobile industry, where there has been a continuing demand for greater fuel efficiency and higher performance. Both of these can be achieved by reducing the weight of vehicles, and by using materials with high thermal conductivity for some specific parts. For example, the low density of aluminum is of particular importance in the reciprocating parts of an engine; the lower inertia permits increased engine speed and efficiency. The high thermal conductivity of aluminum is advantageous for thermally loaded parts such as pistons, cylinder blocks and heads. Today, aluminum has replaced steel in automobile wheels, because of its superior heat dissipation during braking, which

allows for improved road handling and decreased tire wear. In addition, weight savings of about 25 kg can be achieved by using aluminum in place of steel. Due to their much lighter weight, Al-Si castings have gradually replaced automobile parts such as transmission cases, intake manifolds, and certain engine blocks and cylinder heads, that were formerly monopolized by cast iron.

Palazzo,[11] in a 1977 study, showed a direct correlation between vehicle weight and fuel consumption. In a survey according to Armstrong,[12] a cast iron engine block replaced by an Al-Si casting results in direct weight savings of about 50%, with indirect weight reductions of an additional 25%. Ford and Alusuisse have published estimates of fuel savings through the use of aluminum.[1] For example, Ford has shown that a 200 kg weight reduction leads to a fuel reduction of 1 liter for every 120 km. This amounts to savings of about 1000 liters over the life of the vehicle. A study by Alusuisse[1] demonstrates that the replacement of steel components by 50 kg of aluminum results in fuel savings of almost 850 liters over a ten-year period.

Aluminum casting alloys are commonly grouped into various alloy series, depending upon the alloying elements they contain. A detailed description of the designation system is provided in the following section (2.2). Among the most common aluminum casting alloys are 319.0 (Al-6Si-3.5Cu), 332.0 (Al-9.5Si-3Cu-1.0Mg), 355.0 (Al-5Si-1.3Cu-0.5Mg), A356.0 (Al-7Si-0.3Mg), A357.0 (Al-7Si-0.5Mg), 380.0 (Al-8.5Si-3.5Cu), 383.0 (Al-10.5Si-2.5Cu), 384.0 (Al-11.2Si-3.8Cu), 390.0 (Al-17.0Si-4.5Cu-0.6Mg), 413.0 (Al-12Si) and 443.0 (Al-5.2Si). Their properties are summarized in Table 2.1 (except for 383.0 and 384.0 alloys).

Table 2.1. Characteristics of various aluminum-silicon casting alloys[1]

Alloy	Casting Method	Resistance To Tearing	Pressure Tightness	Fluidity	Shrinkage Tendency	Corrosion Resistance	Machin-ability	Weldability
319.0	S, P	2	2	2	2	3	3	2
332.0	P	1	2	1	2	3	4	2
355.0	S, P	1	1	1	1	3	3	2
A356.0	S, P	1	1	1	1	2	3	2
A357.0	S, P	1	1	1	1	2	3	2
380.0	D	2	1	2	-	5	3	4
390.0	D	2	2	2	-	2	4	2
413.0	D	1	2	1	-	2	4	4
443.0	P	1	1	2	1	2	5	1

Ratings: 1 - best, 5 - worst; S = sand casting, P = permanent mold casting

2.2 DESIGNATION SYSTEM OF ALUMINUM CASTING ALLOY SERIES

The most commonly used designation system for aluminum casting alloys is the three-digit system (*i.e.*, 1xx.x, 2xx.x, *etc.*) proposed by the Aluminum Association (AA).[13] The first digit indicates the alloying group. The second and the third digits identify the specific aluminum alloy according to its alloying elements, or indicate aluminum purity for the aluminum (1xx.x) series. A decimal value always follows, where decimal .0 in all cases represents chemical composition limits for casting, while decimals .1 and .2 concern chemical composition limits for ingots. Several AA alloy designations also include a prefix letter, which distinguishes alloys of a general composition (with the same alloy number) only in percentage of impurities or minor alloying elements, *e.g.*, 319, A319 and B319.

The AA designations of aluminum casting alloy series are given as follows.[13]

1xx.x Series: Controlled unalloyed compositions (pure aluminum).

2xx.x Series: Aluminum alloys containing copper as the major alloying element. Other alloying elements may be specified.

3xx.x Series: Aluminum-silicon alloys containing magnesium and/or copper.

4xx.x Series: Binary aluminum-silicon alloys.

5xx.x Series: Aluminum alloys containing magnesium as the major alloying element.

6xx.x Series: Unused.

7xx.x Series: Aluminum alloys containing zinc as the major alloying element.

8xx.x Series: Aluminum alloys containing tin as the major alloying element.

9xx.x Series: Unused.

2.3 HEAT TREATMENT OF ALUMINUM CAST ALLOYS

Aluminum castings must meet specific properties, such as strength and hardness, as well as resistance to wear, creep or fatigue, when they are used for automotive applications. These properties are effected by selecting different combinations of alloying elements, thermo-mechanical history and heat treatment.[14]

Heat treatment plays the most important role after the castings have been produced. Different types of heat treatment sequences or tempers are used to attain various property specifications. The main objectives[15] of heat treatment are to:

a) Increase strength and produce the particular mechanical properties that are associated with specific final tempers,

b) Stabilize mechanical or physical properties or resistance to corrosion, and avoid changes that would otherwise occur with time at normal or elevated temperatures,

c) Insure dimensional stability during service, particularly for parts that operate at elevated temperatures and require close dimensional control, and

d) Relieve residual stresses induced by differential deformation or non-uniform cooling resulting from casting, quenching, welding or forging operations.

2.3.1 Mechanism of Strengthening Through Heat Treatment

Strengthening is the most common phenomenon that occurs in cast aluminum alloys during the heat treatment processing. This phenomenon is normally related to solution heat treating and precipitation (or age) hardening. The change in solid solubility with temperature is a primary factor with respect to the effect of heat treatment on alloying elements. Another fundamental factor influencing the kinetics of the solid-state reactions of a given solute is its mobility in the aluminum solid solution.[16]

Solution Heat Treating Aluminum cast alloys always contain amounts of alloying elements that are more soluble at elevated temperatures than at room temperature, which exceed the equilibrium solid limit at room and moderately higher temperatures. Thus, the holding of these alloys at an elevated temperature (slightly below the eutectic temperature) causes the alloying elements to go back into solid solution. If the alloy is then cooled very rapidly (quenched), a solid-solution supersaturated condition is obtained, giving the excessive solutes (alloying elements) – over the amount actually soluble at low temperature – a tendency to precipitate. The driving force of precipitation increases with the degree of supersaturation, decreasing temperature and increasing solute atom percentage, as well as atomic mobility (which is reduced as the temperature decreases).

The strength of the alloy is developed as the alloying elements precipitate out of solution with the passage of time. This effect is referred to as precipitation hardening or age

hardening, which may include either natural aging or artificial aging. Thus, the main purpose of solution heat treatment is to put maximum practical amounts of hardening solutes (alloying elements) into solid solution in the aluminum matrix.

Precipitation Hardening (Age Hardening) At relatively low temperatures, and during initial periods of artificial aging at moderate temperatures, the mechanism of strengthening by age hardening involves the formation of coherent clusters of solute atoms, or Guinier-Preston (GP) zones. That is to say, the solute atoms collect into clusters, but still have the same crystal structure as the solvent phase. These clusters cause a great deal of strain because of the mismatch in size between the solvent and solute atoms. An additional strengthening effect also results from interference to the motion of dislocations when they cut the GP zones. As the aging temperature or time are increased, the GP zones are either converted into, or replaced by, transition precipitates, which are particles that have a crystal structure distinct from that of the solid solution and also different from the structure of the equilibrium phase. The strengthening effects of these transition structures are related to the impediment provided by the presence of lattice strains and precipitate particles to the dislocations. Strength continues to increase as the size of these precipitates increases, as long as the dislocations continue to cut the precipitates. By means of precipitation hardening, alloys can reach the highest strengths of which they are capable.

Varying degrees of age hardening occur at room temperature (which is a process of zone formation, not true precipitation[17]). However, artificial aging (or precipitation heat treatment at high temperature) is usually employed to develop maximum strengths as quickly as possible. Figure 2.1 shows an example of the temperature range of solution heat

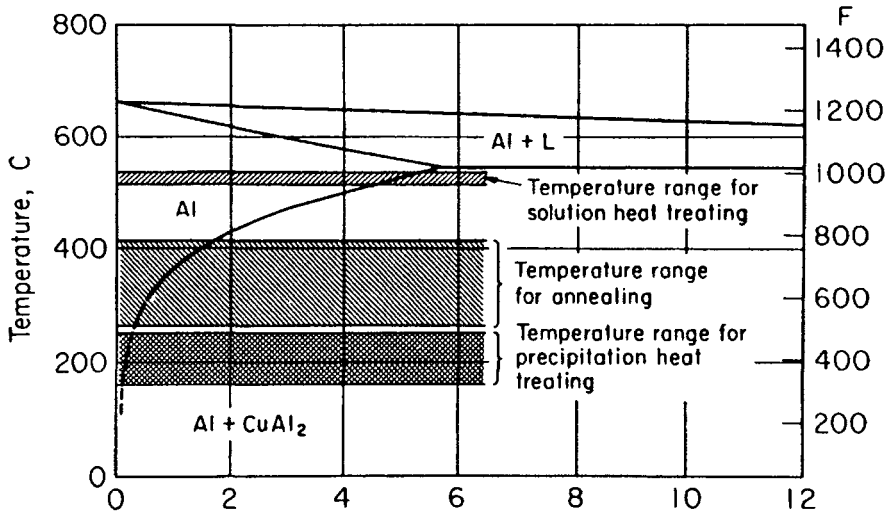

Figure 2.1. Partial equilibrium diagram for aluminum-copper alloys.[15-17]

treating and precipitation heat treating used for aluminum-copper alloys.[15-17] Solution of the relatively large microconstituents present in casting alloys requires longer soaking times than those required in the case of wrought alloys.

2.4 TEMPER DESIGNATION SYSTEM

Different types of heat treatment sequences, *i.e.*, different tempers, are used in Al-Si alloys. They are indicated by a temper designation system, which is used, in general, for all forms of cast aluminum alloys that are strengthened by heat treatment, except ingots. The commonly used temper designations for cast aluminum alloys are as follows.[15-17]

W **Solution heat treated:** An unstable temper applicable only to alloys which age spontaneously at room temperature.

T **Thermally treated to produce stable temper:** Applied to products which are thermally treated, with or without supplementary strain hardening, to produce stable tempers.

The **T** is always followed by one or more digits. A period of natural aging at room temperature may occur between or after the operations used in different **T** tempers. Some of the specific treatments most commonly used are listed below.[15-17]

T5 Cooled from an elevated temperature shaping process and then artificially aged: Applies to products that are not cold worked after cooling from an elevated-temperature shaping process, such as casting.

T6 Solution heat treated and then artificially aged: Applies to products that are not cold worked after solution heat treatment.

T7 Solution heat treated and stabilized: Applied to products that are stabilized after solution heat treatment, to carry them beyond the point of maximum strength in order to provide control of specific characteristics.

In the present work, the T6 temper was applied to Al-Si casting alloys in keeping with the AA recommendations. During solution heat treatment, it is essential to avoid too high a solution temperature, especially in 319 alloys which have a low melting-point Al-$CuAl_2$ eutectic, with a melting temperature of 548 °C, to prevent any appearance of the liquid phase (*i.e.*, incipient melting), which can be detrimental to the mechanical properties. Details of these alloys are discussed in the following section.

2.5 SELECTION OF Al-Si-Cu AND Al-Si-Mg CAST ALLOYS

In the present study, 319 and 356 alloys, belonging respectively to the Al-Si-Cu and Al-Si-Mg groups of the 3xx.x alloy series, were selected for study, being the two most commercially popular alloys (containing high levels of iron (~1.2% max)) used by the

automotive industry. Being the largest consumer of cast Al-Si alloys, the automobile industry consumes well over half of all aluminum castings produced annually in the U.S. and Canada.

2.5.1 Al-Si-Cu (319) Cast Alloys

Al-Si-Cu cast alloys contain both copper and magnesium as the hardening elements, and are mostly used in automotive cylinder heads, internal combustion engine crankcases, typewriter frames and piano plates, as well as other applications where good casting characteristics and weldability, pressure tightness and moderate strength are required. Their physical and mechanical properties are given below.

Chemical Composition: The chemical composition specification limits for the 319 type alloys are listed in Table 2.2. It has been reported that mechanical properties are relatively insensitive to impurities when the impurity limits are exceeded.[16]

Table 2.2. Chemical composition limits of 319 type alloys[16]

AA	Elements (%)									
Alloy	Si	Fe	Cu	Mn	Mg	Ni	Zn	Ti	Others (Total)	Al
319.0	5.5-6.5	1.0	3.0-4.0	0.50	0.10	0.35	1.0	0.25	0.50	bal
319.1	5.5-6.5	0.8	3.0-4.0	0.50	0.10	0.35	1.0	0.25	0.50	bal
319.2	5.5-6.5	0.6	3.0-4.0	0.10	0.10	0.10	0.10	0.20	0.20	bal
A319.0	5.5-6.5	1.0	3.0-4.0	0.50	0.10	0.35	3.0	0.25	0.50	bal
A319.1	5.5-6.5	0.8	3.0-4.0	0.50	0.10	0.35	3.0	0.25	0.50	bal
B319.0	5.5-6.5	1.2	3.0-4.0	0.8	0.10-0.50	0.50	1.0	0.25	0.50	bal
B319.1	5.5-6.5	0.9	3.0-4.0	0.8	0.15-0.50	0.50	1.0	0.25	0.50	bal

As mentioned previously, 319.0 refers to the composition of 319 castings, whereas 319.1 and 319.2 refer to those of the ingots. The prefixes A, B, *etc.* indicate the differences in impurities or minor alloying elements such as Mg. In the present study, both 319.2 and B319.2 alloys were employed, where the B319.2 alloys possess a higher magnesium content (compared to the 319.2 alloys), which helps to accelerate and intensify age hardening during the T6 temper. For this reason, the B319 type alloys are generally preferred in automotive applications.

Physical Constants:

Density (at 20 °C)	2790 kg/m^3
Liquidus temperature	605 °C
Solidus temperature	515 °C
Coefficient of linear thermal expansion (at 20°-200 °C)	23.0 μm/m·K
Specific heat (at 100 °C)	963 J/kg·K
Latent heat of fusion	389 kJ/kg
Thermal conductivity (at 25 °C)	109 W/m·K
Electrical conductivity (volumetric, at 20 °C)	27 %IACS
Electrical resistivity (sand, at 20 °C)	63.9 nΩ·m

Castability and Fabrication: Both sand castings and permanent mold castings are prepared from 319 alloys, as they have very good resistance to hot cracking and solidification shrinkage, as well as good fluidity and pressure tightness. The melting temperature range is around 675°-815 °C, and the casting temperature is about 675°-790 °C. For oxide separation and removal during the foundry processing of these alloys, a gas-type flux such as nitrogen or chlorine, or a solid aluminum chloride base flux is used.

For heat treatment, sand cast alloys are given either T5 or T6 temper treatment, while permanent mold cast alloys are usually given a T6 temper treatment. To fulfill different tempers, a specific solution heat treatment, quenching and aging treatment (for T6 temper) are required. Solution heat treatment is usually carried out at a temperature of 500° to 505 °C, and holding for 12 h (sand casting) or 8 h (permanent mold casting) at this temperature. Quenching is accomplished in water at 65° to 100 °C. Aging (for T6 temper from solution-treated material) is done at 150° to 155 °C, for times ranging from 2 to 5 h.

Mechanical Properties: Typical mechanical properties[16] for cast test bars of alloy 319.0 are shown in Table 2.3.

Table 2.3. Typical mechanical properties of 319.0 alloys[16]

Property	Sand Cast		Permanent Mold Cast	
	As-cast	T6	As-cast	T6
Tensile Strength, (MPa)	185	250	235	280
Yield Strength, (MPa)	125	165	130	185
Elongation, (%)[a]	2.0	2.0	2.5	3.0
Hardness, HB[b]	70	80	85	95
Shear Strength, MPa	150	200	165	185
Fatigue Strength, MPa[c]	70	75	70	...
Compact Yield Strength, MPa	130	170	130	...

(a) in 50 mm or 2 in. (b) 500 kg load; 10 mm ball. (c) at 5×10^8 cycles; R.R. Moore type test.

2.5.2 Al-Si-Mg (356) Cast Alloys

Al-Si-Mg alloys, widely used for load-bearing structural components, as well as in less high-stress applications, contain magnesium as the hardening element. The 356.0 cast

alloys are typically used in the production of aircraft pump parts, automotive transmission cases, aircraft fitting and control parts, water-cooled cylinder blocks, and in other applications where excellent castability, and good weldability, pressure tightness and resistance to corrosion are required. A356.0 cast alloys are typically used in aircraft structures and engine controls, nuclear engine installations, *etc.*, where high-strength permanent mold or investment castings are required. Their physical and mechanical properties are listed below.

Chemical Composition: The chemical composition specification limits for the 356 type alloys are listed in Table 2.4. High copper or nickel levels decrease ductility and resistance to corrosion, whereas a high iron level decreases strength and ductility, so the limitation control or neutralization of these elements is essential.[16]

Table 2.4. Chemical composition limits of 356 type alloys[16]

AA	Elements (%)										
Alloy	Si	Fe	Cu	Mn	Mg	Ni	Zn	Ti	Others Each	Others Total	Al
356.0	6.5-7.5	0.6	0.25	0.35	0.20-0.45	...	0.35	0.25	0.05	0.15	Bal
356.1	6.5-7.5	0.50	0.25	0.35	0.25-0.45	...	0.35	0.25	0.05	0.15	Bal
356.2	6.5-7.5	0.13-0.25	0.10	0.05	0.30-0.45	...	0.05	0.20	0.05	0.15	Bal
A356.0	6.5-7.5	0.20	0.20	0.10	0.25-0.45	...	0.10	0.20	0.05	0.15	Bal
A356.1	6.5-7.5	0.15	0.20	0.10	0.30-0.45	...	0.10	0.20	0.05	0.15	Bal
A356.2	6.5-7.5	0.12	0.10	0.05	0.30-0.45	...	0.05	0.20	0.05	0.15	Bal
B356.0	6.5-7.5	0.09	0.05	0.05	0.25-0.45	...	0.05	0.04-0.20	0.05	0.15	Bal
B356.2	6.5-7.5	0.06	0.03	0.03	0.30-0.45	...	0.03	0.04-0.20	0.03	0.10	Bal
C356.0	6.5-7.5	0.07	0.05	0.05	0.25-0.45	...	0.05	0.04-0.20	0.05	0.15	Bal
C356.2	6.5-7.5	0.04	0.03	0.03	0.30-0.45	...	0.03	0.04-0.20	0.03	0.10	Bal

Compared to 319 alloys, 356 alloys have a stricter control over impurities, especially iron, which is detrimental to the alloy mechanical properties. The deleterious effect of iron on mechanical properties will be discussed in Section 2.7.4.

Physical Constants:

Density (at 20 °C)	2685 kg/m^3
Liquidus temperature	615 °C
Solidus temperature	555 °C
Coefficient of linear thermal expansion (at 20-200 °C)	22.5 μm/m·K
Specific heat (at 100 °C)	963 J/kg·K
Latent heat of fusion	389 kJ/kg
Thermal conductivity (at 25 °C) (T6, permanent mold)	167 W/m·K
Electrical conductivity (volumetric, at 20 °C) (T6, permanent mold)	41 %IACS
Electrical resistivity (sand, at 20 °C)	42.1 nΩ·m

Castability and Fabrication: Both sand and permanent mold castings are prepared from 356 alloys. These alloys also possess excellent resistance to hot cracking and solidification shrinkage, as well as excellent press tightness and fluidity common among Al-Si cast alloys. The corrosion resistance and weldability are also very good, whereas machinability is about average. The melting temperature range is around 675°-815 °C and the casting temperature is about 675°-790 °C.

For heat treatment, sand cast alloys are given either a T5 or T6 temper treatment, while permanent mold cast alloys are usually given a T6 temper treatment. Table 2.5 summarizes the different solution and aging treatments applied to 356 type alloys.[16]

Table 2.5. Heat treatment for cast test bars of alloys 356.0 and A356.0[16]

Casting type	Solution		Aging							
			T51[c]		T6[d]		T7[d,e]		T71[d]	
	Temp. (°C)	Time (h)	Temp. (°C)	Time (h)	Temp. (°C)	Time (h)	Temp. (°C)	Time (h)	Temp. (°C)	Time (h)
Sand castings	535-540	12[a,b]	225-230	7-9	150-155	2-5	225-230	7-9	245-250	2-4
Permanent mold castings	535-540	8[a,b]	225-230	7-9	150-155	3-5	225-230	7-9	245-250	2-4

(a) Soaking-time periods required for average casting after load has reached specified temperature. Time can be decreased or may have to be increased, depending on experience with particular castings.

(b) Cool in water at 65 to 100 °C.

(c) No solution heat treatment.

(d) Start with solution heat-treated materials.

(e) U.S. Patent 1,822,877.

Mechanical Properties: Typical mechanical properties[16] for cast test bars of alloy 356.0 are shown in Table 2.6.

Table 2.6. Typical mechanical properties of cast test bars of alloy 356.0[16]

Property	Sand Cast				Permanent Mold Cast	
	T51	T6	T7	T71	T6	T7
Tensile Strength, MPa	172	228	234	193	262	221
Yield Strength, MPa	140	165	205	145	185	165
Elongation, %[a]	2.0	3.5	2.0	3.5	5.0	6.0
Hardness, HB[b]	60	70	75	60	80	70
Shear Strength, MPa	140	180	165	140	205	170
Fatigue Strength, MPa[c]	55	60	62	60	90	75
Compact Yield Strength, MPa	145	170	215	150	180	165

(a) in 50 mm or 2 in. (b) 500 kg load; 10 mm ball. (c) at 5×10^8 cycles; R.R. Moore type test.

2.6 MECHANICAL PROPERTIES OF Al-Si CAST ALLOYS

Meeting specific mechanical properties is the main objective in the design of aluminum alloys. In this connection, tensile and impact properties are two important mechanical properties that are routinely determined and used in design calculations.

2.6.1 Tensile Properties

Tensile testing is one of the most common methods used to measure the static mechanical properties of a metallic material. Hence, there is more data available on the tensile properties of Al-Si cast alloys and the influence of various factors such as modification and grain refinement on the former, than on any other properties. From a complete record of tensile testing data, a lot of important information can be obtained, such as the properties and degrees of elastic and plastic deformations, yield strength, ultimate tensile strength, the energy needed for tensile fracture, *etc.* The tensile properties of cast Al-Si alloys depend on several and often interrelated variables such as the solidification rate, casting soundness, heat treatment, eutectic modification, magnesium content, *etc.*[1]

The percent elongation to fracture (El%), yield strength (YS), and ultimate tensile strength (UTS) are most common indices for tensile properties. Stress-strain curves recorded from tensile tests are employed to determine these properties. A typical stress-strain curve is shown in Figure 2.2, where the engineering stress s and the engineering strain e are defined as

$$s = \frac{P}{A_0} \tag{2-1}$$

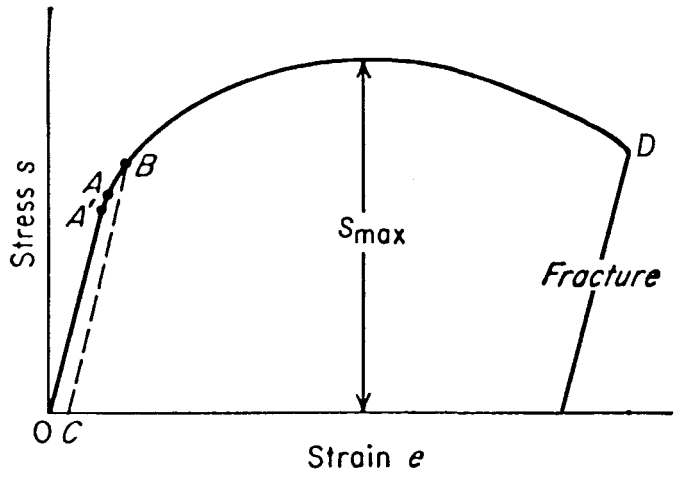

Figure 2.2. Typical tension stress-strain curve.[18]

$$e = \frac{l - l_0}{l_0} \tag{2-2}$$

where P is the load, A_0 is the specimen original (zero stress) cross-section area, l is the specimen gage length at a given load, and l_0 is the original (zero stress) gage length.[18]

Figure 2.2 is divided into two distinct regions: (1) elastic deformation and (2) plastic deformation. Elastic deformation is a temporary deformation, which means the specimen can fully recover when the load is removed. The elastic region in the stress-strain curve is the initial linear portion *OA* within which Hooke's law is obeyed. Point *A* is referred to as the *elastic limit*, and is defined as the greatest stress that the metal can withstand without experiencing a permanent strain when the load is removed. In some cases, only this part exists in the curve, and the fracture corresponds to a brittle fracture. As the determination of the elastic limit is quite tedious, the elastic limit A is often replaced by the *proportional limit, A'*, which is the stress at which the stress-strain curve deviates from linearity. Plastic deformation is a permanent deformation; it is not recovered when the load is removed. The

plastic region is the nonlinear portion, *AD*, and is generated once the total strain exceeds its elastic limit *A*. For engineering purposes, the limit of usable elastic behavior is described by the *yield strength*, given by the point *B* on the curve, defined as the stress which produces a small amount (0.2%) of permanent deformation. The maximum load divided by the original area of the specimen gives the *ultimate tensile strength* (s_{max}), and indicates the maximum stress the specimen can sustain. The final value of strain *e* is normally presented as a percentage, and is called the *percent elongation to fracture*, and indicates the general ability of the metal to be plastically deformed.

2.6.2 Impact Properties

Impact energy, namely impact toughness, is usually defined as the total energy absorbed by a specimen in fracturing it. This fracture occurs under an impact test with a high strain rate, or rapid rate of loading that causes a brittle fracture. Castings that have identical properties when tested in tension or torsion at slow strain rates, can show pronounced differences in their tendency for brittle fracture when tested in an impact test.

Impact values depend strongly on the testing method used. The most common laboratory measurement of impact energy is the Charpy test. The impact energy from the Charpy test correlates with the area under the total stress-strain curve of Figure 2.2, which is defined as toughness. In general, we expect alloys with large values of both strength (YS and UTS) and ductility (percent elongation to fracture) to have large impact fracture energies. Impact data are sensitive to test conditions and test temperatures, as well. For example, body-centered cubic (bcc) alloys show a dramatic variation in fracture mode with

temperature. In general, they fail in a brittle mode at relatively low temperatures and in a ductile mode at relatively high temperatures. They are also affected by modification, particularly if combined with heat treatment, which may lead to an increase of several hundred percent. An example of the load-deflection curve obtained for a Charpy-tested 356 alloy sample studied in the present work is illustrated in Figure 2.3. The *impact energy* is given by the total energy absorbed by the specimen during fracture, *i.e.*, 28.7 J in this case.

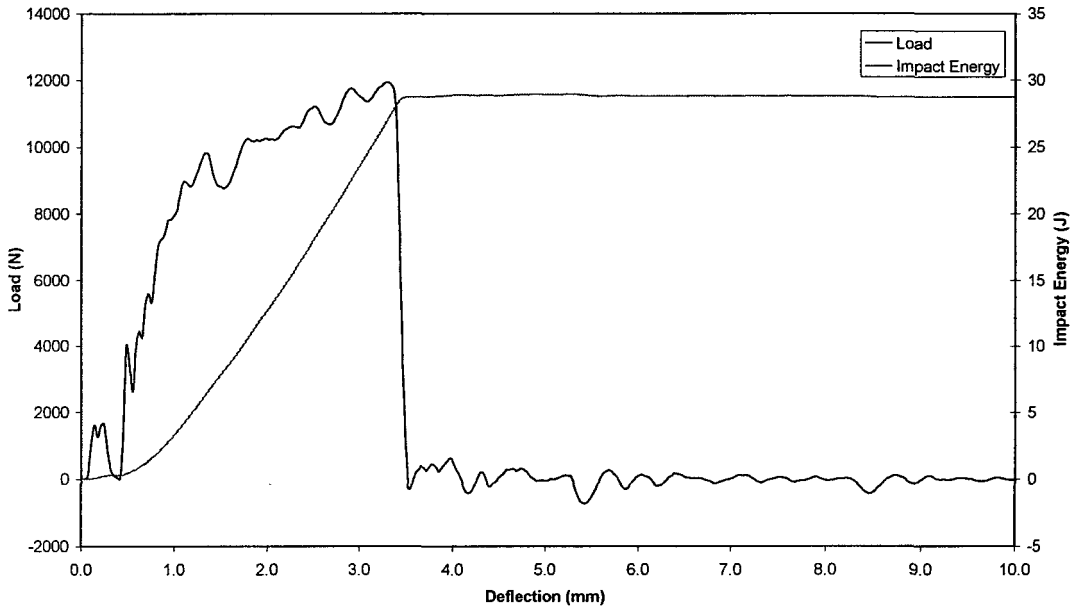

Figure 2.3. A load-deflection curve of a 356 alloy sample (present work).

In Al-Si alloys, the impact strength is a result of the separation of the ductile aluminum matrix from the brittle silicon phase particles. Thus, any process that reduces the size of these particles or increases the separation between them and the aluminum matrix will improve the impact properties. Modification of Al-Si alloys through the addition of a modifying agent such as strontium reduces the size of the silicon particles, whereas solution treatment of these alloys, during which coarsening of the silicon particles takes place,

increases the separation between the aluminum matrix and the silicon particles.[1] Thus, in both cases, the impact energy of the alloy is increased.

2.7 IRON INTERMETALLICS IN Al-Si CAST ALLOYS

Iron is one of the most common impurities normally present in Al-Si cast alloys.[19,20] Iron has a high solubility in molten aluminum and is therefore readily dissolved at all molten stages in production. The solubility of iron in the solid state is, however, very low (only ~0.05 wt% at 600 °C,[17] and even less at room temperature[20]), thus, most of the iron present above this level appears as an intermetallic second phase in combination with Al and other elements, which is detrimental to the mechanical properties. In Al-Si cast alloys the presence of iron, even in small amounts, can decrease the alloy ductility considerably, due to precipitation of the β-AlFeSi phase (details about β-AlFeSi will be discussed later) in the form of intercepted platelets.[21] The β-AlFeSi platelets act as stress raisers, which contribute to the brittleness of materials. Common sources of iron pick-up in foundry processing are from melting equipment and from remelted scrap castings. Increased activity in the recycling of spent automobiles in order to cut down alloy production costs has caused iron levels to increase as high as 1.5-2.0% in these alloys. Iron cannot be readily removed from molten aluminum by conventional foundry treatments. By the use of neutralization and/or modification methods, however, it is possible to reduce the harmful effects of iron intermetallics.

2.7.1 Chemical Composition and Morphology of Iron Intermetallics

The most complete literature review on intermetallic phases has been undertaken by Pearson.[22] A wide range of iron intermetallic particle types is reported in other works.[23-33]

Among these iron intermetallics, the most important ones with respect to Al-Si alloys are the α-AlFeSi (Chinese script) and β-AlFeSi (needle-, or thin platelet-like) phases.

The α-AlFeSi phase has the composition of Al_8Fe_2Si (31.6% Fe, 7.8% Si), and is also often reported as $Al_{15}Fe_3Si_2$ (30.7% Fe, 10.2% Si), with a probable composition range of 30-33% Fe, 6-12% Si. It is reported as having a hexagonal structure[25] with parameters a = 12.3 Å, c = 23.6 Å, a density of 3.58 g/cm^3, and appears in the form of Chinese script particles. The composition of the β-AlFeSi phase is Al_5FeSi (25.6% Fe, 12.8% Si). Phragmen[32] has reported that the β-AlFeSi phase has 27% Fe and 13.5% Si (within the range of 25-30% Fe, 12-15% Si). It has a monoclinic structure with parameters a = b = 6.12 Å, c = 41.5 Å, A = 91°, a density of 3.30-3.35 g/cm^3, and appears in the form of thin platelets (or needles) in the microstructure. Examples of α-AlFeSi ($Al_{15}(Mn,Fe)_3Si_2$) and β-AlFeSi (Al_5FeSi) phase particles obtained in 319 alloys are shown in Figure 2.4.[34]

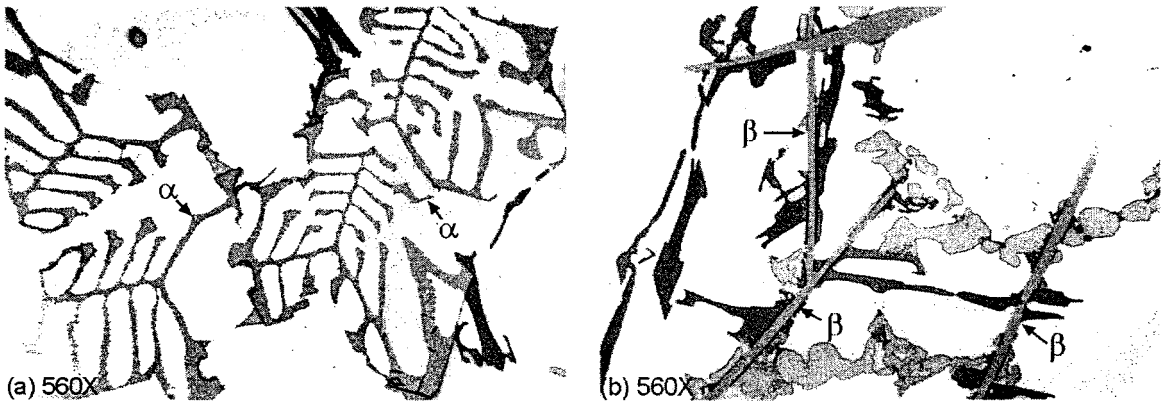

Figure 2.4. Microstructure of alloy 319 showing (a) α-$Al_{15}(Fe,Mn)_3Si_2$ phase, (b) β-Al_5FeSi phase.[34]

The α-AlFeSi and β-AlFeSi have different growth modes.[35,36] The α-AlFeSi phase shows an irregular, curved crystal growth conforming to the complicated shape of the

interdendritic spaces during solidification. It has a nonfaceted interface with the aluminum matrix, exhibits no growth twinning, which allows for a better bonding with the aluminum matrix. The formation of the phase particle is controlled by the temperature gradient and by the diffusion of atoms in the liquid metal. This type of growth occurs at high driving forces of solidification or rapid cooling, *i.e.*, at high undercooling, ΔT. The undercooling, ΔT, is usually defined as the temperature difference between the lowest temperature achieved before the start of freezing and the horizontal part of a cooling curve, as depicted in Figure 2.5.[37] The β-AlFeSi phase grows in a lateral or faceted mode which is poorly bonded to the aluminum matrix and contains multiple (001) growth twins parallel to the growth direction. This type of growth occurs at low driving forces or at slow cooling, *i.e.*, at low degrees of undercooling, ΔT.

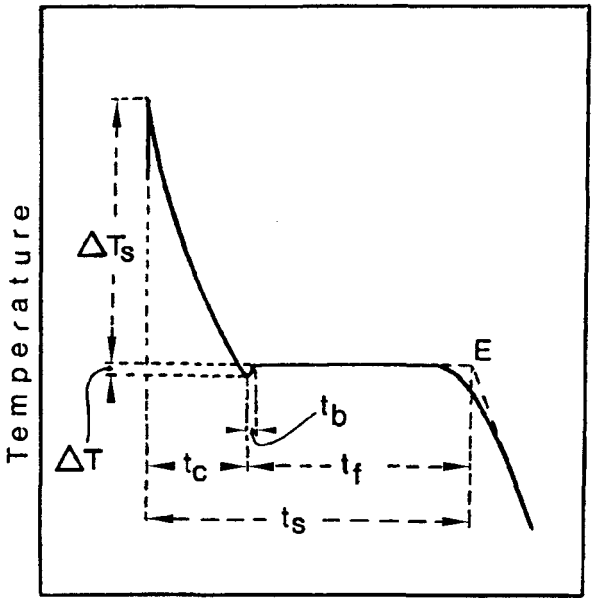

Figure 2.5. Schematic diagram of a typical cooling curve. ΔT_s – superheat, ΔT – undercooling, t_c – cooling time, t_f – freezing time, t_s – solidification time. E – end of solidification, taken as the intersection of tangent to steep part of cooling curve and horizontal arrest.[37]

2.7.2 Formation of Iron Intermetallics

In this section, the formation of iron intermetallics is discussed, with respect to the different alloying elements, melt additives and impurities present in the alloy. Among these, iron obviously will have the most apparent effect. However, other elements such as manganese, chromium, beryllium, magnesium, *etc.*, also play an important role.

2.7.2.1 Effect of Iron Content

In general, the length of the β-Al_5FeSi platelets increases with increase in the iron content and decrease in the cooling rate.[27,38] Gustafsson *et al.*[27] investigated the microstructure of cast aluminum alloys (Al-7 pct Si-0.3 pct Mg, or A356) as a function of Fe and Cr contents and the solidification rate. They observed that the length of both β platelets and the arms of the α script phase increase with increasing iron content and decreasing solidification rate, as shown in Figure 2.6, where the cooling rate is indicated in terms of the dendrite arm spacing (DAS). As the iron level of the alloy increases, the number of Al_5FeSi platelets (or needles as they appear in optical micrographs) does not increase appreciably, but their size does. Thus, when the iron content is above 0.7%, the Al_5FeSi compound tends to crystallize in the form of extremely large particles, *i.e.*, in primary crystal form.[39]

Evensen and Pedersen[40] studied the influence of iron on the microstructure in AlSi7Mg0.3 alloy by varying the iron content from 0.15 to 0.8%, and casting the alloy in a wedge-shaped mold. According to them, the size and volume fraction of the β-Al_5FeSi

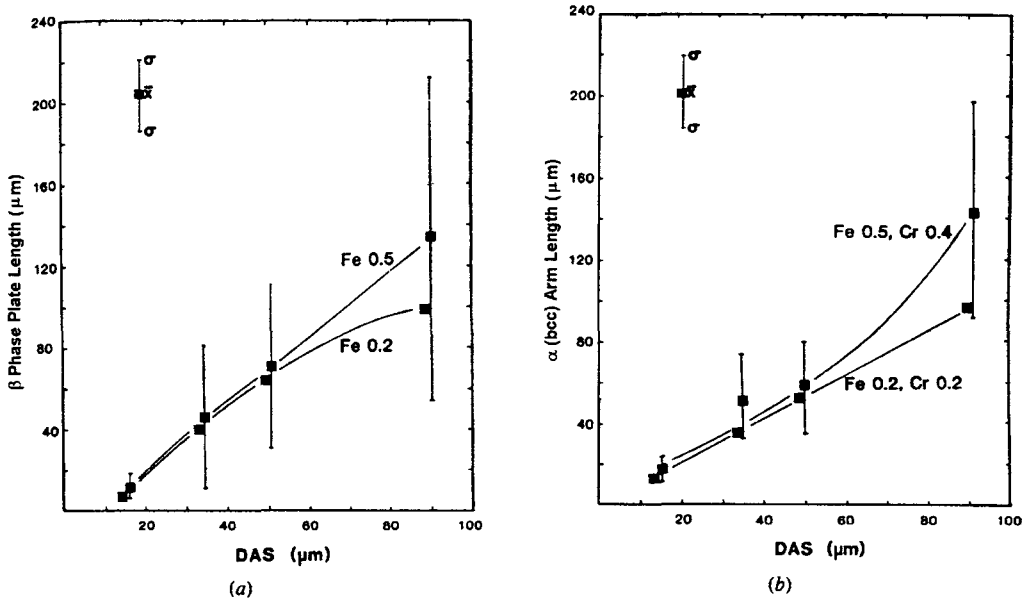

Figure 2.6. Length measurement of β-platelet and α-script particles: (a) β-platelets in A356 alloys with different iron levels; (b) α-scripts in A356 alloys with different iron and chromium levels.[27]

phase formed were found to increase with increasing iron content and decreasing solidification rate.

Yaneva *et al.*[31] studied the appearance of iron intermetallic phases in Al-Si cast alloys containing different levels of Fe and Mn. They showed that for a given Mn content, the percentage of the β-phase formed (referred to as m-phase in the original article), increased rapidly with increase in the iron content, as depicted in Figure 2.7.

In their study of Al-Si-Cu (319) foundry alloys, Samuel *et al.*[41] have also pointed out that increasing the iron content results in the precipitation of long, thick needles of the β-AlFeSi phase. They also observed that these needles are often branched into several needles, and that large shrinkage cavities can be formed within the casting due to the inability of the liquid metal to feed into the spaces between the branched needles.

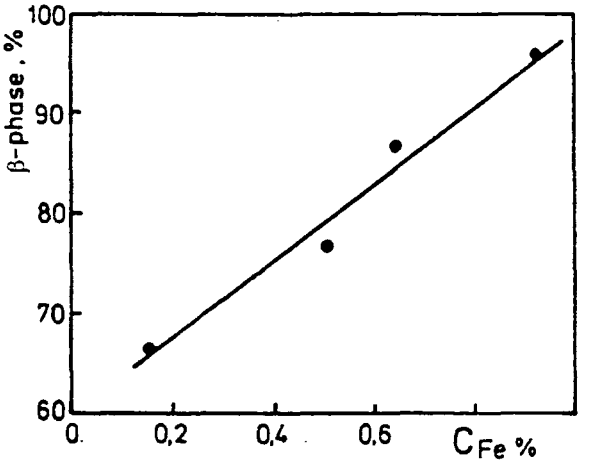

Figure 2.7. Dependence of the percentage of β-phase *vs.* iron content in Al-Si alloys.[31]

2.7.2.2 Effect of Other Elements

Unlike iron, which is favorable for the formation of iron intermetallics, *manganese* (Mn) is the common alloying additive used to neutralize the effect of iron and to modify the morphology and type of intermetallic phases formed.[27,42,43] According to Mondolfo,[42] manganese is the best neutralizing additive for iron correction, among others such as chromium (Cr), cobalt (Co), molybdenum (Mo) and nickel (Ni). Iglessis *et al.*[44] showed that the effectiveness of manganese addition contributed to the precipitation of iron intermetallics in the form of the α-Chinese script $Al_{15}(Fe,Mn)_3Si_2$ phase, or sludge particles when chromium is also present.

The simplified phase diagrams of the Al-Si-Fe system at constant manganese levels are shown in Figure 2.8,[34] where it can be seen that increasing the manganese content expands the α-AlFeMnSi phase region. As a result, crystallization of the α-AlFeMnSi phase is possible even at a high level of iron. The morphology and chemical composition of this phase is very similar to the α-AlFeSi phase obtained in alloys without manganese, except

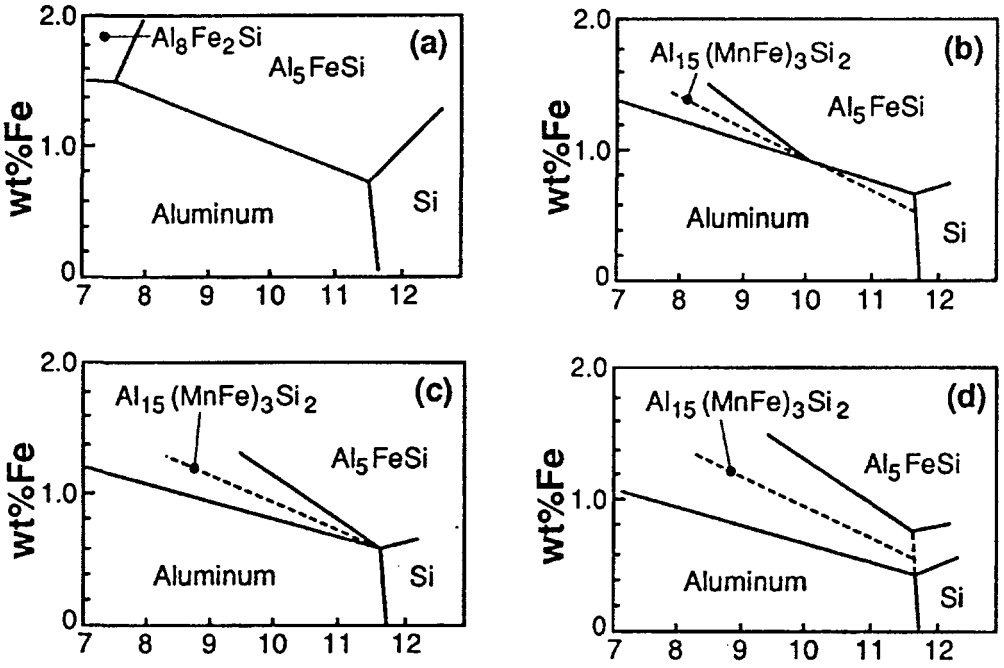

Figure 2.8. Simplified phase diagrams of the Al-Fe-Si system at constant Mn levels of (a) 0%, (b) 0.1%, (c) 0.2%, and (d) 0.3%.[34]

that some solution of manganese is observed in the former case. This phase can dissolve a fairly good amount of copper, chromium, nickel, *etc.*, if they are present as alloying elements. The latter replace part of the iron and, thus, the overall chemical composition of the phase remains almost the same.

According to the ANSI/ASTM specification,[45] if the Fe content exceeds 0.45%, the content of Mn should be no less than half that of Fe. Colwell and Kissling[46] pointed out that when the manganese content is half that of iron, it breaks down the long needles of the β-AlFeSi phase and thus helps both the mechanical properties and castability. Mascré[47] studied Al-13Si alloy with varying contents of Fe and Mn (up to 1.2 and 1.3%, respectively), using test bars cast in sand and in permanent molds. From his results, he

arrived at a general "neutralization" formula for sand mold and permanent mold castings given by:

$$Mn\% = 2(Fe\% - 0.5) \quad (2\text{-}3)$$

Iwahori *et al.*[38] studied the feedability of AC2B (Al-Si-Cu) alloy and pointed out that the growth of shrinkage porosity is encouraged by an increase in iron content. This is due to the crystallization of needle-like iron compounds at an early stage of solidification. When Mn is added to the alloy, the morphology of the iron compound changes to Chinese script, and the occurrence of shrinkage porosity is inhibited by the improved feedability of the alloy, which is then able to compensate for solidification shrinkage.

Komiyama *et al.*[48] showed that the manganese content has a strong effect on the alloy tensile strength only at iron contents higher than one percent. However, when the Mn:Fe ratio exceeds a certain limit, then Mn addition has a harmful effect, as shown in Figure 2.9. Narayanan *et al.*[49] found that at low cooling rates, the morphology of the iron intermetallics changed to script type with Mn addition, whereas at high cooling rates, both the α and β phases crystallized.

The morphology of the β-AlFeSi phase in aluminum casting alloys is also affected by the addition of other trace elements such as Cr, Be and Mg. These are discussed below in brief.

Chromium behaves in the same way as manganese. Gustafsson *et al.*[27] observed that the morphology of the β-AlFeSi phase is altered to Chinese script with chromium addition in an Al-7% Si-0.3% Mg alloy containing 0.52% Fe. Similar observations have been reported by Granger.[50] In his work, a complex intermetallic called "sludge" is formed with

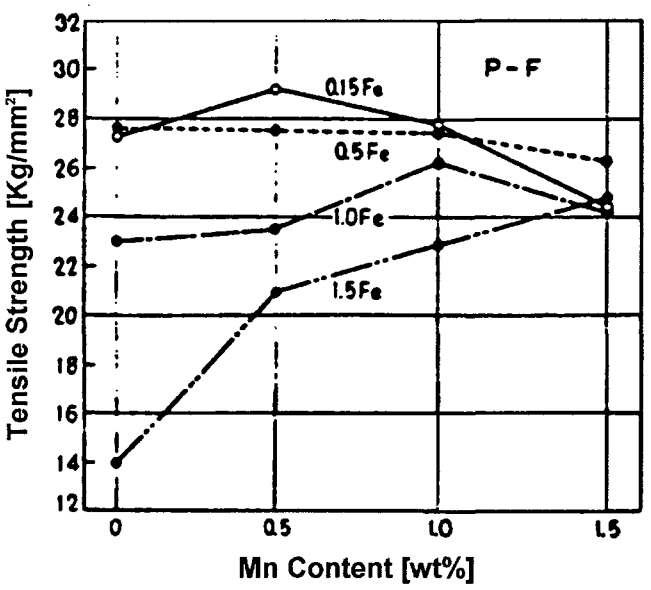

Figure 2.9. Effect of Mn content on the tensile strength of Al-9.2Si-4Cu-0.5Mg alloy at various Fe contents.[48]

aluminum, silicon, iron, manganese and chromium. Sludge particles have a high melting point and high specific gravity. To avoid sludge formation, a "sludge factor" (SF) given by

$$\text{Sludge Factor (SF)} = \%\text{Fe} + 2(\%\text{Mn}) + 3(\%\text{Cr}) \qquad (2\text{-}4)$$

is suggested as a guide for these alloys.[50,51] With the casting temperature for die casting alloys around 650 °C, a sludge factor of 1.8 is considered normal.

Due to its unique physicochemical characteristics, *beryllium* is usually used in aluminum casting alloys to reduce oxidation of the molten metal, to obtain a cleaner alloy. This allows for an increase in the magnesium content and hence accelerates the hardening process when the alloy is heat-treated in the T6 condition.[52] Table 2.7 shows the physical properties of Be, Mg and Al. Note that beryllium has the smallest atomic diameter, the highest melting point, and a high boiling point. Thus, the diffusion of the small beryllium

Table 2.7. Data pertaining to Al, Be and Mg metals[53]

Metal	Atomic Wt.	Atomic Dia. (KX Units)	Density (g/cc)	Atomic Volume cm^3/g atom	Melting Point	Boiling Point
Be	9.01	2.26	1.85	4.9	1284 °C (2343 °F)	2400 °C (4352 °F)
Mg	24.3	3.20	1.74	14.0	650 °C (1202 °F)	1202 °C (2196 °F)
Al	27.0	2.86	2.70	10.0	660 °C (1220 °F)	1339 °C (2442 °F)

ions into the oxide film formed at the surface of the melt will cause a contraction of the oxide, establishing a denser, more protective film that will prevent further attack from oxygen and nitrogen present in the atmosphere.[53]

The addition of beryllium in aluminum alloys causes the precipitation of the iron intermetallics in the form of "$Al_5BeFeSi$" in a smaller, more globular form, rather than as large, brittle platelets of Al_5FeSi. The small, globular particles of the beryllium-containing compound eliminate the embrittling and weakening effect of the platelets. The beryllium addition also modifies the β-AlFeSi phase into Chinese script but the amount of beryllium used is smaller than other trace elements.[53]

Beryllium has a marked effect on the strength and mechanical properties of 356 variant-T6 aluminum alloys. Both in sand castings and in chilled castings, at any aging temperature or time used experimentally, ultimate strength and yield strength are found to increase, but elongation is not affected. Bailey[54] showed that part of the alloy strength, as tested in bending, increased with the increase in beryllium content. Murali *et al.*[55,56] showed that the addition of small amounts of beryllium to Al-7% Si-0.3% Mg-0.6% Fe alloy results in the formation of a new Be-Fe phase (Al_8Fe_2SiBe), which has a morphology of hexagonal shapes or Chinese scripts, and is seen only inside the α-Al dendrites. This nucleation

mechanism is quite different from that of the β-AlFeSi phase in the unmodified alloy and leads to superior mechanical properties. The presence of Be also results in some grain refinement. Compared to other neutralizing elements, beryllium is used in very low concentrations due to its toxicity.

Magnesium is normally used to improve the alloy mechanical properties through the precipitation of the Mg_2Si intermetallic. Samuel *et al.*[57] have observed that the addition of 0.35% Mg to commercial 319 aluminum alloys changes the β-Al_5FeSi phase to $Al_5Mg_3FeSi_6$ phase. Increasing the magnesium content increases the volume fraction of this phase. Magnesium up to 0.5% contributes to both strength parameters and to the alloy ductility.[58] However, DasGupta *et al.*[59] observed that increasing the magnesium content up to ~0.59% has a negligible effect on the mechanical properties of the 319 aluminum alloys, either in the as-cast or in the T5 conditions.

2.7.3 Fragmentation and Dissolution of Iron Intermetallics

The α-AlFeSi phase is considered less detrimental to the mechanical properties compared to the β-AlFeSi phase.[43] Thus, altering β-AlFeSi into α-AlFeSi is advantageous from the point of view of mechanical properties. Various means have been developed to reduce the harmful effects of iron intermetallics in Al-Si alloys. Among them, strontium modification and heat treatment are most commonly used, and will be reviewed in detail as they are also related to the present work. Another method – the addition of neutralizing elements – has already been reviewed in the previous section.

2.7.3.1 Strontium Modification

Strontium, a surface-active element, is a well-known additive in cast Al-Si alloys. It is commonly employed to modify the shape of the eutectic silicon from acicular to fibrous,[60,61] called "eutectic modification," in order to improve the mechanical properties. It is also reported to be able to alter the acicular β-AlFeSi intermetallic particles into the Chinese script form (α-AlFeSi).[62,63] Mulazimoglu *et al.*[63] have claimed that only 0.015 wt% of Sr is required to neutralize 0.5 wt% Fe, which is quite low compared to the Mn or Cr (>0.1 wt %) additions required.

Samuel *et al.*[21] have studied the effect of strontium on the formation of the β-AlFeSi phase in 319 type alloys. According to them, the addition of 300 ppm strontium accelerates the fragmentation and dissolution of the β-AlFeSi phase and the formation of the blocky $CuAl_2$ intermetallic phase during solidification. In addition, fragmentation of the β-AlFeSi phase in the Sr-modified alloys is associated with an increase in yield strength. Similarly, in 413 alloy also, it has been reported that the addition of strontium leads to fragmentation of the β-Al_5FeSi platelets and an increase in the amount of α-AlFeSi, as shown by the quantitative metallographic results depicted in Figure 2.10.[33]

Kulunk and Zuliani[64] studied the effect of strontium on 380 high-pressure die-casting alloy. They showed that reduction in the size and number of iron intermetallic phase particles by the addition of strontium leads to an increase in the tolerance of these alloys to higher iron concentrations, without altering the mechanical properties. It has been found that the addition of 0.04-0.06% of strontium to A413, 413P, and 413 alloys modifies the

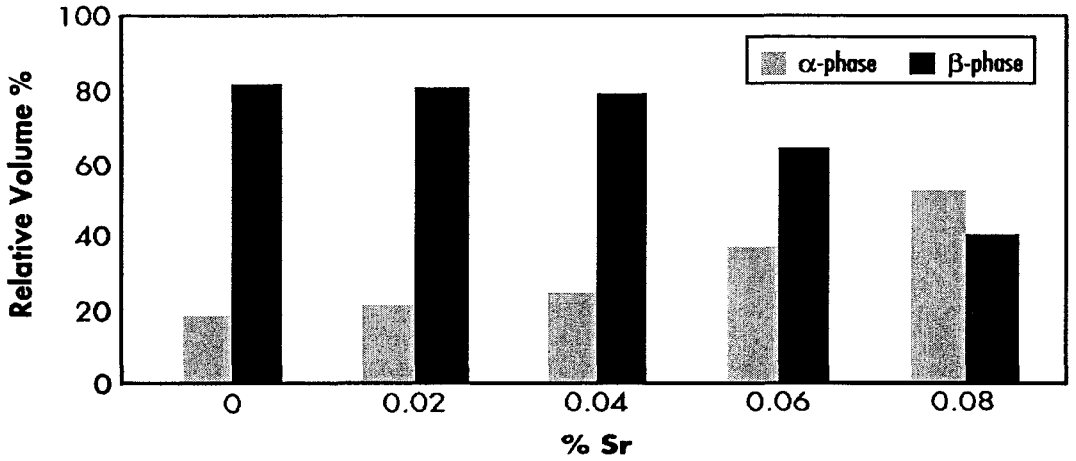

Figure 2.10. Variation in the amounts of α- and β-AlFeSi as function of Sr content in 413 alloy solidified at rates typical of sand casting.[33]

size of the intermetallic phase particles and enhances the transformation of the β-AlFeSi phase into the α-Al_8Fe_2Si phase.[65]

2.7.3.2 Non-Equilibrium Heat Treatment

Partial or complete dissolution of the harmful β-iron intermetallics into the Al-Si matrix through non-equilibrium heat treatment is found to be another way to neutralize the detrimental effect of iron intermetallics.

Non-equilibrium heat treatment is distinguished from normal heat treatment by the higher heat treatment temperatures involved. Normal heat treatment, or equilibrium heat treatment, as suggested in the many heat treatment specifications listed by the Aluminum Association (AA), generally restricts solution temperatures below the final solidification point to prevent any appearance of the liquid phase, which is known to be detrimental to the mechanical properties. That is to say, grain boundary melting and other localized melting are undesirable, and should be avoided by all means during solution heat treatment. Under

such heat treatment conditions, the iron intermetallics do not undergo any change. According to Griger *et al.*,[36] the β-AlFeSi phase that forms in cast Al-Fe alloys containing a high silicon content does not dissolve, but its morphology is changed slightly by heat treatment with the addition of a small amount of manganese or chromium. The α-AlFeSi phase becomes more stable. As reported by Gustafsson *et al.*,[27] no changes are noted in the size, number, or morphology of the α and βphases during T6 heat treatment of A356 alloys containing small amounts of manganese or chromium.

Non-equilibrium heat treatment was suggested by Shimizu *et al.*[66] for AC2B (Al-Si-Cu) aluminum alloy to improve its mechanical properties. This treatment involves a regular T6 temper heat treatment, but with a solution temperature higher than the final solidification temperature *i.e.*, the Al-$CuAl_2$ eutectic temperature. The dissolution of iron intermetallics is found to improve with increase in the solution temperature.

A similar non-equilibrium heat treatment was carried out by Narayanan *et al.*,[Error! Bookmark not defined.,67] to study the dissolution behavior of iron intermetallics in 319 alloys containing 1.0% Fe. In their study, they found that the β-AlFeSi platelets dissolved with increasing solution temperature, while the α-AlFeSi phase did not undergo any dissolution. In addition, the solution temperature was more important than the solution time, and the addition of manganese hindered the dissolution kinetics of the iron intermetallics. They showed that the optimum solution temperature for low-Fe alloys lies between 515° and 520 °C, in which temperature range a maximum amount of the iron intermetallics dissolves in the aluminum matrix.

Samuel *et al.*[41] reported that the solution heat treatment of iron-containing Al-Si cast alloys accelerates the dissolution of the β-Al_5FeSi phase. The minimal β-Al_5FeSi needle length is achieved after 30 h in unmodified alloys, and after 10 h in Sr-modified alloys. The dissolution of the β-Al_5FeSi phase occurs by its decomposition into Al_6Fe and Si. The mechanism of dissolution comprises the rejection of Fe and Si from the β-Al_5FeSi phase needles at their ends (rather than along their sides), which explains the noticeable decrease in the needle length rather than in its thickness.

2.7.4 Effect of Iron Intermetallics on Mechanical Properties

Many researchers have investigated the effect of iron on the mechanical properties of Al-Si alloys. In his review on iron in aluminum casting alloys, Couture[43] reported that the addition of iron to aluminum-silicon alloys is detrimental to the mechanical properties. Increasing the iron content from 0.5 to 1.2% in an Al-13%Si casting alloy dramatically reduces the mechanical properties, particularly the ductility, due to the formation of β-phase platelets.[68]

Vorob'ev *et al.*[69] claimed that even a small Fe addition to Al-Si alloys seriously diminishes tensile strength and ductility, due to the formation of the brittle β-Al_5FeSi intermetallic at cooling rates normally employed in sand and permanent mold castings (about 0.9 °C/s in sand castings and 10 °C/s in permanent mold castings). The hard, brittle β-Al_5FeSi platelets have a relatively low bond strength with the matrix.[42]

According to Bonsack,[70] any amount of Fe over 0.5% will be present as an Al-Fe silicide in the form of large needles which, up to about 0.8% Fe, increase the alloy strength

and hardness, with a slight reduction in ductility. Above 0.8% Fe, both strength and elongation deteriorate rapidly, and there is a deleterious effect on the machinability, as well. Hajas[71] has reported that the formation of Al_5FeSi causes stress cracking and void formation in Al-10Si-Mg alloy castings. Iron contents up to 0.2% improve the tensile strength, while higher levels reduce the tensile strength and elongation, and increase hardness. Komiyama *et al.*[48] have observed that in Al-9.2Si-4Cu-0.5Mg alloy, hardness increases, whereas tensile strength and elongation decrease with increase in the iron content. The tensile strength markedly decreases when the iron content exceeds 0.5%.

Komatsu *et al.*[72] have pointed out that iron exerts a detrimental effect on the impact strength of Al-Si alloys due to the formation of $FeAl_3$ crystallites, as shown in Figure 2.11. The formation of these undesirable crystallites is not changed by solution heat treatment at

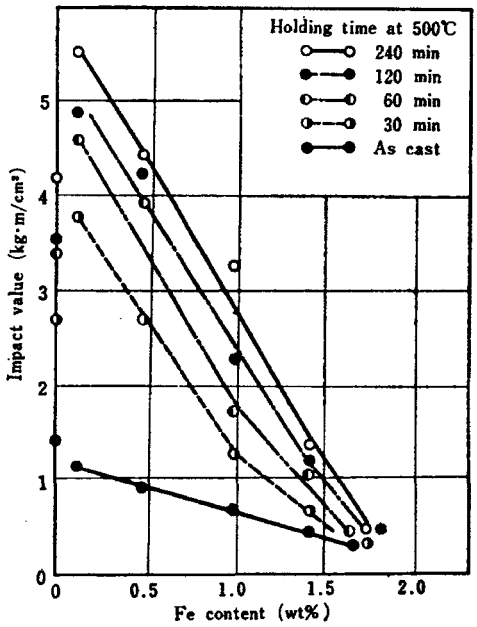

Figure 2.11. Effect of Fe content on the impact strength of Al-11%Si alloys for holding times of 30-240 min at 500 °C.[72]

500 °C, resulting in low impact energy values similar to that obtained in the as-cast condition when the iron level exceeds 1.5%.

With regard to the effect of iron content on the mechanical properties of A356 type alloys, Nishi *et al.*[73] showed that the mechanical properties of Al-Si-Mg-Zn alloys were further deteriorated with the increase in iron content, and it was desirable to keep the iron content lower than 0.15%. Beck and Veda[74] however, found that iron in the range of 0.09-0.58% had little effect on the aging characteristics of A356 alloys: increasing the Fe content lowered the ductility, with marginal effects on yield strength and hardness.

2.8 POROSITY IN Al-Si CAST ALLOYS

In the metallurgical context, porosity refers to the presence of minute holes or cavities in a solid metal. Porosity is one of the defects normally present in Al-Si cast alloys. Extensive studies have been conducted, since the early 1950s, to understand the origins and characteristics of porosity formation.[75-77] To date, it is quite well understood that casting porosity is caused by the cooperative effects of shrinkage and dissolved gas; that is (a) shrinkage created by the density difference between the liquid and solid states of the metal, as well as inadequate liquid mobility (bad feeding), and (b) the evolution of dissolved gases (mainly hydrogen) due to the difference in the solubilities of these gases in the solid and liquid phases of the metal.[4-8]

In commercial practice, the formation of porosity is always considered to be a function of alloy composition, melt hydrogen level, and foundry processing parameters such as cooling rate, modification, alloying elements, grain refinement, inclusions, *etc.* With

mechanical degassing facilities and some typical fluxes, it is possible to minimize the porosity content.

Porosity in a casting always deteriorates its mechanical properties. It is particularly harmful to the ductility, fracture toughness, fatigue life and, in some cases, the surface finish of the casting.[2] A reduction in the casting size, depreciation in corrosion stability and a particularly bad influence on the dynamic strength was generally observed, as well.[3]

2.8.1 Types of Porosity

Shrinkage Porosity: The shrinkage that occurs during solidification is the primary source of porosity formation in aluminum castings.[78] In most aluminum cast alloys, the volume shrinkage varies typically from 5 to 8%. Shrinkage porosity also occurs on a "micro" level as *microshrinkage* or *microporosity*, which is dispersed in the interstices of dendritic solidification regions, typically found in alloys with large solidification ranges.

During the course of solidification, several types of feeding are involved at different stages. These include liquid, mass, interdendritic and solid feeding, which occur from the initial through the final stages of solidification. Porosity defects are caused by the limitations of these feeding mechanisms, and it is thought that the interdendritic feeding stage is the most important stage for their creation. Limited or inadequate liquid metal feeding in the dendritic solidification area is the main reason for the observation of *microshrinkage*.[78]

Gas Porosity: The other main source of porosity arises from gas evolution resulting from a decrease in the solubility of the gas during solidification of the liquid metal, as

shown in Figure 2.12, for example, for hydrogen gas in aluminum.[79] The gas rejected can nucleate both in the liquid metal during solidification, and in the solid immediately afterwards, giving rise to two very different kinds of porosity, termed *interdendritic* (or *primary*) porosity and *secondary* porosity, respectively. These effects are typically exhibited by hydrogen in aluminum.[8]

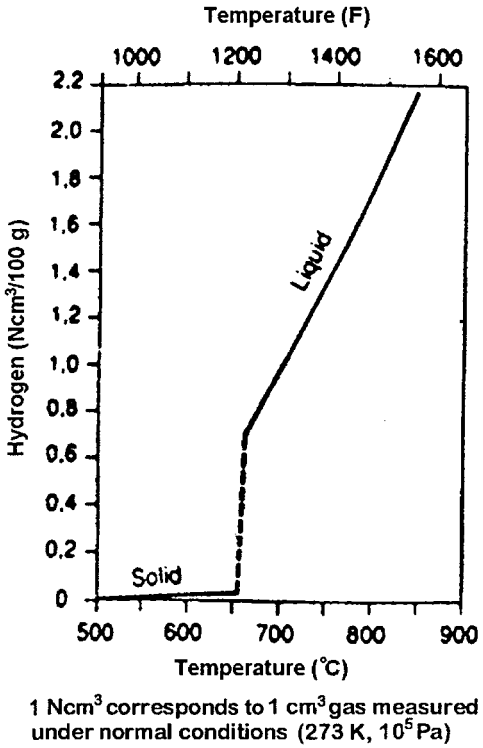

Figure 2.12. Variation of hydrogen solubility in pure aluminum as a function of temperature.[79]

When the hydrogen content of the melt exceeds the solubility limit, the excess hydrogen forms gas bubbles. The pores nucleate and grow in the presence of suitable nucleants; their size and distribution depending on local solidification conditions.[8,80,81] A higher melt hydrogen content will thus increase the porosity in the casting. Pores may form

either prior to, or during solidification. The former are spherical and relatively large, while the latter are small, irregularly shaped, and attributed to shrinkage porosity.[82]

Thomas and Gruzleski[83] have observed that for a given alloy and specific solidification conditions, there is a "threshold hydrogen content" below which no primary porosity is formed and that the tendency for porosity formation is reduced with an increase in cooling rate and a decrease in the alloy freezing range. Also, for hydrogen contents above the threshold value, there is approximately a linear relation between hydrogen and the pore volume fraction, as depicted in Figure 2.13.[84] The porosity has a close relationship with the initial hydrogen content in the melt.[85-87]

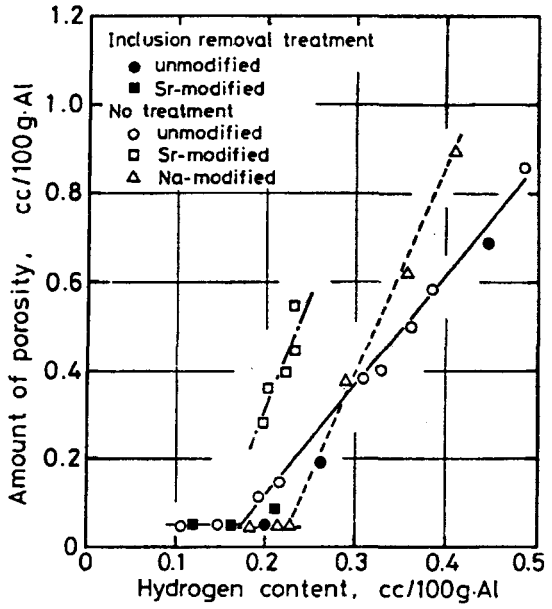

Figure 2.13. Porosity *vs.* hydrogen content in unmodified and modified Al-Si alloys.[84]

The growth process in porosity formation in aluminum alloys as suggested by Pehlke,[88] is depicted in Figure 2.14. The nucleation of gas porosity is found to take place at the base of α-Al dendrite arms, Figure 2.14(a). The synergism (between the shrinkage and gas

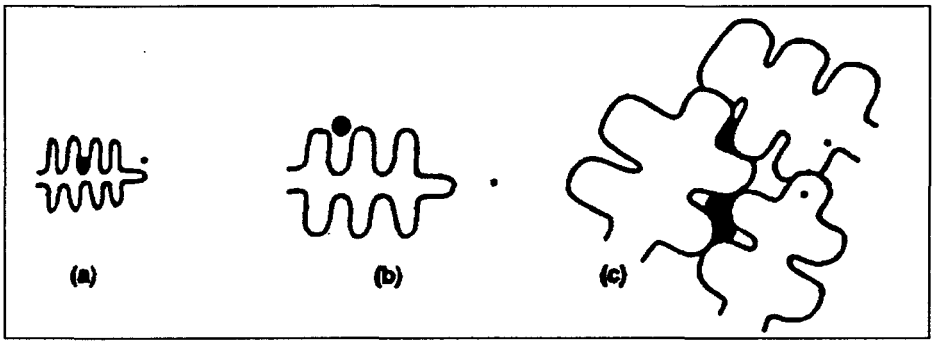

Figure 2.14. Growth process of porosity formation.[88]

porosities) which, surmounts the large negative free energy required to form a gas-metal surface, makes such a process easier. With the progress of solidification, porosity growth is observed due to the higher potential for gas evolution. Such growth makes the radius of the porosity large enough to overcome the gas-metal interfacial energies, eventually leading to the detachment of porosity from the dendrite, Figure 2.14(b). Convective forces also play a role in such detachment. With the further progress of solidification, collision happens among neighboring dendrites, making it difficult for interdendritic feeding. Therefore, porosity growth is thought to be necessary for the compensation of solidification shrinkage (Figure 2.14 (c)). It seems that the simultaneous occurrence of shrinkage and gas evolution is essential to the formation of porosity defects.[89]

2.8.2 Effect of Alloying Elements on Porosity Formation

Silicon is the major alloying element in Al-Si alloys. It also plays an important role in porosity formation. Iwahori *et al.*[90] studied the process of solidification in Al-Si alloy castings containing various levels of silicon. They found that with increasing silicon content, shrinkage porosity was more likely to occur, but could be controlled by increasing

the cross-section area of the riser neck of the casting mold. Chen and Engler[91,92] made a quantitative analysis of the effect of silicon concentration on porosity formation. They reported that silicon affects porosity formation by changing the mode of solidification. As silicon is added to pure aluminum, pore formation is increasingly favored by the spongy dendritic solidification caused by the increase in silicon content. As the eutectic composition is approached, the tendency for porosity formation decreases, due to the decrease in freezing range and resultant lack of a dendritic structure.

In their study on porosity formation in Al-Si alloys containing different silicon contents, Emadi and Gruzleski[4] have reported that A356 type alloys (containing 7 wt% Si) may well be the alloys most prone to porosity formation among all Al-Si alloys with silicon contents ranging from 5.7 wt% to 8.1 wt%. The results of Edwards *et al.*[93] on microporosity formation in Al-Si-Cu-Mg casting alloys, however, appear to be different. According to them, increasing the silicon level from 4.5 to 9% decreases the amount of microporosity, presumably due to the decrease in the freezing range of the alloy.

Magnesium acts as a hardening element in both Al-Si-Cu and Al-Si-Mg alloys. Its presence reduces percentage porosity without a noticeable change in pore size or shape, as reported by Roy *et al.*,[94] who investigated porosity formation in Al-Si-Cu alloys. They observed that the role of magnesium in reducing percentage porosity is more pronounced when the hydrogen content is higher (~0.5 mL/100g Al in their case). According to Edwards *et al.*,[93] the effect of magnesium on microporosity formation in Al-Si-Cu casting alloys is not consistent. However, in most of the alloys, magnesium appears to decrease the

porosity by amounts ranging from ~0.005% to ~0.3%, and this effect is more evident at the riser end of the casting.

Copper is another hardening element in Al-Si-Cu alloys. Edwards *et al.*[93] found that adding copper significantly increases the amount of microporosity, due probably to the effect that copper has on solidification shrinkage and hydrogen gas pressure. Roy *et al.*[94] observed that copper in Al-Si alloys is present as $CuAl_2$ or in a complex form. The $CuAl_2$ phase particles may assist in pore formation in the absence of the needle-like β-Al_5FeSi intermetallic phase. However, they are not effective in the presence of the latter.

2.8.3 Effect of Melt Treatment Additives and Impurities on Porosity Formation

Melt treatments using special additives are very common in foundry processing. For example, *strontium* is normally used to enable the eutectic modification of silicon particles, *i.e.*, to modify the shape of the eutectic silicon from acicular to fibrous. On the other hand, *titanium* is employed as a grain refiner, to reduce the grain size in a casting and thus improve its mechanical properties. Impurities like *iron* are invariably present in Al-Si alloys. All these elements have different effects on porosity formation.

As mentioned previously, the addition of strontium favors the mechanical properties. However, it has an undesirable effect on porosity formation. Sigworth *et al.*[95] have observed that the addition of Sr and Be promotes gas porosity formation in slowly cooled sections of Al-Si alloy castings. Fang and Granger[2] found that the modification of A356 alloy by strontium increases both the pore volume fraction and pore size for the same hydrogen content. Samuel *et al.*[96] and Roy *et al.*[94] studied the porosity and fracture

characteristics observed in 319.2 alloy castings, and in particular, the influence of hydrogen and strontium content on porosity and tensile properties. They found that porosity increased with increasing hydrogen content, and also with the addition of strontium.

Emadi *et al.*[97] have indicated that Na and Sr reduce the surface tension of the melt and increase the volumetric shrinkage, thus facilitating porosity formation. Argo and Gruzleski[98] studied the porosity formation in aluminum casting alloys, in both the unmodified and Sr-modified conditions. They found that with Sr addition, microshrinkage and the volume of slumping and contraction increased, whereas the pipe volume decreased. The strontium concentration itself appeared to be unimportant. They proposed that the increased porosity was due to problems associated with interdendritic feeding. As can be seen from Figure 2.15, modification suppresses the eutectic transformation temperature without changing the liquidus temperature in hypoeutectic alloys.[99] This results in an increase in the freezing range and the length of the mushy zone, which causes feeding difficulties and a subsequent increase in microshrinkage.

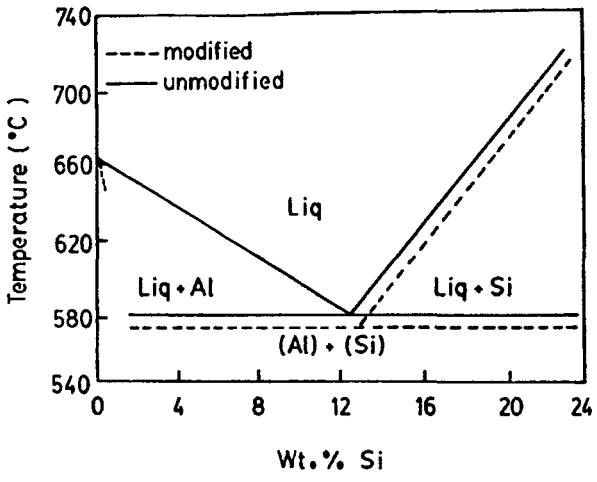

Figure 2.15. Suppression of the eutectic transformation temperature due to modification.[99]

According to Sigworth,[100] among the several advantages of grain refining, the primary one is an improvement in the amount and distribution of porosity and shrinkage in alloys that tend to form microporosity; especially those with a long freezing range. Grain refining will also reduce the amount of porosity formed in an alloy containing small or moderate amounts of gas.[101]

Roy *et al.*[102] have reported that, as a grain refiner, TiB_2 results in increasing nucleation sites as well as the number of grains, which lead to a marked reduction in pore size and an increase in pore density. In another study, they pointed out that reducing grain size (*i.e.*, increasing the total grain boundary facet length) is another parameter to be considered in reducing pore size in grain-refined materials.[94]

The work of Tynelius[103] on microporosity evolution in A356 alloy showed that the morphology of the solid-liquid interface and the resulting microstructure determine the morphology of the micorporosity obtained. The pores were seen to be present in the grain boundaries. Grain refining (using Al- 5 wt pct Ti- 1 wt pct B alloy, and measured in terms of 0.02 wt pct Ti addition) decreased the grain size and, hence, the maximum pore length, in keeping with the shorter grain facets. Area percent porosity and areal pore density increased with grain refiner addition, while the maximum pore area remained unchanged. From these investigations, Tynelius[103] concluded that the TiB_2 particles provide nucleation sites for pores, without influencing the interfacial tension. The latter is the parameter that controls pore size.

Taylor *et al.*[104] observed that iron added to a commercial, unmodified, nongrain-refined Al-Si-Cu-Mg based casting alloy AA309 (305 in AA designation), causes a

threefold porosity effect when the iron level is greater than 0.4%. In contrast, when the iron level is less than 0.4%, the total porosity values decrease with the increase in iron content, as shown in Figure 2.16. Iwahori *et al.*[38] found that, in castings of an AC2B alloy (Al- 6 pct Si- 3.2 pct Cu), when the iron level is greater than 0.5%, larger riser sizes are required in order to avoid the formation of shrinkage-porosity defects. They suggested that β-Al_5FeSi intermetallic platelets restrict liquid metal feeding during the casting process.

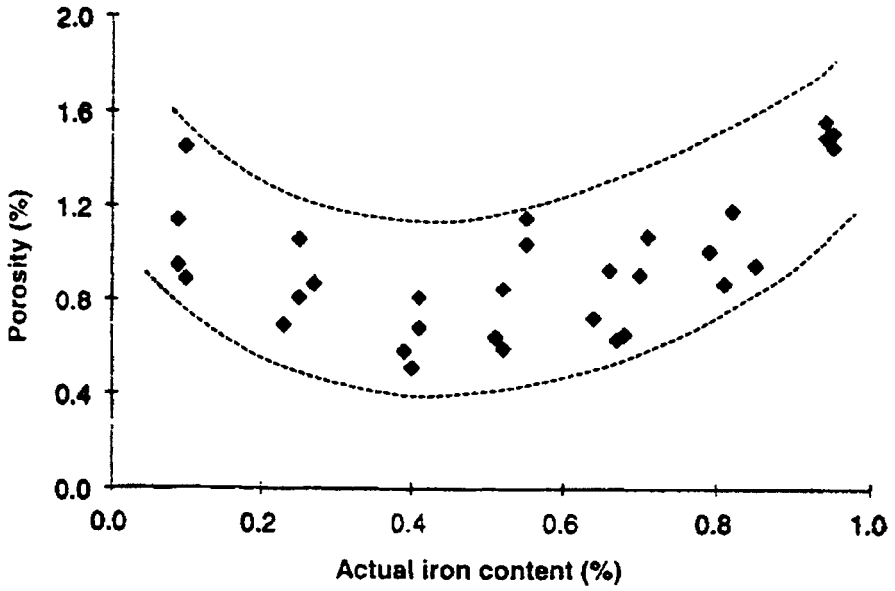

Figure 2.16. Plot of percentage porosity *vs* iron content in AA309 alloy castings.[104]

In their study on porosity formation in Al-Si-Cu alloys, Roy *et al.*[94] found that β-Al_5FeSi intermetallics are very active sites for pore nucleation and also physically constrain the growth of pores (as depicted in Figures 2.17 and 2.18, respectively), thus influencing the ultimate pore shapes. Magnesium and iron appear to have a negligible effect on porosity distribution at contents less than about 0.5%.

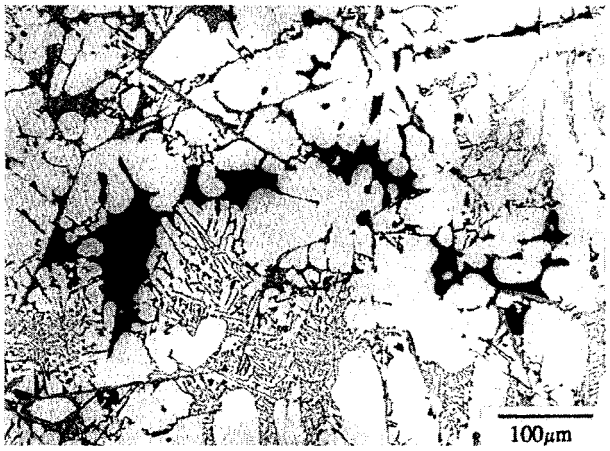

Figure 2.17. Pore size and distribution in 1 wt pct Fe-containing 319 alloy showing nucleation of pores along the long sides of β-needles.[94]

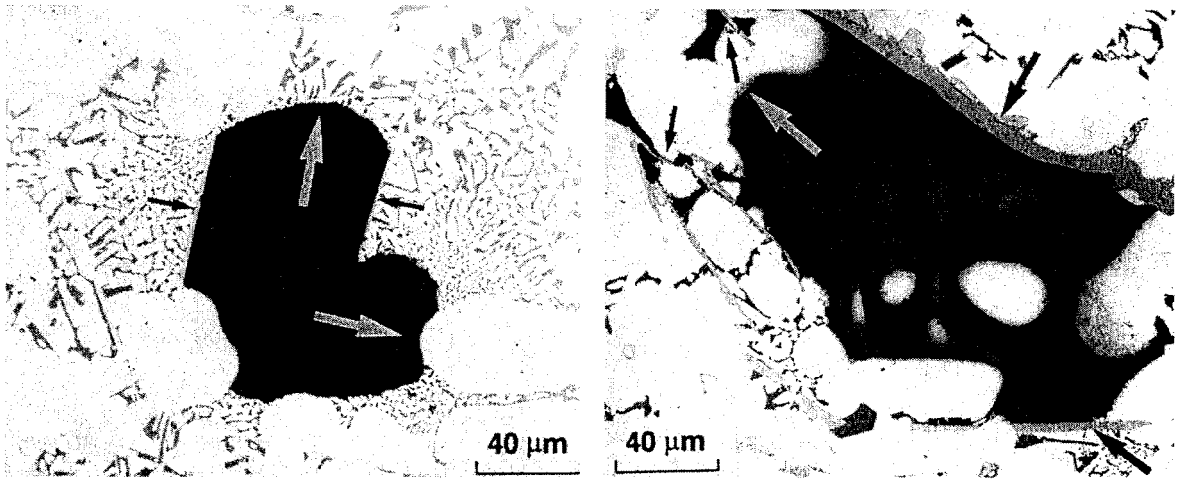

Figure 2.18. Role of β-Al_5FeSi needles in restricting the growth of (a) a gas pore and (b) a shrinkage pore. Note the presence of small pores along the long sides of the β needles, delineated by the short arrows.[94]

2.8.4 Effect of Cooling Rate on Porosity Formation

The cooling rate affects the pore size by the way it affects the local solidification structure (*i.e.*, the dendrite cell spacing), which, in turn, controls the threshold cell size and hence the pore size.[78] Fang and Granger[2] have shown that for a given melt hydrogen content, an increase in the cooling rate decreases both the total amount of porosity (pore

volume fraction) and the average pore size (equivalent average pore diameter) in both modified and unmodified A356 alloys, as shown in Figures 2.19 and 2.20, respectively.

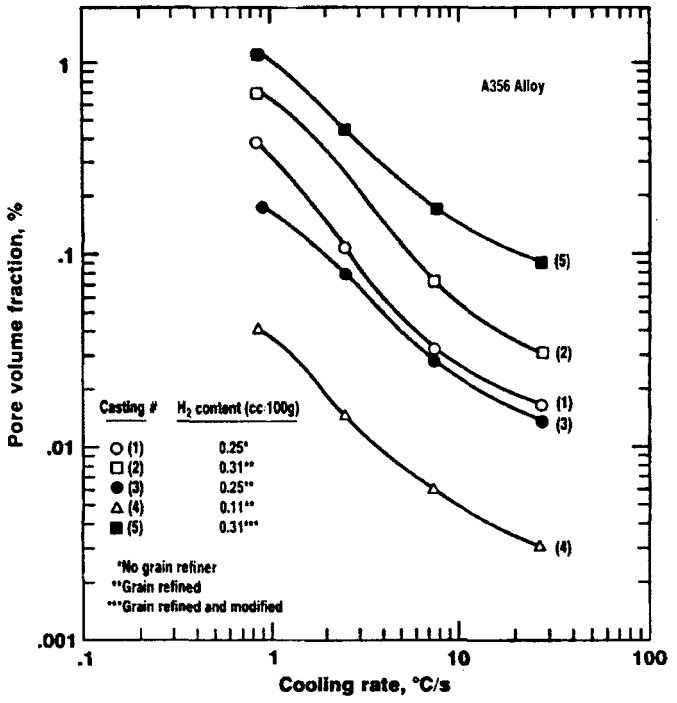

Figure 2.19. Pore volume fraction as a function of cooling rate in A356 alloy castings.[2]

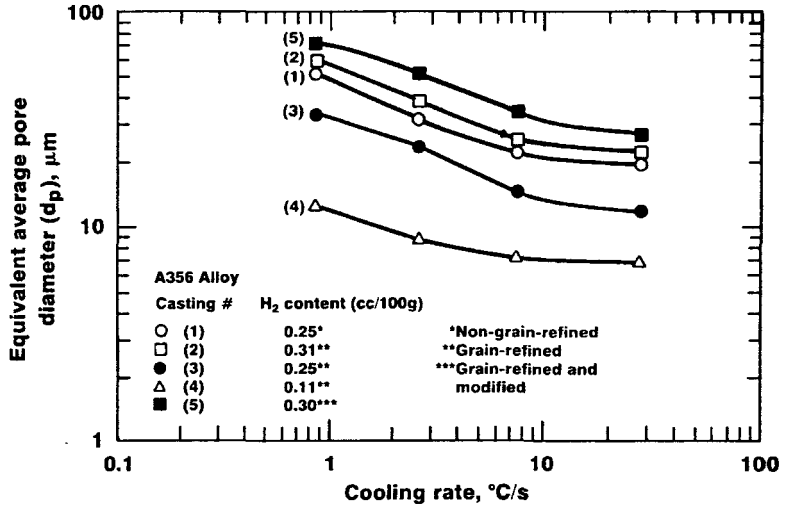

Figure 2.20. Equivalent average pore diameter as a function of cooling rate in A356 alloy castings.[2]

In a study related to her Ph. D. dissertation, Tynelius[103] observed that in A356 alloys, the area percent porosity, maximum pore length and maximum pore area increased with the local solidification time for a constant melt hydrogen content. From their observations of pore characteristics in A356 and A319 castings, Shivkumar *et al.*[105] found that in the case of the A356 alloy, when the local solidification time is increased, the pore distribution is skewed towards large pore sizes, and the amount of porosity and maximum pore size increase, whereas in A319 alloys, only the former is apparent. Emadi and Gruzleski[4] found that in Al-Si alloys, for a given melt hydrogen content, the pore volume fraction and the pore size decrease as the cooling rate increases. This cooling rate dependence of the pore volume fraction increases markedly at lower cooling rates, typically less than 1 °C/sec.

2.8.5 Effect of Porosity on Mechanical Properties of Al-Si Cast Alloys

The effect of porosity on the mechanical properties of castings has been investigated in several studies. Eady and Smith[106] considered the effect of large volume fractions of porosity, up to 7%, on the mechanical behavior of Al-7%Si alloys containing 0.1~0.47% Mg. They found that only the low yield stress varieties of the alloy (Mg contents less than 0.26%) tolerate porosity levels in excess of 1%, in which case the tensile ductility decreases with the level of porosity. McLellan[107] reported that increasing metal soundness in terms of porosity results in a higher elongation to fracture in alloy A357. Another example of the deleterious effect of hydrogen porosity on yield strength and the ultimate tensile strength of sand cast 356-T6 aluminum castings is shown in Figure 2.21, obtained by Traenkner,[108] where it can be seen that both UTS and YS decrease with the increase of porosity.

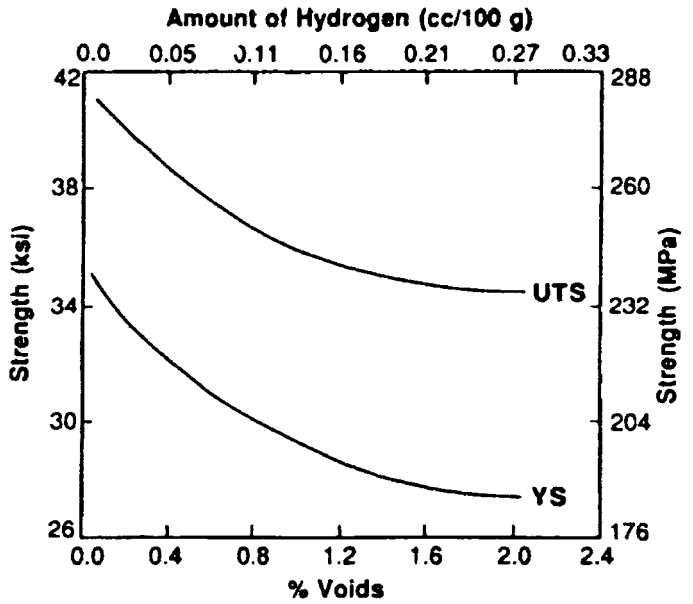

Figure 2.21. Effect of hydrogen porosity on the mechanical properties of sand cast 356-T6 Al castings.[108]

Herrera and Kondic[109] and Surappa *et al.*[110] carried out studies on Al-Si and Al-Si-Mg alloys containing low porosity levels (< 0.4%). Both studies showed that, if the decrease in tensile strength were plotted against either the length or the projected area of the pores on the fracture surface, a relatively good correlation between the tensile properties and average volume fraction of porosity could be obtained. Surappa *et al.*[110] showed that the decrease in the elongation to fracture could be related to the projected area of the pores on the fracture surface. They also pointed out that the ductility and strength of the Al-7Si-0.3Mg-T6 alloy depend mainly on the size of the macropores on the fracture surface, rather than the volume percent porosity obtained by density measurements. The results of Herrera and Kondic[109] prompted them to conclude that density is the least promising parameter for studying the quantitative effects of cavities on the strength properties of a cast alloy.

Radhakrishna *et al.*[111] have reported that the relationships obtained between porosity and the three tensile properties (UTS, YS and El%) are nonlinear. The shape of such nonlinear graphs gives an indication of the pronounced influence of porosity on the properties, especially at lower porosity levels. Even an increase of about 0.5 vol pct in the porosity value can bring down the strength and ductility to dangerously low levels. Among the properties measured, UTS seems to be the one most affected by porosity, followed by YS and El%. The work of Pan *et al.*[112] on the effects of solidification parameters on the feeding efficiency of A356 alloy shows, however, that the UTS-porosity pct relationship is linear, whereas the El%-porosity pct relation is a logarithmic one, as can be seen from Figures 2.22 and 2.23, respectively.

More recently, Cáceres and Selling[113] have studied the effect of different types of defects on the tensile behavior of Al-7Si-0.4Mg-T6 alloy, using samples containing either

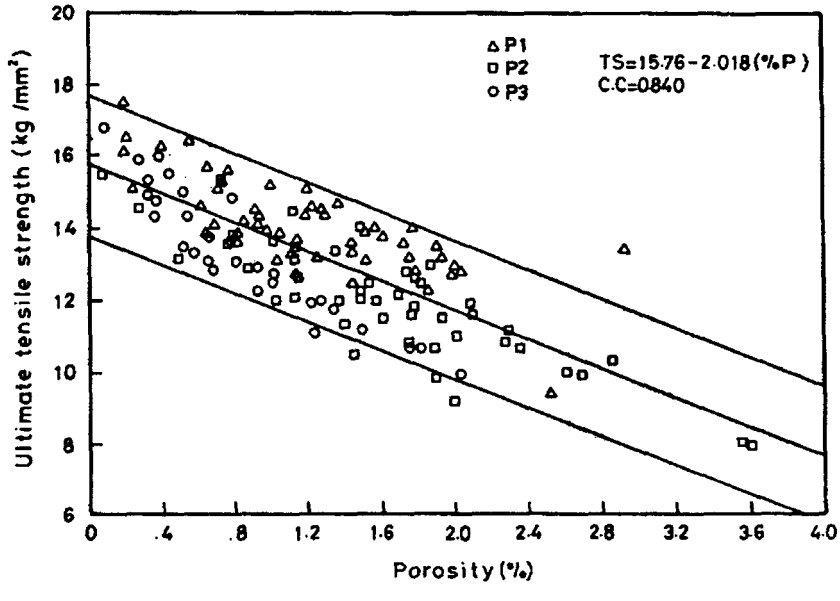

Figure 2.22. Correlation of tensile strength with porosity in A356 alloy castings.[112]

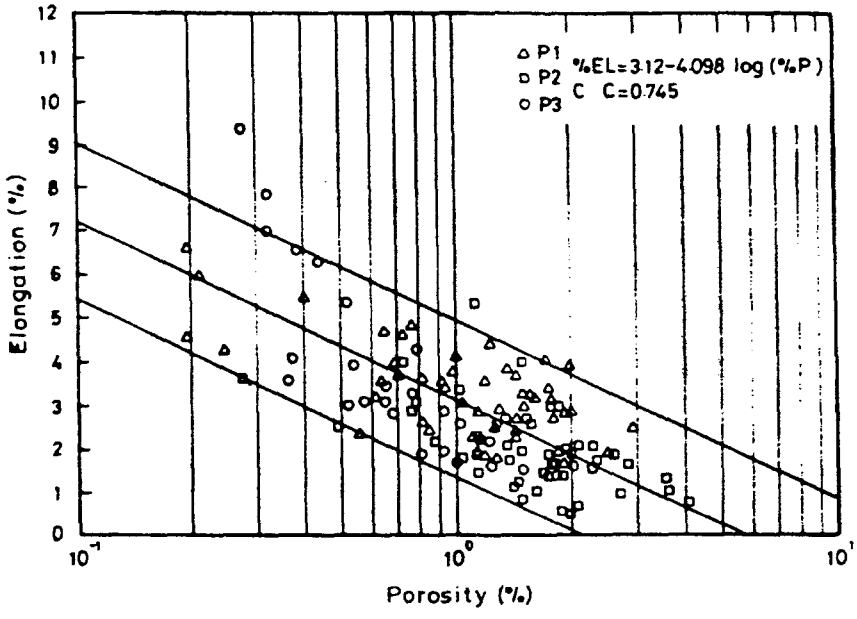

Figure 2.23. Correlation of percent elongation with porosity in A356 alloy castings.[112]

entrapped dross and oxide films, gas porosity or small drilled holes. They have observed that the tensile properties show little or no correlation with the bulk porosity content, especially in the case of samples containing dross and oxide films. In contrast, the decrease in tensile ductility and strength are found to correlate with the area fraction of defects observed on the fracture surface of the samples.

Samuel *et al.*[114] studied the relations between the melt and solidification parameters, porosity content, microstructure, tensile properties and fracture behavior in unidirectionally solidified 319.2 alloy castings. They found that both ultimate tensile strength and ductility are sensitive to variations in porosity and solidification conditions, varying in a non-linear fashion with respect to both, while the yield strength remains practically unaffected. In another study,[96] they pointed out that pores deform plastically, leading to the fracture of intermetallic phase particles at the pore edges.

2.9 FRACTURE BEHAVIOR OF Al-Si CAST ALLOYS

The knowledge of fracture behavior is important in upgrading material specifications, improving product design, and analyzing failures for improved product reliability.[115] Basically, Al-Si alloys are a combination of the high strength, brittle Si phase and the low strength, ductile Al matrix. Clearly, therefore, the fracture behavior will be controlled by the characteristics of these constituent phases.

2.9.1 Fracture Mechanisms

Studies of the fracture mechanisms of Al-Si cast alloys appear to have started in the 1960s.[116-118] To date, there are many investigations that are reported in the literature. Hafiz and Kobayashi[119] carried out a study on the relation between microstructure and fracture behavior in Al-Si casting alloys. They found that at the very beginning, the voids are generally initiated at silicon particles. The individual voids then grow and coalesce, creating microcracks in the eutectic region. These microcracks link up to form the main crack and then the final fracture.

Dighe and Gokhale[120] observed that in Al-Si-Mg cast alloys, the fracture path goes through fractured silicon particles, debonded silicon particles, and the aluminum matrix. Failure occurs mainly because of the gradual debonding and fracture of silicon particles, followed by inter-linkage of these damaged silicon particles through cracks that ultimately cause the fracture.

Voigt and Bye[121] pointed out that in A356 alloys, crack initiation or propagation is preceded by fracture of the silicon particles at relatively low values of strain. Further

straining causes selected microcracks to link up with other neighboring microcracks in the same eutectic region to initiate the primary crack, or to link up with the propagating crack front. Fracture paths tend to follow the eutectic regions in the microstructure and avoid the pro-eutectic α-aluminum regions.

Surappa *et al.*[122] investigated the deformation and fracture behavior in a cast Al-7Si-0.3Mg alloy using a microstructural approach. They observed that microcracks appear immediately after the onset of plastic deformation in sand-cast alloys. These microcracks are associated with brittle grain boundary cracking and the cleavage of plate-shaped iron intermetallics. Intense shear bands usually propagate preferentially along grain boundaries. Microcracks grow and link along these shear bands. In die-cast alloys, the microcracks are also observed early on in the deformation process. These microcracks are located at interdendritic boundaries, and occur due to the fracture of small intermetallic particles. With an increase in strain, more and more silicon particles at grain boundaries begin to fracture and to decohere, but no localized shear occurs as in the case of the sand-cast alloys.

Thus, it is generally accepted that the failure or fracture of A356 or A357 alloys occurs in three stages: (i) silicon particle cracking at low plastic strains (1-2%); (ii) as deformation proceeds, cracked particles generate localized shear bands which form microcracks by joining adjacent cracked particles; and (iii) microcrack coalescence followed by propagation, leading to final fracture.[123]

Although the above failure/fracture mechanism is generally accepted, the identification of the fracture path, however, differs among various researchers. Frederick and Bailey[118]

observed that the fracture in Al-Si-Mg casting alloys occurs almost exclusively along the dendrite cell boundaries, which suggests a transgranular fracture path.

Voigt and Bye[121] studied the microstructural aspects of fracture in A356 alloys, both with and without Sr-modification, in the as-cast and heat-treated conditions. They found that the cracks may sometimes propagate along the grain boundaries, but in general, crack propagation occurs in a transgranular manner and follows the eutectic regions, independent of the grain boundaries themselves.

Fat-Halla,[124] on the other hand, found that in a rapidly solidified Sr-modified A356 alloy, the fracture follows an intergranular path, while slowly solidified sand-cast alloys show a tendency towards transgranular fracture. The observations of Surappa *et al.*[122] on the deformation and fracture of cast A356 alloy suggest that sand-cast samples show an intergranular fracture path, whereas die-cast samples exhibit a transgranular fracture mode. Coade *et al.*[125] reported an intergranular fracture mode in an Sr-modified Al-7%Si-0.4%Mg alloy with a small dendrite cell size.

Fracture behavior investigations covering intergranular and transgranular fracture types are also reported in several other works.[96,126-133] These are described in the following section, in relation to the various parameters that influence fracture characteristics.

2.9.2 Effect of Microstructural Parameters on Fracture Behavior

In Al-Si cast alloys, since the silicon particles are more brittle than the aluminum matrix, it is expected that these particles will have an important effect on fracture behavior. Other microstructural parameters, such as the dendrite arm spacing and the iron

intermetallics and other constituents present in the structure would also be expected to influence fracture characteristics.

2.9.2.1 Silicon Particles

In all the investigations described previously, it is found that silicon particles play an important role in the fracture behavior of Al-Si alloys. In their study on the relationship between fracture properties and the microstructure of hyper-eutectic Al-Si alloys, Okabayashi *et al.*[126] reported that the crack propagation behavior is governed by the primary silicon particles, where the cracks propagate by the successive cleavage of these particles.

According to Dighe and Gokhale,[120] in commercial A356 alloy, the fracture path of tensile-tested specimens primarily goes through the largest silicon particles, which constitute less than 1% of the overall population of silicon particles in the bulk microstructure. Cáceres and Griffiths[127,128] have pointed out that, in Al-7Si-0.4Mg casting alloys, the larger and longer silicon particles are more prone to cracking. In coarser structures, silicon particle cracking occurs at low strains, while in finer ones, the progression of damage is more gradual. The authors observed that in the former case, broken particles were found on both cell and grain boundaries, with no evident preference for either; whereas in the latter case, cracking was initiated on the grain boundaries.

Saigal and Berry[129] showed that increasing the Si particle size or aspect ratio results in a detrimental effect on the crack initiation stress (where the aspect ratio represents the ratio of the maximum length to the minimum length of the silicon particle). Hafiz and

Kobayashi[119] suggested that in Al-Si casting alloys a low aspect ratio and better circularity of silicon particles increases alloy resistance to fracture, due to the influence of silicon particles on the first stage of the crack, *i.e.*, void nucleation.

Voigt and Bye[121] found that, even though the Sr-modified eutectic silicon microstructure is considerably finer than the unmodified one, the pre-fracture and fracture events observed in the modified alloys are similar to those observed in the unmodified case. However, the amount of strain required for microcrack initiation and propagation is increased with Sr modification.

2.9.2.2 Dendrite Arm Spacing

Samuel and Samuel[96] found that in 319.2 end chill castings, in general, fracture surfaces of alloys obtained close to the chill (5 mm above the chill end, DAS ~15 μm) displayed a transgranular mode, whereas at a higher distance from the chill (100 mm above the chill end, DAS ~93 μm), the fracture surface was of intergranular type, customarily associated with brittle, low-ductility materials.

Similarly, Cáceres *et al.*[130] observed that the fracture path in Al-Si-Mg alloys is transgranular in large dendrite cell size material but becomes intergranular in small cell size material, *i.e.*, the fracture mode is predominantly intergranular at small dendrite arm spacings, but becomes transgranular at large dendrite arm spacings, regardless of the magnesium content of the alloy.[131] Wang and Cáceres[123] also observed that in Al-Si-Mg alloys with large dendrite arm spacings (DASs), fracture occurs along the dendritic cell

boundaries, while for alloys exhibiting small DASs, the final fracture tends to occur along the grain boundaries.

2.9.2.3 Iron Intermetallics

As mentioned previously in Section 2.9.1 in relation to the work of Surappa *et al.*,[122] iron intermetallics can also have a significant influence on fracture behavior. In sand-cast 356 alloys, the microcracks observed immediately after onset of deformation are associated with brittle grain boundary cracking and cleavage of plate-shaped iron intermetallics, as shown in Figure 2.24 (a) and (b), respectively. Microcracks grow and link along the shear bands. The presence of porosity can support shear band formation but it does not initiate shear bands in the absence of intermetallic particles. In die-cast 356 alloys, all microcracks are formed due to fracture of small iron intermetallic particles which are located at interdendritic boundaries.

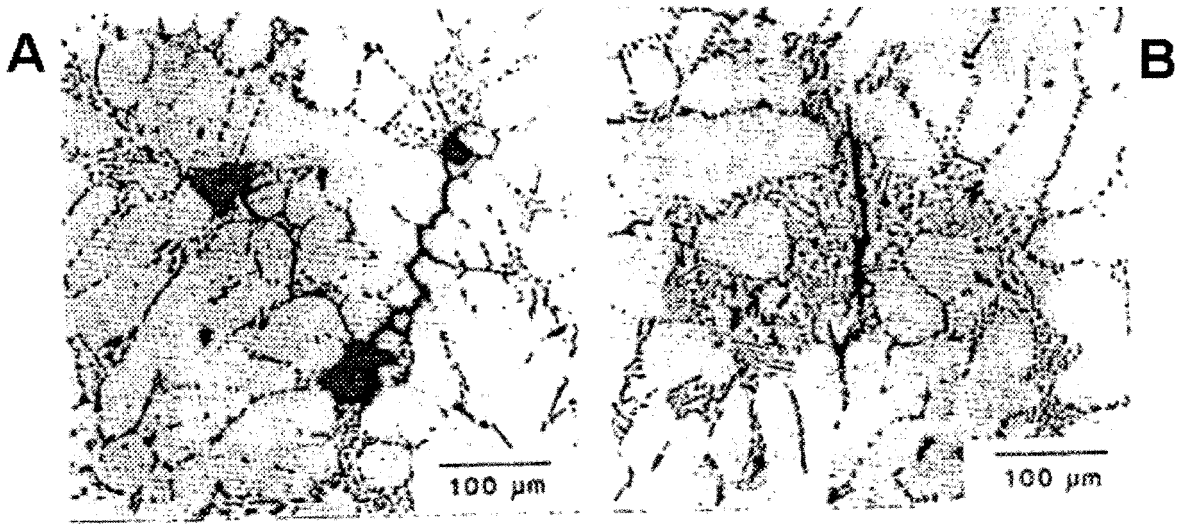

Figure 2.24. Damage in sand-cast 356 alloys showing: (a) grain boundary cracks bound by pores; (b) fractured iron intermetallic particles (tensile axis horizontal).[122]

Kato[132] performed *in-situ* microstructure observations during tensile deformation using scanning electron microscopy. He found that the needle-like β-iron intermetallics crack easily in the earlier stages of deformation, whereas the Chinese script particles (α-iron phase) can stand a higher stress. When the form of iron intermetallics was changed from Chinese script to needle-like, crack initiation did not occur at the silicon particles but at the iron intermetallics.

Villeneuve and Samuel[133] found that in tensile-fractured samples of as-cast Al-13%Si-Fe alloy, cracks are observed within the β-Al_5FeSi platelets rather than at the β/Al interface, as shown in Figure 2.25. This is due to the brittle nature of the β-phase, where the platelets split into two halves. They also observed that in Al-Si-Cu (319) cast alloys, fragmentation of the β-Al_5FeSi needles (with the addition of Sr, or Sr + Be) or their transformation into α-

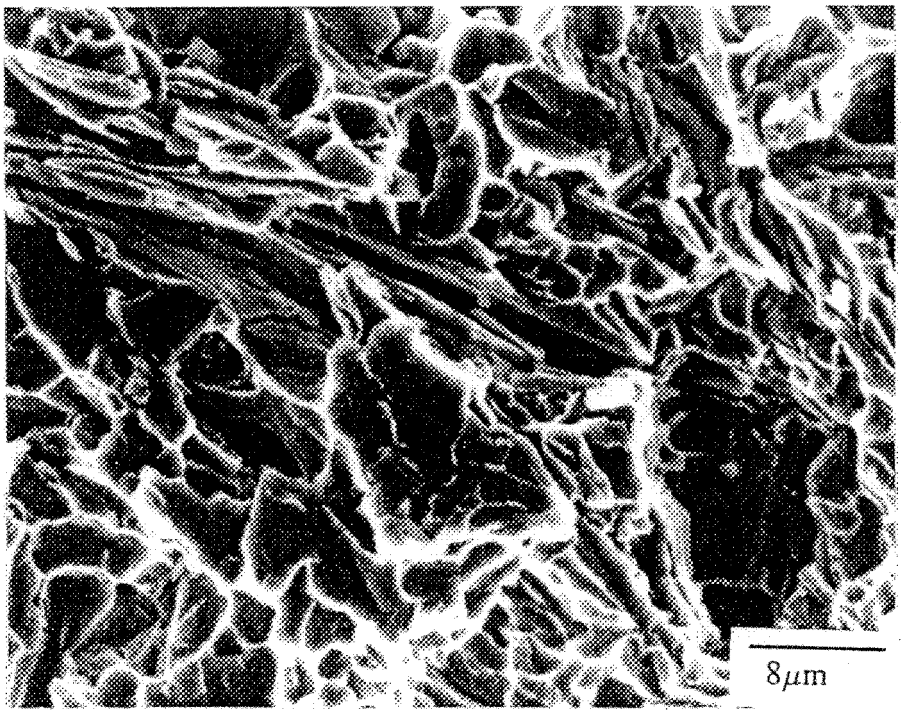

Figure 2.25. Fracture surface of a tensile-fractured Al-13%Si-Fe alloy sample (as-cast).[133]

$Al_{15}(Fe,Mn)_3Si_2$ in the form of Chinese script (with Mn/Fe ratio ~0.7) or sludge (with the addition of 0.1% Cr) results in a dimpled rupture surface.[41]

Holeček *et al.*[134] studied the influence of iron content on the embrittlement of eutectic Al-Si alloys, with iron contents up to 1.75%. They found that in tensile-fractured samples, the fracture surfaces changed when the iron contents exceeded 0.7%, due to the appearance of the primary iron-rich phase – Al_5FeSi. With the increase in iron, the number of fracture facets of these primary phase particles increases at the cost of the fractured eutectic, untill finally, the fracture surface consists entirely of cleaved areas of the primary iron-rich phase (often showing secondary cracks). Similar observations were also noted in impact-tested samples.

Murali *et al.*[19] investigated the effect of iron on the fracture toughness and microstructures of squeeze-cast Al-7Si-0.3Mg alloy, using standard Charpy V-notch impact test specimens. With ~0.7% Fe present in the alloy, brittle cleavage and intergranular fracture were observed due to the presence of β-Al_5FeSi.

CHAPTER 3

EXPERIMENTAL PROCEDURE

CHAPTER 3

EXPERIMENTAL PROCEDURE

3.1 INTRODUCTION

In the present study, 319 and 356 type alloys were selected as representing the Al-Si-Cu and Al-Si-Mg alloy systems, respectively. Both experimental and industrial alloys were used. The iron levels were varied from 0.2 to 0.8 wt% in the 319 alloys, and from 0.1 to 0.6 wt% in the 356 alloy, covering the range of Fe levels normally observed in industry (secondary materials). The alloy melts were also modified with Sr, in keeping with regular melt treatment practices, to study the effect of modification on the alloy properties.

Castings were carried out using an end-chilled refractory mold that provided unidirectional solidification and hence, cooling rates that varied along the height of the casting. Identical castings were prepared for metallographic analysis, and tensile and impact testing, in order to correlate the microstructural characteristics with the properties observed. Three important microstructural aspects were considered: the dendrite arm spacing, as determined by the solidification rate, and the porosity and iron intermetallics formed in these alloys as a function of the iron level present in the latter, as well as that due to the addition of Sr in the Sr-modified cases. Microstructural observations of porosity and iron intermetallic characteristics were carried out using optical microscopy in conjunction

with image analysis (for quantification purposes). Fractography of the impact-tested samples was also done to determine the crack initiation and propagation characteristics in the various alloys.

3.2 EXPERIMENTAL PROCEDURE

The primary A356.2 and experimental 319 alloys used in this study were supplied in the form of 12.5-kg ingots. The chemical compositions of the as-received alloys are listed in Table 3.1. The two 319 alloys used differ from each other in their Mg contents, where the B319.2 alloy contained 0.4 wt% Mg compared to that of 0.002 wt% in the 319.2 alloy. The Mg level of 319 alloys used in automotive applications is generally of the order of ~ 0.4 wt%.

Table 3.1. Chemical compositions of 319 and 356 alloys

Study	AA	Elements (wt%)									
Code	Alloy	Si	Cu	Mg	Fe	Mn	Zn	Ti	Sr	Pb	Al
EA	319.2	6.06	2.98	0.002	0.12	0.023	0.006	0.007	0.0003	--	bal.
IA	319.2	6.12	3.57	0.0719	0.405	0.0939	0.0483	0.138	0.00024	--	bal.
IB*	B319.2	6.22	3.21	0.40	0.15	0.026	0.0034	0.0075	--	--	bal.
IC	A356.2	6.78	0.02	0.33	0.11	0.04	0.04	0.08	--	0.03	bal.

* EB alloy was prepared from EA alloy where the Mg level was increased to 0.4 wt%.

Alloy codes A, B and C were used to identify the 319.2, B319.2 and A356.2 alloys, respectively. In addition, codes E and I were used to distinguish the experimental alloys from the industrially obtained materials. Column 2 of Table 3.1 identifies the different alloy categories. By comparing experimental alloys (where there is a stricter composition

control) with their industrial counterparts over minor elements, the implication of impurities on the mechanical properties could also be investigated.

3.2.1 Melt Preparation and Casting Procedures

The ingots were melted in a silicon carbide crucible of 7 kg capacity, using an electric resistance furnace (temperature deviation of ± 5°C). The melting temperature was held at 735 ± 5°C. For the three alloys studied, various alloy melts were prepared using different Fe levels.

319 alloys: 0.2, 0.4, 0.6 and 0.8 wt%;

356 alloy: 0.12, 0.2, 0.4 and 0.6 wt%;

The Fe additions were made using Al-25% Fe master alloy in the required amounts. To promote iron dissolution (especially at high iron levels), the melt temperature was kept at ~ 80-100 °C above the respective alloy melting point.

In all cases, the melts were degassed using pure, dry argon, *i.e.*, the hydrogen level was kept to a minimum, at ~0.1 mL/100g (where an AlScan^{TM} apparatus was used to monitor the hydrogen level). Degassing was done using a rotary impeller (30 min at 150 rpm). Strontium additions of 200-250 ppm were made to the degassed melts, to compare modified and unmodified structures. Also, Al-5% Ti-1% B master alloy was added to all the melts, for grain refining purposes.

Castings were done in a rectangular end-chill mold, as shown in Figure 3.1(a). The four walls of the mold are made of refractory material, while the bottom is a water-chilled copper base, to promote directional solidification and ensure proper thermal insulation. The

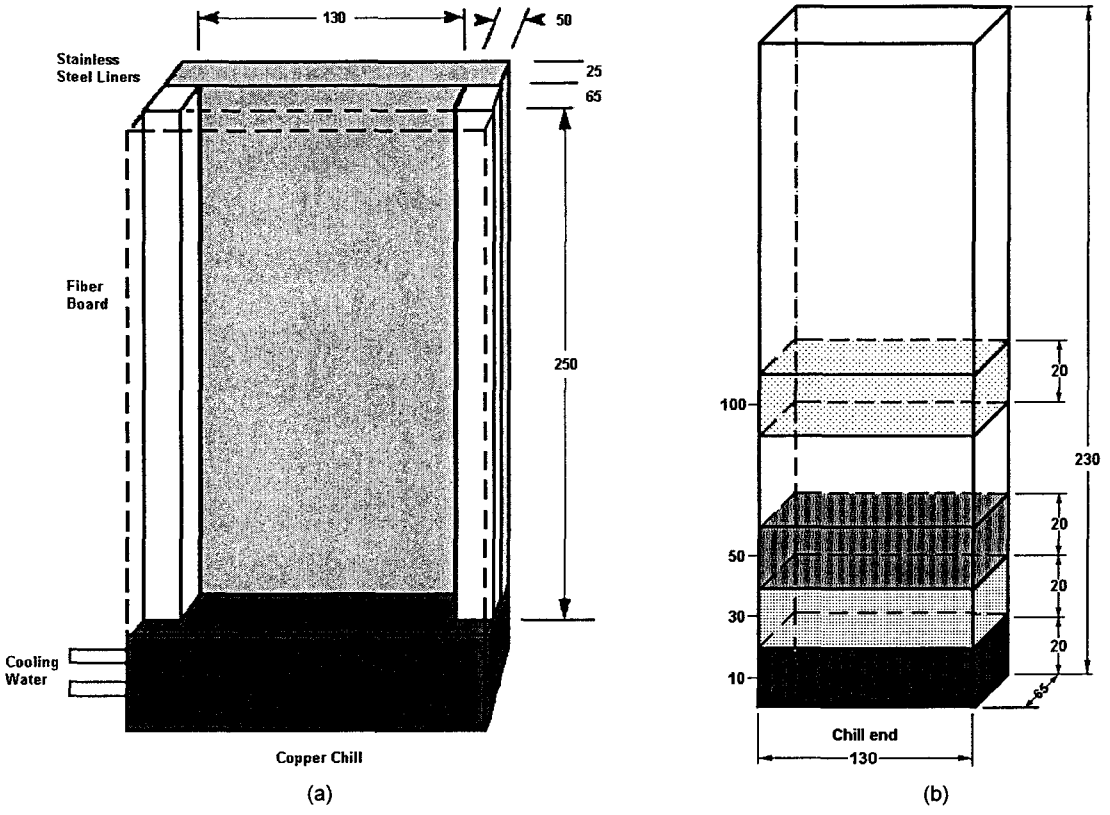

Figure 3.1. Casting preparation. (a) End chill mold scheme, (b) end chill casting showing specimen sectioning scheme.

molten metal was poured through 20 ppi (8 pores/cm) ceramic foam filter discs fitted into the riser above the sprue, to avoid incident inclusions. Such a mold has to be assembled each time for a casting. This is a lengthy procedure, involving great care in the assembling of the mold walls, as the refractory material used often cracks during casting. Once assembled, the mold must be preheated at ~135°C, to remove all moisture from the walls. Thus, at most, two castings can be prepared in one day.

Using this mold arrangement, casting blocks were produced that exhibited a range of dendrite arm spacings (DASs) along the length of the casting, corresponding to solidification rates that decreased (and, hence, DASs that coarsened) with increasing

distance from the chill end. Table 3.2 indicates the average DASs that were obtained for the 319 and 356 alloys, corresponding to different distances from the chill end. For each pouring/casting, samplings for chemical analysis were also taken, to determine the exact composition of the melt. Chemical analyses were carried out at GM facilities in Warren, MI. Also, for each set of melt conditions, identical castings were prepared for metallographic observation (1 casting), and tensile (1 casting in 319 alloys, 2 castings in A356.2 alloys) and impact testing (1 casting).

Table 3.2. DAS values obtained at various levels of the end-chilled castings for the three alloys used

Level	Distance from chill end (mm)	Average DAS (μm)	
		Alloys 319 (A & B)	Alloy A356.2 (C)
1	10	23	23
3	30	47	39
5	50	60	53
10	100	83	75

3.2.2 Sample Preparation

For the preparation of all samples (metallography, tensile and impact), 20 mm thick specimen blanks were sectioned from each casting, such that their centerlines passed through four pre-selected heights of 10, 30, 50 and 100 mm above the chill end (see Figure 3.1(b)), to obtain microstructures that corresponded to the DASs shown in Table 3.2. The rest of the casting was kept aside for use in the preparation of further melts if required.

3.2.2.1 Metallography

For each of the castings prepared for metallographic observations, four samples (3 cm × 2 cm) were sectioned at 10, 30, 50 and 100 mm levels above the chill end, to obtain microstructures corresponding to different DASs, as mentioned previously. The samples were mounted in bakelite and polished, using a BUEHLER Variable Speed Grinder-Polisher to the desired fine finish (0.25 μm diamond paste). Details of the grinding and polishing procedure are shown in Table 3.3. In each stage of the procedure, the coolant used also acted as a lubricant and ensured constant cleaning of the paper and the specimen simultaneously. Care was taken to see that the pressure exerted on the specimen was high enough to ensure proper cutting by the abrasive and a sufficient rate of abrasion, without unwanted production of heat and premature wear and tear of the abrasive.

Table 3.3. Grinding and polishing procedure of metallographic samples

Stage	Abrasive	Particle Size (μm)	Coolant	Pressure (lb)	Time (min)
1	SiC (120)	100	Running Water	15	2:30
2	SiC (240)	50	Running Water	15	3:45
3	SiC (320)	35	Running Water	15	4:00
4	SiC (400)	26	Running Water	15	4:45
5	Diamond	6	Special Oil	32	3:30
6	Diamond	1	Special Oil	32	3:30
7	Diamond	0.25	Special Oil Running Water	25 1	2:30 5:00

Note: *Special oil* means *BUEHLER Metadi Fluid*

3.2.2.2 Tensile Testing

From the castings prepared for tensile testing, 20 mm specimen blanks were cut from each casting, such that their centerlines passed through heights of 10, 30, 50 and 100 mm above the chill end (see Figure 3.1(b)). From each blank, it was possible to machine three tensile test specimens. Samples were machined according to the dimensions shown in Figure 3.2. The gage length of the samples is 2 in. (50.8 mm). Thus, for each melt condition and level above the chill end, three (319 alloys) or six (356 alloy) tensile test specimens were obtained. Prior to testing, the samples were T6-heat treated, in keeping with the standard Aluminum Association recommendations.

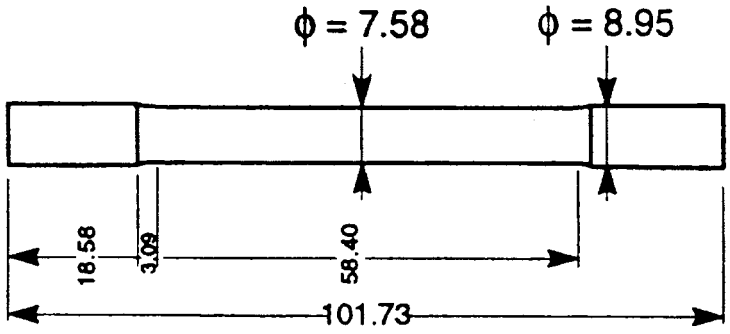

Figure 3.2. Tensile test specimen.

3.2.2.3 Impact Testing

Impact values depend strongly on the testing method used. In the present study, Charpy unnotched simple beam impact samples were used, since the Charpy test is the most common laboratory method for the measurement of impact energy. The specimens were machined in accordance with ASTM E23 standards.[135] The standard proportions are shown in Figure 3.3. As was done in the case of the tensile test specimens, four such samples were

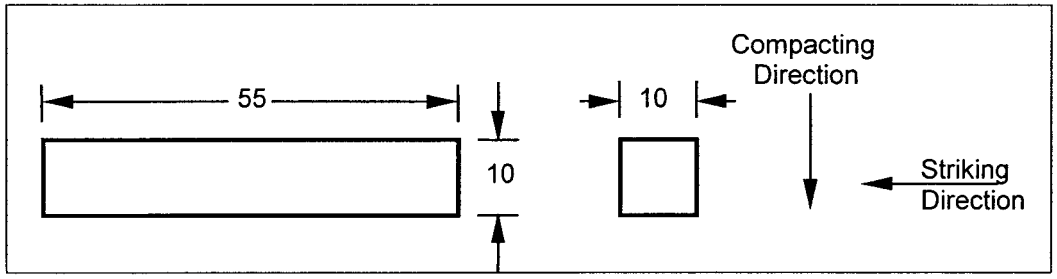

Figure 3.3. Charpy unnotched simple beam impact test specimen (all dimensions in mm).

obtained from each of the four 20 mm-thick specimen blanks sectioned from each casting. In this case, four impact test specimens were obtained for each melt condition and level above the chill end. Again, prior to testing, the samples were T6-heat treated.

3.2.3 Microstructural Characterization

As the present study involved noting both qualitative and quantitative aspects of the microstructures of the different alloys, metallographic observations were carried out using optical microscopy in conjunction with image analysis. Scanning electron microscopy was used to analyze the fracture surfaces of selected impact samples, where both secondary and backscattered beam techniques were used to examine the fracture process and crack propagation.

3.2.3.1 Metallography and Image Analysis

Microstructures of the polished surfaces were examined using an optical microscope. The α-aluminum dendrite arm spacings, β-Al_5FeSi intermetallic phase characteristics and porosity were analyzed and quantified using a Leco 2001 image analyzer in conjunction with the optical microscope (Olympus BH2-UMA). Measurements carried out included:

(a) determination of the DAS of the sample microstructure;

(b) porosity measurements including area percentage porosity, and individual pore feature parameters of area, length and aspect ratio;

(c) measurements of the needle-like β-Al_5FeSi iron intermetallic phase (actually β-platelets), including length, thickness and density (number per unit area of the sample).

For the porosity and β-platelet measurements, the number of fields examined ("field" representing the field of observation of the optical microscope, and covering an area of 2.2608×10^4 μm^2 at a magnification of 500×) for each sample were chosen such that the entire sample surface was traversed in a regular, systematic manner, and the porosity or β-platelet characteristics noted for each field. As a rule, the outer edges of a sample were avoided in taking these measurements (to avoid any distortions that occurred in the peripheral regions). Due to the fact that several of the intermetallic phases observed in the microstructure had the same level of grayness when observed on the monitor of the image analyzer, the samples had to be etched in an H_2SO_4 solution, which changed the color of the β-platelets from pale gray to dark gray (almost black). As pores appear black in the microstructure, the porosity measurements were carried out first, before the samples were etched for the β-platelet measurements. The results obtained from these measurements were statistically analyzed and tabulated. Porosity measurements were carried out at 50×, while the DASs and β-platelets measured at 200× (or 500×). The thickness of the β-platelet were measured at the highest magnification of 1000×. In the case of the impact-tested samples, metallographic samples were also prepared from longitudinal and transverse sections of the

fractured samples, as shown in Figure 3.4. The white lines indicate how the samples were sectioned. The longitudinal section (a) was polished and examined under the optical microscope, while the transverse section (b) containing the fracture surface was used for fractography.

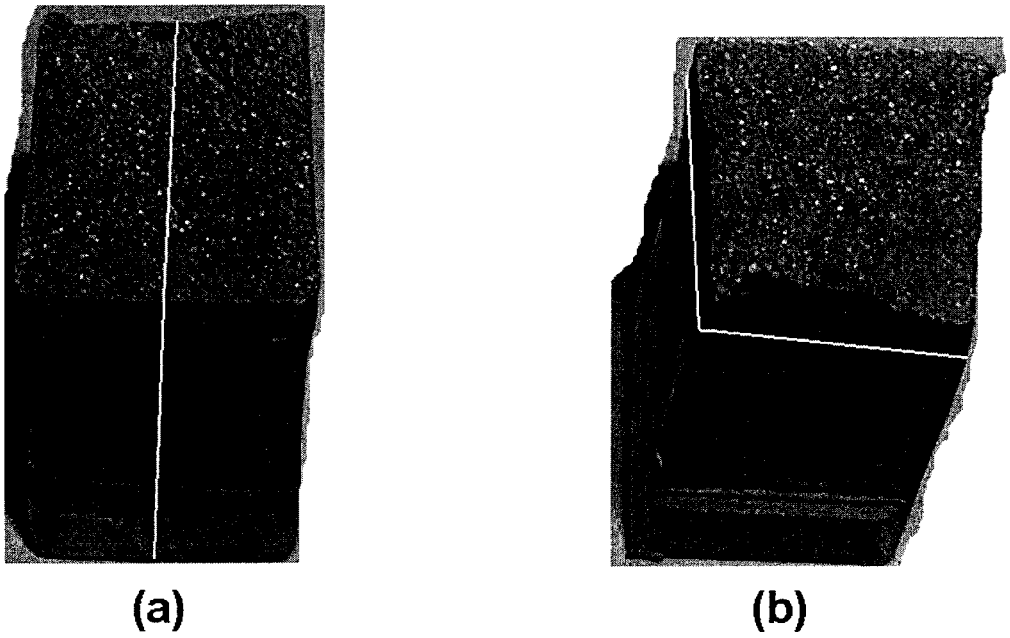

Figure 3.4. An impact-tested specimen showing the location of metallographic samples used for fractographic examination: (a) optical microscopy and, (b) SEM.

In this regard, it is important to understand how the β-platelet measurements were carried out; as opposed to measuring all the β-platelets in a certain number of fields, the β-platelet characteristics were determined from the measurements of 120-150 platelets (depending upon the sample), where the three largest platelets were measured in each field of the 50 fields that were observed over the entire sample. This procedure was adopted on the assumption that larger β-platelets were more detrimental to the alloy properties. However, for purposes of measuring the β-platelet density, all β-platelets were counted in

each of the 50 fields observed for every sample. The porosity parameters measured were area percentage porosity, pore area, pore length and pore aspect ratio, as well as the pore count. The raw data from the image analysis measurement for each sample was further analyzed to obtain average and maximum values of pore area and pore length. Pore densities were also calculated.

3.2.3.2 Fractography

Fracture surfaces of impact-tested samples were examined in order to determine the crack initiation and propagation behavior with respect to the alloy compositions and melt treatment conditions. Samples were cut approximately a quarter inch from the fracture surface, as shown in Figure 3.4(b), where the upper part was used for examination. Extra care was taken during the cutting to avoid contamination of the fracture surface. The bottom of the sample was ground to flatten it, then mounted on a standard base with a special glue. Several samples were kept together in a box and classified systematically according to their chemical compositions and melt treatment conditions before they were placed into the specimen chamber of a scanning electron microscope. The SEM work was carried out at Noranda Technology Centre (Montreal), using a scanning electron microscope operating at 15 kV.

3.3 Mechanical Testing

As mentioned previously, for each alloy composition and melt condition, 3 (in 319 alloys) or 6 (in A356.2 alloys) test bars were machined from each specimen blank such that their center lines corresponded to the four levels (10, 30, 50 and 100 mm) above the chill

end. Thus, for 34 compositions and conditions in all, a total of 504 tensile test specimens were prepared for testing.

Similarly, a total of 288 impact test specimens were machined (four from each specimen blank).

The tensile and impact tests were carried out as described below.

3.3.1 Tensile Testing

In keeping with Aluminum Association recommendations, all the tensile test samples were T6 heat-treated. The heat treatment was carried out in a GS Blue M Electric air-forced furnace (with a temperature deviation of ±1 °C), as follows:

Alloys A and B: 8 h at 500 °C (solution heat treatment), followed by quenching in warm water (~60 °C), followed by immediate aging at 155 °C for 5 h (artificial aging).

Alloy C: 8 h at 540 °C (solution heat treatment), quenching in warm water (~60 °C), followed by natural aging at room temperature for 24 h, then artificial aging at 155 °C for 5 h.

The gage lengths of heat-treated samples were marked using a special marker, and their actual diameters were measured before testing. Samples were then tested at room temperature using an Instron Universal Testing machine (Figure 3.5), to obtain yield strength (YS), ultimate tensile strength (UTS) and percent elongation at fracture (%El), at a loading speed of 0.02 in/min (0.5 mm/min). The machine was calibrated every time before any testing was carried out. The test data was collected automatically by a data-acquisition system attached to the Instron testing machine. As the maximum limit of the extensometer

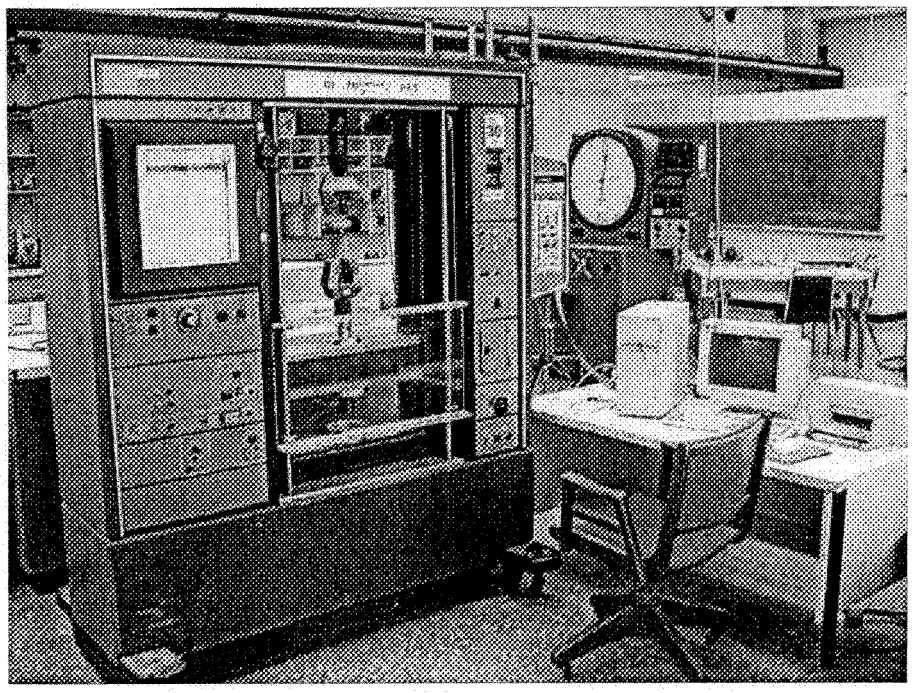

Figure 3.5. An Instron Universal Testing machine with data-acquisition system.

used was 10%, the extensometer was removed from the sample when the elongation exceeded this value. In such cases, the final elongation was measured manually with the help of a micrometer. The average %El, YS or UTS value obtained from the three samples was considered as the value representing a specified condition.

3.3.2 Impact Testing

All test samples were heat-treated similar to tensile samples. The impact tests were carried out at McGill University (Montreal) using a computer-aided instrumented SATEC SI-1 Universal Impact Testing Machine of SATEC System Inc. (Model SI-1B-1692), as shown in Figure 3.6. This machine is equipped with bolt-on weights in addition to the pendulum. The pendulum is capable of being latched in two separate modes, known as "high latch" and "low latch," providing a total of four operating capacities, *viz.*, a capacity

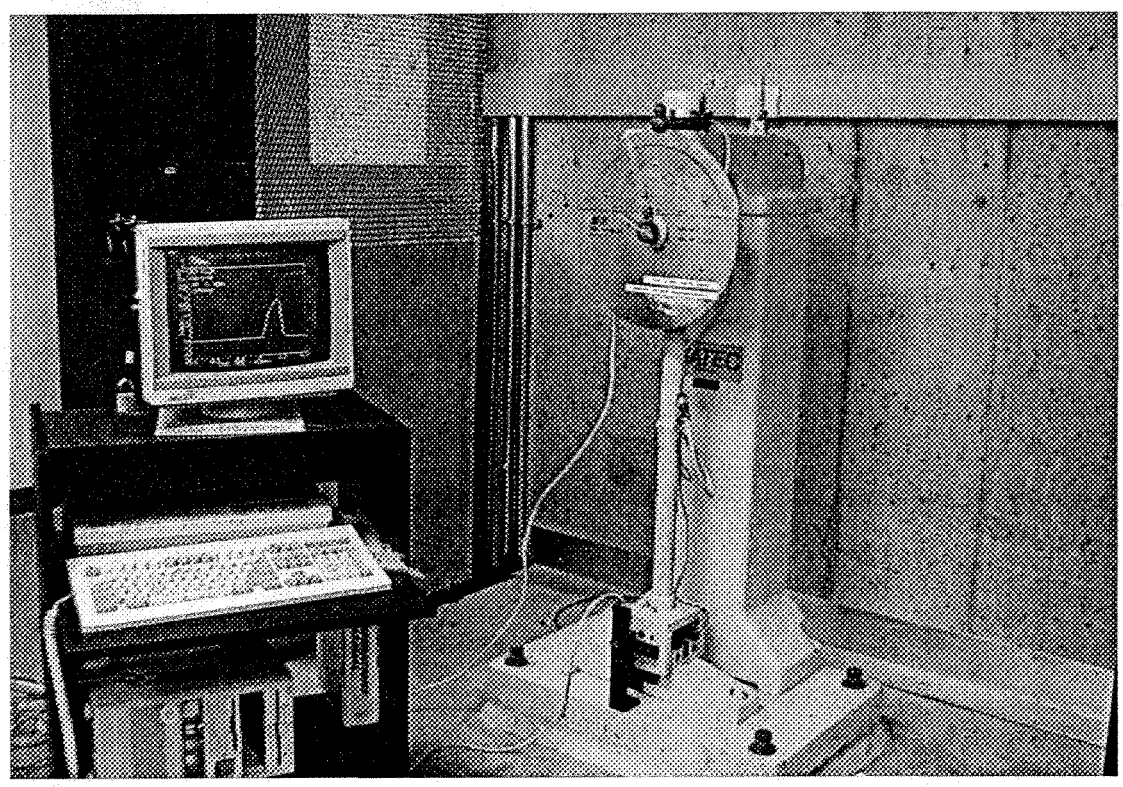

Figure 3.6. A computer-aided instrumented SATEC SI-1 universal impact testing machine, with a Dynatup IBM/PC impact testing system for data acquisition.

of 25 ft-lbs (33.9 J) on low latch and 60 ft-lbs (81.3 J) on high latch without the bolt-on weights attached, and a capacity of 50 ft-lbs (67.8 J) on low latch and 120 ft-lbs (162.7 J) on high latch with the additional weights attached. During testing, different pendulum weights and positions were employed, corresponding to the ductilities of the samples. The load-deflection curves and energies absorbed were obtained with a Dynatup IBM/PC Impact Testing System. The average value of the energies obtained from the four samples tested for each alloy condition (and level above the chill end) was taken as the impact energy of that alloy condition. Secondary and backscattered beam techniques were used to examine the crack paths in the fractured specimens with respect to microstructural constituents.

CHAPTER 4

TENSILE PROPERTIES AND MICROSTRUCTURE

CHAPTER 4

TENSILE PROPERTIES AND MICROSTRUCTURE

4.1 INTRODUCTION

Tensile testing is one of the most common methods used to measure the static properties of a metallic material. The directly obtained results after a tensile test are percent elongation at fracture (%El), 0.2% offset yield strength (YS), and ultimate tensile strength (UTS). In some cases, only percent elongation and ultimate tensile strength can be recorded if a test sample is too brittle. The definitions of these three parameters have already been interpreted in detail in Chapter 2.

Tensile properties depend directly on the alloy microstructure. In the Al-Si-Cu and Al-Si-Mg alloys studied in the present work, the as-cast alloy microstructure consists of the aluminum matrix (α-Al dendrites), silicon particles, intermetallic phases, non-metallic inclusions and porosity. Among these, iron intermetallics and porosity are the main microstructural features that will be emphasized in the present study, since they are considered to be primarily responsible for any deterioration in alloy properties, as discussed in Chapter 2.

The alloy microstructure is controlled by several factors, among them being the chemical composition (including trace elements and impurities), the melt treatment

conditions, the solidification rate and the heat treatment applied. Iron is the least desirable among the impurity elements present in the alloy, as it not only forms harmful iron intermetallics, but also facilitates porosity formation due to the presence of these intermetallics. Strontium is a common modifying agent used to modify the shape of the eutectic silicon from acicular to fibrous (termed "eutectic modification"). Addition of strontium changes the morphology and size of the iron intermetallics as well, but also favors the formation of porosity. The cooling rate has a direct effect on grain size and can also affect the size of the microconstituents that precipitate and the porosity formed. These, in turn, can affect the fracture behavior of the alloy sample. With respect to the Al-Si-Cu and Al-Si-Mg alloys, copper and magnesium are used as alloying elements for strengthening purposes after heat treatment. All these parameters provide a complicated effect on the tensile properties, as will be discussed in this chapter.

The tensile test results of elongation, ultimate tensile strength and, in some cases, the yield strength, are usually considered separately when the effect of one or more parameters such as alloy composition, melt treatment, solidification rate, heat treatment, *etc.* on the properties is studied. However, in 1980, Drouzy *et al.*[136] proposed another method for the interpretation of tensile properties. They defined two variables, *quality index* and *probable yield strength*, both of which were obtained as functions of UTS and elongation through a plot of UTS *vs.* log Elongation. According to them, these variables, being directly related to the alloy physical properties and varying independently of each other, would facilitate tensile data interpretation. Thus, it was possible to use tensile test results more effectively by considering the properties globally, instead of individually.

4.1.1 Quality Index and Probable Yield Strength

The concept of the quality index, Q, together with the probable yield strength YS, was developed by Drouzy, Jacob and Richard[136] to interpret tensile results when they observed that, as a particular batch of Al-7Si-Mg alloy samples was aged, the plot of ultimate tensile strength versus the logarithmic value of elongation (tensile ductility) followed a linear relationship with a slope of -150, as shown in Figure 4.1. The change in ultimate tensile strength and log (%El) follows an iso-Q line, or, in other words, lower ductility due to the increased strength, keeping the "quality" of the alloy constant. By contrast, if ductility is reduced at a constant yield strength, for instance by increasing the dendrite arm spacing (DAS) or the iron content of the alloy (with the ageing condition and Mg content remaining unchanged), the quality is said to decrease, as shown in Figure 4.2.

It was also found that yield strength could be estimated with a good approximation from the ultimate tensile strength and elongation, resulting in the iso-YS lines of Figures 4.1 and 4.2. Drouzy *et al.*[136] proposed the following equations to present the correlation:

$$Q = UTS + K \log (El) \tag{4-1}$$

$$YS = a\ UTS - b \log (El) + c \tag{4-2}$$

where the coefficient K is chosen so as to make Q practically independent of the degree of hardness of the alloy, and a, b and c depend upon the nature of the alloy. Also, K, a, and b are greater than zero, and the two expressions are valid only when $El \geq 1\%$.

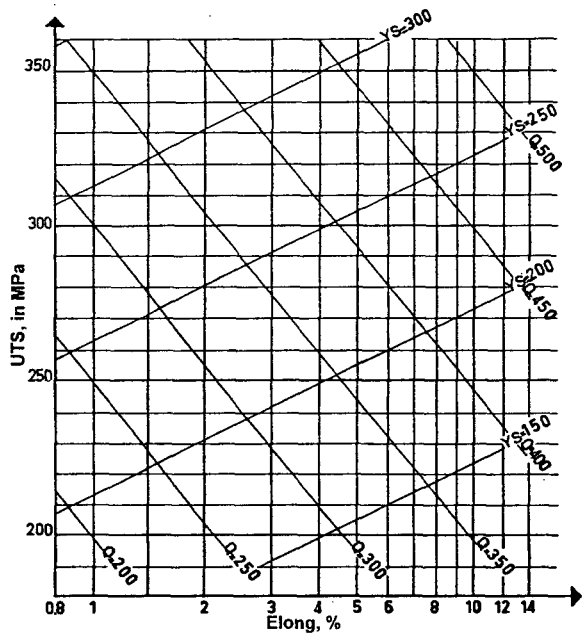

Figure 4.1. UTS-elongation diagram of heat-treated Al-7Si-Mg alloys with a double series of lines of equal quality index (iso-Q lines) and lines of equal probable yield strength (iso-YS lines).[136]

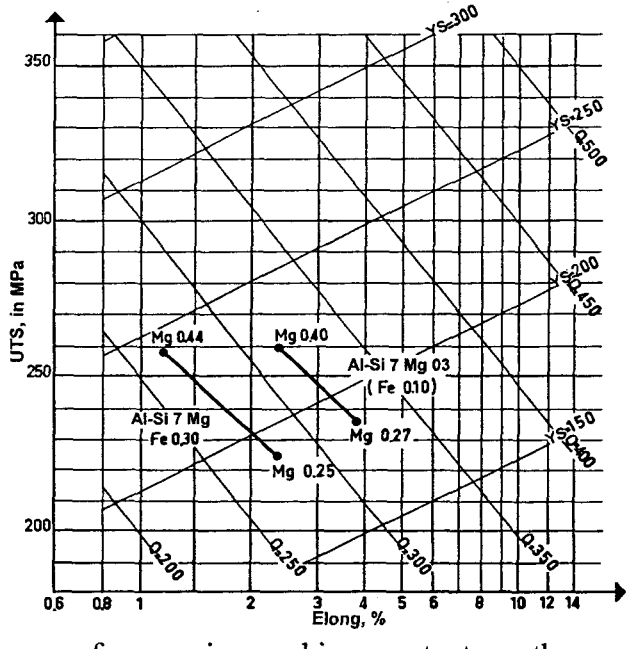

Figure 4.2. Influence of magnesium and iron contents on the mechanical properties of a sand-cast Al-7Si-Mg alloy. Magnesium causes the yield strength to vary and does not affect the quality index. The opposite is true for iron.[136]

Quality index and probable yield strength are thought much better than the ultimate tensile strength and elongation, since they are in direct relation with the physical phenomena which govern the properties of the alloy and vary independently from each other. The quality index depends essentially upon the compactness of the casting and the fineness of its structure, or in other words, on the quality of the sample. Thus, it is practically determined by the solidification conditions. In contrast, probable yield strength characterizes the degree of hardening, and thus depends primarily upon tempering treatment parameters, such as magnesium content, tempering time and temperature.[136] The quality index concept is also widely used by the casting industry as a simple but powerful tool to assess or predict the effect of changes in the chemical composition, solidification conditions, microstructure and heat treatment on the ductility and tensile strength of Al-Si-Mg casting alloys.[137]

Recently, Cáceres *et al.*[137-140] did some extensive work on the quality index concept, to come up with a rationale for the parameters used in this approach. They employed an analytical model in their studies, where true stress and true strain were utilized. The relationship between the true stress/strain, strain hardening exponent and a specific material constant (*e.g.*, 430 MPa in 356 alloys) was discussed and the commonly-used engineering stress/strain values were applied in place of the true stress/strain. The onset of necking was, however, determined using the Considère criterion (the strain hardening parameter $\gamma = 1 \cong \frac{1}{\sigma}\frac{d\sigma}{d\varepsilon}$), and the engineering strain at the onset of necking was considered as representing the maximum practical elongation due to the loss in load-carrying ability once strain localized in the neck. Based on these, the following equations were then proposed:

$$\sigma = K[\ln(1+\varepsilon)^n]e^{-\ln(1+\varepsilon)} \cong K\varepsilon^n e^{-\varepsilon} \quad (4\text{-}3)$$

$$q = \mathrm{El}/\varepsilon^* \cong \mathrm{El}/n \quad (4\text{-}4)$$

The sign $\cong$ indicates that the difference between the true and engineering strain has been ignored; σ represents the engineering stress, ε, the engineering strain, ε^*, the strain at the onset of necking, El, the elongation to fracture, K, the material constant, γ, the strain hardening parameter, n, the strain hardening exponent, and q, the relative ductility.[a]

Iso-n (with specific YS value) and iso-q lines were drawn from the above equations. After these curves were superimposed on the common iso-Q and iso-YS curves, Cáceres *et al.* pointed out that a constant Q value means that relative ductility (which is defined as the fraction between ductility and the maximum practical elongation) is constant, while the yield strength lines represent flow curves of the material in different aging conditions (although the DASs may be different). They also mentioned that the rationale for the common Q and YS is not suitable for Al-Cu alloys, since the strength coefficient of these alloys changes with the aging time.

4.1.2 Phases in Al-Si-Cu and Al-Si-Mg Alloys

During solidification, various reactions take place, as the alloy melt cools, and the phases corresponding to these reactions precipitate.

Bäckerud *et al.*[34] investigated the solidification process in various alloys, by employing the thermal analysis technique, followed by a subsequent metallographic examination of

[a] In most textbooks, the Greek letter σ/ε represents the true stress/strain while the English letter *s/e* means the engineering set. Greek letters are used here in order to avoid confusion between engineering stress and the symbol of natural log base.

samples sectioned from the solidified castings. The polished metallographic samples were examined using scanning electron microscopy (SEM) and energy dispersive X-ray spectrometry (EDX) for identifying the various phases. The phases were quantified using heat transport equations that included latent heat evolution. The different reactions and various phases in Al-Si-Cu and Al-Si-Mg alloys observed by these researchers, and also observed in the present study, are described in the following sections.

4.1.2.1 Alloy 319.2 (alloy A)

This hypoeutectic alloy contains 6.5% Si, 3.5% Cu, and other trace elements such as Fe, Mn and Ti. During solidification, the main sequence of phase precipitation that occurs is as follows.

1. Formation of a dendritic network of α-aluminum;
2. The aluminum-silicon eutectic reaction;
3. Precipitation of secondary eutectic phases like $CuAl_2$.

In addition, precipitation of iron- and manganese-containing phases, *e.g.*, the α-$Al_{15}(Mn,Fe)_3Si_2$ and β-Al_5FeSi intermetallics also takes place. These α- and β-iron intermetallics normally precipitate after the initial dendrites have formed but before the appearance of the Al-Si eutectic, *i.e.*, in a pre-eutectic reaction. However, the β-iron phase can also precipitate as a co-eutectic phase. Towards the end of the solidification process, $CuAl_2$ and other more complex phases with low melting points will precipitate from the remaining liquid, in which any Si, Fe, Mg, Cu and Zn left over may participate.[34]

If high iron and manganese levels are present in the alloy, and the cooling rate is low, the α-$Al_{15}(Mn,Fe)_3Si_2$ phase will precipitate as a primary phase, in the form of coarse particles termed "sludge," having polygonal or star-like morphologies.

Bäckerud *et al.*[34] have also listed the reactions that occur during the solidification of alloy 319.1, which differs slightly in chemical composition from the alloy 319.2. Thus, the sequence of reactions during solidification and the phases observed remain the same in both alloys, and are listed in Table 4.1,[34] together with the corresponding temperature of each reaction. The characteristics and compositions of these phases are provided in Table 4.2.[34]

Table 4.1. Reactions observed during solidification of alloy 319.2[34]

Reaction No.	Reactions	Suggested temperature, °C
1	Development of dendritic network	609
2a	Liq. → Al + $Al_{15}Mn_3Si_2$	590
2b	Liq. → Al + Al_5FeSi + $Al_{15}Mn_3Si_2$	590
3	Liq. → Al + Si + Al_5FeSi	575
4	Liq. → Al + $CuAl_2$ + Si + Al_5FeSi	525
5	Liq. → Al + $CuAl_2$ + Si + $Al_5Mg_8Cu_2Si_6$	507

Table 4.2. Phases observed by optical microscopy/SEM/EDX in alloy 319.2[34]

No.	1	2	3	4	5	6
Phase	α-Al*	Si*	$CuAl_2$*	Al_5FeSi*	$Al_{15}(Mn,Fe)_3Si_2$*	$Al_5Mg_8Cu_2Si_6$
Characteristics	Dendrite	Gray	Pink particle	Needle	Brown Chinese script	Brown bulk

* Confirmed by X-Ray Diffraction (XRD).

4.1.2.2 Alloy B319.2 (alloy B)

This alloy is very similar to alloy 319.2, except for its higher magnesium content. According to Bäckerud *et al.*,[34] the increased level of magnesium does not change the solidification process significantly, except that an increased amount of the $Al_5Mg_8Cu_2Si_6$ phase is observed, as shown in Tables 4.3 and 4.4 (taken from their data for B319.1 alloy[34]). At high iron concentrations, an increased range for the existence of the Al_5FeSi phase is perceived.

Table 4.3. Reactions observed during solidification of alloy B319.1[34]

Reaction No.	Reactions	Suggested temperature, °C
1	Development of dendritic network	602
2a	Liq. → Al + $Al_{15}Mn_3Si_2$	590
2b	Liq. → Al + $Al_{15}Mn_3Si_2$ + Al_5FeSi	590
3	Liq. → Al + Si + Al_5FeSi	575
4	Liq. → Al + $CuAl_2$ + Al_5FeSi + Si	525
5	Liq. → Al + Si + $CuAl_2$ + $Al_5Mg_8Cu_2Si_6$	507

Table 4.4. Phases observed by optical microscopy/SEM/EDX in alloy B319.1[34]

No.	1	2	3	4	5	6
Phase	α-Al	Al_5FeSi	$Al_5Mg_8Cu_2Si_6$	$CuAl_2$	Si	$Al_{15}(Mn,Fe,Cu)_3Si_2$
Characteristics	Dendrite	Needle	Grey brown bulk	Pink particle	Gray	Brown Chinese script

4.1.2.3 Alloy A356.2 (alloy C)

This alloy belongs to the Al-Si-Mg system with magnesium as the major alloying element (0.35 wt%) and copper in the amount of 0.02 wt%. The main sequence of phase

precipitation during solidification is listed in Table 4.5, and differs from the 319 alloys in the precipitation of the secondary eutectic phases (*i.e.*, Mg_2Si instead of $CuAl_2$, *etc.*). The corresponding phases and their characteristics are given in Table 4.6.

Table 4.5. Reactions observed during solidification of alloy A356.2[34]

Reaction No.	Reactions	Suggested temperature, °C
1	Development of dendritic network	615
2a	Liq. → Al + Si	
2b	Liq. → Al + Al_5FeSi	
3a	Liq. → Al + Si + Al_5FeSi	575
3b	Liq. + Al_5FeSi → Al + Si + $Al_8Mg_3FeSi_6$	567
4	Liq. → Al + Mg_2Si + Si	555
5	Liq. → Al + Si + Mg_2Si + $Al_8Mg_3FeSi_6$	554

Table 4.6. Phases observed by optical microscopy/SEM/EDX in alloy A356.2[34]

No.	1	2	3	4	5
Phase	α-Al	Si	$Al_8Mg_3FeSi_6$	Mg_2Si	Al_5FeSi
Characteristics	Dendrite	Gray	Brown script	Black	Needle

Due to the high purity of A356 alloy, it is difficult to nucleate the silicon crystals after the development of the dendritic network, thus some Al_5FeSi phase may precipitate before the start of the main eutectic reaction, as indicated by reaction 2b in Table 4.5. Some of this phase later transforms into $Al_8Mg_3FeSi_6$ via a peritectic reaction.[34] Particles of the secondary eutectic phase, Mg_2Si, also appear in the microstructure on account of the high Mg content of the alloy.

4.2 RESULTS AND DISCUSSION

Tensile tests were carried out on 319 and 356 alloy samples obtained from specimen blanks sectioned at the heights of 10, 30, 50 and 100 mm above the chill end of each casting (referred to as levels 1, 3, 5 and 10, respectively). The different cooling rates corresponding to these levels can also be expressed in terms of the dendrite arm spacing (or more accurately, the secondary dendrite arm spacing, SDAS, often quoted in the literature and in the present case as simply DAS) values, since it is well know that the cooling rate has a direct effect on the latter, as given by the following empirical equation:[141]

$$d = b(CR)^{-n} \tag{4-5}$$

where d is the average secondary dendrite arm spacing in μm, CR is the cooling rate in °C/s, b is a constant that depends on system parameters such as the diffusion coefficient in the liquid state, the solid-liquid interfacial energy, and the equilibrium freezing range of the alloy, and the exponent n is close to 0.33 in Al-Si alloys.[142,143] The DAS values obtained from the different levels (*i.e.*, cooling rates) for the 319 (A and B) and 356 (C) alloys used are shown in Table 4.7.

Table 4.7. DAS values obtained at various levels of the end-chilled castings for the three alloys used

Level	Distance from chill end (mm)	DAS (μm)	
		Alloys 319.2 (A & B)	Alloy A356.2 (C)
1	10	23	23
3	30	47	39
5	50	60	53
10	100	83	75

All the samples were T6 heat-treated prior to testing, in keeping with Aluminum Association recommendations. The ultimate tensile strength (UTS), yield strength (YS) and percent elongation (%El) values obtained were analyzed with respect to the different parameters involved, *viz.*, cooling rate or DAS, iron content, β-Al_5FeSi intermetallic size, porosity, alloy composition, Sr-modification, and so forth. These will be discussed in the following sections. The relationships between UTS and percent elongation were also analyzed in the form of log UTS-log %El plots, similar to the UTS-log %El plots discussed by Drouzy *et al.*[136] and Cáceres *et al.*[137-140] Such a representation was found to provide a fairly reasonable interpretation of the obtained results.

4.2.1 Effect of Iron Content and Cooling Rate

The effect of different iron contents on the tensile properties of alloy 319.2 (alloy A), alloy B319.2 (alloy B) and alloy A356.2 (alloy C), in unmodified and Sr-modified conditions, at different cooling rates, are shown in Figures 4.3 through 4.9. As DAS gives a better physical representation of the cooling rate, it will be used henceforth throughout the text in place of the cooling rate.

4.2.1.1 Alloy 319.2 (alloy A)

The tensile properties of unmodified experimental 319.2 alloy as a function of iron content and cooling rate are shown in Figure 4.3, where each curve in the three tensile property diagrams (elongation, yield strength, ultimate tensile strength) represents a specific cooling rate (corresponding to levels 1, 3, 5 and 10 above the chill end, or DASs of 23, 47, 60 and 83 μm, respectively). Similarly, Figure 4.4 represents the tensile test results

obtained for the Sr-modified experimental A alloy, while Figures 4.5 and 4.6 represent those for the industrial A alloy.

Overall, both percent elongation and ultimate tensile strength are found to decrease with a decrease in the cooling rate (increase in DAS) and an increase in the iron level. Considering one iron level at a time, the decrease in properties with respect to the cooling rate is in accord with the results obtained by other investigators,[96,144-146] where the different cooling rates were achieved using various casting molds or chill ends, *e.g.*, permanent and sand molds, or metallic and non-metallic chill-ends in a step-cast sand mold. With the decrease of DAS, the size and/or amount of the microconstituents that precipitate decreases accordingly, and a finer dispersion can be achieved as well. For example, the size and shape of the eutectic silicon becomes smaller and less acicular,[144] giving a finer eutectic structure (termed "quench modification"[147]). The amount of the second phase particles is also observed to decrease.[145] Also, due to the finer microstructure, any pores formed are smaller, a more uniform pore distribution is achieved, and the tendency to form interconnected porosity is reduced. Hence, ductility and tensile strength increase.

From Figure 4.3(a), for unmodified 319.2 alloy, with the increase of iron content, an overall decreasing trend in elongation is observed at all cooling rates, with a certain amount of data scatter for the DAS-23 μm (level 1) samples. Three main features are noted:

(i) The drop in elongation with increasing iron content is sharpest at the highest cooling rate (level 1 – DAS: 23 μm);

(ii) The difference in the decrease in elongation from one level to the next at any Fe content is also greatest between DASs 23 and 47 μm (levels 1 and 3);

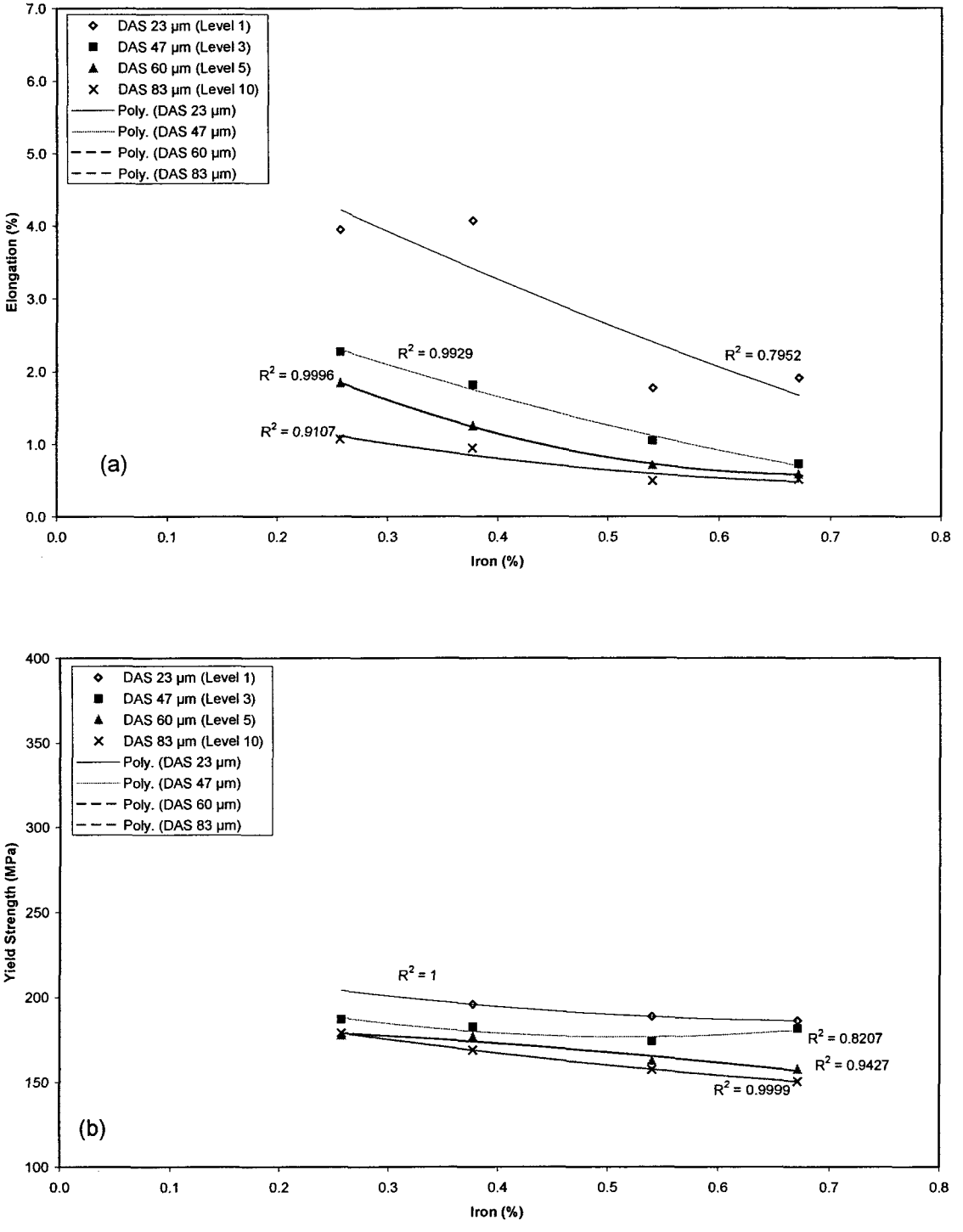

Figure 4.3. Tensile properties *vs.* iron content (experimental 319.2 alloy, 0 ppm Sr).

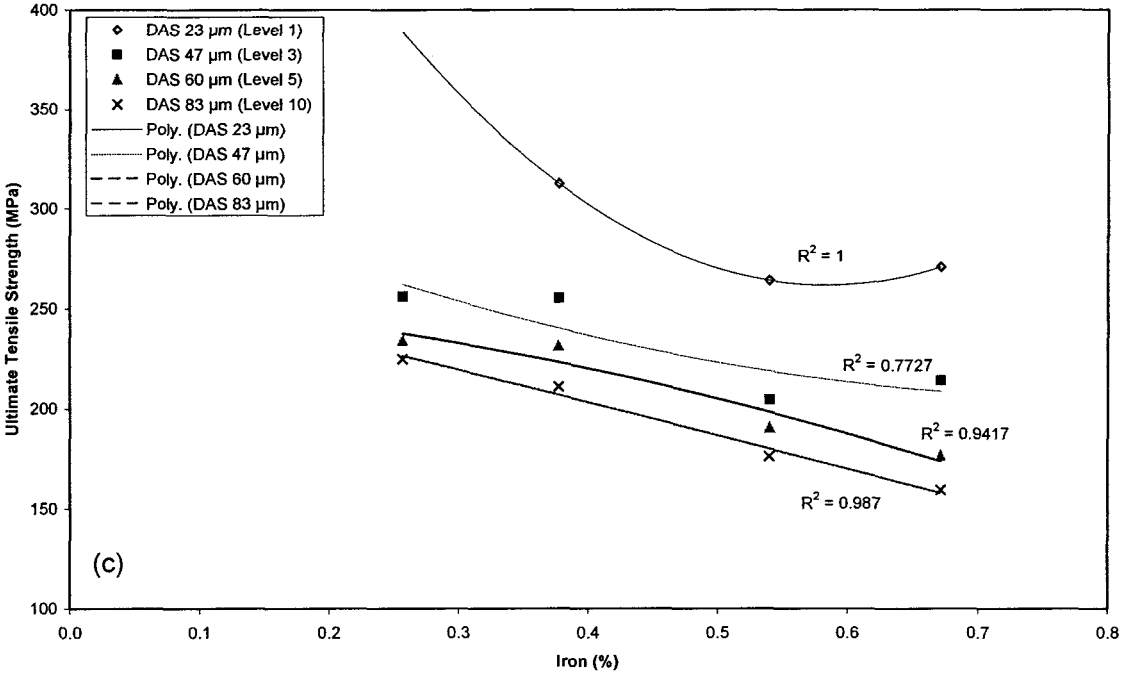

Figure 4.3. Tensile properties *vs.* iron content (experimental 319.2 alloy, 0 ppm Sr).

(iii) At the highest Fe content, above DAS-47 μm (level 3) the elongation remains almost the same.

These observations can be explained in terms of the precipitation of the brittle plate-like β-iron intermetallic phase, which is very harmful to the ductility of the material. In the present study, the greatest increase in the β-platelet length with respect to iron content was observed at a DAS of 23 μm, or the highest cooling rate, as iron increased from 0.377 to 0.54%. Such increases were much smaller at other cooling rates. Moreover, the β-platelet lengths observed at the highest cooling rate were much smaller, even at the highest iron level. As will be discussed later in Section 4.2.2.1, within certain β-platelet lengths or areas, the drop in percent elongation is very sharp, while beyond that, it is more moderate, hence, the first two observations of Figure 4.3(a). At the highest Fe level, above DAS ~47 μm, the

variation in β-platelet sizes is not very apparent, and the effect on ductility is not much different, either; therefore, similar ductility values are obtained. The discrepancies observed at the highest cooling rate are also explained in terms of the β-platelet lengths.

Figure 4.3(b) shows the yield strength curves, which are similar to those of elongation; that is, with the increase in the cooling rate and decrease in iron content, YS increases. The discrepancy observed at the lowest cooling rate (DAS 83 μm) and lowest iron level (0.26%) was so small that it could be ignored. With regard to iron, the decrease in YS was less sharp compared to the %El curves. For all cooling rates, the largest decrease in YS was observed to be at 0.54% iron. The difference in YS between adjacent cooling rates varies somewhat inconsistently with the increase in iron content.

The correlation between YS and cooling rate observed in the above case is in accordance with the observations of Boileau *et al.*,[144] and Meyer *et al.*,[146] while different from that of Samuel and Samuel.[96,148] The latter observed that YS remains constant regardless of solidification time. According to Boileau *et al.*,[144] yield strength in heat-treated 319.2 alloys depends upon the type, size and distribution of precipitates. Normally, the precipitates do not vary a lot among different samples under the same heat treatment conditions, regardless of cooling rate and iron content. Therefore, yield strength should not vary with the cooling rate, (or DAS), which is in accordance with the results of Samuel and Samuel.[96,148]

On the other hand, the amount of eutectic $CuAl_2$ does not remain constant as the solidification time changes.[144] With the decrease in the cooling rate, more time is provided, which favors the precipitation of the eutectic $CuAl_2$ phase. Thus less copper is available to

form the strengthening precipitates during heat treatment, which leads to a lower yield strength. From Equation 4 in Table 4.1, it is reasonable to assume that with the increase of iron, more β-iron and $CuAl_2$ particles will tend to precipitate, thus deteriorating the yield strength.

The ultimate tensile strength curves obtained (Figure 4.3(c)) are also similar to those of percent elongation. The observations at the highest cooling rate are very similar to those of Figure 4.3(a). However, as no reading was available for the lowest iron content (the data could not be properly recorded), the trend line does not appear identical. In this case, maximum data scatter occurs at DAS of 47 μm. Also, the difference in UTS between adjacent cooling rates is almost unaffected by the variation in iron content.

The β-iron intermetallics have a detrimental effect on the tensile strength as well. As will be discussed in Section 4.2.2.1, the effect is more gradual than that on ductility. These observations and the difference between the highest cooling rate and others can be explained in terms of the fracture mechanisms involved, as both the β-iron intermetallic and eutectic Si particles play important roles in determining the UTS. The details of the fracture mechanism will be elaborated upon in section 4.2.2.1, where the correlation between tensile properties and β-iron intermetallic size will be discussed.

The tensile properties of the experimental A alloy in the Sr-modified condition are shown in Figure 4.4, with respect to the iron content and cooling rate. Compared to the results depicted in Figure 4.3(a), the elongation curves of Figure 4.4(a) reveal that at the lowest iron levels, the difference in the decrease in elongation becomes greater as the DAS increases, *viz.* the elongation decreases faster as DAS increases. This indicates that in the

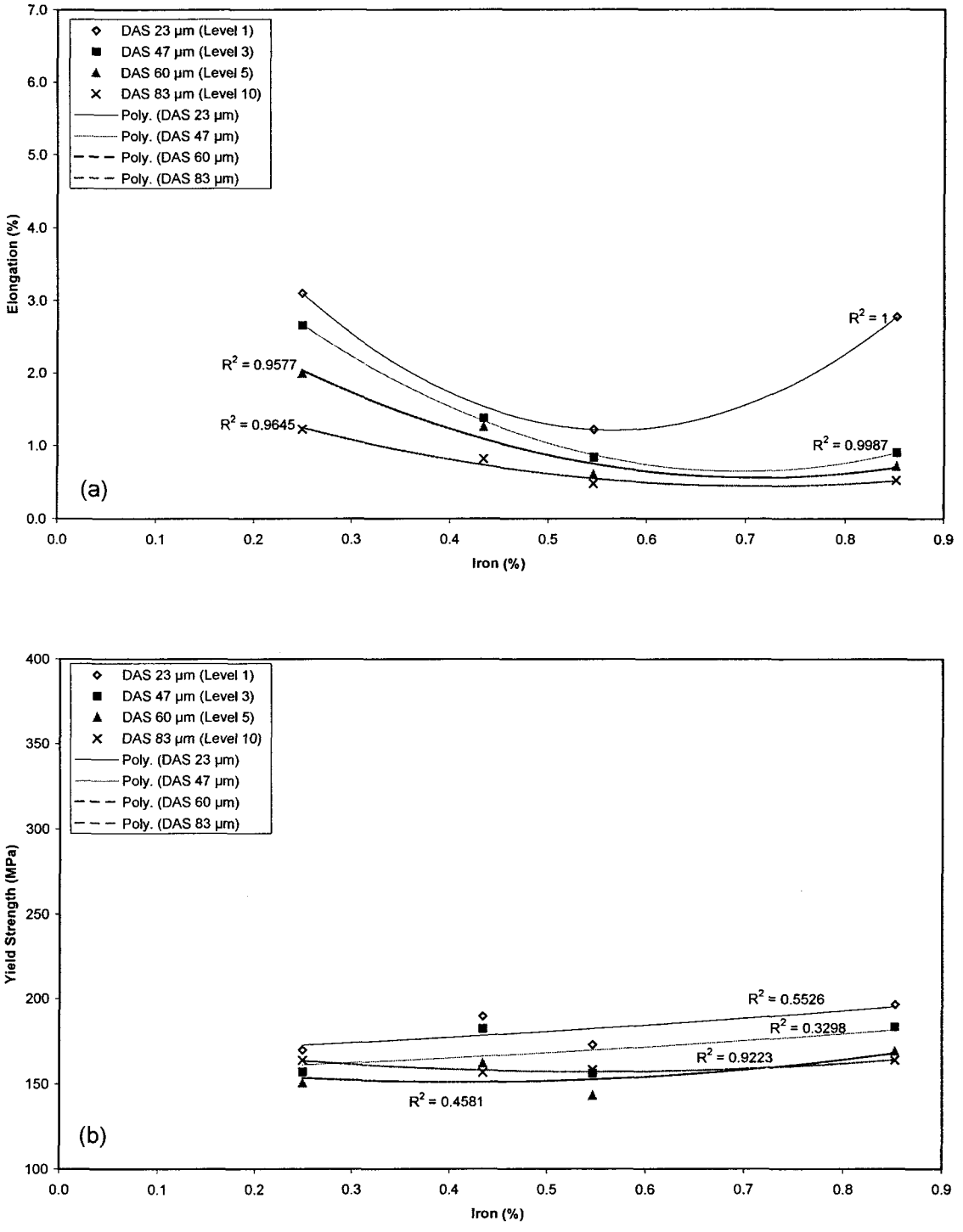

Figure 4.4. Tensile properties *vs.* iron content (experimental 319.2 alloy, 200 ppm Sr).

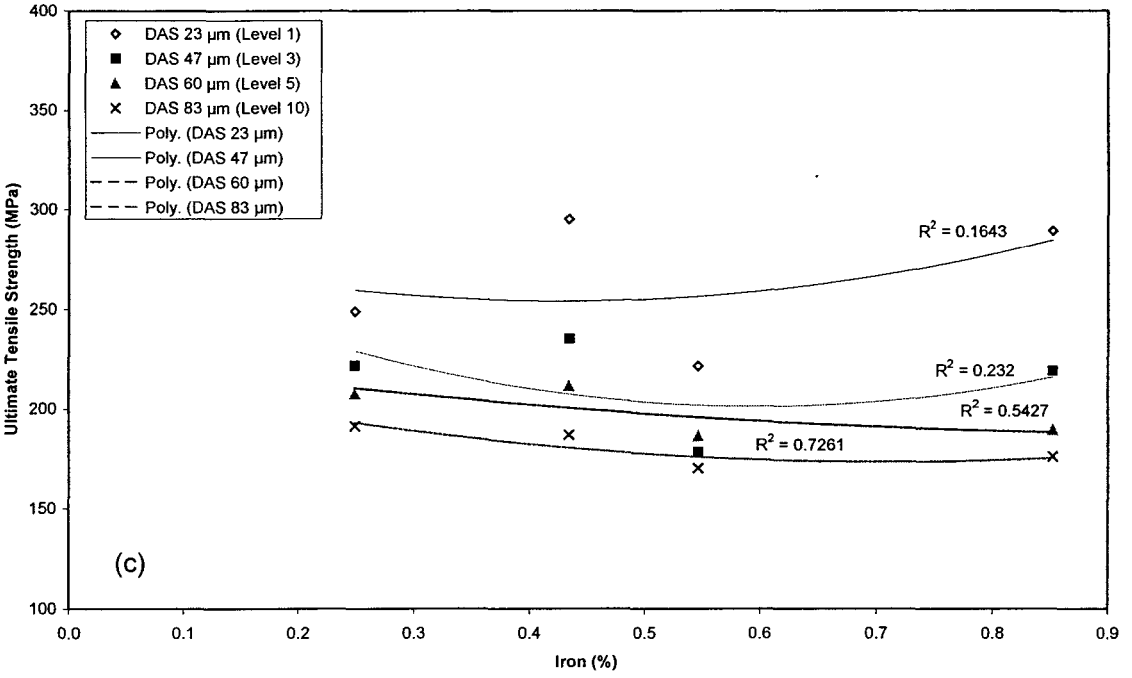

Figure 4.4. Tensile properties *vs.* iron content (experimental 319.2 alloy, 200 ppm Sr).

unmodified condition, when a low or moderate amount of iron is present, only very high cooling rates can improve elongation significantly, whereas in the Sr-modified case, even a small increase in the cooling rate may affect elongation considerably. This is due to the fact that, in the unmodified condition, for the same iron content, the cooling rate is the main parameter that controls the β-platelet size. Thus, only the highest cooling rate will provide β-platelets small enough to achieve such high improvements in %El. In the Sr-modified samples, however, the β-platelet size is controlled by the cooperative effect of the cooling rate and strontium modification. Any improvement in the cooling rate combined with Sr modification will decrease the β-platelet size significantly and increase the %El. Obviously, the combined effect will be less apparent at high cooling rates.

Figure 4.4(a) shows that, at the higher iron levels, the elongation does not vary too much beyond DASs of 47 μm. Nevertheless, at the highest cooling rate (DAS ~23 μm), the elongation increases significantly at 0.852% Fe level, attaining a value similar to that displayed at the lowest Fe content (0.249 wt%).

While the elongation decreases with the increase in iron content, a slight increase is observed on going from 0.6 to 0.8% Fe at DASs of 47 μm or higher. This increase becomes significant at the highest cooling rate (DAS 23 μm). These results appear contradictory, as the β-platelet sizes (length and thickness) continued to increase with the increase in iron level and DAS. One possible explanation for this could be as follows: as the metallography and tensile test samples were obtained from different castings, their respective iron levels might not have been identical from casting to casting. Moreover, samplings for chemical analysis taken prior to each series of castings, the iron contents obtained in each would not reflect any changes in local iron concentration. Thus, in the present case, the iron level is much lower than its average of 0.8%.

The yield strength curves shown in Figure 4.4(b) are different from those obtained for the unmodified samples. Although an overall decrease was observed with the increase in DAS, similar to that in Figure 4.3(b), an overall increase was observed with the increase in iron, which contradicts Figure 4.3(b). Also, the data scatter is much more in this case, since, among the four curves, only the one at 83 μm DAS exhibits a good R^2 value, with all the others showing very poor (or no) fit. At 83 μm DAS, the YS stays approximately the same, within a standard deviation of ± 4 MPa.

These results indicate that, with Sr modification, the YS is more difficult to predict. According to Samuel *et al.*,[148] Sr addition allows for the dissolution of a large proportion of the β-iron intermetallics in the aluminum matrix. Such dissolution could affect the $CuAl_2$ phase since many $CuAl_2$ particles precipitate along the β-iron platelets. Meanwhile, Sr addition also leads to local segregation of Cu in areas away from the eutectic Si regions, leading to the formation of the block-like $CuAl_2$ phase rather than the finer (Al + $CuAl_2$) eutectic, which has a lower Cu content (28%, *cf.* ~40% in the former). Thus, the interplay of all these factors would make it difficult to interpret the YS values observed.

Overall, the UTS of the Sr-modified alloys, Figure 4.4(c), appears to remain stable with an increase in Fe content, decreasing slightly, particularly at the lower cooling rates, *e.g.*, from ~191 MPa to ~170 MPa at the DAS of 80 μm (*cf.* ~226 to 160 MPa in the unmodified alloys). Strontium thus appears to have a stabilizing effect on the alloy tensile strength at DASs of 47 μm and above. This is useful when trying to maintain the overall strength in the thicker sections of a casting.

The increases in UTS observed at various points on the four curves with an increase in iron content, particularly that observed at 0.852% Fe for all the cooling rates, are in accordance with the results obtained by other investigators.[70,149-151] It is reasonable to propose that, as the iron increases, more of the hard β-Al_5FeSi particles (Sr-modified) are dispersed within the aluminum matrix (although the size increases too), thus improving the UTS. Nevertheless, the reason for the data scatter remains unknown. With the increase of the cooling rate, the data scatter increases. According to Narayanan,[10] the addition of iron affects the eutectic Si particle size as the nucleation and growth of Si crystals takes place on

the β-Al_5FeSi platelets. Since this may not always occur, it is possible that data scatter appears. The higher the cooling rate, the more difficult it is to predict the effect of iron on Si particles, and the worse the data scatter.

Figure 4.5 shows the tensile properties of the unmodified industrial 319.2 alloy, as a function of Fe content and cooling rate. In comparison with Figure 4.3(a), all the data fit the trend line very well at DAS 23 μm in Figure 4.5(a). In fact, the data at all cooling levels show a very good conformity with their respective trend lines ($R^2 \geq 0.98$ for all the curves). Best elongation is obtained at the lowest Fe level and highest cooling rate (finest DAS). The decrease in elongation with respect to Fe levels and the cooling rate is otherwise similar to that exhibited by the experimental alloy. Nevertheless, the nature of the curves in Figure 4.5(a) indicates that beyond Fe levels of 0.4 wt%, no improvement in elongation can

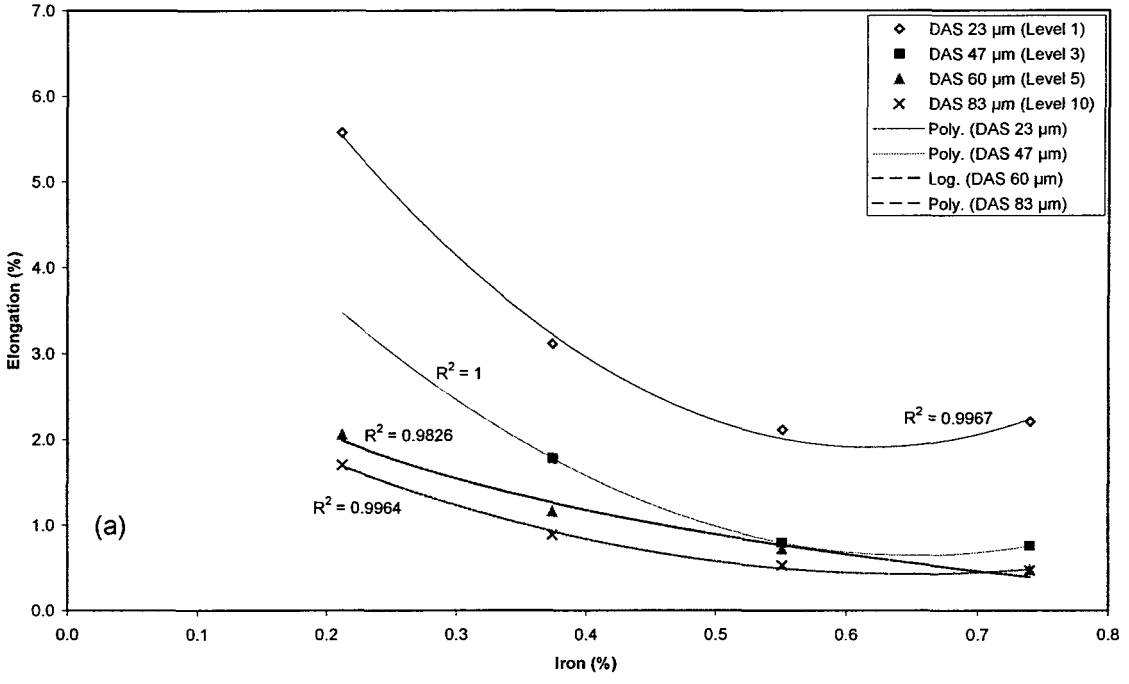

Figure 4.5. Tensile properties *vs.* iron content (industrial 319.2 alloy, 0 ppm Sr).

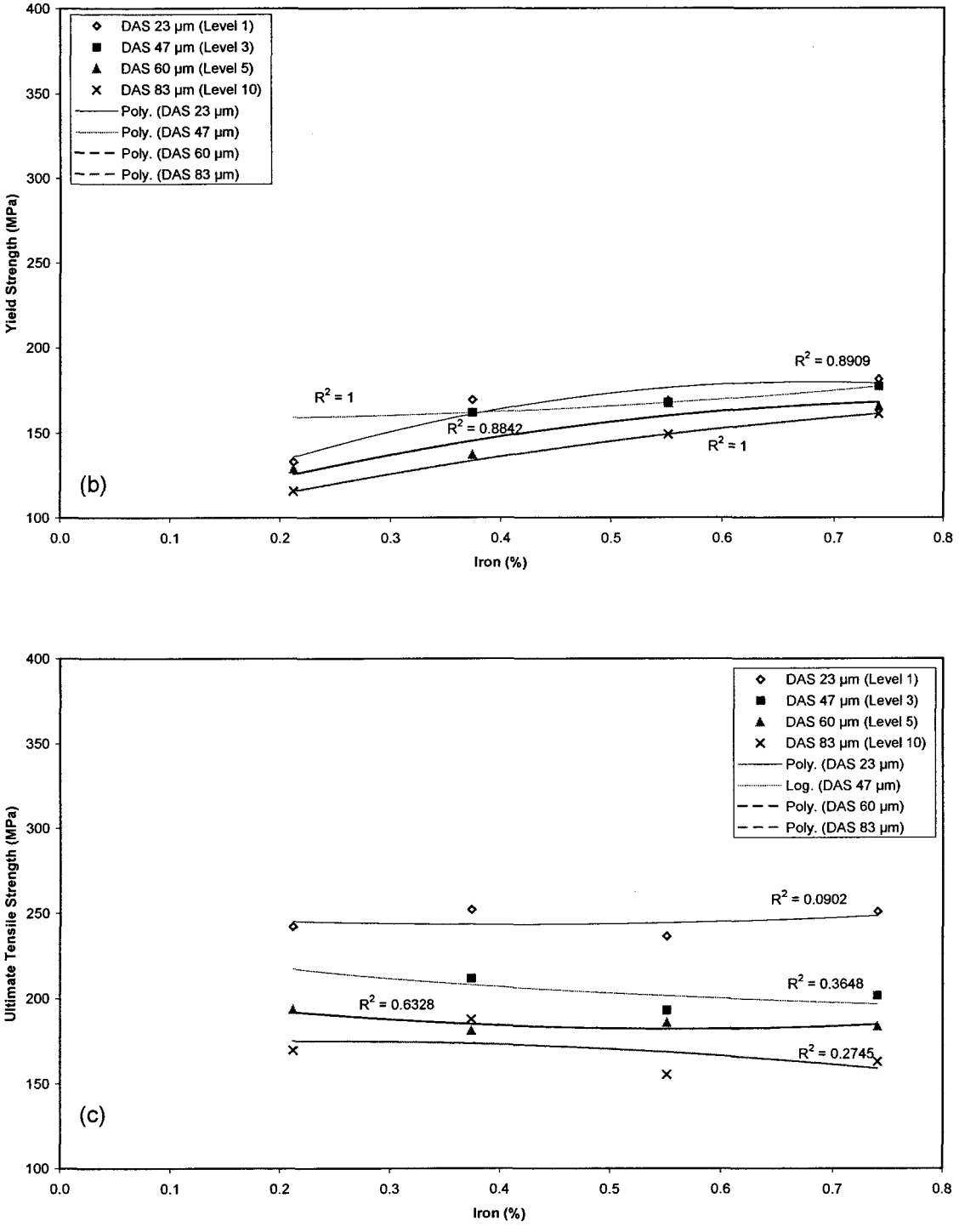

Figure 4.5. Tensile properties *vs.* iron content (industrial 319.2 alloy, 0 ppm Sr).

be obtained by increasing the cooling rate, at least for DASs up to 47 μm. This can be attributed to the greater amount of impurities present in the industrial alloy compared to the purer experimental alloy. The presence of these "impurities", such as Mg and Mn, will neutralize the harmful β-Al_5FeSi intermetallics, particularly at the lowest iron level, where the Fe/Mn ratio is close to 2:1, a ratio that favors the precipitation of the Chinese script α-$Al_{15}(Fe,Mn)_3Si_2$ iron intermetallic phase over that of the pre-eutectic β-Al_5FeSi, thus improving the mechanical properties, particularly ductility. This fits well with the much higher ductility values observed at 0.212% Fe level of this version of 319.2 alloy, as the values are higher than those exhibited by the experimental alloy at all cooling rates. The presence of Mg can also transform the β-Al_5FeSi phase into the α-Al_8Mg_5FeSi phase, which is less harmful to the properties.

The curves in Figure 4.5(b) are similar to those in Figure 4.4(b), that is, with the increase of the cooling rate and iron content, an overall increase of YS is observed. One cannot actually comment upon the trend line exhibited at DAS 47 μm due to the lack of data for the 0.212% Fe-containing alloy. Apart from that, the effect of DAS on YS is very consistent in that the YS increases with decreasing DAS. As these observations are similar to those of Figure 4.3(b), the same explanation holds good in this case, as well. With the increase in DAS, more time is provided for the precipitation of the $CuAl_2$ phase, thus decreasing the YS. The effect of iron content on YS is also very consistent, in that the YS increases with increasing iron content in a similar fashion for all DAS values. These observations are similar to those of Figure 4.4(b). That is to say, with the increase of iron, more primary β-Al_5FeSi particles precipitate, which, together with the Mn and Mg in the

alloy, lessen the amount of co-eutectic or post-eutectic β-Al_5FeSi available for the precipitation of the $CuAl_2$ phase. Thus, the YS increases.

Figure 4.5(c) depicts the effect of iron and cooling rate on the ultimate tensile strength of the industrial A alloy. As the cooling rate decreases, the UTS also decreases. The Fe content apparently does not affect the UTS at any specified DAS. Nevertheless, compared with the experimental alloy, the UTS levels are lower in the industrial alloy, even at the highest cooling rate. This can be attributed to the impurities present in the latter. Thus, any amelioration at the lower Fe contents are masked by the harmful effects of these impurities.

Figure 4.6 depicts the tensile properties of the Sr-modified industrial alloy. It is observed that Sr addition improves the elongation significantly, Figure 4.6(a), particularly at the higher cooling rates. As observed in the previous cases, the elongation decreases with the increasing Fe content. However, the values of elongation obtained at every Fe content/DAS level are higher than those obtained in all the other alloys. Also, there is a clear gap between the elongation values from one level to the next, no matter what the Fe level. In other words, cooling rate has more weightage than the Fe-content in determining the elongation that may be achieved in this alloy.

The yield strength curves obtained for the modified industrial 319.2 alloy, Figure 4.6(b), are consistent with those of the unmodified alloy (Figure 4.5(b)). The increase in YS is consistent with respect to the increase in both iron content and cooling rate. Thus, in general, we can say that the yield strength increases with the increase in iron concentration of the alloy, irrespective of whether the alloy is modified or not. Only a marginal difference in the YS values was observed between the two conditions. This could indicate that, in the

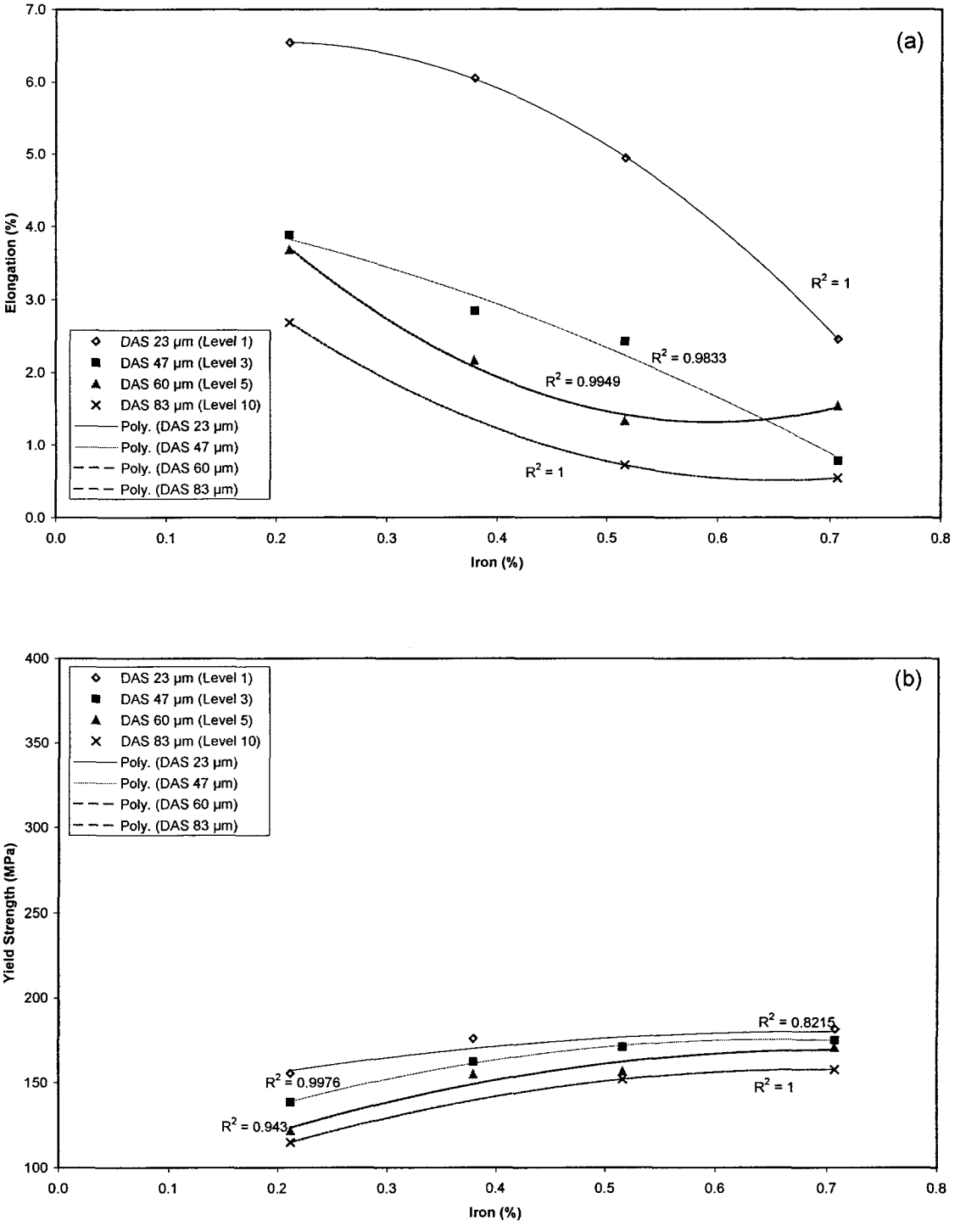

Figure 4.6. Tensile properties *vs.* iron content (industrial 319.2 alloy, 200 ppm Sr).

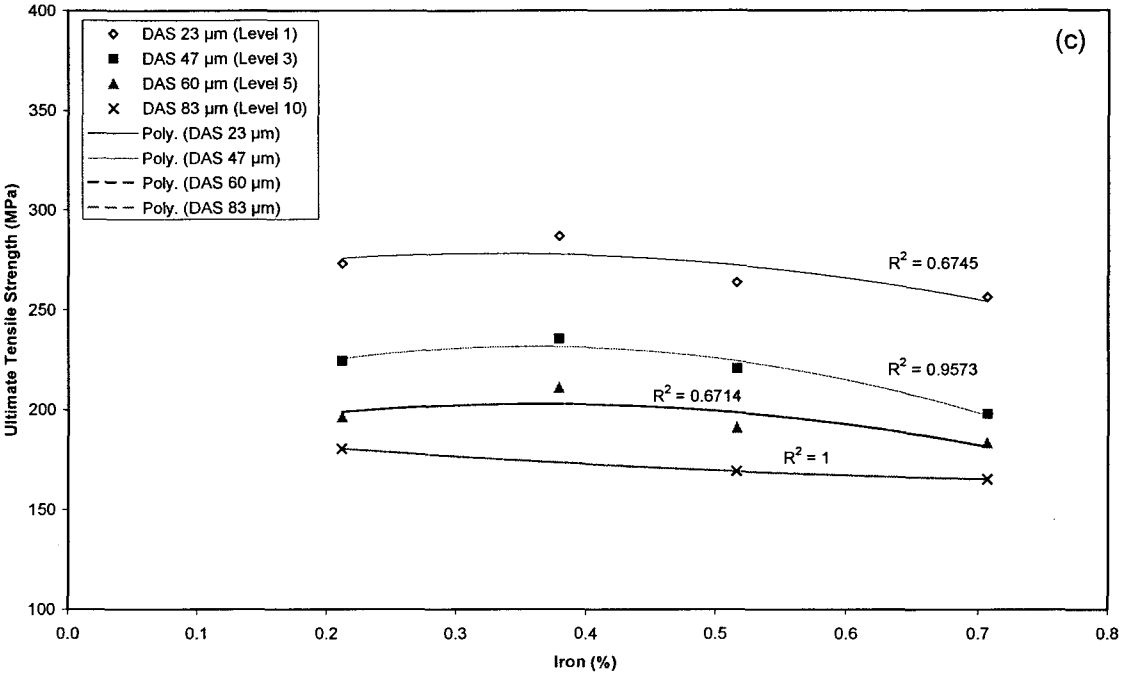

Figure 4.6. Tensile properties *vs.* iron content (industrial 319.2 alloy, 200 ppm Sr).

commercial 319.2 alloy, Sr modification does not affect the precipitates which are hardenable upon heat treatment.

The ultimate tensile strength curves, Figure 4.6(c), display similar characteristics as those of the unmodified alloy (Figure 4.5(c)). Again, compared to the latter, the UTS values are higher at the highest cooling rate as well as at the other levels. Similar to the elongation curves, there is a clear gap in the UTS curves from one level to the next. Apart from the very small decrease observed at the highest Fe levels, Fe does not appear to affect the UTS. The strength and elongation levels achieved indicate that strontium modification is an important means to enhance the mechanical properties of commercial 319.2 alloy, or 319 type alloys in general.

4.2.1.2 Alloy B319.2 (alloy B)

As mentioned previously, alloy B differs from alloy A on account of its higher magnesium content. Thus, any differences in tensile properties of the two alloys could be related to the difference in their magnesium contents.

It should be mentioned here that in the case of the B alloy, only two levels of iron for the experimental alloy and three levels of iron for the industrial alloy were studied. Also, when conducting the tensile tests, some of the samples were so brittle that no yield strength values could be recorded. Consequently, due to the fewer data that were collected, the results have been presented in the form of histograms grouping all conditions together for each tensile property. These histograms are shown in Figure 4.7, where the effect of the cooling rate and iron content on the mechanical properties are plotted for the B319.2 experimental (EB) and industrial (IB) alloys, with and without Sr. The effect of the cooling rate on elongation and ultimate tensile strength is quite simple, that is, with the increase of cooling rate, elongation and ultimate tensile strength increase, as depicted in Figures 4.7(a) and 4.7(c), respectively, similar to that observed in alloy A. This was observed in all cases, for experimental and industrial alloys, in both unmodified and Sr-modified conditions. This is due to the effect of the cooling rate on the size of the microconstituents (including β-iron intermetallics and Mg-containing intermetallics) and porosity, and their distribution. Among these, the effect of the β-phase platelet size plays the most important role, as the drop in ductility relates very well with the change in the β-platelet sizes obtained at different cooling rates.

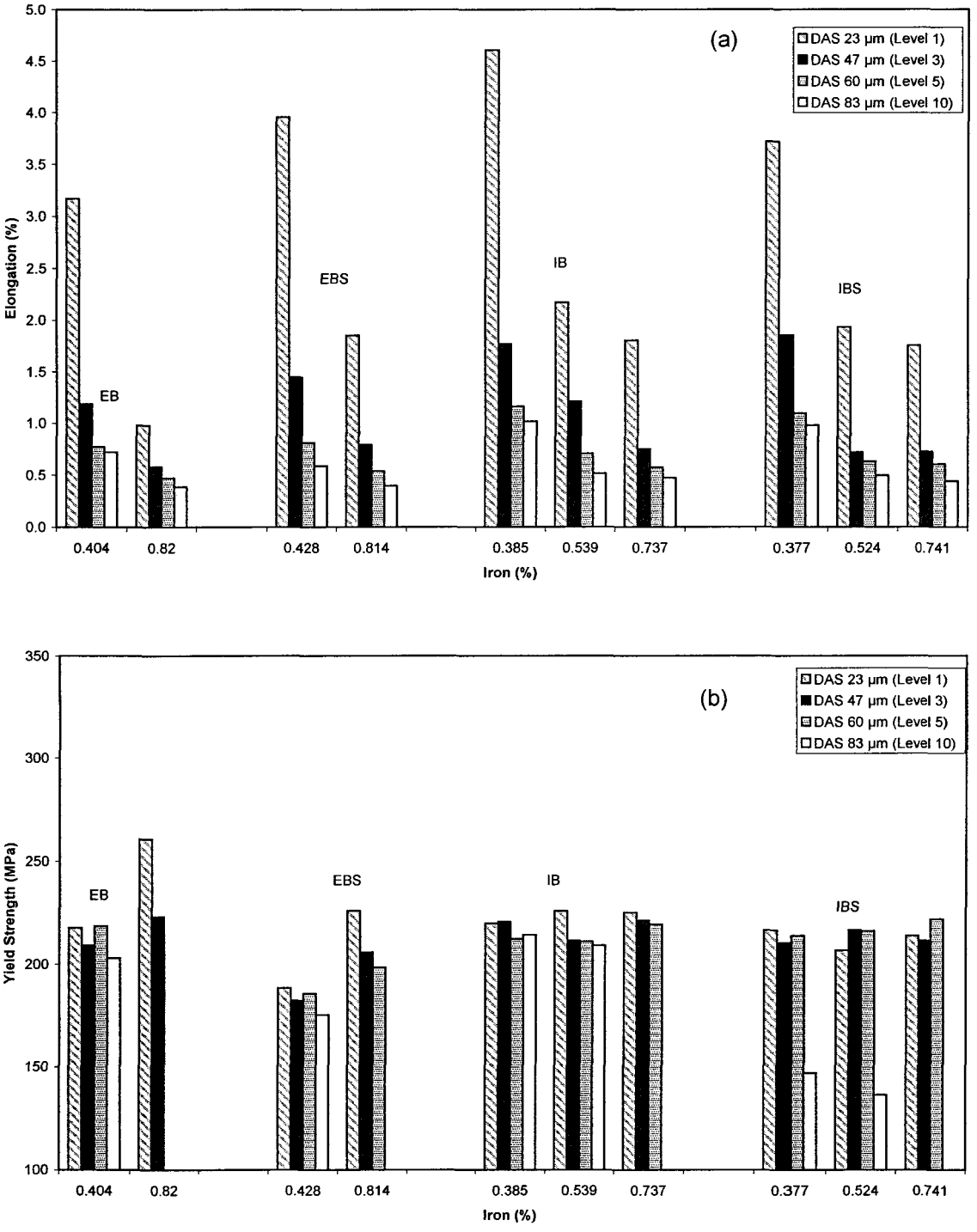

Figure 4.7. Tensile properties as a function of iron content and DAS for alloy B319.2: EB – experimental, 0 ppm Sr; EBS – experimental, 250 ppm Sr; IB – industrial, 0 ppm Sr; IBS – industrial, 250 ppm Sr.

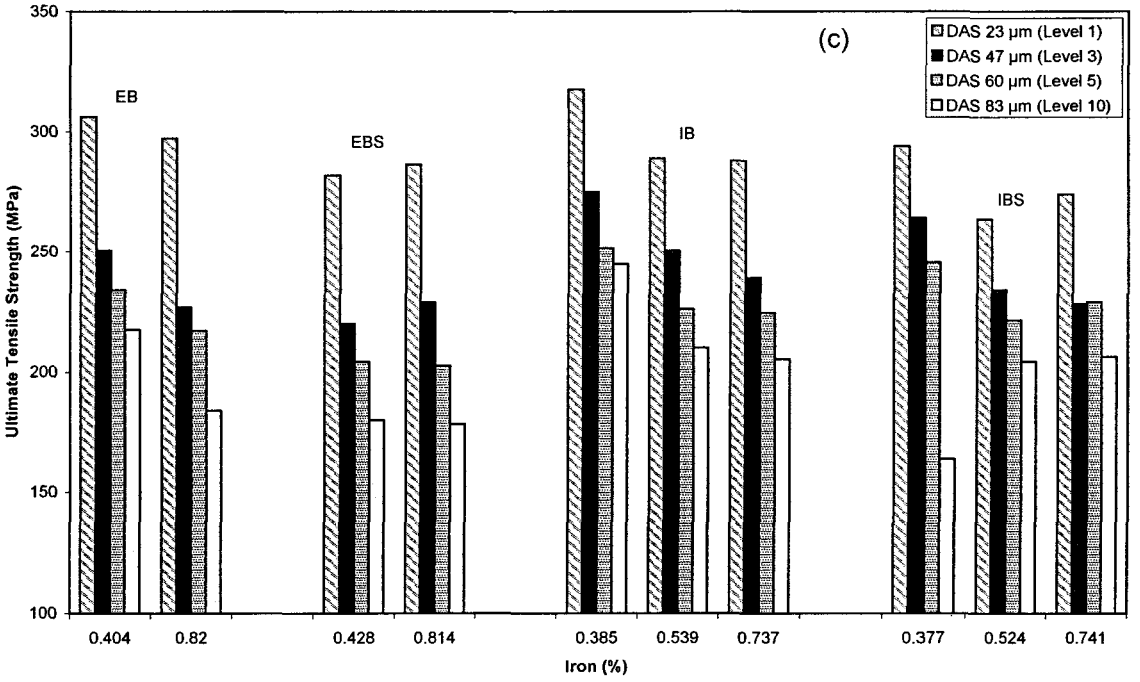

Figure 4.7. Tensile properties as a function of iron content and DAS for alloy B319.2: EB – experimental, 0 ppm Sr; EBS – experimental, 250 ppm Sr; IB – industrial, 0 ppm Sr; IBS – industrial, 250 ppm Sr.

Likewise, for the same reasons, with an increase in iron content also, the elongation decreases. The drop is most significant between iron levels of ~0.38 and ~0.56% when the DAS changes from 23 to 47 µm, Figure 4.7(a). As the cooling rate decreases further, the difference decreases. The highest elongation (4.6%) is obtained for the unmodified industrial alloy at the highest cooling rate (DAS 23 µm) and low iron level (0.385%) conditions.

Compared to the 319.2 alloys (lower-Mg version), for the same iron level and DAS value, the ductilities observed are lower for most samples. Samuel *et al.*,[96,148] however, observed that with Mg addition, transformation of the β-Al_5FeSi phase into the Chinese script-like α-$Al_8Mg_3FeSi_6$ phase takes place. The latter, with its more compact morphology

is less harmful to the mechanical properties, thus improving the ductility. The lower ductilities observed in the present case can be related to the longer β-platelet lengths observed in the B319.2 alloys. This is probably due to the increase in the eutectic reaction time corresponding to the higher Mg content of the alloy. According to Moustafa *et al.*,[152] longer eutectic reaction times were observed in 413.1 alloy with Mg additions of 0.1 to 0.4 wt%. The co-eutectic β-iron intermetallic would thus have a longer growth time, which would yield larger β-phase platelets than in the Mg-free alloy. However, this explanation may still not suffice to account for the large-sized β-platelets observed in the B319.2 alloys, since, even with the longer growth time, the co-eutectic β-platelet size is normally smaller than the primary one. In other words, most of the large-sized β-platelets observed in these alloys are pre-eutectic β-phase platelets, and not co-eutectic.

With respect to yield strength, as can be seen from Figure 4.7(b), the effect of the cooling rate is not very apparent in either experimental or industrial alloys (*cf.* alloy A, where cooling rate had a consistent effect). Two exceptions are noted: in the experimental alloy, both the unmodified and modified alloys exhibit considerably higher yield strengths at 0.82% Fe levels and highest cooling rates, compared to the other samples. Secondly, in the case of the Sr-modified industrial alloy, the yield strength decreases dramatically when the DAS increases from 60 μm to 83 μm, *i.e.*, by 31% and 37% at iron levels of 0.377% and 0.524%, respectively. This would probably have also been the case at the highest iron concentration (0.741%), since no yield strength could be recorded.

In spite of the limitations of not being able to obtain yield strength values for all samples, in the experimental alloys, the YS was found to increase with increase in iron

content at any given cooling rate, both in the unmodified and Sr-modified conditions. The increment decreased as the DAS increased. In the industrial alloy, however, most YS values lay within 216 ± 5 MPa for both the unmodified and Sr-modified alloys. The only exceptions observed were in the case of the modified alloy at Fe levels of 0.38 and 0.52%, where the YS dropped by as much as 32 and 37% (to 147 and 136 MPa) at the two Fe levels, respectively.

With respect to ultimate tensile strength, a decrease in UTS with increasing iron content is observed in the unmodified alloy, Figure 4.7(c). This indicates that, although the B alloy possesses a higher magnesium content, iron addition can still be deleterious to the mechanical properties when strontium is not present. Compared to the low-Mg version (A alloys), most of the samples possess higher UTS values in general. This is due to the presence of a larger amount of Mg_2Si particles in the matrix which increases the strength.

In the Sr-modified alloys, when the iron level is increased from ~0.4 to 0.82%, ultimate tensile strength increases slightly, by ~5-8 MPa in the experimental alloy at DAS values of 23 and 47 μm. In the case of the industrial alloy also, when the iron level increases from 0.52 to 0.74%, the UTS increases by about 10 and 5 MPa, at DAS values of 23 μm and 60 μm, respectively. The severest reduction in UTS is observed in the case of the modified industrial alloy at the lowest Fe content (0.377%) and largest DAS (83 μm), where the UTS decreases by 33.2% (*cf.* that at 60 μm DAS) and by ~19.8% and 20.5% at higher Fe levels (0.52 and 0.74 wt%, respectively).

4.2.1.3 Alloy A356.2 (alloy C)

The alloy A356.2 has a high magnesium, but very low copper content. Its tensile properties and microstructural characteristics will therefore be controlled by these compositional factors.

The effects of iron concentration and cooling rate on the tensile properties of the alloy are depicted in Figures 4.8 and 4.9 for the unmodified and Sr-modified cases, respectively. As in the 319 alloys, overall, both elongation and ultimate tensile strength increase with increase in cooling rate and decrease in iron content, with a few discrepancies observed in UTS in the unmodified alloy. This is in accordance with the results of the work of Boileau *et al.*[153] on A356-T6 alloys. Also, more linear relations were obtained in the modified C alloy, indicating that the β-platelet size has a direct effect on ductility than in the alloys A and B.

Nonetheless, the data scatter is more apparent in Figures 4.8 and 4.9 compared to alloys A and B, especially at the highest cooling rates (DASs 23 and 39 μm). This could be attributed to the fact that two batches of the industrial base alloy were employed to prepare the castings. Another reason for the scatter could be related to the machining defects introduced during the preparation of the test samples from the specimen blanks. The data scatter in the Sr-modified case is much less (*cf.* R^2 value of 0.90 with 0.78 for the unmodified alloy for the log UTS-log %El curves, Table 4.8, shown later in Section 4.2.5.3).

Compared to the 319.2 alloys in the unmodified condition, for the same iron content and cooling rate, the ductilities observed in the A356.2 alloy are generally higher (this was

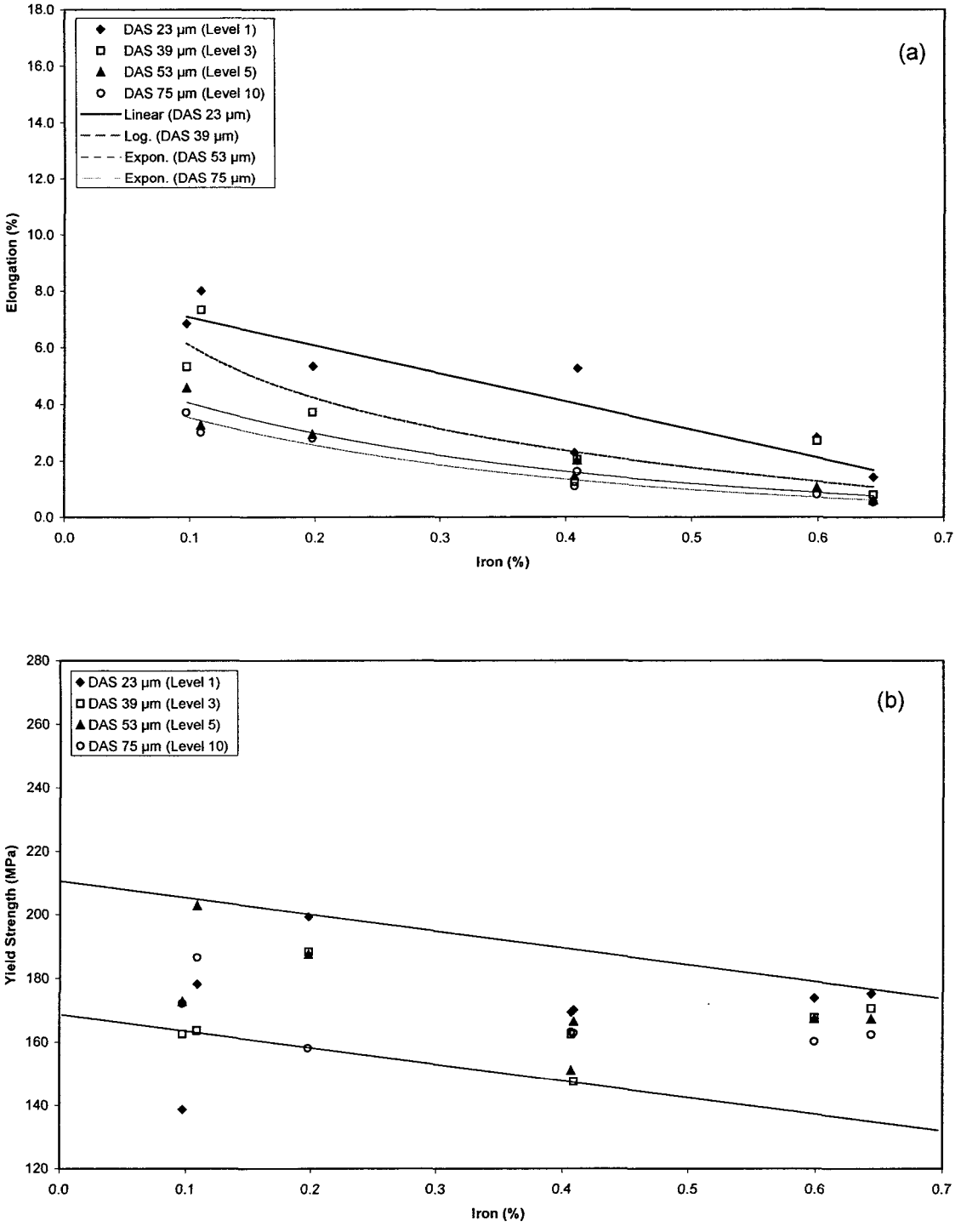

Figure 4.8. Tensile properties *vs.* iron content (industrial A356.2 alloy, 0 ppm Sr).

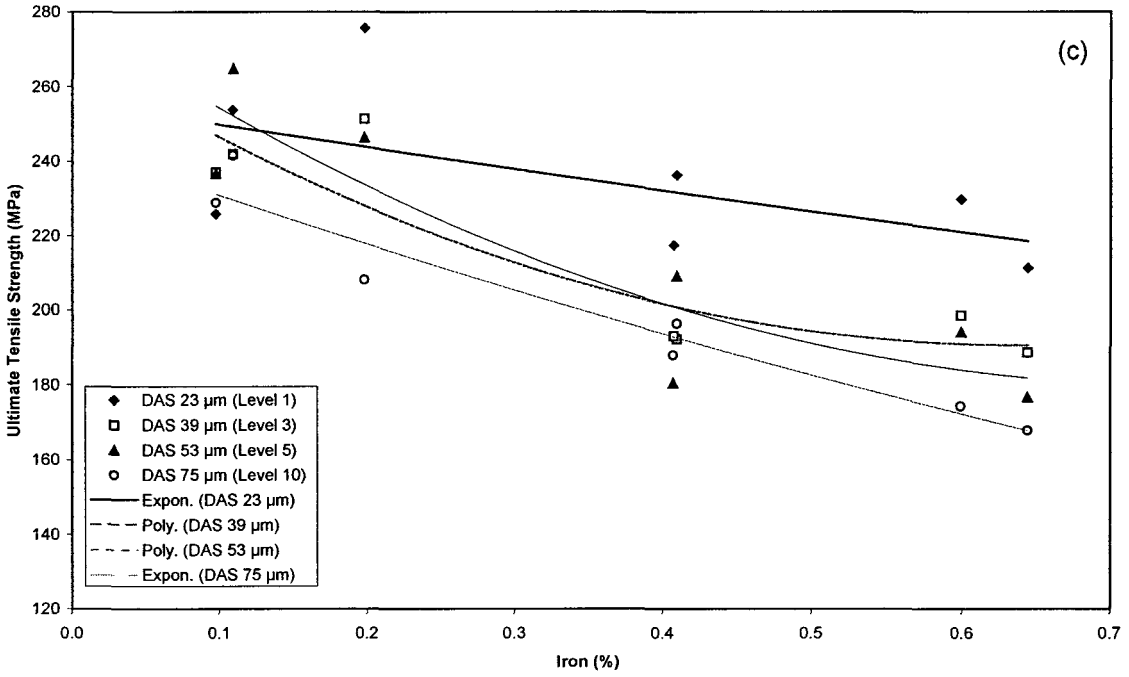

Figure 4.8. Tensile properties *vs.* iron content (industrial A356.2 alloy, 0 ppm Sr).

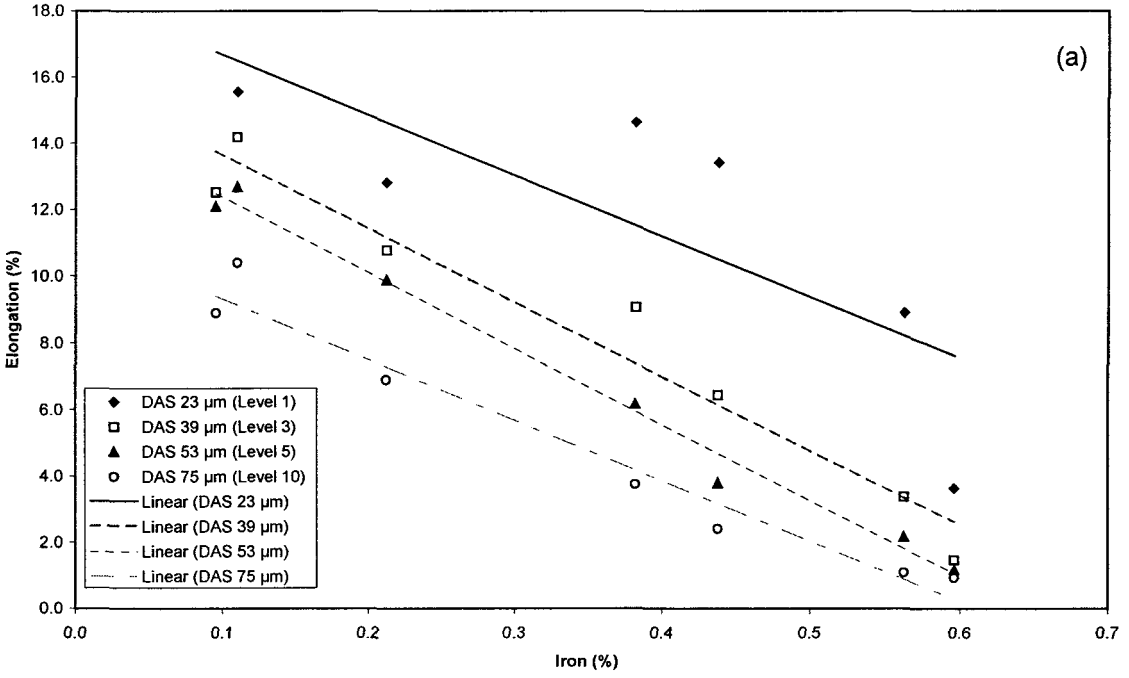

Figure 4.9. Tensile properties *vs.* iron content (industrial A356.2 alloy, 300 ppm Sr).

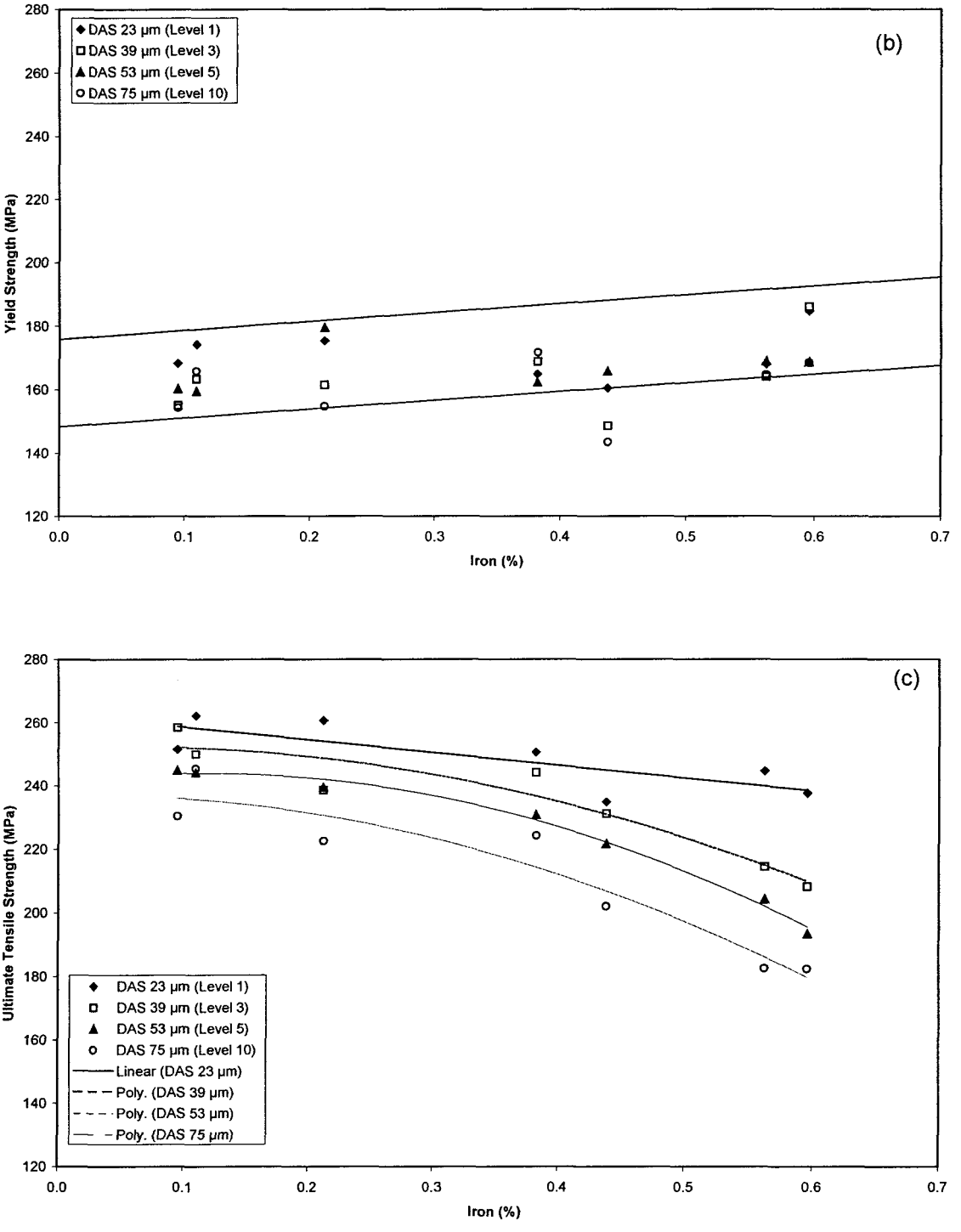

Figure 4.9. Tensile properties *vs.* iron content (industrial A356.2 alloy, 300 ppm Sr).

found to be the case for all the samples from one batch and for most from the other batch). The smaller β-platelets sizes and the same (or smaller) DAS values obtained in the A356.2 alloys (at the four levels above the chill end) explain why this is so. Sr addition has a significant impact on alloy ductility, as can be observed by comparing Figures 4.8(a) and 4.9(a). The decrease in β-platelet size due to Sr-modification, and the change in morphology of the eutectic Si particles from acicular to fibrous result in much higher ductilities.

For ultimate tensile strength, most of the UTS values in one batch of A356.2 alloy samples were higher than those of the 319.2 alloys. Furthermore, at highest cooling rate (23 μm DAS in both alloys), much higher values were observed in the case of the A356.2 alloys. In the other A356.2 batch, most samples had lower UTS values than the 319.2 alloys. The reason for this is unclear, as the UTS obtained in A356.2 alloys is normally higher than that observed in 319.2 alloys.

The correlation between yield strength, iron content, and cooling rate is quite different from that observed in the 319 alloys (alloys A and B). As can be seen from Figures 4.8(b) and 4.9(b), no definite effect of iron content and cooling rate on yield strength is observed. Instead, the YS values lie distributed within a band. In the unmodified alloy, the band width is ~48 MPa and displays a general decreasing trend with increasing iron level. On the other hand, the modified alloy exhibits an opposite trend, *viz.*, the YS increases with the increase in iron content, and the values lie within a much narrower band, of ~25 MPa width. This suggests that Sr addition is helpful in stabilizing the precipitation hardening phase particles in the alloy.

It is not easy to compare the yield strengths of 319.2 and A356.2 alloys. Apparently, the different precipitation hardening elements that come into play in each case make such a comparison difficult. However, on the other hand, the presence of two precipitation hardening elements (Mg and Cu) in B319.2 alloy allows for the latter to display higher yield strengths than the A356.2 alloy which only contains magnesium.

4.2.2 Effect of the β-Iron Intermetallic Size

The size of the β-iron intermetallics is determined by several factors, among them the iron content, cooling rate, melt additives and other alloying elements.[27,31,38-49,57,59] Thus, the β-iron intermetallic size is also expected to affect the tensile properties. In the following sections, the effects of the β-iron average maximum platelet length and average maximum platelet area on the tensile properties have been singled out for discussion, being the two parameters that most affect the properties. The β-iron average maximum platelet length was obtained as follows: for each metallographic sample 20 fields were examined. In each field, the lengths of three longest β-iron platelets were recorded. The average of these 60 lengths was defined as the β-iron average maximum platelet length. Similarly, the corresponding average maximum thickness was also calculated. The β-platelet average maximum area was obtained by multiplying the average maximum length and the average maximum thickness values for each sample. As only one independent variable (average maximum length or average maximum area) has been used to plot the charts, it is possible to group the different conditions (experimental/industrial alloys, unmodified/Sr-modified cases) in one chart to facilitate comparison.

4.2.2.1 Alloy 319.2 (alloy A)

Figures 4.10 and 4.11 show plots of the tensile properties of the 319.2 alloys as a function of β-platelet size. Clearly, with the increase of β-platelet average maximum length and average maximum area, the percent elongation and ultimate tensile strength decrease considerably in all cases (experimental/industrial alloys, unmodified/Sr-modified conditions). Also, the data in each case fit their trend lines fairy well (note the R^2 values listed in the figures). Up to β-platelet sizes corresponding to ~100 μm length or 400 μm^2 area, the elongation and ultimate tensile strength decrease very rapidly with the increase in size of the β-platelets. Thereafter, the change is more gradual. This indicates that, when the β-iron platelet size is smaller than a certain value, even a small increase in the size deteriorates the elongation and UTS considerably. Beyond this value, no significant improvement in elongation and UTS can be achieved, even with the use of high cooling rates.

The fracture of these samples is mainly controlled by the Si particles and the β-iron intermetallics, where the importance of the β-iron intermetallics increases as their size increases. Up to a β-platelet size corresponding to ~100 μm length or 400 μm^2 area, both these factors influence fracture behavior. As the change in Si particle size is slower than that of the β-iron intermetallics with the increase of iron, the decrease in ductility and tensile strength takes place much more gradually. Beyond these values, the fracture mostly depends on the β-iron intermetallics size. Since it is very easy to break through these platelets, only marginal differences in energy are required to break the samples having

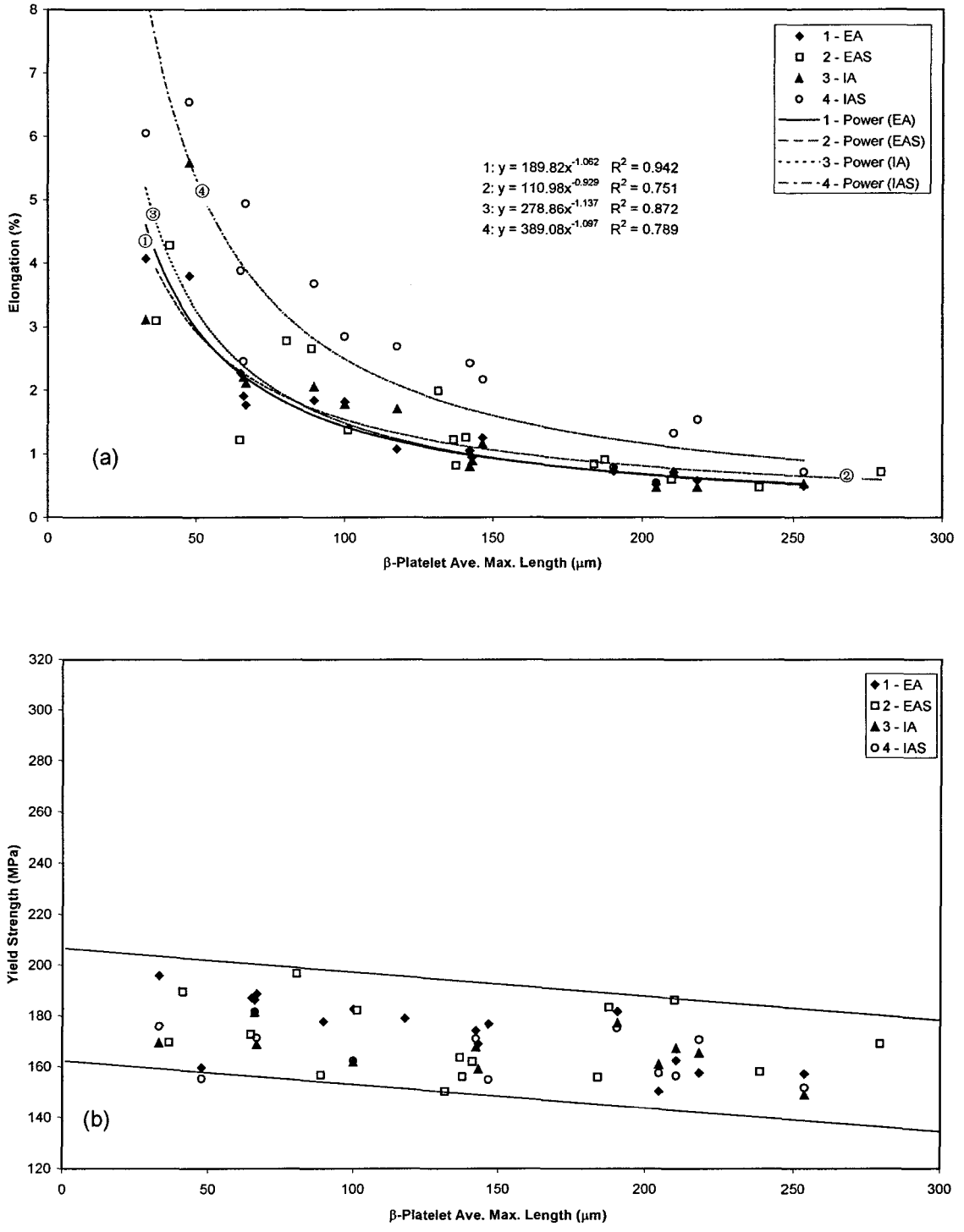

Figure 4.10. Tensile properties *vs.* β-platelet ave. max. length (experimental and industrial A alloy, 0 ppm and 200 ppm Sr).

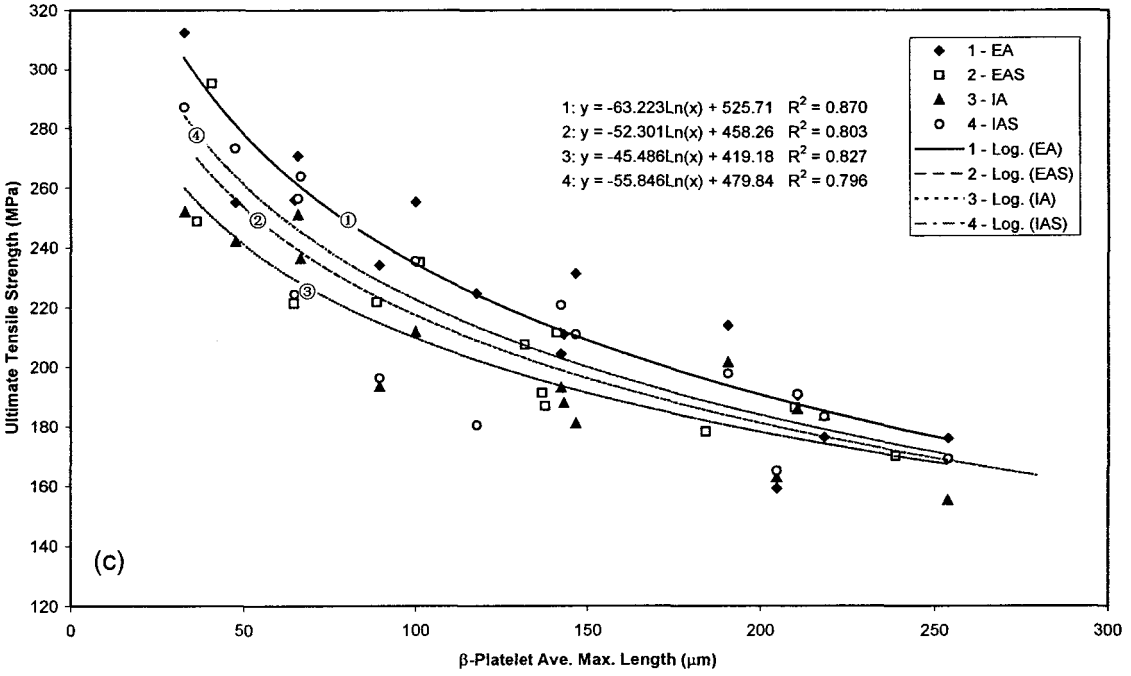

Figure 4.10. Tensile properties *vs.* β-platelet ave. max. length (experimental and industrial A alloy, 0 ppm and 200 ppm Sr).

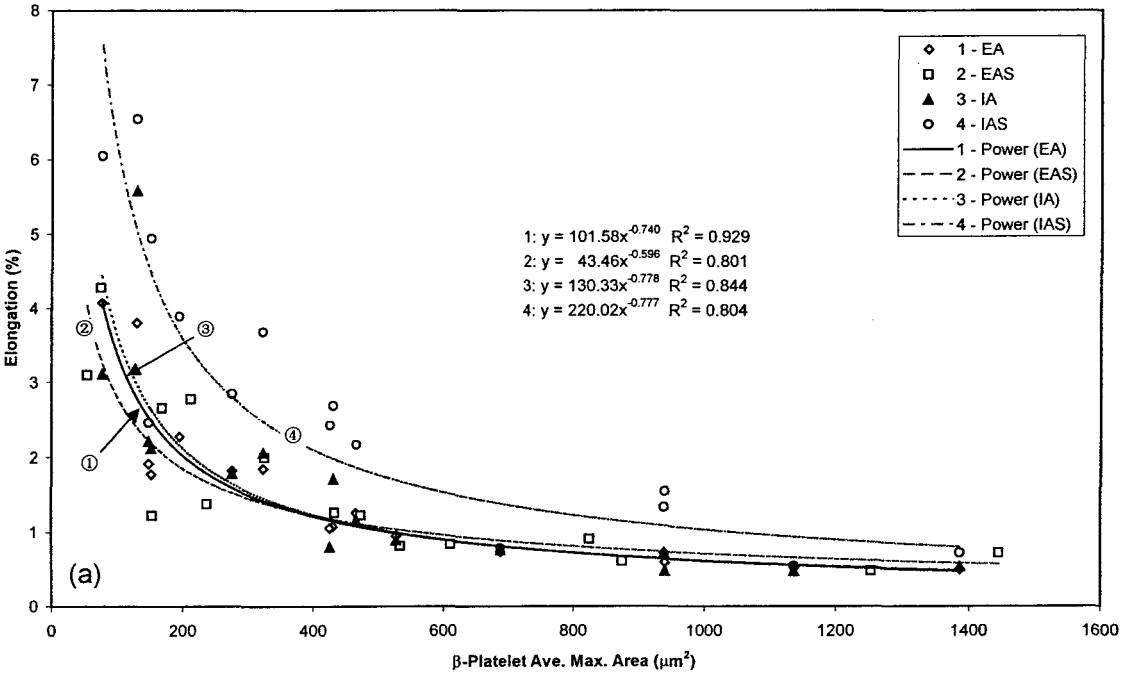

Figure 4.11. Tensile properties *vs.* β-platelet ave. max. area (experimental and industrial A alloy, 0 ppm and 200 ppm Sr).

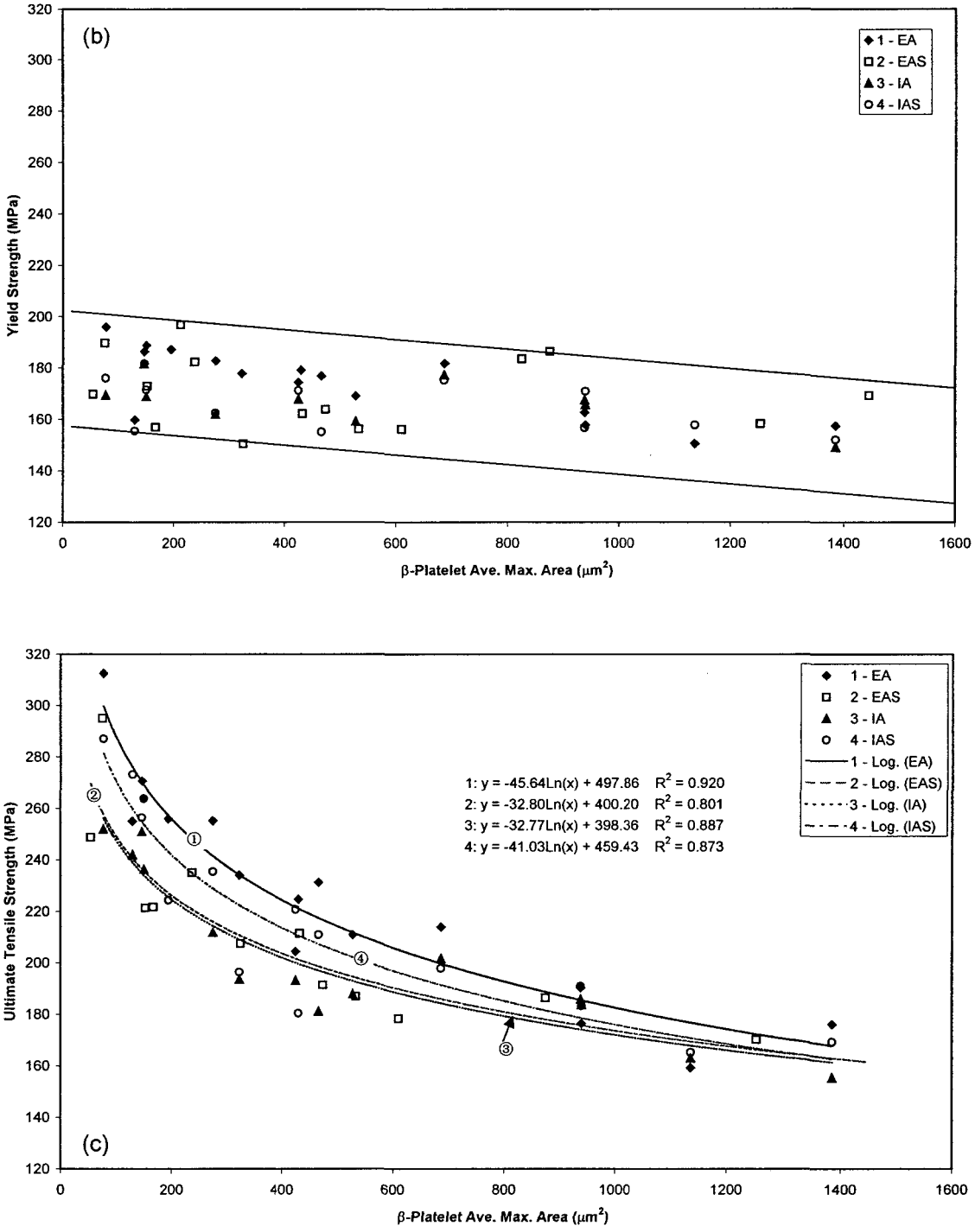

Figure 4.11. Tensile properties *vs.* β-platelet ave. max. area (experimental and industrial A alloy, 0 ppm and 200 ppm Sr).

different β-iron intermetallic sizes. Thus, with the increase in the size of β-iron intermetallics, the decrease in ductility and tensile strength becomes very gradual.

In Figures 4.10(a) and 4.11(a), the overall relations between elongation and β-iron platelet size in the unmodified and Sr-modified experimental alloys and the unmodified industrial alloy are almost the same, as the trend lines in the three cases almost overlap. This indicates that, in these cases, elongation is mainly controlled by the size of the β-phase platelets. The trend line for the Sr-modified industrial alloy samples is well above the other three in Figures 4.10(a) and 4.11(a), showing that this alloy exhibits much better elongation than the others at the same β-iron intermetallic sizes. Thus, while the size of β-platelets primarily controls the elongation (as the trend line is almost parallel to the other three), other factors such as the tramp elements present in the industrial alloy may also be responsible and should be taken into consideration to explain the elongation values observed. Further work needs to be carried out in this respect, to arrive at definite conclusions. However, this is not within the scope of the present study.

With regard to the yield strength, the effect of β-platelet size does not provide a regular correlation, as can be seen from Figures 4.10(b) and 4.11(b). For the four alloys and conditions studied, specific β-platelet sizes can result in the highest yield strength, or the lowest, for the same alloy/condition. The scatter of the data indicates that yield strength is independent of the β-iron platelet size. Nevertheless, the yield strength values are distributed within a band with respect to the β-platelet size, similar to that observed in the yield strength *vs.* iron content plots for alloy A356.2 (Figures 4.8(b) and 4.9(b)).

In the case of ultimate tensile strength, with respect to the β-platelet lengths, the trend lines for the four alloys are similar to each other and more evenly spaced out, Figure 4.10(c), whereas those shown in Figure 4.11(c) reveal that the Sr-modified experimental alloy and the unmodified industrial alloy exhibit very close values of UTS. Again, in this case, it is expected that the UTS is controlled not only by the β-iron intermetallics size, but also by other microstructural parameters, *e.g.*, the hard Si particles, tramp elements, *etc.* which may also increase the UTS to some extent.

4.2.2.2 Alloy B319.2 (alloy B)

The effect of β-platelet size on the tensile properties of alloy B is similar to that observed in alloy A, as depicted in Figures 4.12 and 4.13, except that the decrease in ultimate tensile strength is much more gradual in comparison to alloy A (see Figures 4.12(c) and 4.13(c)).

In the case of elongation, the trend lines are similar to each other and lie close to one another, Figures 4.12(a) and 4.13(a). Compared to alloy A, the lines for the unmodified and Sr-modified industrial B alloy samples almost overlap. This indicates that, in B319.2 alloys, the size of the β-iron platelets is the primary parameter controlling elongation, and other variables, such as the Mg_2Si particles present in the matrix (due to the higher Mg content), provide only a small contribution.

With regard to the yield strength, for the four alloys/conditions studied, no regular relation between the β-platelet size and yield strength could be observed, similar to the case of alloy A, Figures 4.12(b) and 4.13(b). Compared to alloy A, the band widths are smaller

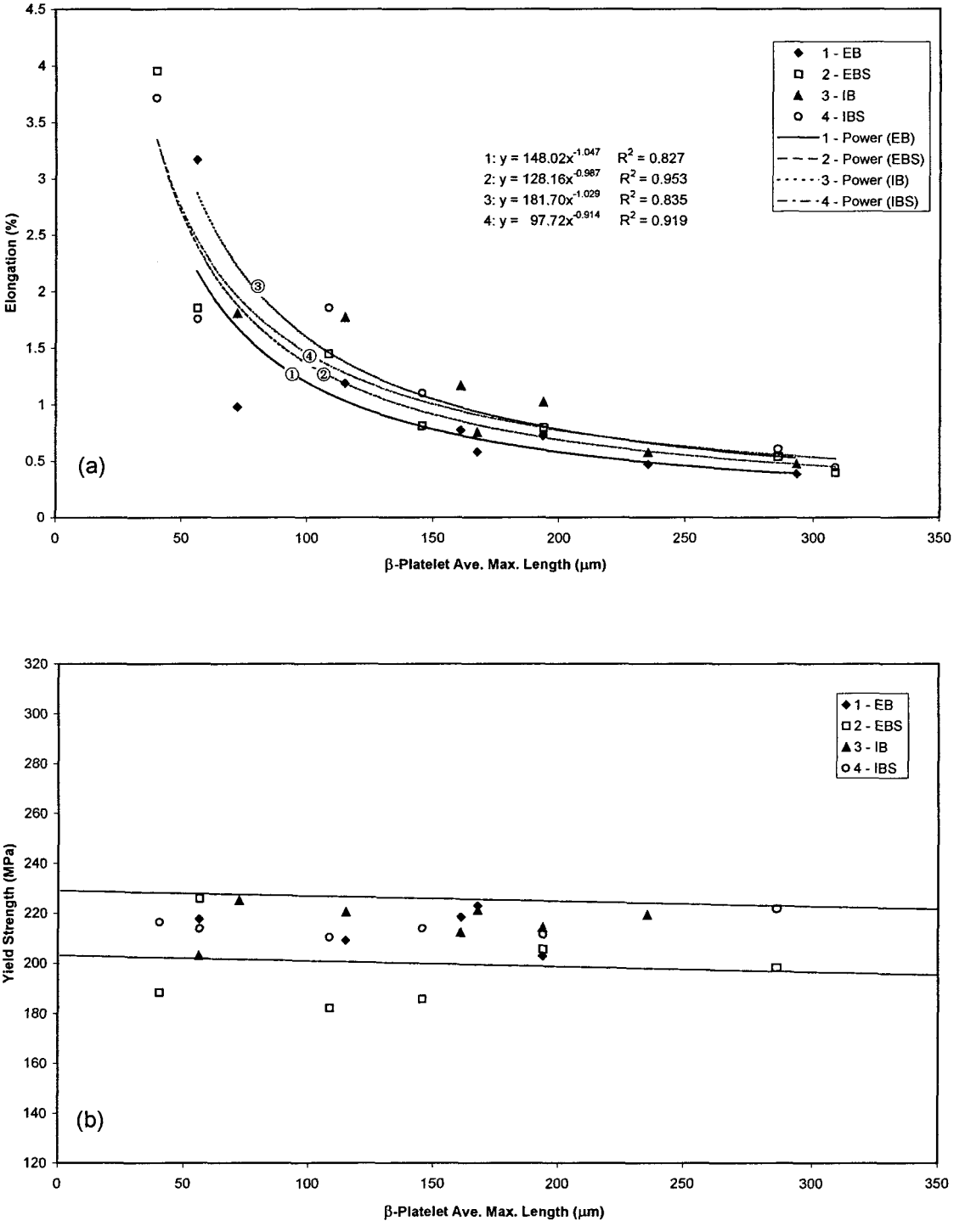

Figure 4.12. Tensile properties *vs.* β-platelet ave. max. length (experimental and industrial B alloy, 0 ppm and 250 ppm Sr).

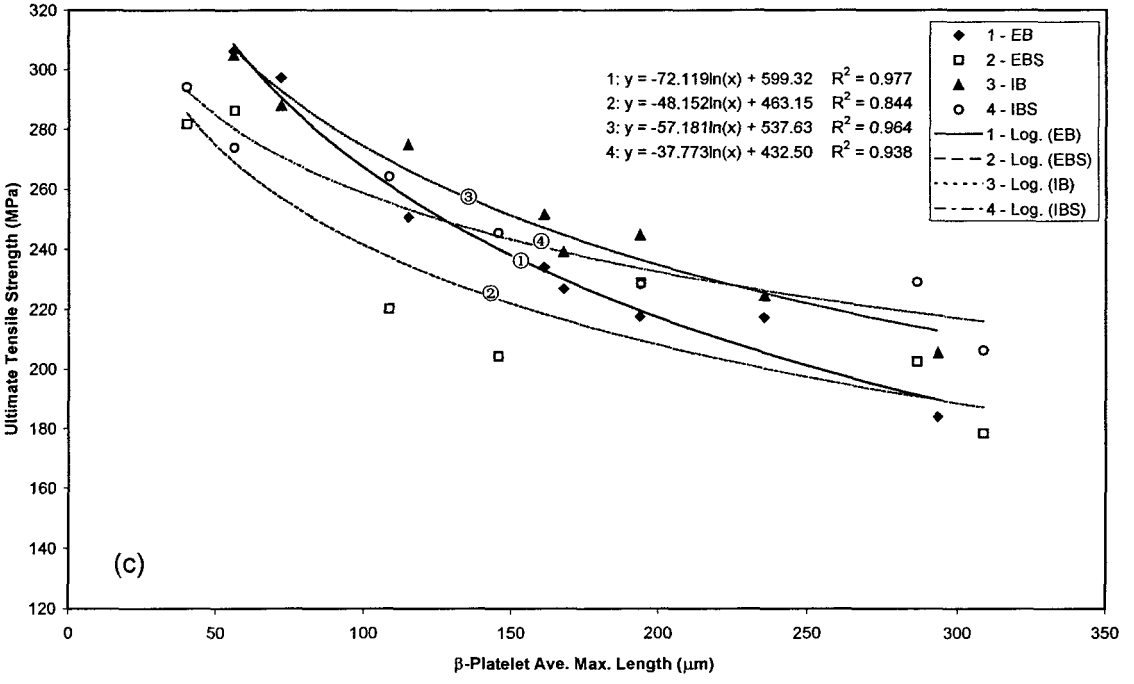

Figure 4.12. Tensile properties *vs.* β-platelet ave. max. length (experimental and industrial B alloy, 0 ppm and 250 ppm Sr).

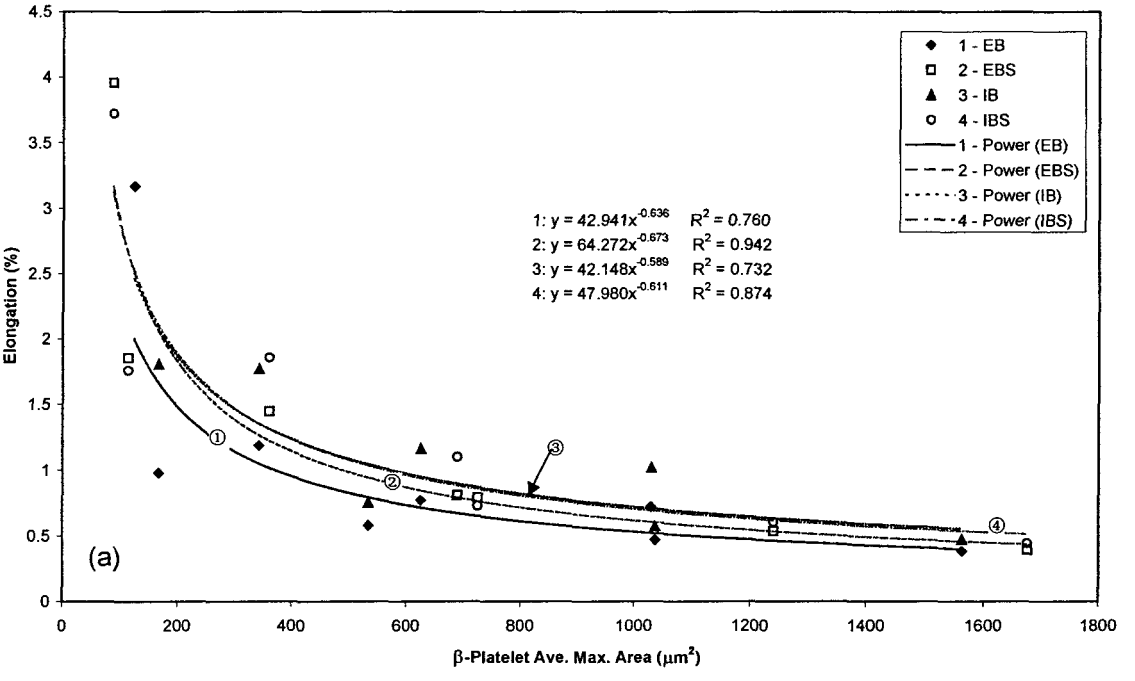

Figure 4.13. Tensile properties *vs.* β-platelet ave. max. area (experimental and industrial B alloy, 0 ppm and 250 ppm Sr).

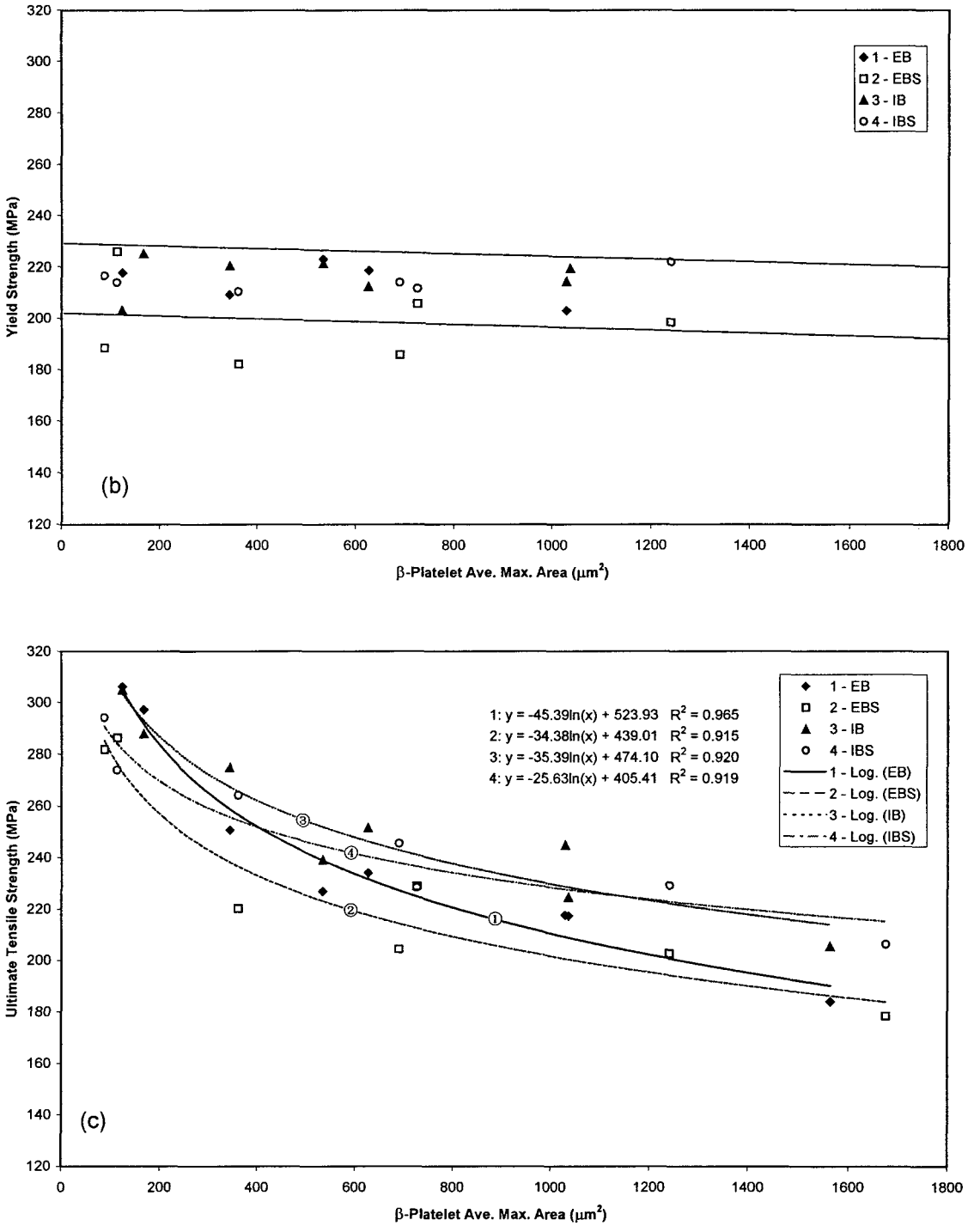

Figure 4.13. Tensile properties *vs.* β-platelet ave. max. area (experimental and industrial B alloy, 0 ppm and 250 ppm Sr).

in this case (*cf.* ~27 MPa with ~45 MPa), the distribution is much more even within the bands, and only a very slight decreasing trend in YS towards larger β-platelet sizes is observed. Thus, it is reasonable to assume that the higher Mg level of the alloy aids in stabilizing the yield strength of such Al-Si-Cu alloys.

As mentioned previously, the ultimate tensile strength of the B alloys is different from that of alloy A. In all alloys/conditions, there is a slow and steady decrease in UTS with the increase in the β-platelet size, Figures 4.12(c) and 4.13(c). With the increase in β-platelet size, the difference in UTS between the unmodified and Sr-modified alloys decreases, in both experimental and industrial alloys. In other words, since Sr modification decreases the size of the β-iron intermetallics, therefore, at a specific β-platelet size, the iron content will be lower in the unmodified alloy, or the cooling rate higher, or both. As the amount of β-iron intermetallics increases, for the same β-platelet size, the difference in iron content or cooling rate between modified and unmodified conditions will decrease, leading to a decrease in the difference in UTS values observed in the two conditions.

In contrast, however, the difference in UTS between the experimental and industrial alloys is seen to increase, as one approaches larger β-platelet sizes, in both the unmodified and Sr-modified conditions. Although the exact reason for this cannot be pointed out, it is very likely that the tramp elements present in the industrial alloy, react with the iron to form additional intermetallics which, dispersed in the aluminum matrix, would increase the UTS, thereby increasing the difference in UTS values observed in Figures 4.12(c) and 4.13(c) between the experimental and industrial alloys.

4.2.2.3 Alloy A356.2 (alloy C)

The effects of the β-platelet size on the tensile properties of A356.2 alloy are plotted in Figures 4.14 and 4.15. As Figures 4.14(a) and 4.15(a) show, within a certain β-platelet range (~70 μm length or ~300 μm^2 area), elongation drops very rapidly with small increments in β-platelet size. While the effect is similar to that observed in the 319 (A and B) alloys, two points of difference are noted: the drop in elongation is (a) much sharper in the A356.2 alloys, and (b) takes place within a smaller range of β-platelet sizes (*cf.* 70 μm/300 μm^2 with 100 μm/400 μm^2 in the 319 alloys). Thus, in Al-Si-Mg alloys, only smaller β-iron intermetallics can be tolerated if the requirements for satisfactory ductility are to be met. Alloy C has an overall higher ductility than alloys A and B, particularly in the Sr-modified case, where the samples obtain much higher elongations than the unmodified samples. As Figures 4.14(a) and 4.15(a) show, a relative increase in elongation of about 170% is observed in the modified alloy at a β-platelet length of 30 μm. With respect to the same iron content, however, the increase in elongation will be higher in the Sr-modified alloys, since the β-platelet sizes will be smaller. Therefore, with an increase in the β-platelet size the drop in elongation will proceed much faster, and at β-platelet sizes smaller than the 70 μm and 300 μm^2 values quoted earlier, the drop in elongation should be much faster with the increase in the β-platelet size in this alloy than that observed in alloys A and B. For example, when β-platelet lengths increase from ~50 μm to ~110 μm, decreases of 2.26 and 6.14% (absolute values) were observed in the unmodified and Sr-modified cases for the C alloy, compared to 3.87 and 3.2% in alloy A, and 1.98 and 2.51% in alloy B, respectively (these values referring to experimental or industrial alloys,

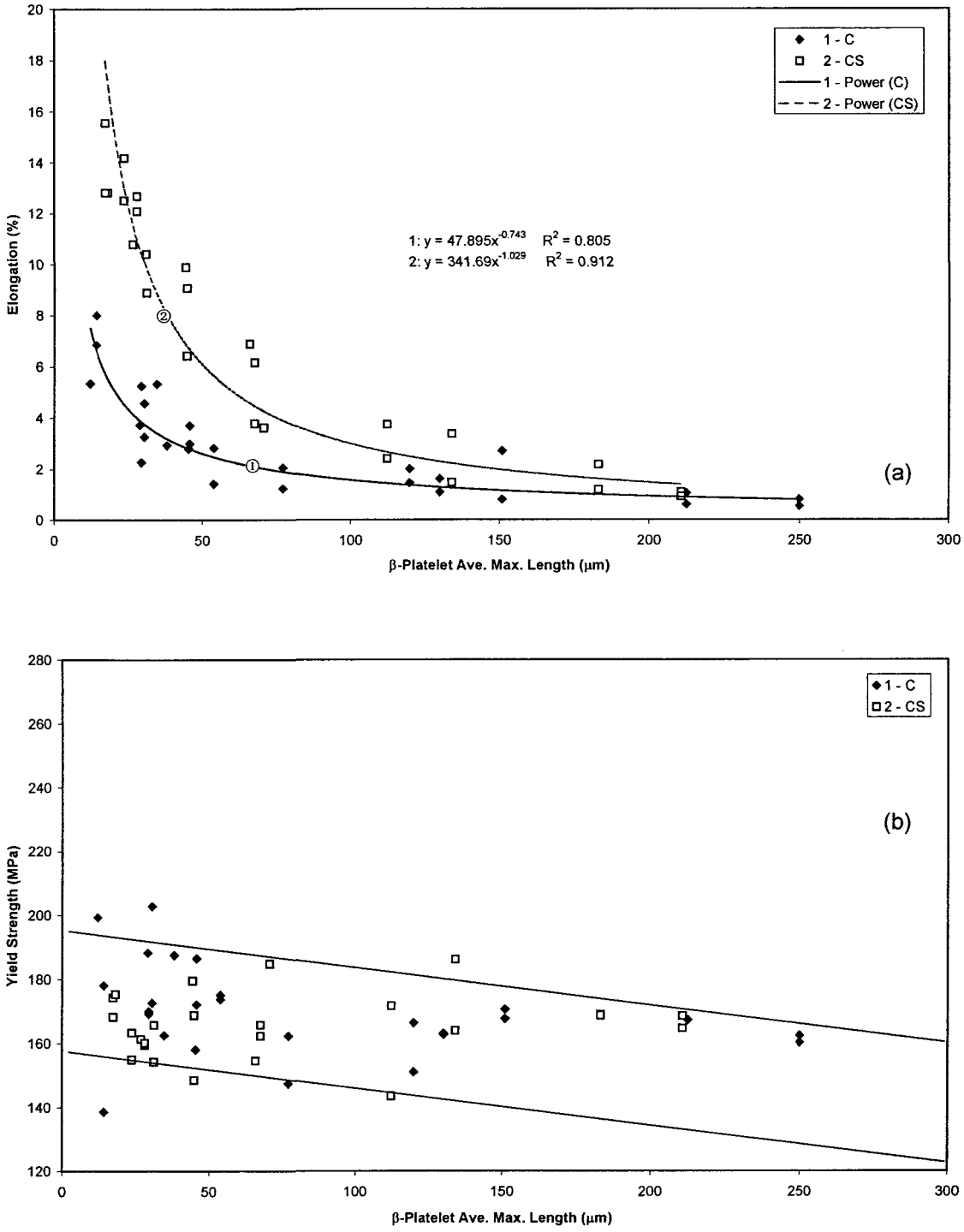

Figure 4.14. Tensile properties *vs.* β-platelet ave. max. length (industrial C alloy, 0 ppm and 300 ppm Sr).

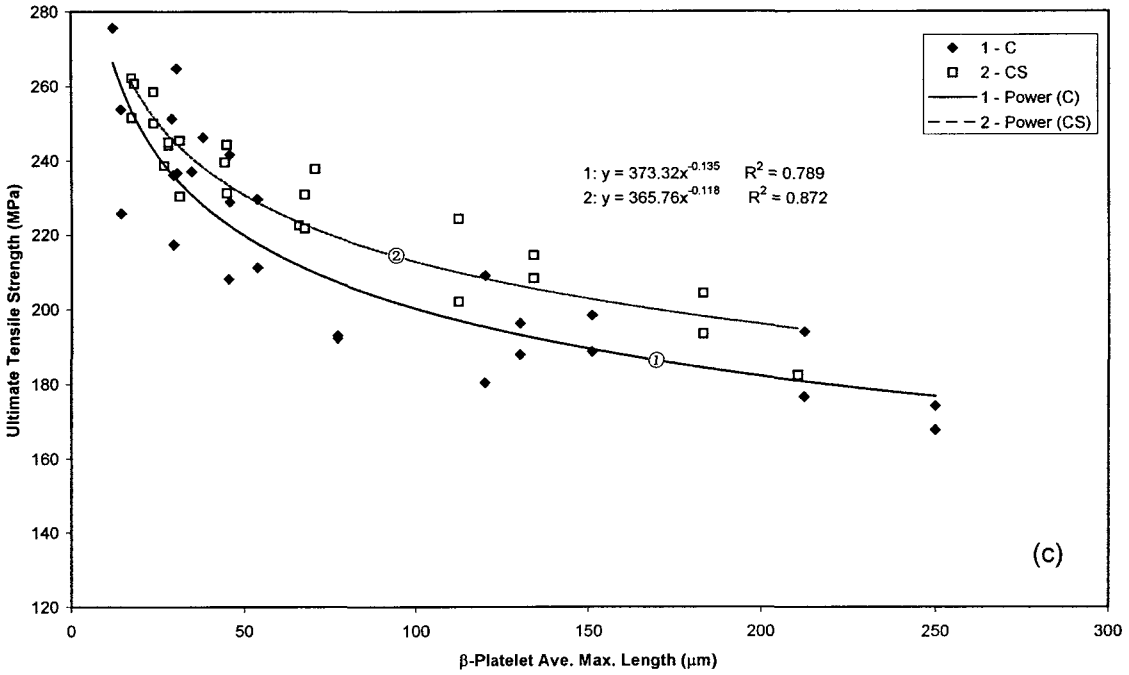

Figure 4.14. Tensile properties *vs.* β-platelet ave. max. length (industrial C alloy, 0 ppm and 300 ppm Sr).

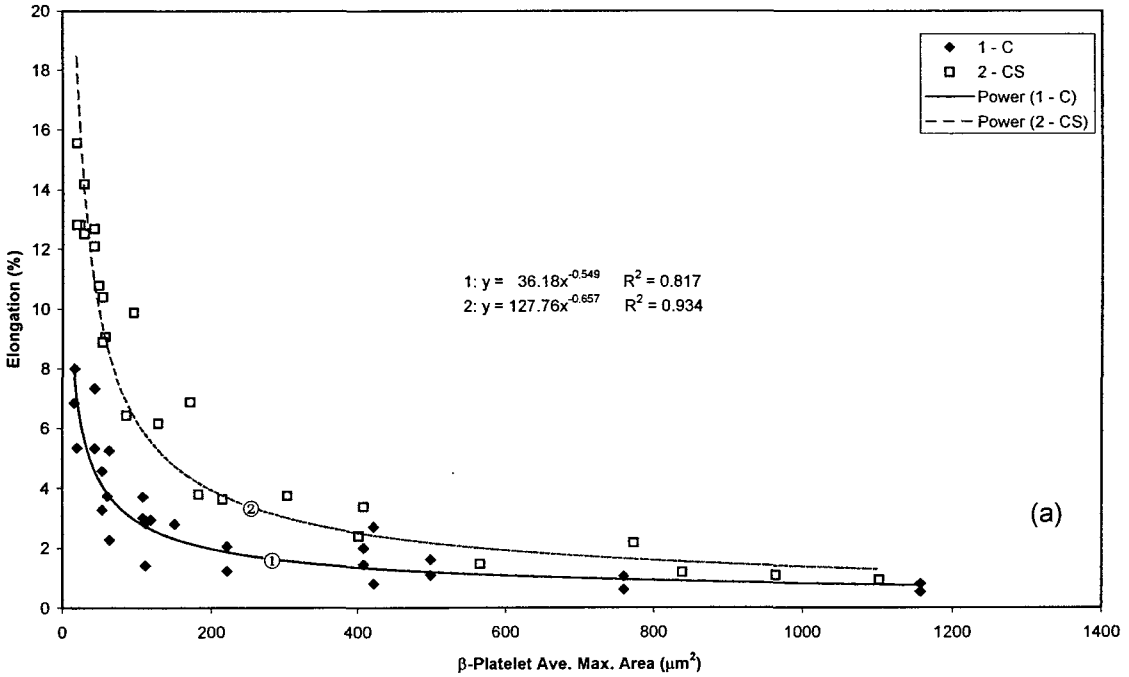

Figure 4.15. Tensile properties *vs.* β-platelet ave. max. area (industrial C alloy, 0 ppm and 300 ppm Sr).

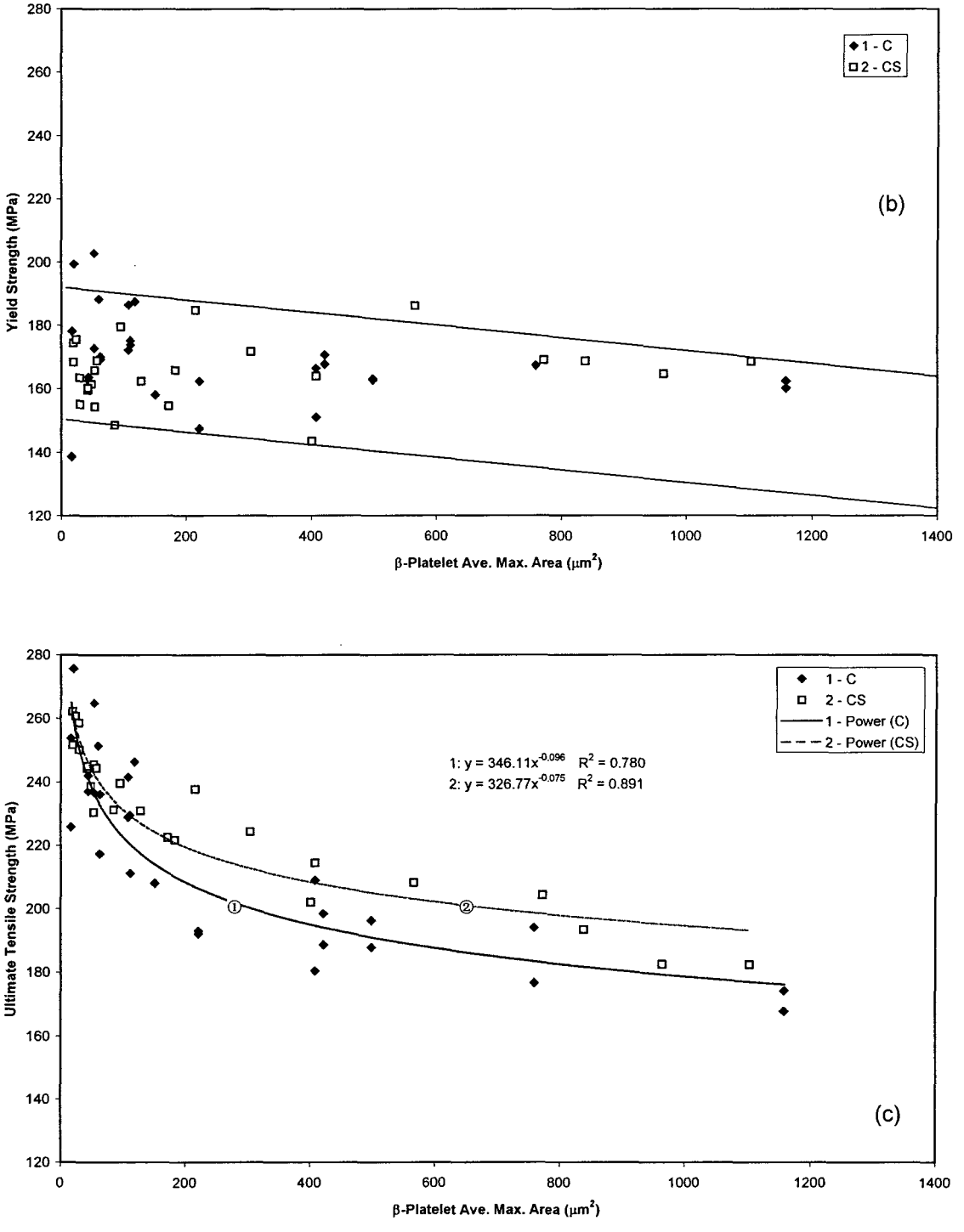

Figure 4.15. Tensile properties *vs.* β-platelet ave. max. area (industrial C alloy, 0 ppm and 300 ppm Sr).

whichever provided higher differences in elongation between the two conditions). As the elongation drops very rapidly only when the β-platelet lengths are smaller than 70 μm, the above range does not give the best illustration for the A356.2 alloy, but still a fairly good one. It must be remembered that the size of the β-platelet is only one of the important factors controlling elongation, particularly in the Sr-modified alloy, where the modification of the eutectic Si particles also plays an important role.

With respect to yield strength, the effect of β-platelet size in the A356.2 alloy is similar to that of alloys A and B, Figures 4.14(b) and 4.15(b). The slope of the band in the two figures is about the same as that observed in alloy A (Figures 4.10(b) and 4.11(b)), but more severe when compared to alloy B (Figures 4.12(b) and 4.13(b)). Also, the yield strength values obtained are the lowest among the three alloys. Most of the data points are concentrated in the region to the left, corresponding to β-platelet lengths less than 150 μm or β-platelet areas less than 500 μm^2 in the respective figures.

In the case of ultimate tensile strength, the decrease with respect to β-platelet size is continuous and gradual, Figures 4.14(c) and 4.15(c), and is similar to that observed for the B319.2 alloy (Figures 4.12(c) and 4.13(c)). However, unlike alloy B, the difference between the unmodified and Sr-modified samples increases with increase in the β-platelet size. In the pure version of the A356.2 alloy used in our study, at small β-platelet sizes, the Si particle sizes are also small (in keeping with the small DAS at high cooling rates). Thus, although Sr modification can further refine the size of the β-iron intermetallics and modify the Si particles, the resultant decrease is not very apparent. As the β-platelet size increases, however, the difference between modified and unmodified Si particles becomes much

greater (at low cooling rates), resulting in increasing the gap between the UTS values of the unmodified and modified alloy samples. Although much better elongations were observed in this alloy than in the 319 alloys, the best UTS values are still lower than those obtained in alloys A and B.

We have seen how, for the three alloys studied, the yield strength shows no definite relation with regard to the β-iron intermetallic size. This can be explained by means of the schematic diagram shown in Figure 4.16, which illustrates the stress-strain curve(s) obtained under high Fe-low cooling rate and low Fe-high cooling rate conditions; these conditions representing the two ends of the range of Fe contents-cooling rates covered in the study. For a specific alloy, as the iron content and cooling rate change, so does the stress-strain curve, going from a maximum at the low Fe-high cooling rate point situated

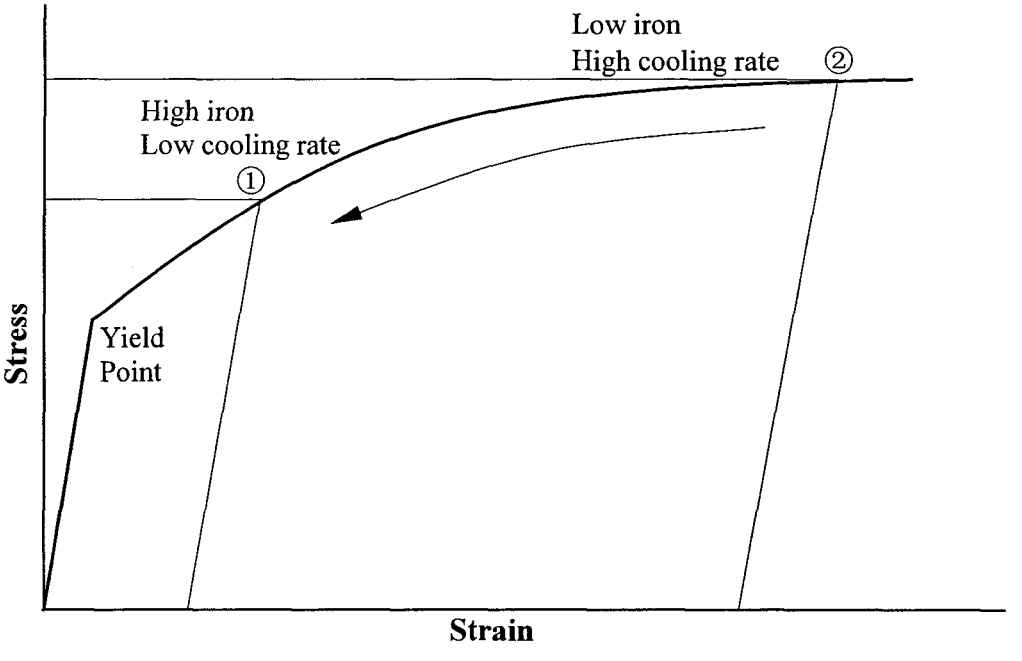

Figure 4.16. Schematic stress-strain curve showing the relative stability of YS with respect to iron content and cooling rate.

near ② (where high ductilities and tensile strengths are obtained) all the way down to ①, representing the high Fe-low cooling rate condition (where both ductility and tensile strength are lowered). In either of these conditions, however (or those in between), the yield point remains unchanged, explaining why the yield strength is unaffected by the alloying or solidification conditions.

4.2.3 Effect of Porosity

In the present study, porosity characteristics were analyzed and quantified using a Leco 2001 image analyzer in conjunction with an optical microscope (Olympus BHU-2). The following porosity parameters were measured: area percent porosity (percentage porosity over a constant sample surface area), pore area, pore length, pore aspect ratio and pore count. From these, the parameters that determine the quality and size of porosity, *i.e.*, pore volume percentage, pore density, average and maximum pore areas, average and maximum pore lengths, were obtained for each alloy sample condition.

The effect of these parameters on the mechanical properties is not the same. Although porosity volume percentage has been employed as the defining characteristic of porosity by many investigators, Herrera and Kondic[109] have suggested that this parameter is not appropriate for studying the quantitative effects of porosity on UTS, since a uniformly distributed porosity seldom occurs in typical alloy castings. According to them, the pore area and pore length parameters give a better correlation with the tensile properties.

In the present study, only the effects of pore length and pore area on the tensile properties of alloys A and C were studied, representing the 319 and 356 alloys, since

insufficient data was obtained with the B319.2 alloy. Of these, the maximum pore area and maximum pore length values; showed a better relation with the tensile properties than the average area and length values; the maximum pore area parameter displaying the better correlation of the two.[154] Thus, only the effect of the maximum pore area on the tensile properties has been discussed in the following sections.

4.2.3.1 Alloy 319.2 (alloy A)

Figure 4.17 shows the correlations between the tensile properties and maximum pore area for all the alloy samples obtained from 319.2 alloys, and is similar in appearance to the plots of tensile properties *vs.* β-platelet characteristics observed in Figures 4.14 and 4.15 for the A356.2 alloys. In general, with the increase in maximum pore area, an overall decrease in all the properties was observed, in accordance with the results of other investigators.[109,114]

In the case of elongation, Figure 4.17(a), the trend lines for the Sr-modified samples lie away from and above those of the unmodified ones, while the latter almost overlap. The plots are different from those shown in Figures 4.10(a) and 4.11(a). This indicates that maximum pore area is not the primary parameter controlling elongation, as different elongations are obtained in different alloy samples at the same values of maximum pore area. In the unmodified industrial alloy and the unmodified and Sr-modified experimental alloys, the elongation drops very quickly up to maximum pore area sizes of ~50×10^3 μm^2; beyond that, elongation remains almost the same in each case. In the Sr-modified industrial

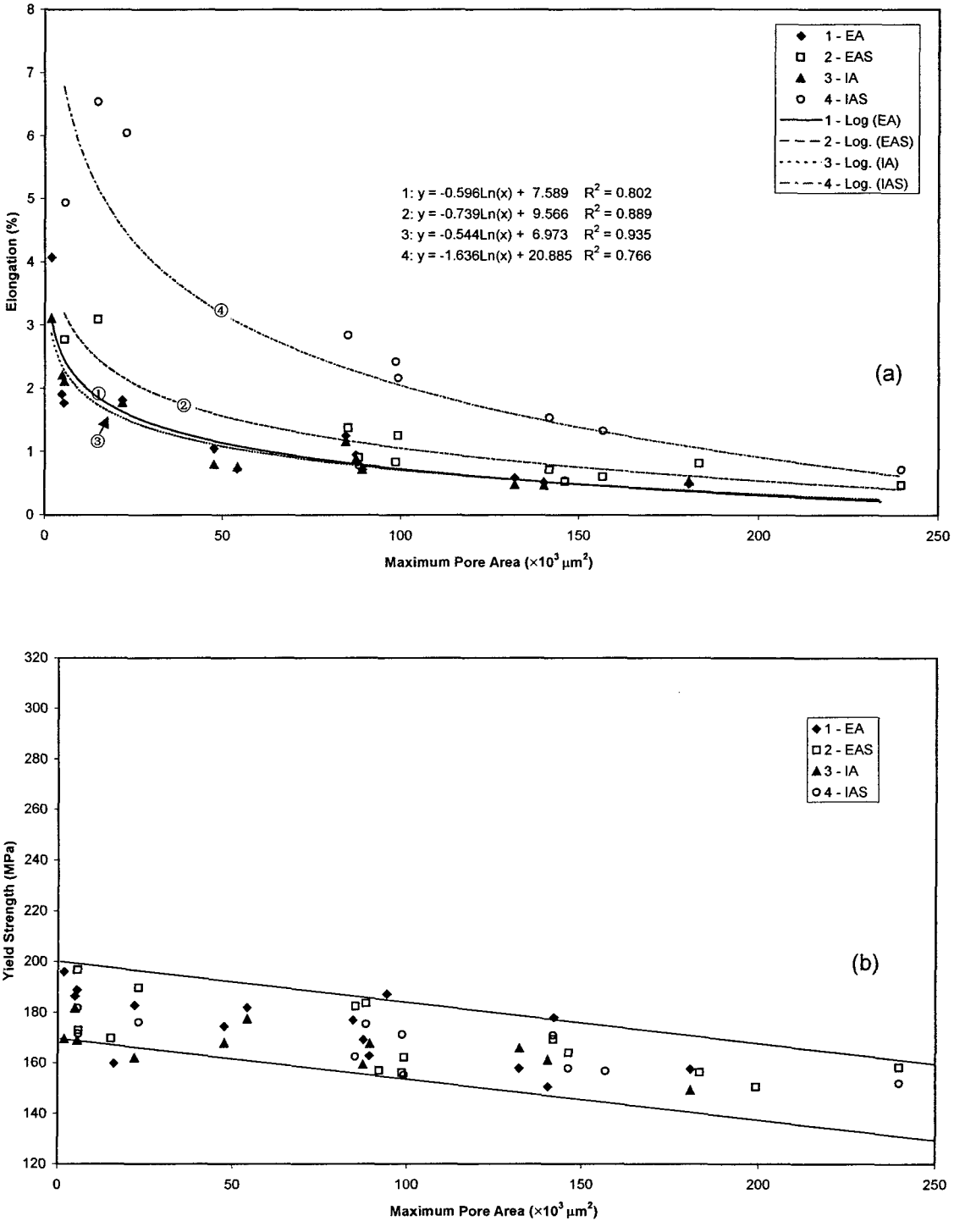

Figure 4.17. Tensile properties as a function of maximum pore area (experimental and industrial A alloy, 0 ppm and 200 ppm Sr).

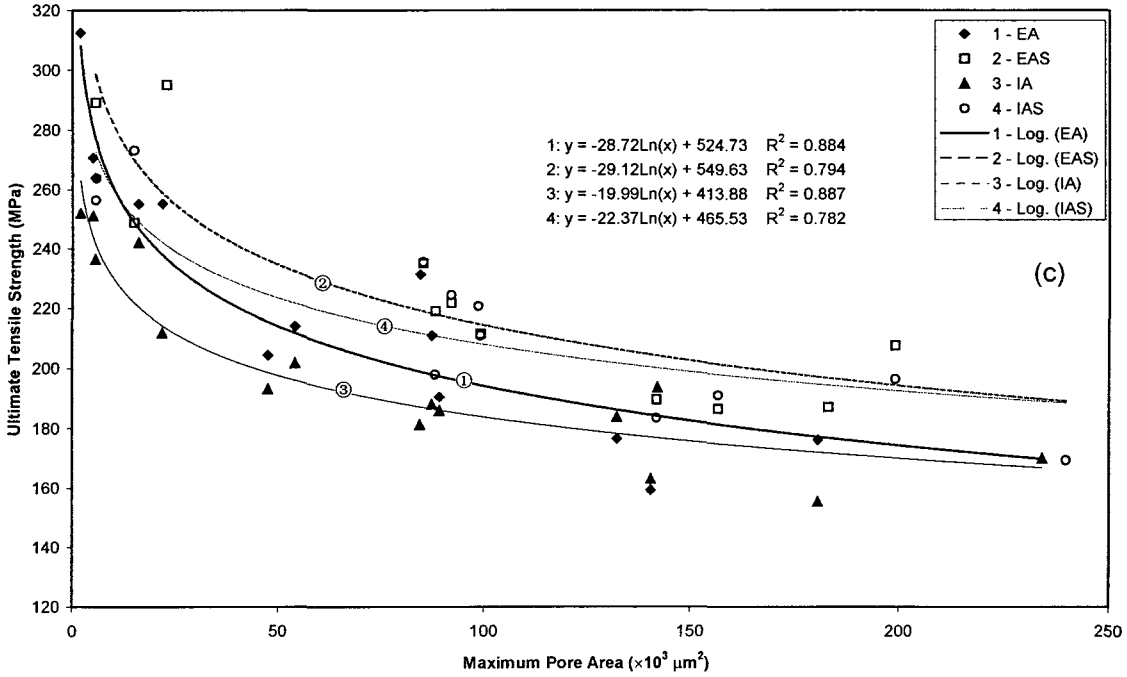

Figure 4.17. Tensile properties as a function of maximum pore area (experimental and industrial A alloy, 0 ppm and 200 ppm Sr).

alloy, the decrease in elongation is more gradual over the range of maximum pore areas observed.

Strontium modification improves elongation significantly, particularly in the industrial 319.2 alloy. As it also facilitates porosity formation, much larger maximum pore areas are obtained in the modified alloys for the same alloy/cooling rate conditions, thus shifting the trend lines to the right, and contributing to "higher elongations" at the same values of maximum pore area observed compared to the unmodified alloys. Nevertheless, although Sr addition favors the formation of porosity, larger porosity sizes can be tolerated to achieve the same level of ductility, due to its beneficial effect on both the β-iron intermetallic and eutectic Si particles.

The effect of maximum pore area on yield strength, Figure 4.17(b), is similar to that of the β-platelet size; that is, the yield strengths are distributed within a band, of ~40 MPa width, showing an overall decreasing trend with an increase in pore size.

Towards smaller maximum pore sizes ($< 15 \times 10^3$ μm^2), considerable differences in ultimate tensile strength are observed between the experimental and industrial alloys in both the unmodified and Sr-modified cases, Figure 4.17(c). These differences decreases as the maximum pore area increases. It should be borne in mind that maximum pore area is not an independent parameter, as it is controlled by other variables like iron content, cooling rate, strontium modification, *etc.* and their effects are also implicated in the correlations observed in Figure 4.17(c). Strontium modification increases the tensile strength significantly; the differences in the UTS values between unmodified and Sr-modified alloys increasing with the increase in maximum pore area, and remain more or less constant after the pore sizes of 50×10^3 μm^2. As in the case of elongation, this is due to the increase in pore size upon modification.

4.2.3.2 Alloy A356.2 (alloy C)

In this alloy, the data scatter in the tensile properties with respect to maximum pore area was so large that no single correlation line could be obtained for either the unmodified or Sr-modified alloys, Figure 4.18.

As can be seen from Figures 4.18(a) and 4.18(c), for both the unmodified and Sr-modified alloy samples, the elongation and ultimate tensile strength values appear distributed within a band. The scatter within the bands is obvious, although, in the Sr-

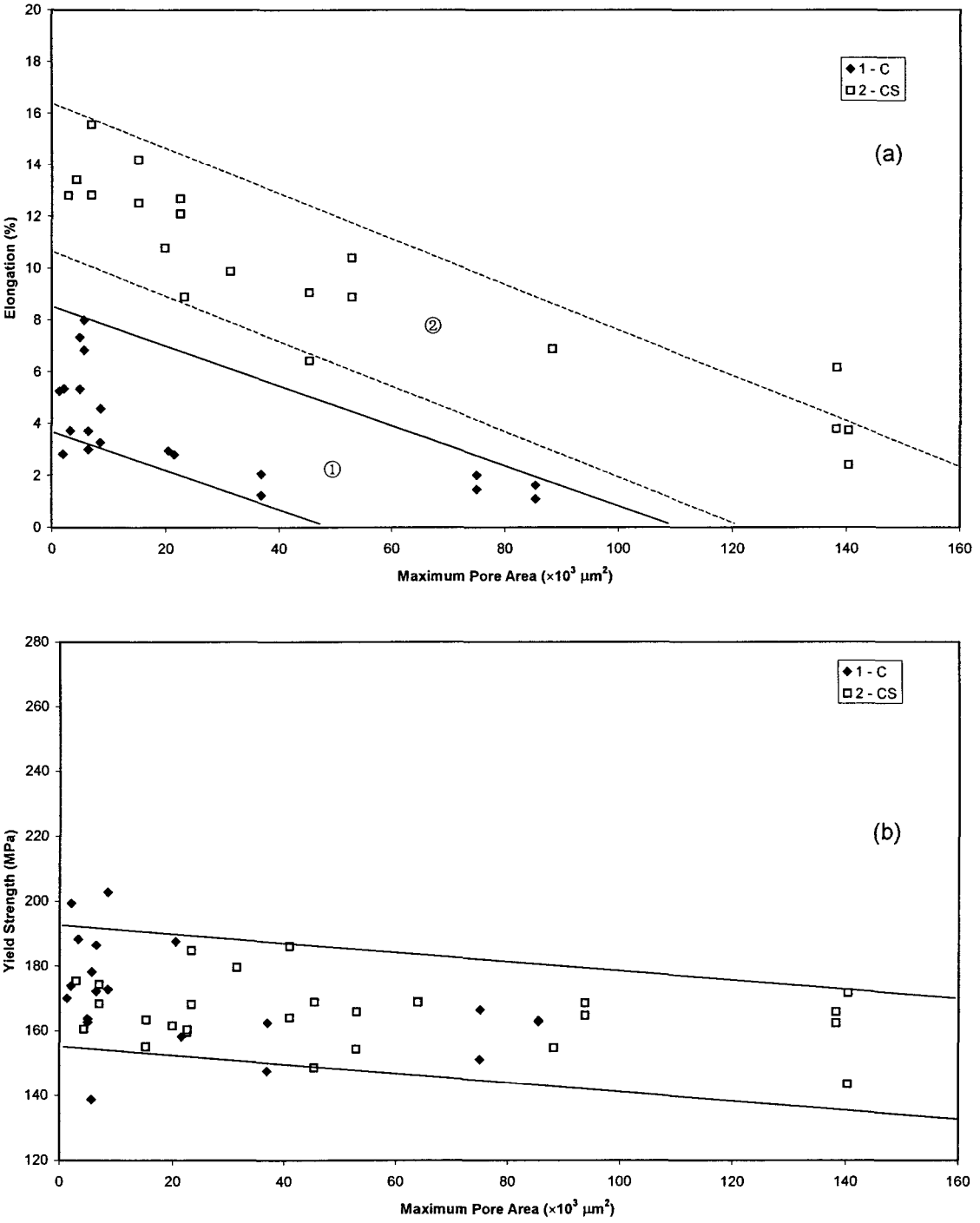

Figure 4.18. Tensile properties as a function of maximum pore area (industrial C alloy, 0 ppm and 250 ppm Sr).

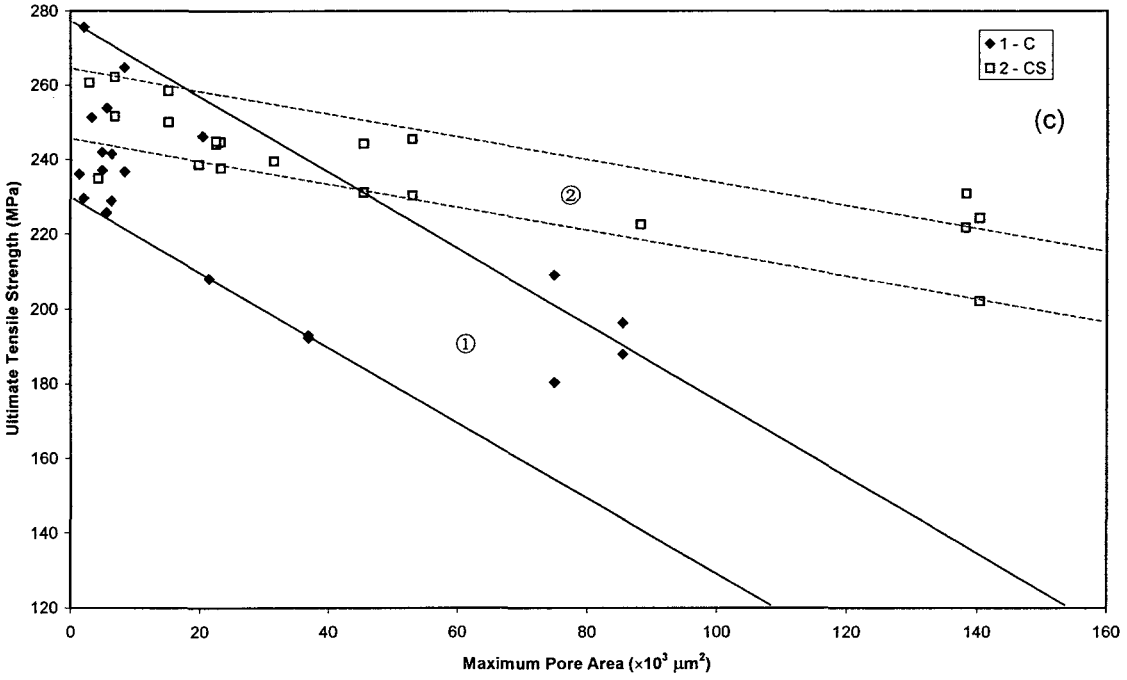

Figure 4.18. Tensile properties as a function of maximum pore area (industrial C alloy, 0 ppm and 250 ppm Sr).

modified condition, the data are distributed more uniformly within the bands. For the unmodified alloy, most of the data are accumulated to the left, in the region where maximum pore area is less than 15×10^3 μm^2. However, while there is no overlap between the two bands in the case of elongation, Figure 4.18(a); in the case of the tensile strength, the two bands overlap and some of the tensile strength values duplicate for maximum pore areas $< 20 \times 10^3$ μm^2. The effect of porosity on yield strength, Figure 4.18(b), is similar to that observed in 319.2 alloy.

4.2.4 Effect of Strontium

Although the effect of strontium on tensile properties has been incorporated in the previous sections in comparing the Sr-modified alloys with the unmodified alloys, in this

section we will review its effect on the properties in the context of experimental *vs.* industrial alloys for the three alloys studied. The best way to evaluate the effect of strontium would be to focus on the tensile properties *vs.* iron/cooling rate plots. However, as the data for the unmodified and Sr-modified 319.2 and A356.2 alloys were plotted separately, the tensile properties *vs.* β-platelet size/maximum pore area plots have been employed instead in alloys A and C, while in alloy B, all the available plots were utilized.

4.2.4.1 Alloy 319.2 (alloy A)

From Figures 4.10(a) and 4.11(a), we can see that for the percent elongation, not much difference between unmodified and Sr-modified alloys is observed for the experimental alloys. That is to say, when the alloy used is pure (experimentally prepared), strontium modification exerts almost no influence on the elongation. This can be attributed to the interaction of the beneficial and negative effects of Sr on alloy microconstituents. Although the β-platelet size becomes smaller due to strontium modification and the morphology of the eutectic Si changes from acicular to fibrous in the pure alloy, these changes are not as significant as the increase in pore sizes. Thus, any amelioration with respect to the former is masked by the latter.

In the industrial alloy, however, strontium modification has a significant effect on the percent elongation, as the trend line for the Sr-modified samples appears much higher than that for the unmodified alloy samples, at all β-platelet sizes, *viz.*, at all iron levels and DAS values studied. Thus, as mentioned previously, the tramp elements present in the alloy are

expected to play a role in enhancing ductility. However, further investigations are required to confirm this.

The effect of strontium modification on yield strength, Figures 4.10(b) and 4.11(b), appears to be negligible. When the yield strength values in both unmodified and Sr-modified alloys were compared, it was found that strontium modification could either improve or deteriorate the yield strength, but to a very small extent, *i.e.*, mostly within ±5%. Therefore, the overall effect of strontium modification could be ignored. This confirms that yield strength is mainly controlled by the type and amount of strengthening particles that precipitate in the alloy upon heat treatment.

With respect to ultimate tensile strength, it is clear that the effect of strontium modification depends upon the chemical composition of the alloy (*i.e.*, source of the alloy), as can be seen from Figures 4.10(c) and 4.11(c). Strontium modification increases the UTS levels in the industrial alloy, but reduces those of the experimental alloy, in general, so that the difference in UTS levels between experimental and industrial alloys is much less than when the alloys are not modified. Thus, strontium modification is useful in maintaining a consistent UTS level in 319.2 alloys coming from different sources. Moreover, as it also enhances the ductility of the industrial alloy (Figures 4.10(a) and 4.11(a)), optimum tensile properties could be achieved by this means, even when using inexpensive, secondary alloys.

4.2.4.2 Alloy B319.2 (alloy B)

Figures 4.12 and 4.13 show the effect of strontium modification in the B319.2 alloy, which differs from that of alloy 319.2 due to its higher magnesium content. An overall increase in elongation is observed with strontium modification in the experimental alloy, Figures 4.12(a) and 4.13(a), while in the industrial alloy, a slight decrease is observed, Figure 4.12(a).

As Figures 4.12(b) and 4.13(b) show, strontium does not appear to affect the yield strength. However, when the yield strength values are analyzed with respect to the iron level/cooling rate, strontium modification actually decreases the yield strength slightly in most cases, particularly in the experimental alloy, Figure 4.7(b). As the lowest yield strengths were observed in the Sr-modified industrial alloy, it is reasonable to suggest that the Sr may react with some of the Mg, leaving less Mg available to form Mg_2Si, thereby decreasing the yield strength.

The differences in ultimate tensile strength between alloys A and B after Sr modification are very distinct, Figures 4.12(c) and 4.13(c), as discussed previously. In the modified B alloys, the UTS decreases in both experimental and industrial alloys. Also, the difference in UTS between the unmodified and Sr-modified alloys decreases in both experimental and industrial alloys with the increase in β-platelet size, iron level, or DAS value. Again, the same reasoning may be applied here, as explained previously in the case of the yield strength.

4.2.4.3 Alloy A356.2 (alloy C)

Strontium modification improves the elongation significantly in the A356.2 alloy, particularly when the β-platelets are smaller than ~70 μm in length (or ~300 μm^2 in area), as depicted in Figures 4.14(a) and 4.15(a). This improvement decreases as the β-platelet size increases. As the size of the β-iron intermetallics in the unmodified and Sr-modified alloys does not vary much, the change in morphology of the intermetallics upon modification is expected to play the main role in this case.

The yield strength of the A356.2 alloy decreases slightly with strontium addition. As no regular correlation with β-platelet size is observed, this decrease cannot be readily discerned from Figures 4.14(b) and 4.15(b).

With respect to ultimate tensile strength, however, improvement in UTS is easily observed in the strontium modified alloy, Figures 4.14(c) and 4.15(c), which increases with an increase in the β-platelet size. Thus, strontium modification is very effective in improving the tensile properties of A356.2 alloys.

4.2.5 Correlation between Elongation and Ultimate Tensile Strength

As mentioned in Section 4.1, two types of methods can be employed to discuss the tensile properties, *viz.*, the traditional means to study the elongation, UTS and YS separately with the effect of one or more parameters, or considering the properties globally using analyzing means such as quality index. The former has already been elaborated in the previous section, while the latter, using the form of log(UTS)-log(%El) plots (similar to the

UTS-log(%El) plots in others work with regard to quality index[136-140]) will be carried out in the following, with the details in each alloy employed in the present study.

4.2.5.1 Alloy 319.2 (alloy A)

Figure 4.19 shows the log(UTS) *vs.* log(%El) plot in the 319.2 alloys for the experimental and industrial alloys, in the unmodified and Sr-modified conditions. All individual data points were plotted in the figure, *i.e.*, corresponding to all cooling rates and all iron contents (as against the averages of three tests in previous figures). While the same results are obtained as reported previously, the four straight lines in Figure 4.19 show this trend more clearly than in the plots shown in the previous sections. Due to the data scatter, however, the R^2 values are not close to 1. Nevertheless, they provide sufficient indication of the general trend with regard to the iron content and cooling rate: lowest properties (percent elongation and UTS) are observed for samples corresponding to high Fe-low cooling rate conditions, whereas highest properties are observed corresponding to low Fe-high cooling rate conditions, irrespective of the alloy condition (*i.e.*, experimental, industrial, unmodified or Sr-modified alloy). In other words, the "quality" of the alloy changes with the change of iron content and cooling rate. Both the cooling rate and iron content influence the size and amount of the β-Al_5FeSi intermetallic formed, the latter decreasing with a decreasing iron content and increasing cooling rate. In contrast, an increasing size and volume fraction of the brittle β-Al_5FeSi phase with increasing iron content and a low cooling rate will deteriorate the mechanical properties, or the quality of the alloy significantly.

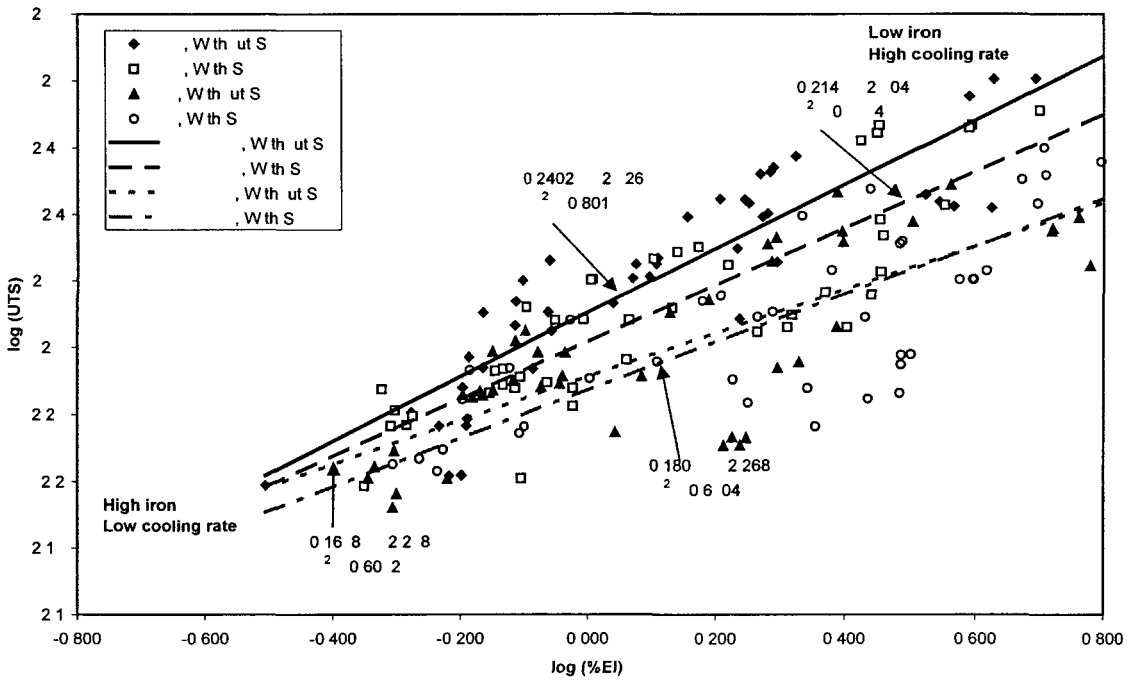

Figure 4.19. Plot of log (UTS) *vs.* log (%El) for alloy 319.2 (alloy A). E: experimental alloys; I: industrial alloys.

The direction of the trend lines in Figure 4.19 is different from that of Figure 4.1 in that they are not parallel, or that of Figure 4.20 which shows the tempering curves of a sand-cast Al-7Si-Mg03 alloy at different temperatures as a function of time.[136] This is because the results of Figures 4.1 and 4.20 depict only one alloy composition and casting condition, but different heat treatment processes. The results of Figure 4.19, on the other hand, comprise different chemical compositions and cooling rates, but the same heat treatment condition. Thus, while it may not be possible to draw iso-Q or iso-YS lines, in the present log(UTS)-log(%El) plots, in fact, both the plot of Drouzy *et al.*[136] (Figure 4.2), and Figure 4.19 show that the quality index (or quality) of the alloys decreases with an increase in the iron level. This observation can be found in different heat treatment conditions and fits quite well with our results.

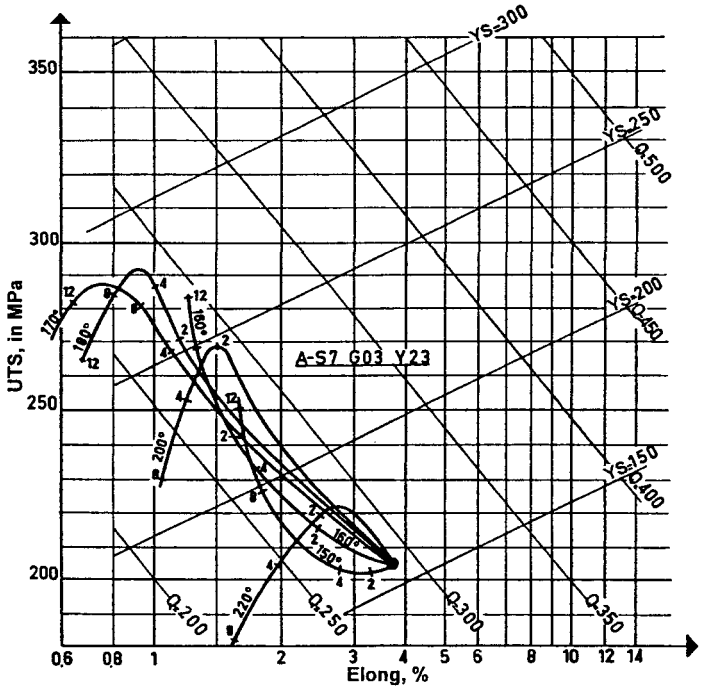

Figure 4.20. Tempering curves for sand-cast Al-7Si Mg03 alloy at different temperatures as a function of time. These curves have a general orientation in the direction of the iso-Q lines. The numbers in the curves indicate the time used for tempering.[136]

In Figure 4.19, although with strontium modification, the trend lines fall below those of the unmodified alloys; strictly speaking, however, one may not conclude that the quality index of these alloys decreases with Sr modification. First of all, as iso-Q lines cannot be drawn in these plots, no direct comparison can be made. Secondly, the trend line for the modified alloy diverges from that for the unmodified alloy in the case of the experimental alloy, but converges in the case of the industrial alloy towards the low Fe/high cooling rate corner of the plot.

Furthermore, suppose a line parallel to the log(%El) axial were drawn in Figure 4.19, then the points in the trend lines intercepting this line would have the same log(UTS) (*i.e.* UTS) value, but the log(%El) (or %E) value in the Sr-modified alloys would be higher than

those in the unmodified alloys. Conversely, for the same percent elongation value, the ultimate tensile strength values for the unmodified alloys would be higher than those for the modified alloys. This implies that the change in quality index due to Sr-modification cannot be readily determined using such log(UTS)-log(%El) plots (obtained from alloy samples covering different alloying conditions and melt treatments, but subjected to the same heat treatment condition (T6)). These plots, however, are quite useful in determining the general trend in tensile properties with respect to the iron content and cooling rate. According to the definition of Q from Equation 4.1, the Q value of the Sr-modified alloys will be higher in the first case (experimental alloy), but lower in the second (industrial alloy).

4.2.5.2 Alloy B319.2 (alloy B)

The overall trend for percent elongation and ultimate tensile strength shows an increase with the decrease in iron content and an increase in the cooling rate. As can be seen from Figure 4.21, the fairly good R^2 values (except in the case of the Sr-modified experimental alloy), indicate that, as in the case of the A alloy, the mechanical properties or "quality" of the alloy increases at low iron and high cooling rates. Also, strontium modification appears to have a more significant effect on the experimental alloy than on the industrial alloy, as the corresponding Sr-modified trend line drops down much further. Compared to the plot of Figure 4.19, the effect of Sr-modification is consistent in both alloys, from one corner of the plot to the other, even if it is much more moderate in the industrial alloy. Furthermore, the parallel nature of the trend lines implies that, for a certain alloy composition, a specific

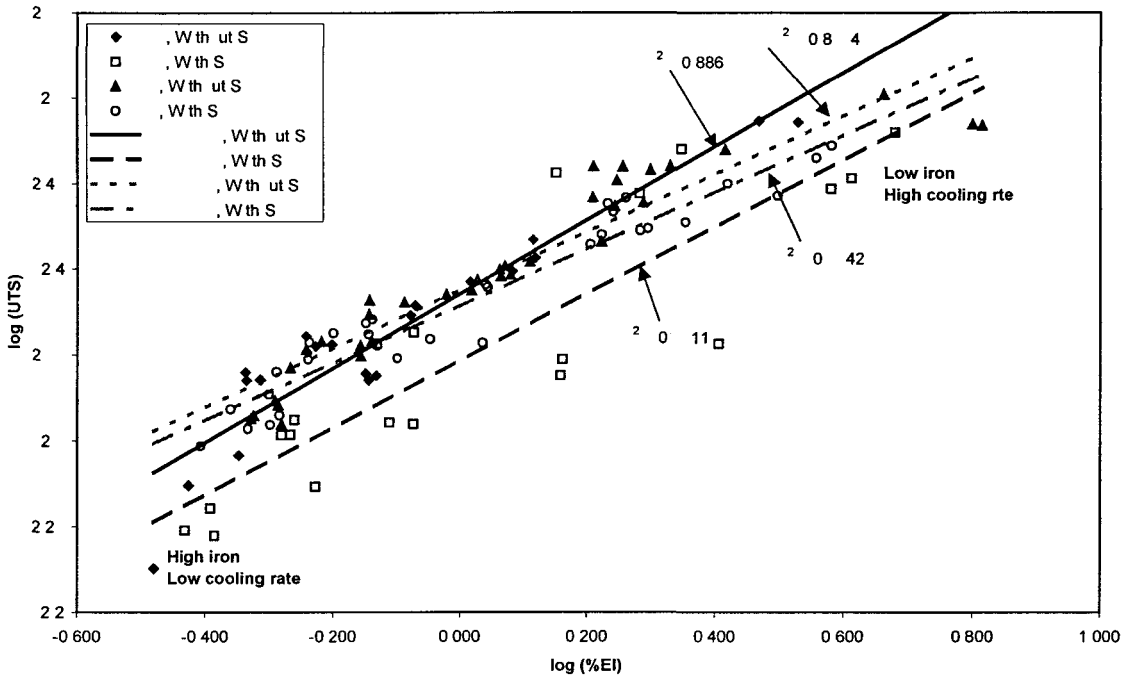

Figure 4.21. Plot of log (UTS) *vs.* log (%El) for alloy B319.2 (alloy B). E: experimental alloys; I: industrial alloys.

Sr addition would produce the same diminution in tensile properties over a range of iron levels and cooling rates.

4.2.5.3 Alloy A356.2 (alloy C)

Similar to the 319 alloys, an overall increase in elongation and ultimate tensile strength is also observed with an increase in cooling rate and decrease in iron concentration in the A356.2 alloy, as shown in Figure 4.22. Also, the trend line for the modified alloys lies below that of the unmodified alloys but shows a better correlation (*cf.* an R^2 value of 0.90 with 0.77for the unmodified alloys).

In conclusion, therefore, the plots in Figures 4.19, 4.21 and 4.22 reveal that, in the case of the experimental 319 alloys, the variation in elongation and ultimate tensile strength, *i.e.*,

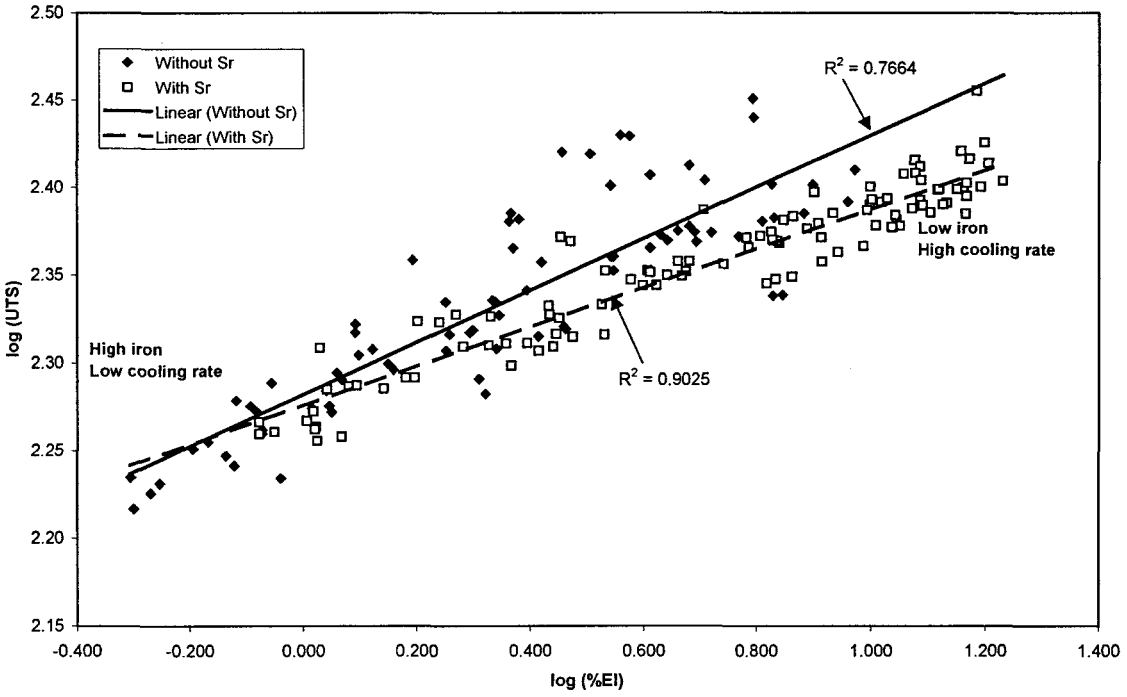

Figure 4.22. Plot of log (UTS) *vs.* log (%El) for alloy A356.2 (alloy C).

the change in quality index with respect to iron content and cooling rate, is more systematic in the unmodified condition, whereas in the industrial alloys, the modified alloys show a far better correlation for both 319 and 356 alloys. The R^2 values listed in Table 4.8 support this statement.

Table 4.8. R^2 values of trend lines in the log (UTS)-log (%El) plots shown in Figures 4.19, 4.21 and 4.22.

Alloy	Experimental		Industrial	
	no Sr	with Sr	no Sr	with Sr
A	0.80	0.73	0.61	0.67
B	0.89	0.79	0.90	0.93
C	–	–	0.77	0.90

4.2.6 Microstructure

As tensile properties depend directly on alloy microstructure, the optical microstructures of all the different alloy samples obtained from the three alloys were examined. In this section, representative micrographs of the 319.2 and A356.2 alloys will be shown covering both sides of the Fe content-cooling rate range, *viz.* low (to medium) Fe content-high cooling rate samples and high Fe content-low cooling rate samples, in both the unmodified and Sr-modified conditions.

4.2.6.1 Alloy 319.2

The optical microstructure of an unmodified 319.2 alloy sample containing 0.4% Fe, obtained at the highest cooling rate (DAS 23 μm) is given in Figure 4.23(a). Besides the aluminum matrix, the main phases observed are eutectic Si (1) and $CuAl_2$ (2) particles. The acicular eutectic Si particles are readily observed in the unmodified alloy, but the β-iron intermetallics are not, at this magnification, since their size is very small. This explains the combination of good ductility and tensile strength observed in all the unmodified samples.

Figure 4.23(b) shows the microstructure of the same alloy, containing 0.8% Fe, also unmodified, but taken at the lowest cooling rate. Besides the aluminum matrix, the acicular Si particles and $CuAl_2$ phase, several additional features are noted:

i) The needle-like β-platelets are readily observed, as both the number and size of β-platelets are greater than that of the previous sample;

ii) The grain size and other microconstituents (silicon and $CuAl_2$) are larger than in the previous sample;

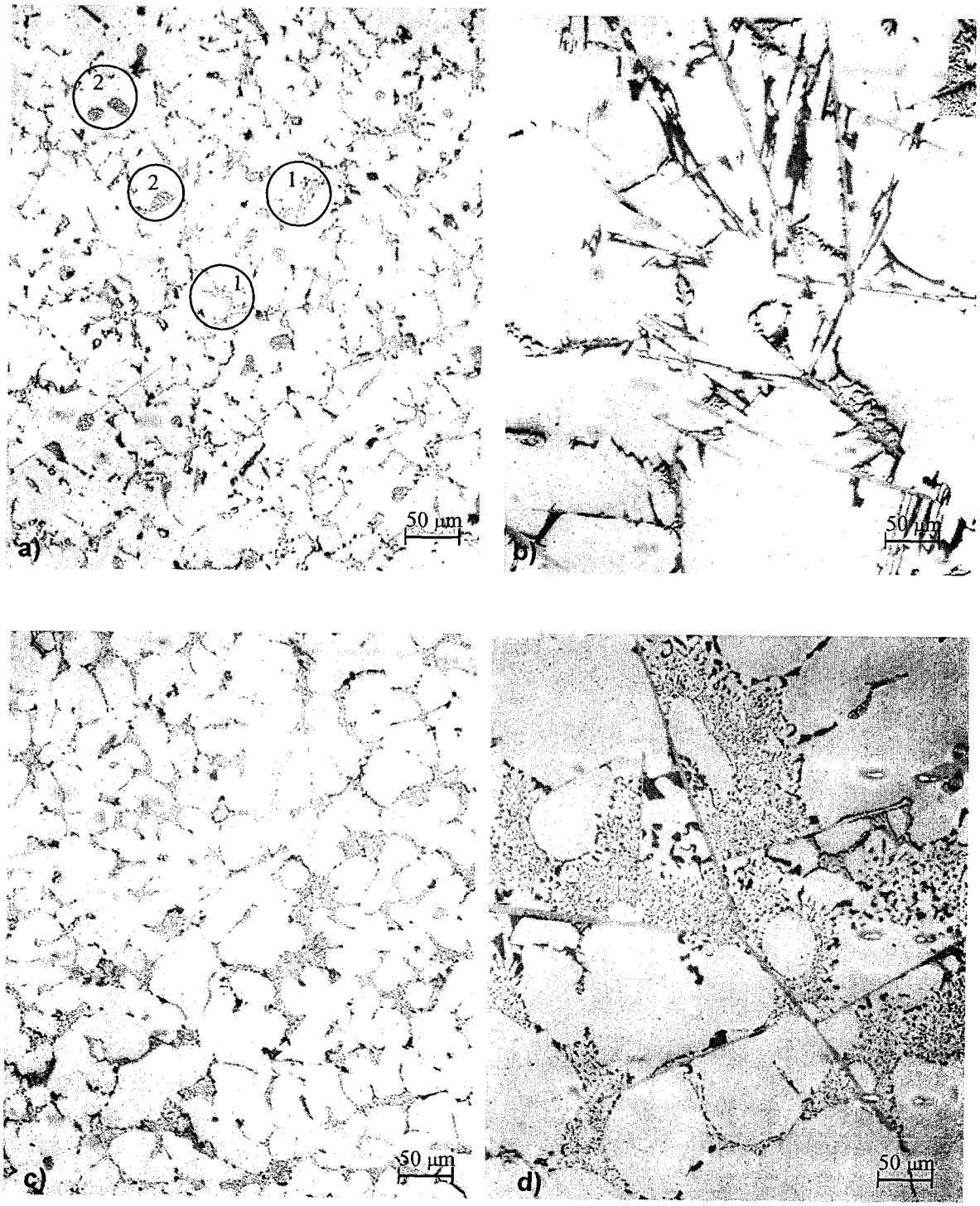

Figure 4.23. Optical microstructures of 319.2 alloy samples (Mag: 200× for all samples). (a) 0.4% Fe, DAS 23 µm, unmodified; (b) 0.8% Fe, DAS 83 µm, unmodified; (c) 0.4% Fe, DAS 23 µm, Sr-modified; (d) 0.8%Fe, DAS 83 µm, Sr-modified.

iii) Most of the $CuAl_2$ particles and many Si particles are seen to lie along the β-phase platelets, suggesting that β-platelets favor the formation of Si and $CuAl_2$ particles, and that most of them precipitate in a pre-eutectic reaction.

All of these features decrease the alloy resistance to fracture significantly, thus explaining the low ductilities and tensile strengths of these samples.

The microstructure of the Sr-modified 319.2 alloy sample containing 0.4% Fe and obtained at the highest cooling rate is shown in Figure 4.23(c). The most important difference observed regarding the unmodified alloy samples is the morphology of the Si particles. The fine, fibrous Si particles provide the higher ductility observed in these samples.

Figure 4.23(d) shows the microstructure of a modified 319.2 alloy sample, containing 0.8% Fe, and obtained at the lowest cooling rate. Compared to the corresponding unmodified sample, Figure 4.23(b), the fibrous eutectic silicon particles and fragmentation of the β-platelets due to Sr-modification can be observed, as indicated by the serrated surface instead of the faceted one. This provides an improvement in both ductility and tensile strength.

4.2.6.2 Alloy A356.2

Figure 4.24(a) gives the microstructure of an unmodified A356.2 alloy sample containing 0.1% iron (lowest level) and obtained at the highest cooling rate. The main phases observed here are the aluminum dendrites and the eutectic Si particles. Compared to the 319.2 alloy sample with medium iron content, the acicular Si particles in this case are

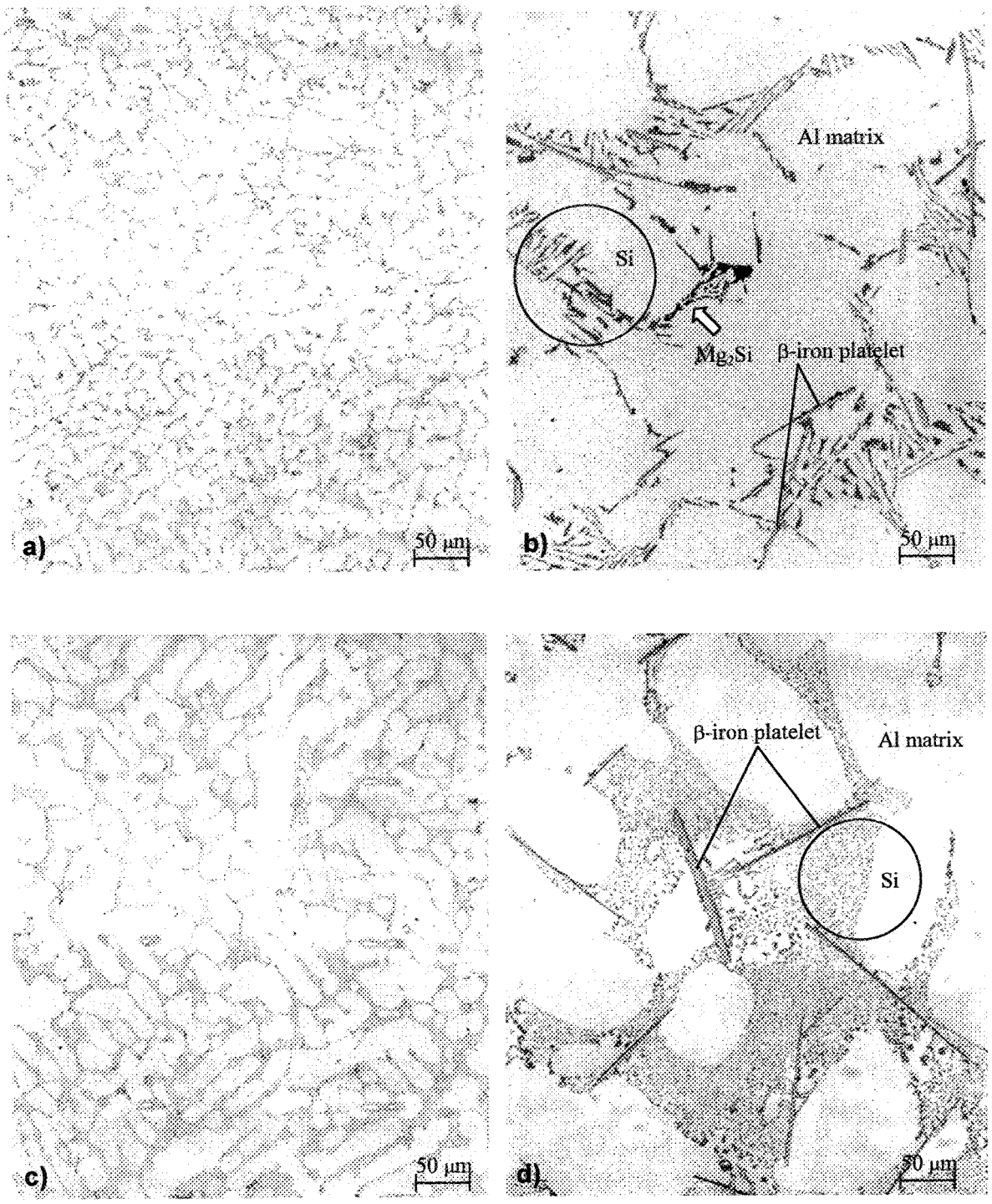

Figure 4.24. Optical microstructures of A356.2 alloy samples (Mag: 200× for all samples. (a) 0.1% Fe, DAS 23 μm, unmodified; (b) 0.6% Fe, DAS 75 μm, unmodified; (c) 0.1% Fe, DAS 23 μm, Sr-modified; (d) 0.6%Fe, DAS 75 μm, Sr-modified.

much finer and better distributed along the interdendritic boundaries. Due to the purity of the alloy (even if it is industrial) and the maximum cooling rate employed, the presence of other phases, including Mg_2Si is negligible, explaining the higher ductility and lower tensile strength of the sample.

The microstructure of an unmodified A356.2 alloy sample containing 0.6 wt% iron and obtained at the lowest cooling rate is shown in Figure 4.24(b). Compared to the previous micrograph, all the microconstituents, including the grain size of aluminum matrix, are much bigger. The large, acicular Si particles are distributed along the aluminum interdendritic boundaries; some are precipitated along the β-iron intermetallic platelets, observed as long needles all over the matrix. Their detrimental effect on the mechanical properties, particularly ductility, explains why this alloy exhibits the lowest ductility and tensile strength (lowest quality index). Some black Mg_2Si Chinese script particles are also observed (arrowed), due to the sufficient solidification time for their precipitation.

The microstructure of a modified A356.2 alloy sample taken at the lowest iron content and highest cooling rate is shown in Figure 4.24(c). Compared to the unmodified sample, Sr alters most of the Si particles from acicular to fibrous. The fibrous Si particles are better distributed along the interdendritic boundaries, and in larger areas. Thus, a better ductility is obtained upon Sr modification. However, as β-iron intermetallic and Mg_2Si particles are still not readily observed, no difference in tensile strength between the unmodified and Sr-modified conditions is observed.

The microstructure of the modified A356.2 alloy sample containing 0.6 wt% (highest) iron content and obtained at the lowest cooling rate is shown in Figure 4.24(d). Compared

to the unmodified condition, the most important feature is the change in morphology of the eutectic Si particles, from acicular to fully fibrous, which significantly increases the alloy properties. Long-sized β-platelets can still be observed. Although their sizes do not seem to decrease very much, from the unmodified to the modified condition transformation from β-Al_5FeSi to α-$Al_8Mg_3FeSi_6$ can be observed in certain cases.

Overall, to obtain the combination of high ductility and high tensile strength, or "quality" of the alloy, microstructure with small grain size (and consequently, small microconstituent sizes), fibrous Si particles, and small size and volume fraction of β-iron intermetallics are required. On the other hand, for a microstructure with a large grain size (and the microconstituents sizes, as well), acicular Si particles and large size and volume fraction of β-iron intermetallics yield poor quality, or a combination of both poor ductility and poor tensile strength.

CHAPTER 5

IMPACT PROPERTIES

CHAPTER 5

IMPACT PROPERTIES

5.1 INTRODUCTION

Impact energy normally means the total energy absorbed by a specimen in fracturing it when it is tested under high strain rate or rapid loading. Impact values depend strongly on the testing method used. The most common laboratory measurement of impact energy is the Charpy test. The impact energy from the Charpy test correlates with the area under the total stress-strain curve of Figure 2.2 shown in Chapter 2.

In the present study, a computer-aided Instrumented Charpy Impact test was employed, which provided the load-time information in addition to the energy absorbed. The instrumented test allows one to separate the energy absorbed into (1) the energy required to initiate fracture (designated E_I), called the *pre-maximum load energy*, (2) the energy required to propagate brittle fracture, or the *post-maximum load energy*, and (3) the energy associated with shear lip formation, or the *post-brittle fracture energy*, as illustrated in Figure 5.1. In most cases (including that of Al-Si alloys), the latter two join together and cannot be readily distinguished, as depicted by the "crack propagation impulse" area marked II in Figure 5.2, which is considered as the *crack propagation energy* (designated E_P). Thus, the impact energy is the sum of these three energies (as illustrated in Figure 5.1)

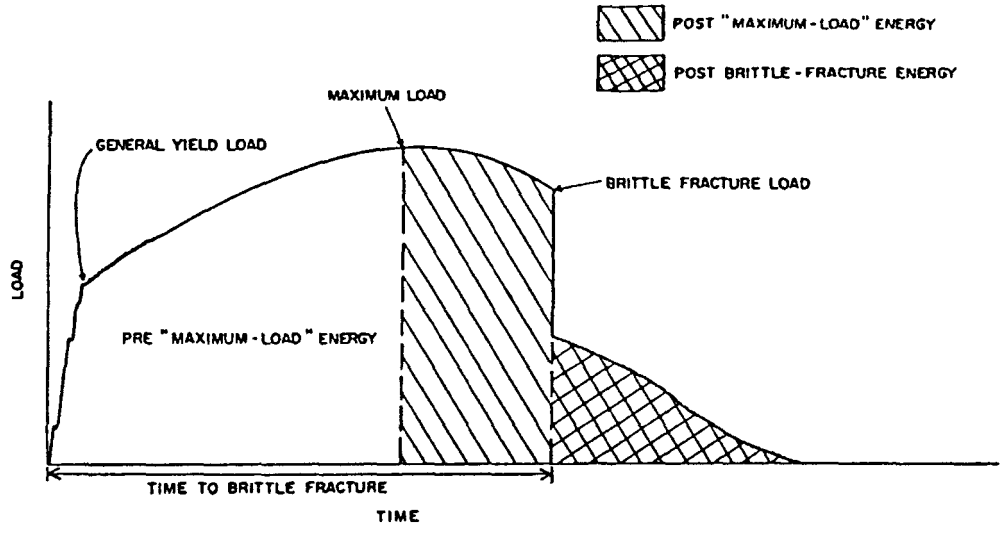

Figure 5.1. An idealized load-time trace for an impact Charpy V-notch specimen.[155]

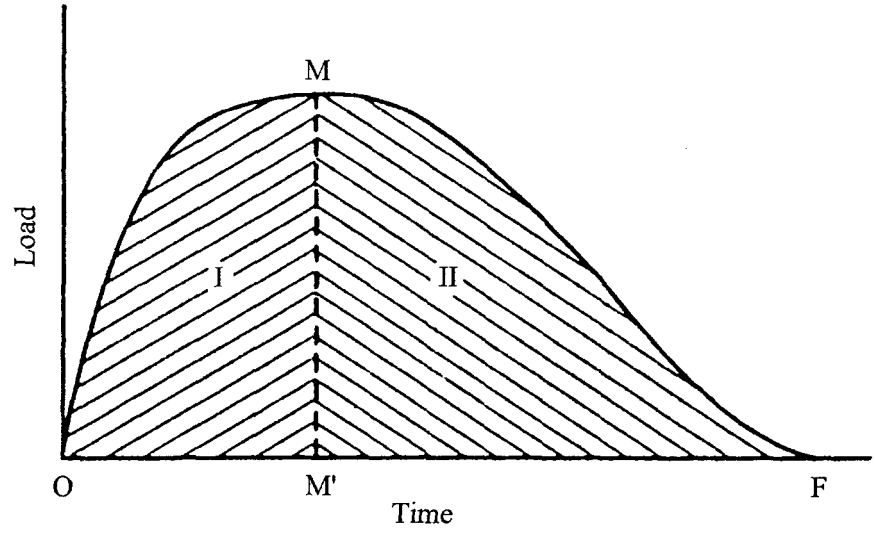

Figure 5.2. Schematic representation of relation between load and time in Charpy impact test. **M**: Maximum load; **I**: Crack initiation impulse; **II**: Crack propagation impulse; **OM'**: Crack initiation time; **M'F**: Crack propagation time.[72]

or the sum of the two energies (*viz.*, energy for crack initiation and energy for crack propagation) represented by the area under the load-time curve in Figure 5.2, or the *total energy* (designated E_T) in the present work. Impact energy is also strongly dependent on the

alloy microstructure, which is mainly controlled by the different alloying and melt processing parameters. The correlation between impact energy and the parameters of cooling rate, iron content, β-iron intermetallic size and porosity characteristics is the main focus of this chapter. In our study, Charpy unnotched samples were employed, in order to increase the accuracy of the measurement and to emphasize the effect of the microstructure. When a notch is present, the impact energy obtained is much lower than that obtained with an unnotched sample, and may be more dependent on the notch geometry than on the microstructure.[156] Such observations have been reported by other researchers in their studies on the impact properties of Al-Si cast alloys. Some of these studies will be reviewed briefly in the following sections, in the context of the alloy and microstructural parameters investigated in the present work.

5.1.1 Effect of Sample Configuration

Impact values depend strongly on the sample configuration, particularly when a notch is present, in which case the energy obtained will be much lower than that of an unnotched sample, and will be more dependent on the notch geometry, rather than on the microstructure. This will decrease the accuracy in evaluating the effect of alloying and melt processing parameters on the impact energy.

The impact energies of unnotched, U-notched and V-notched samples of 356 alloys were determined by Tsukuda *et al.*[157] Keeping all other parameters the same, the unnotched samples had much higher impact values than the notched samples. The U-notched samples possessed somewhat higher impact energies than the V-notched samples. The largest

improvements were observed on going from the V-notched to the unnotched samples; most of them being more than 200% (highest: 247%, lowest: 146%). Between the U-notched and V-notched samples, the former showed improvements of ~60% over the latter (highest: 65%, lowest: nil).

The difference between the load-time curves of ϕ-notch and U-notch specimens of Al-Si alloys from the work of Komatsu *et al.*[72] is shown in Figure 5.3. The configuration of the ϕ-notch specimens used in their study is shown in Figure 5.4, while the U-notch specimens were made according to JIS Z 2202 (No. 3) specifications. Higher energy can be obtained from the ϕ-notch specimen. Since the impact energy of Al-Si alloys is quite low compared to that of steel samples, it is reasonable to employ samples which can provide higher values and thus facilitate the analysis with respect to alloying and melt processing parameters.

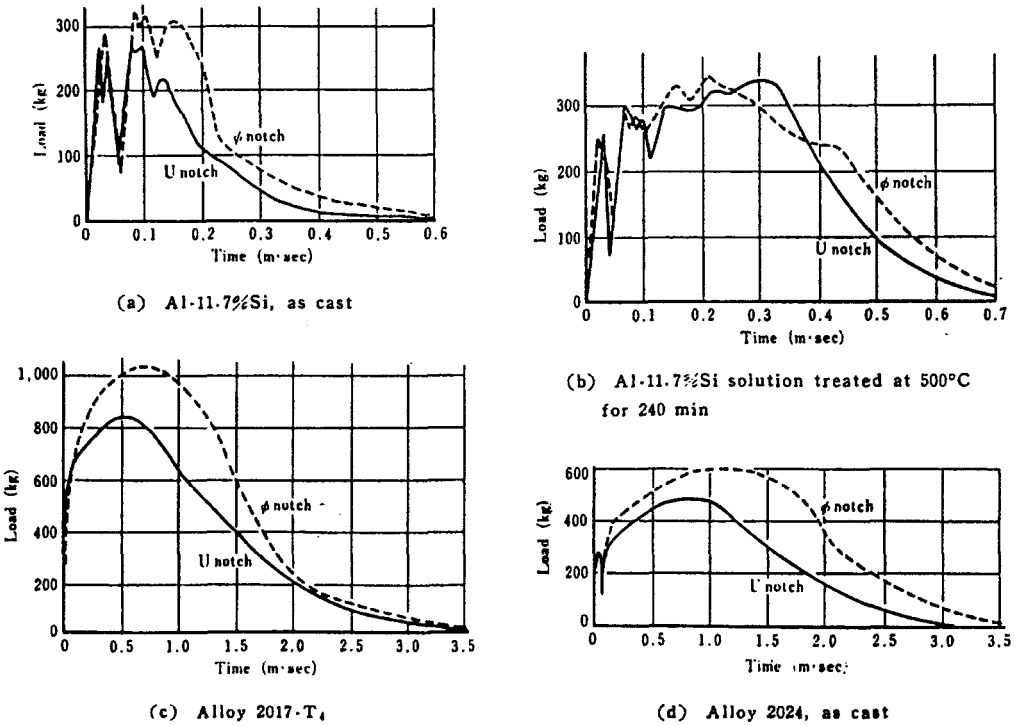

Figure 5.3. Load-time relationship for ϕ-notch and U-notch specimens.[72]

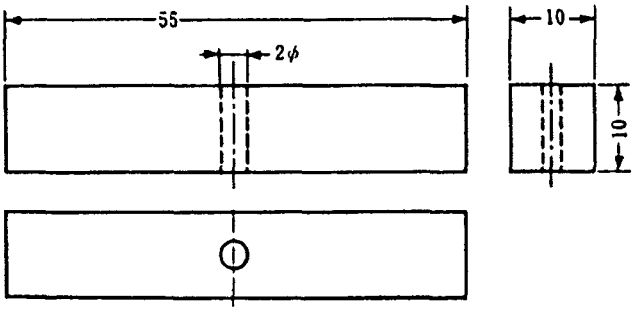

Figure 5.4. Dimensions of Charpy test specimens (mm).[72]

A comparison between impact energies obtained from Charpy V-notch (same as Charpy single beam specimen type A, ASTM E23[135]) and Mesnager (Charpy specimen type C, ASTM E23[135], but with possibly different depth) samples was conducted by Richard.[158] The latter type generally yielded higher values, and an impact energy correlation between the two sample types in aluminum alloys was obtained as follows:

$$E_{Mesnager} = 1.6 \times E_{Charpy} + 0.3 \qquad (5\text{-}1)$$

with $E_{Mesnager}$ being expressed in J/cm^2, and E_{Charpy} in J units of energy.

In North America, ASTM E23[135] samples are the most commonly employed for impact testing. The dimensions of such samples are the same as that of the unnotched samples used in the present work (shown in Figure 3.3 in Chapter 3), except for the notch configuration. With the notched Al-Si alloy samples used by Shivkumar *et al.*,[159,160] very low impact energies were obtained in their work compared to those obtained under the same conditions by Paray *et al.*[156] who used unnotched samples instead (*cf.* 7.8 J with 15.12 J for unmodified 356 alloys, and 13.1 J with 22.82 J for modified 356 alloys). As unnotched samples were employed in our study, higher impact energies were also expected to be obtained.

5.1.2 Effect of Cooling Rate

Cooling rate has a direct effect on the size and distribution of microstructural phases obtained in a casting. Consequently, it should have a direct effect on the impact energy, as well.

Hotta *et al.*[161] studied the impact energy of AC4C (356) and AC2B (B319) alloys under different cooling rate conditions (*viz.*, different solidification times), in as-cast and T6 heat-treated conditions. The results for the T6 heat-treated alloys are shown in Figure 5.5. It is very clear that, with the decrease in solidification time (*i.e.*, increase in cooling rate), the impact energies increase correspondingly. Castings that have solidified in 700 to 800 sec possess impact energies less than half that of castings solidified in 20 sec. This is attributed to the coarsening of the eutectic compounds and an increase in the grain size and microporosity observed with the increase in solidification time.

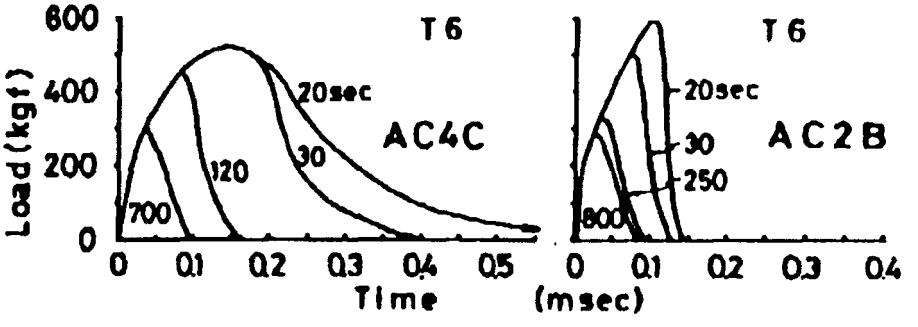

Figure 5.5. The effects of solidification time on the load-time relations in AC4C (356) and AC2B (B319) alloys (T6 treatment).[161]

Hafiz and Kobayashi[162] also compared the impact energies of eutectic Al-Si alloy samples obtained at different cooling rates, using two different mold types (steel and graphite) for casting. The impact energy values obtained at high cooling rates (steel mold)

were superior to those obtained at low cooling rates (graphite mold) for the same Sr contents, as can be seen from Figure 5.6. According to the authors, high cooling rates scale down the dimensions of the Si particles (not their shape or arrangement), which reduces the amount of primary Si in the matrix, leading to an increase in the amount of Al-dendrites.

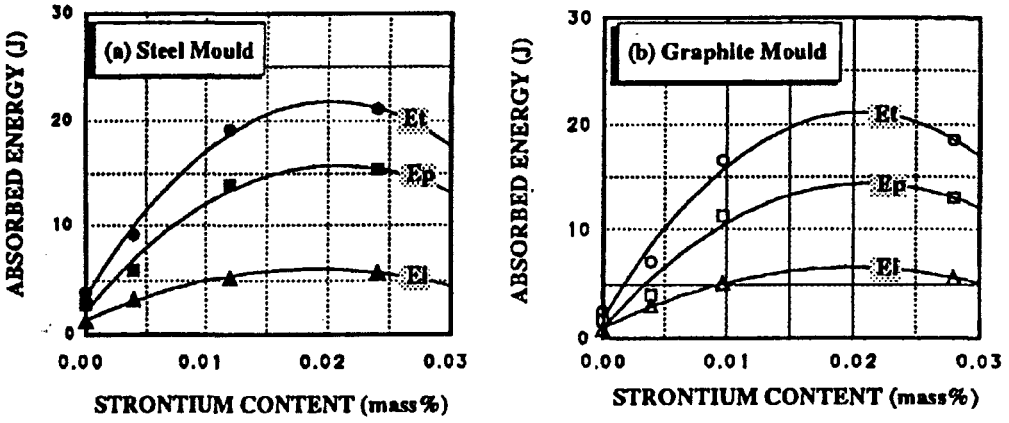

Figure 5.6. Impact toughness of eutectic Al-Si alloy as a function of Sr-content and solidification cooling time.[162]

Shivkumar *et al.*[159,160] investigated the impact energy of 319 and 356 alloys, employing two different cooling rates (sand mold and water-cooled copper mold), T6 heat treatment (with varying solution heat treatment times) and different test temperatures. The results of the samples solution heat-treated for 8 h, and impact-tested at room temperature (conditions similar to the present study) showed that the impact energies obtained at the higher cooling rate were higher in both 319 (*cf.* 0.88 J with 0.74 J for the unmodified, and 1.80 J with 1.36 J for the Sr-modified samples) and 356 (*cf.* 7.8 J with 1.4 J for the unmodified, and 13 J with 3 J for the Sr-modified samples) alloys. Such differences result from the much finer silicon particles obtained in the water-cooled copper mold casting compared to those

in the sand mold casting. This refinement of silicon at high growth rates is often referred to as "quench modification" and results from a change in the molecular attachment kinetics.[163]

Similar observations were made by other researchers,[156,158,164-166] where the different cooling rates were variously achieved by using different molds with the same dimensions, or the same mold type with different dimensions, or by using a mold that provided directional solidification, similar to the case in the present study.

Compared to tensile properties, cooling rate has a more significant influence on impact properties, *viz.*, impact energy is more sensitive to microstructural changes than are the tensile properties. According to Richard,[158] small variations in microstructure influence impact energy more than elongation. The presence of microconstituents in the form of platelets (*e.g.*, the eutectic Si particles), and their effect on the sample notch, degrade impact energy more than elongation. Tsukuda *et al.*[164] also reported that impact energies of Al-Si alloys were more sensitive to the as-cast microstructure than the tensile properties.

5.1.3 Effect of Iron Content

The work of Komastu *et al.*[72] shows that iron imparts a detrimental effect to the impact strength of Al-Si alloys due to the formation of Al-Si-Fe compounds. The results are depicted in Figures 2.11 and 5.7. With the increase in iron content, both the size and amount of the needle-like Al-Si-Fe compounds increase. The morphology and distribution of these undesirable constituents are not changed by solution heat treatment at 500 °C, resulting in low impact energy values, similar to that obtained in the as-cast condition when the iron level exceeds 1.5%. Another interesting result is that in the heat-treated condition,

the impact values of pure Al-Si alloys are lower than those of Al-Si alloy with 0.13% iron, as can be seen from Figure 5.7.

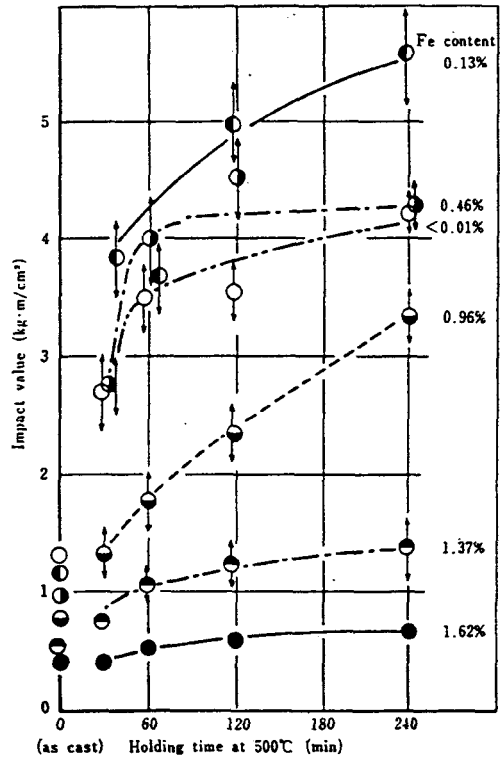

Figure 5.7. Impact value *vs.* holding time at 500 °C for Al-11%Si alloys containing Fe.[72]

The effect of iron on the mechanical properties of Al-Si-Mg cast alloys was investigated by Tsukuda *et al.*[167] It was found that increasing the iron from 0.1 to 1.90% in an Al-7%Si-0.23%Mg alloy reduces the impact strength exponentially, due to the increase in the size and volume fraction of the needle-like iron compounds, particularly when the iron was more than 0.73%, when primary iron compounds also appeared.

Nishi and Kobayashi[168] studied the impact behavior of various basic aluminum casting alloys. Among them, Al-Cu-Si alloys (AC4B) were found to have the lowest impact values

due to the acicular eutectic Si and the hard iron secondary phase particles present in the structure (further details are elaborated in section 5.1.5, under the effect of alloy type).

5.1.4 Effect of Modification

The main aim of modification is to alter the morphology and distribution of the eutectic Si particles, in order to improve the mechanical properties. Another important purpose is to neutralize the detrimental effect of the plate-like iron intermetallics and further improve the mechanical properties.

Kato *et al.*[169] compared the effect of various modifier elements, *i.e.*, Na, Sb, Sr and Li, on the fatigue and impact properties of Al-Si casting alloys. The chemical composition of the alloy and the amounts of modifier elements used are listed in Table 5.1.

Table 5.1. Chemical compositions of the modified Al-Si-Mg-Fe alloys used in the work of Kato *et al.*[169]

	Si	Mg	Fe	Na	Sb	Sr	Li	Al
Na-treated	7.08	0.23	0.17	0.01	--	--	--	bal
Sb-treated	7.14	0.22	0.15	--	0.12	--	--	bal
Sr-treated	7.05	0.23	0.16	--	--	0.015	--	bal
Li-treated	6.94	0.24	0.17	--	--	--	0.16	bal

From quantitative analysis, the roundness factor of the eutectic Si particles was about the same for each modifier element in the T6-treated alloys, but the particle sizes differed, and were largest for the Li-modified alloy, followed by the Sr-modified alloy, and smallest for the Sb- and Na-treated alloys. Impact energy was influenced by the morphology of the eutectic Si particles, depending on the modifier used. The eutectic Si particles of the Sb-

modified alloy were more spherical, followed by those treated with Sr, Na and Li, and the impact values also ranged (from highest to lowest) in that order. Similarly, the modification effects of Na, P and Sb have also been studied to some extent in other investigations.[72,164] An example of eutectic modification using Na and P is given in Figure 5.8.

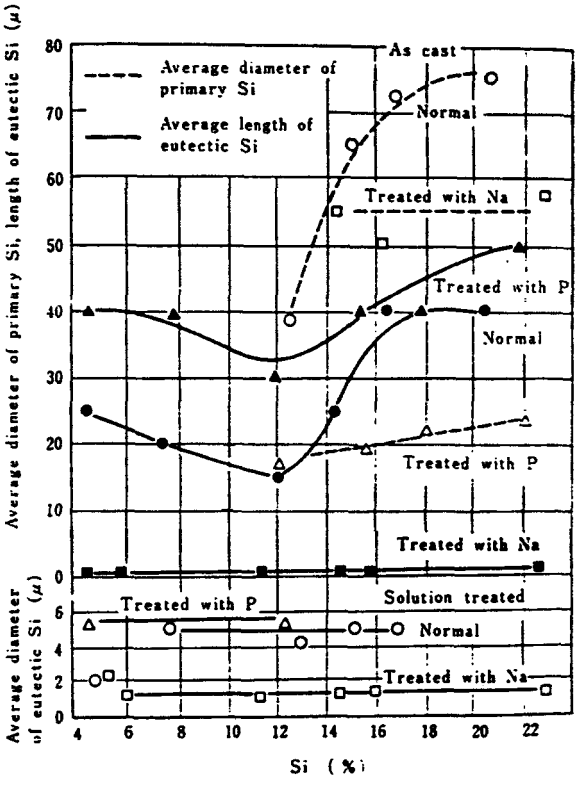

Figure 5.8. Eutectic modification effect of Na and P in Al-Si alloys.[72]

Among all the elements used for modification, Sr is the one most commonly employed in Al-Si alloys, and has been extensively investigated over the last three decades.[1] Shivkumar *et al.*[159,160] studied the impact properties of 319 and 356 alloys in the as-cast and Sr-modified conditions. They found that, in 319 alloys, while Sr refines the eutectic Si and the Fe- and Cu-rich phases in the interdendritic regions, only the Si particles undergo a

major morphological change, from coarse, branched and interconnected flakes to a connected, fibrous structure. Similar observations were noted for the 356 alloys. In both alloys, the effects of modification were more significant at low cooling rates. The iron and copper contents were not discussed in detail in their work.

Hafiz and Kobayashi[162] also pointed out that in eutectic Al-Si alloys, the improvement in impact energy with modification depends not only on the Sr level, but also on the cooling rate during solidification. A low Sr level (~0.0044 mass%) is insufficient for achieving complete modification. The under-modified structure is comprised of areas of fibrous and lamellar eutectic Si. With an increased amount of Sr, primary Si is eliminated, the primary Al-rich phase is increased, and finely distributed Si is observed throughout the eutectic matrix. Thus, while fast cooling rates provide superior impact energies, the toughness of the low cooling rate samples is improved to a large extent with modification.

5.1.5 Effect of Alloy Type

As different alloys exhibit different microstructures, it is natural to expect that their impact energies will also differ, depending on the type and amount of microconstituents and defects present in the latter.

Nishi and Kobayshi[168] carried out instrumented Charpy impact tests on basic aluminum casting materials such as pure aluminum, Al-Si (eutectic), Al-Cu-Si (380) and Al-10%Mg (wrought) alloys, the chemical compositions of which are shown in Table 5.2. According to them, the impact values varied (starting from the highest) in the following order: pure aluminum >> Al-Si (Na-modified) > Al-Si (non-modified) > Al-Mg ≈ Al-Cu-Si, as

depicted in Figure 5.9. One important reason for the low impact value of the Al-Cu-Si alloy was its high iron content, compared to the other alloys.

Table 5.2. Chemical compositions of alloys used for impact testing by Nishi and Kobayashi[168]

Alloy	Composition (wt%)							
	Cu	Si	Mg	Zn	Fe	Mn	Ni	Ti
99.0 Al	0.002	0.08	0.010	0.010	0.15	0.001	0.005	0.003
Al-Si	--	12.92	0.008	--	0.14	--	--	--
Al-Cu-Si	3.53	9.25	0.008	--	0.44	--	--	--
Al-Mg	0.003	0.14	10.00	0.019	0.13	--	0.005	0.004

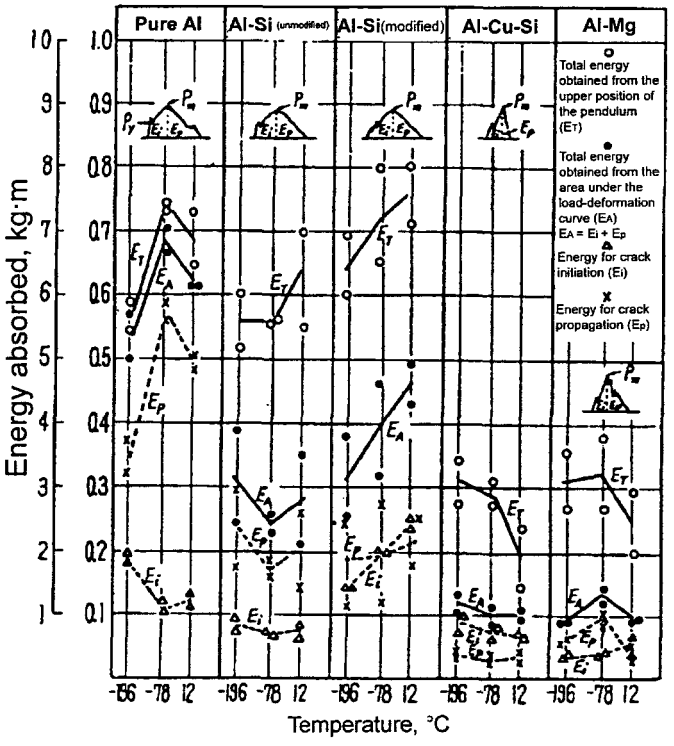

Figure 5.9. Energies absorbed during impact tests for various alloys (a lager size scale was used for pure aluminum).[168]

In the studies of Shivkumar *et al.*[159,160] on 319 and A356 alloys, the dendrite arm spacings (DASs) obtained in the two alloys using the same mold did not differ much, as can be seen from Table 5.3. However, the A356 alloys had higher impact energies than the 319 alloys under the same conditions (as-cast or T6). According to them, A356 is generally considered to be a relatively pure alloy with strict limits on impurity concentrations such as that of Fe, whereas in 319 alloys the iron level can be much higher (*cf.* ~0.2% max in A356 with ~0.85% in 319). Thus the impact energy or toughness of 319 alloys is limited by the Fe-containing intermetallic phases.

Table 5.3. Impact energy data obtained by Shivkumar *et al.* [159,160] for 319 and A356 alloys

Alloy	Sand mold						Water-cooled copper mold					
	Unmodified			Sr-modified			Unmodified			Sr-modified		
	DAS (μm)	Condition	E_T (J)	DAS (μm)	Condition	E_T (J)	DAS (μm)	Condition	E_T (J)	DAS (μm)	Condition	E_T (J)
319	50	As-cast	**0.63**	49	As-cast	**1.36**	22	As-cast	**0.68**	22	As-cast	**2.0**
		T6	**0.74**		T6	**1.36**		T6	**0.88**		T6	**1.80**
A356	48	As-cast	**1.1**	47	As-cast	**2.3**	24	As-cast	**2.0**	23	As-cast	**10.8**
		T6	**1.4**		T6	**3.0**		T6	**7.8**		T6	**13.1**

Similar studies were carried out by Paray *et al.*[156] on Al-Si foundry alloys, where the iron contents in their 356 and 319 alloys were 0.11% and 0.42%, respectively. They attributed the relatively low impact energies of the 319 alloys (compared to 356) to their different fracture behavior: in the 356 alloy, fracture behavior is controlled by the amount, size and morphology of the brittle eutectic Si particles, while in the 319 alloy, it is controlled by the $CuAl_2$ phase. The presence of copper appears to alter the fracture

behavior of the Al-Si alloy significantly. This appears to be reasonable, for the same iron content, the 356 alloy (AC4C) still possesses a higher impact energy than the B319 alloy (AC2B), as reported by Hotta *et al.*[161]

5.2 IMPACT TEST RESULTS OBTAINED IN THE PRESENT STUDY

Impact tests were carried out on industrial 319 and 356 alloy samples obtained from specimens sectioned at the heights of 10, 30, 50 and 100 mm above the chill end of each casting (referred to as levels 1, 3, 5 and 10, respectively, or by the corresponding DASs shown in Table 4.7 in Chapter 4). All the samples were T6-heat-treated in keeping with Aluminum Association recommendations. For each sample, the load, deflection and energy data were recorded automatically with respect to the corresponding time (time interval: 0.01 msec). From these, the load-time and energy-time curves, total energy (E_T), and the energies for crack initiation (E_I) and crack propagation (E_P) could be obtained for each sample.

Average crack speed is a useful parameter to characterize the crack propagation phenomenon. In the current study, this was defined as the sample width divided by the total time that elapsed from the moment the load was exerted to the moment it was removed. A correlation between average crack speed and iron content will be presented in this chapter.

As the total energy (E_T) is normally taken to represent the impact energy, this parameter will be mainly used to discuss the alloy impact properties in relation to the different alloying and melt processing parameters, *viz.*, iron content, strontium modification, cooling rate, iron intermetallic size and porosity, as was done for the tensile

properties. Relationships between the impact energy and tensile strength and ductility for the two alloys will also be presented.

5.2.1 Load-Time Curve and Average Crack Speed

A typical load-time curve obtained from the present work is illustrated in Figure 5.10, where the curve for the corresponding energy absorbed with respect to time has also been plotted. This plot was recorded from one of the Sr-modified A356.2 alloy samples with the lowest iron content, and obtained at the highest cooling rate (smallest DAS). As expected, this sample exhibited the highest impact energy among all the samples tested.

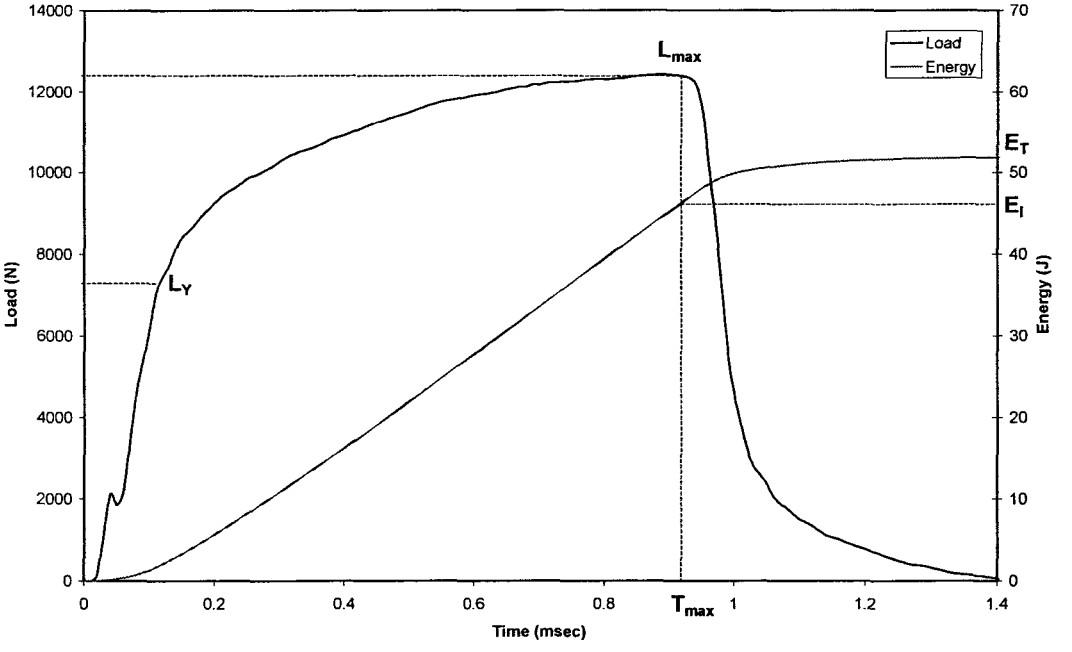

Figure 5.10. Load-time and energy-time curves of an A356.2 alloy sample (0.0937% Fe, 250 ppm Sr, DAS 23 μm) obtained in the present work.

The relative shape of the load-time curve is indicative of the deformation and fracture history of the test specimen. The initial rise, when the load varies linearly with time,

corresponds to the elastic regime (up to the yield load L_Y). The first load fluctuation on the curve (near ~2000 N) is caused by the inertial loading of the *tup* (striking edge of the pendulum) due to the acceleration of the specimen from its rest position,[156] and hence is not considered when analyzing the results. At higher loads, prior to the maximum load L_{max}, the specimen deforms plastically, while after L_{max}, the load decays, indicating a controlled crack propagation. Correspondingly, the energy absorbed by the specimen up to L_{max} is the crack initiation energy, E_I, and that after L_{max} is the crack propagation energy, E_P. The latter is generally determined from the difference between E_I and the total energy, E_T.

Comparing the actual load-time curve in Figure 5.10 with the schematic representation shown in Figure 5.2, it is obvious that in this particular case, the time interval, T_{max}, between zero load (load initiation) and maximum load (L_{max}) is longer than that between T_{max} and the point where the load returns to zero (load removed). In other words, more time is required for crack initiation than for crack propagation. Figure 5.10 shows that, when the load is first exerted on the sample, the yield point (L_Y) is reached in a very short time (~0.12 msec), following which, a much longer time (~0.78 msec) is needed to reach the maximum load (plastic deformation). The energy absorbed by the sample mainly occurs within this time. After that, only about 0.5 msec is required for the crack to propagate through the sample till the final fracture, where a major part of the propagation energy, E_P, is absorbed during a very short time interval (~0.11 msec). Thus, for the sample shown in Figure 5.10, the initiation energy is much higher than the propagation energy.

The average crack speed with respect to iron content, cooling rate and Sr-modification is shown in Figures 5.11(a) through 5.11(c) for the three alloys. The crack speed values

plotted in these figures were selected from samples which corresponded to the extreme ends of the iron and cooling rate range conditions tested (*i.e.*, lowest *vs.* highest), and in the Sr-modified and unmodified conditions. In all the alloys, over the selected conditions, the highest crack speeds were usually obtained from the samples with the highest iron contents, lowest cooling rates, and in the unmodified condition. These samples possessed the lowest impact energies. Some exceptions were found in the 319 alloys with respect to iron level and Sr modification. A decrease in crack speed with increase in iron content was observed in the Sr-modified, low-cooling rate samples of both alloys A and B. These results will be used qualitatively to supplement the analysis of the impact energy results in the sections to follow.

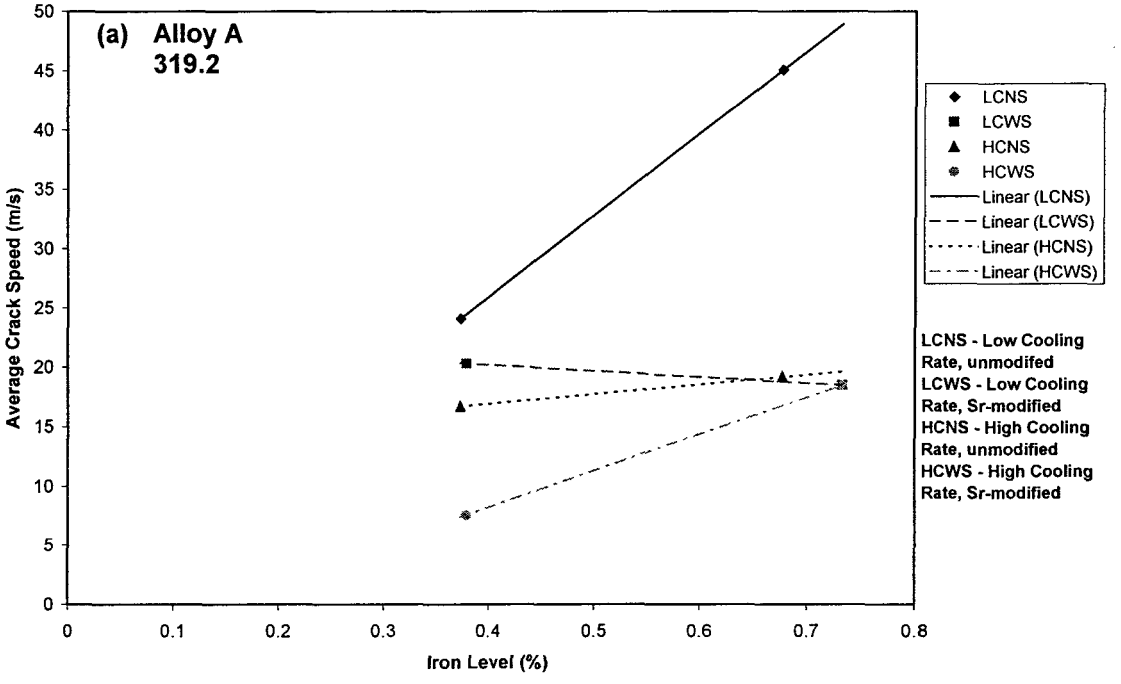

Figure 5.11. Average crack speed as a function of iron, cooling rate and Sr modification in: (a) 319.2, (b) B319.2, and (c) A356.2 alloys.

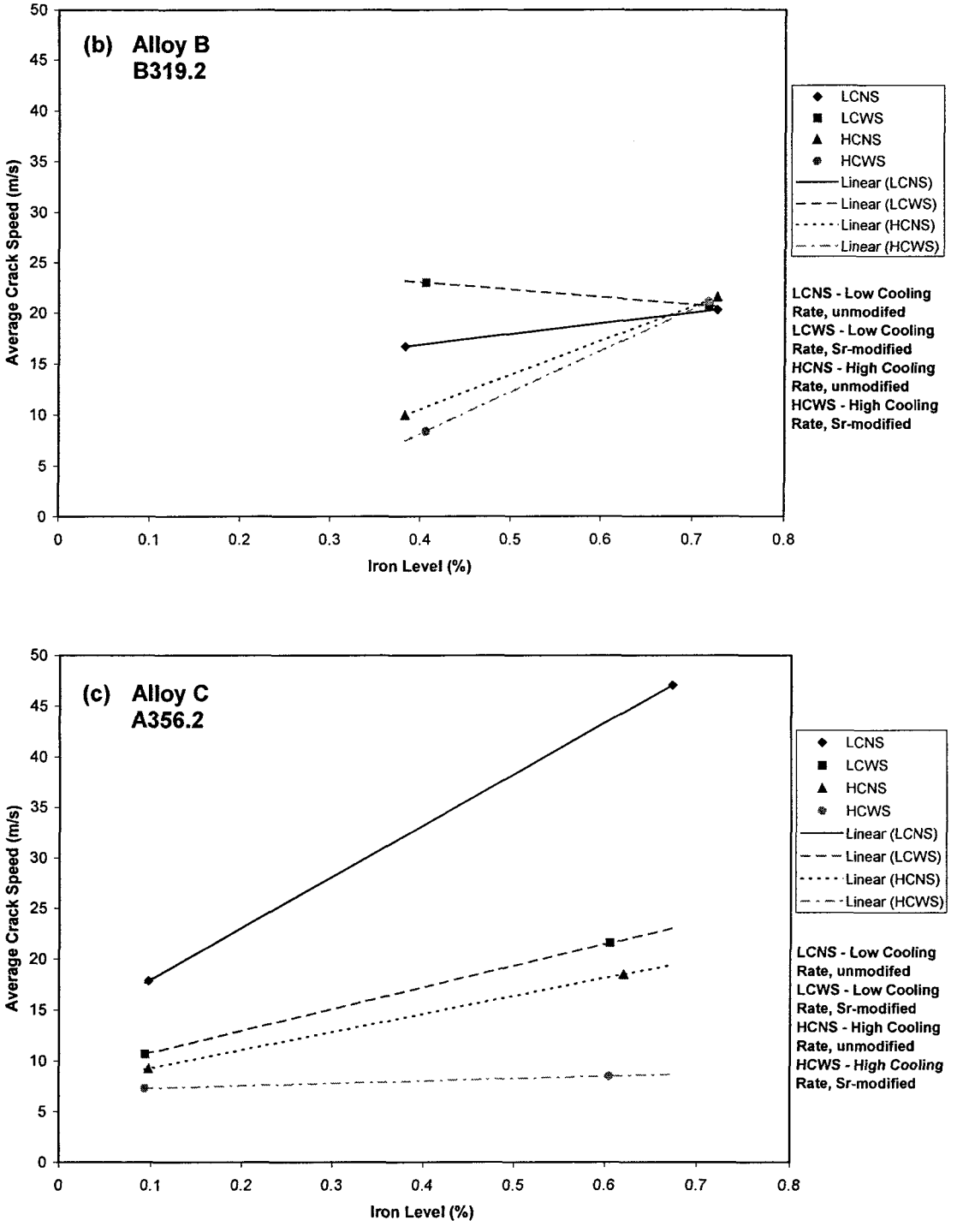

Figure 5.11. Average crack speed as a function of iron, cooling rate and Sr modification in: (a) 319.2, (b) B319.2, and (c) A356.2 alloys.

5.2.2 Effect of Cooling Rate and Iron Content

Tables 5.4 through 5.6 summarize, respectively, the impact test data obtained for the 319.2, B319.2 and A356.2 alloys, while Figures 5.12 to 5.14 depict the effects of the cooling rate (in terms of the different DAS values) and iron content on the impact energy (E_T) obtained for the unmodified and Sr-modified alloy samples in each case.

5.2.2.1 Alloy 319.2 (alloy A)

A decrease in impact energy with respect to an increase in iron content and decrease in cooling rate was observed in alloy 319.2, both in the non-modified and Sr-modified conditions, as seen from Table 5.4 and Figure 5.12, which is in accordance with the results of other researchers.[156,159] Clearly, the highest cooling rate (DAS 23 μm) gives much better values in the unmodified and Sr-modified conditions than any other cooling rate. At the lowest iron content, the impact energies obtained at the highest cooling rate (DAS 23 μm)

Table 5.4. Summary of impact test data for alloy 319.2

Iron Content (%)	Sr Addition	Impact Energy (J)											
		DAS 23 μm (Level 1)			DAS 47 μm (Level 3)			DAS 60 μm (Level 5)			DAS 83 μm (Level 10)		
		E_I	E_P	**E_T**	E_I	E_P	**E_T**	E_I	E_P	**E_T**	E_I	E_P	**E_T**
0.373	No	7.64	4.76	**12.40**	4.17	0.71	**4.88**	2.75	1.64	**4.39**	1.40	2.19	**3.59**
0.379	Yes	16.39	14.57	**30.96**	8.52	2.83	**11.35**	5.64	1.46	**7.10**	2.86	1.46	**4.32**
0.564	No	6.63	1.92	**8.55**	1.65	1.38	**3.03**	1.23	1.37	**2.60**	1.38	1.17	**2.55**
0.556	Yes	9.05	4.48	**13.53**	4.79	0.76	**5.55**	3.40	1.69	**5.09**	1.32	2.38	**3.70**
0.677	No	5.51	0.79	**6.30**	1.64	1.03	**2.67**	1.32	0.91	**2.23**	1.30	0.60	**1.90**
0.733	Yes	8.71	1.31	**10.02**	3.29	0.55	**3.84**	2.10	1.33	**3.43**	1.63	1.43	**3.06**

E_I: energy for crack initiation; E_P: energy for crack propagation; E_T: total energy.
Sr is in the range of 150-230 ppm.

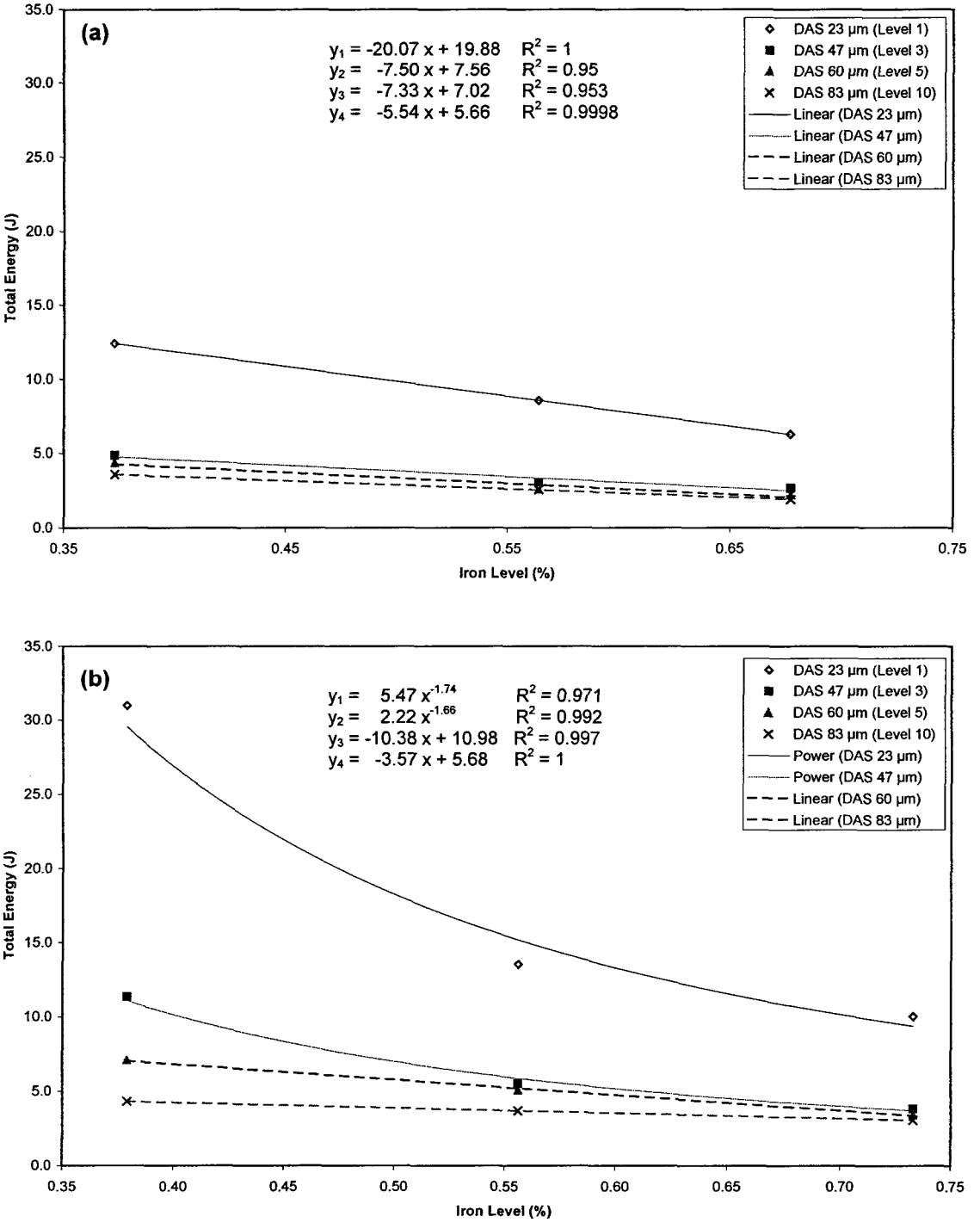

Figure 5.12. Total energy *vs.* cooling rate and iron content in: (a) unmodified and (b) Sr-modified 319.2 alloys.

are about 2.5 and 2.7 times those obtained at the next cooling (DAS 47 μm) in the unmodified and Sr-modified alloys, respectively. Even at the highest iron content, the same holds true.

Apparently, the impact energy is very sensitive to the cooling rate above a certain threshold, with the corresponding DAS representing the fineness of the microstructure and constituents at this cooling rate. Other workers, *e.g.*, Richard[158] and Tsukuda *et al.*[164] have also reported on the sensitivity of impact strength to the as-cast microstructure and to very small variations therein. In the present study, this threshold value appears to correspond to a DAS value of 23 μm, or thereabouts.

The DAS values listed in Table 5.4 are very close to those obtained from the water-cooled copper mold and sand mold castings used in the work of Shivkumar *et al.*[159] (see Table 5.3), allowing us to compare our results with theirs (for similar iron levels). In their work, the impact energy values of 319 alloy castings obtained from sand and copper molds were 0.74 J and 0.88 J in the unmodified condition, and 1.36 J and 1.8 J in the Sr-modified condition, respectively (*cf.* 2.67 J and 6.30 J in the unmodified alloy, and 3.84 J and 10.02 J in the modified alloy in the present work). An improvement with an increase in cooling rate was also observed, although the amount of improvement was smaller than that noted in the present case, due to the different type of test specimens used in their studies, as discussed previously. With notched samples (used by Shivkumar *et al.*[159]), it is very natural to obtain lower impact energy values than with the unnotched samples used in our case, explaining the smaller increments observed in their work with respect to the cooling rate. Another possible reason could be attributed to the higher iron levels used in their work. However,

this would be more of a secondary concern since, after a certain iron level (*viz.*, certain size of iron-intermetallics), the difference in impact values with a further increase in iron content is not very apparent. This point will be discussed more specifically in relation to the effect of the β-Al_5FeSi iron intermetallic phase in Section 5.2.3.

As Table 5.4 and Figure 5.12 show, the differences in impact energy at DASs greater than 23 μm are not very significant. An analysis of the plots in Figure 5.12 shows that the impact energy of the unmodified alloys exhibit linear relations with Fe content at all DAS levels, whereas in the Sr-modified alloys, linear relations are exhibited only at the coarser DASs, with the smaller DASs showing power relations. The respective relations and their corresponding R^2 values are listed in each plot.

The nature of these plots shows that, of the possible factors that influence the impact energy, the cooling rate is the most important; particularly at low Fe levels. At cooling rates corresponding to DASs of 47 μm and above, the impact energy remains more or less the same, and is only very slightly affected by an increase in Fe content, Figure 5.12(a).

As the cooling rate decreases and the iron content is increased, the size of the β-iron intermetallics plays an increasingly important role since it increases much more rapidly under these conditions, whereas both the size and morphology of the Si particles do not change considerably unless the alloy is modified. Also, after the intermetallics have attained a certain size, it is very easy to fracture the sample through the β-iron platelets. Consequently, the impact energies at the lower cooling rates and at intermediate and high iron contents at these cooling rates exhibit only marginal differences.

Addition of Sr, Figure 5.12(b), considerably enhances the already high impact energies observed at the 23 μm DAS level, and is also seen to separate the impact energy curves at larger DASs, indicating its refining effect on the microstructure, and in particular, the Si particles; hence the observed improvements in impact energy. The beneficial effect of Sr modification is again most noticeable at low Fe levels, where the refinement of the Si particles is maximized and the effect of the β-iron platelets is minimized. As before, the impact energy attains its minimum value when the Fe content is as high as 0.8%. In such cases, modifying 319.2 alloy with Sr will serve no purpose, and the only means to increase the impact toughness is through the use of high cooling rates.

Therefore, optimum impact properties of 319.2 alloys can be achieved by (a) keeping the Fe level minimum (< 0.4%), (b) modifying the alloy with strontium (in the range of ~200 ppm), and (c) employing suitable cooling rates capable of providing microstructures with a fineness in the order of ~23 μm DAS or thereabouts (but definitely lower than ~40-45 μm).

While the most common purpose of Sr addition is to modify the eutectic Si particles, *i.e.*, refine their size and change their morphology from plate-like to fibrous, the action of Sr on the fragmentation and dissolution of the β-Al_5FeSi plate-like phase also takes place at the same time. These two aspects are beneficial to the alloy properties in that in both cases, the properties are enhanced as a result of the modification. However, a third, not so beneficial, aspect also appears, particularly in the case of Al-Si-Cu alloys, where the presence of Sr causes segregation of the $CuAl_2$ intermetallic phase in areas away from the eutectic Si regions. This results in the copper-phase precipitating more in its block-like

form than in its finer eutectic-like form. The block-like $CuAl_2$ particles are much harder to dissolve in the matrix even after heat treatment, and so provide other crack-initiation sites in addition to those of the brittle β-Al_5FeSi iron intermetallic platelets. Paray *et al.*[156] have suggested that in copper-containing alloys such as 319 and 332, the fracture behavior is controlled by the $CuAl_2$ particles rather than by the Si particles.

5.2.2.2 Alloy B319.2 (alloy B)

The impact data obtained for the B319.2 alloy is provided in Table 5.5 and plotted in Figure 5.12. In comparison to the 319.2 alloy, this high-Mg version of the alloy shows that the impact energies in both unmodified and Sr-modified alloys follow power relationships with respect to the iron contents at all cooling rates.

Table 5.5. Summary of impact test data for alloy B319.2

Iron Content (%)	Sr Addition	Impact Energy (J)											
		DAS 23 μm (Level 1)			DAS 47 μm (Level 3)			DAS 60 μm (Level 5)			DAS 83 μm (Level 10)		
		E_I	E_P	**E_T**	E_I	E_P	**E_T**	E_I	E_P	**E_T**	E_I	E_P	**E_T**
0.383	No	24.58	2.20	**26.78**	8.07	1.87	**9.94**	6.00	1.68	**7.68**	3.16	1.27	**4.43**
0.406	Yes	31.96	2.25	**34.21**	11.57	1.51	**13.08**	7.75	1.83	**9.58**	4.86	1.53	**6.39**
0.535	No	10.08	1.56	**11.64**	3.48	1.20	**4.68**	2.18	1.17	**3.35**	1.80	1.24	**3.04**
0.526	Yes	11.56	1.76	**13.32**	3.61	1.16	**4.77**	2.66	1.26	**3.92**	1.64	1.16	**2.80**
0.727	No	6.18	1.40	**7.58**	1.89	0.91	**2.80**	1.61	0.92	**2.53**	1.32	1.32	**2.64**
0.718	Yes	6.32	1.24	**7.56**	2.57	1.05	**3.62**	1.81	1.01	**2.82**	1.06	1.05	**2.11**

The definitions of E_I, E_P and E_T, and the amount of Sr added are the same as in Table 5.4.

The presence of ~0.4% Mg in the alloy enhances the impact strength in two ways: first, the amount of Mg_2Si particles that precipitate in the microstructure is increased, which

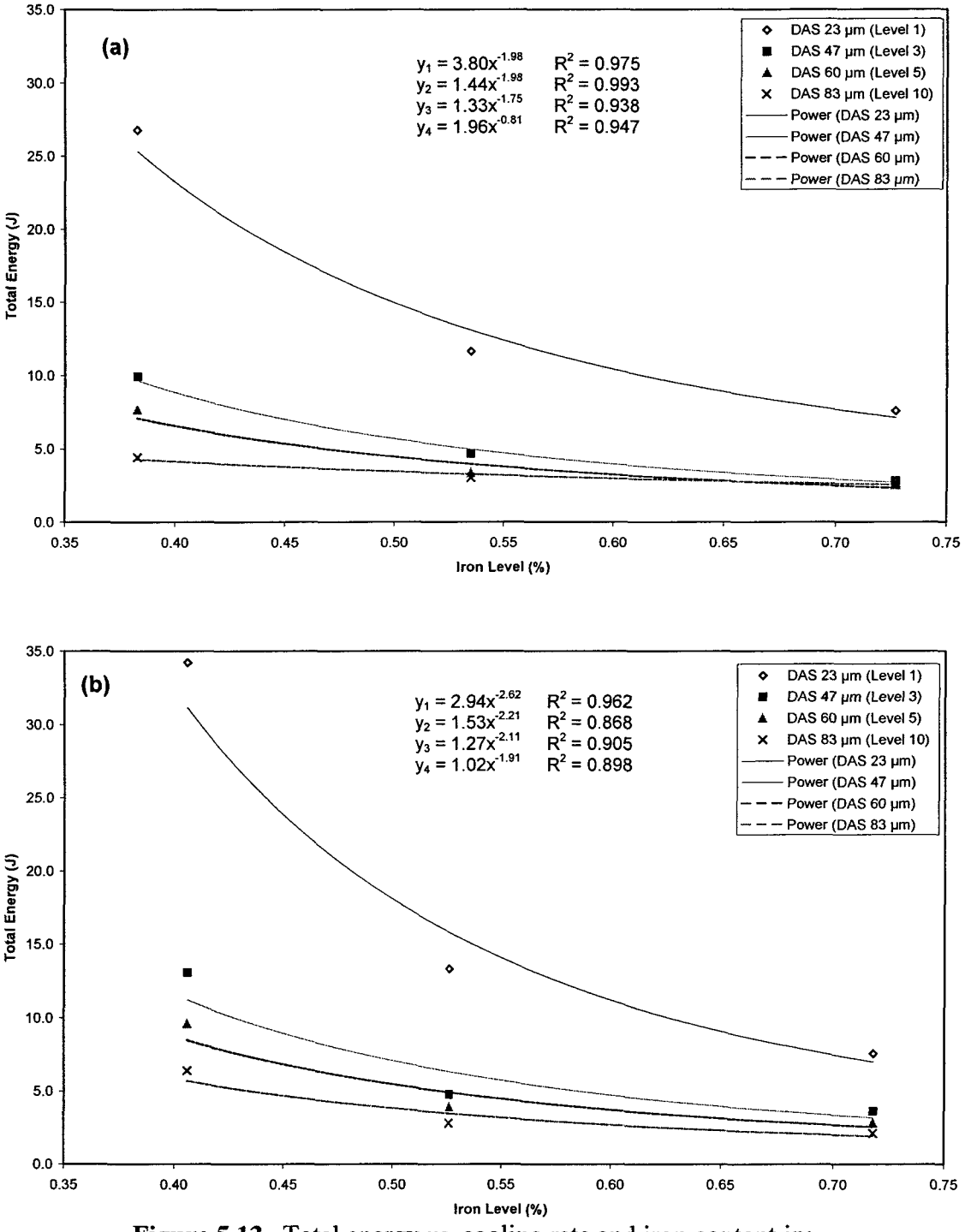

Figure 5.13. Total energy *vs.* cooling rate and iron content in: (a) unmodified and (b) Sr-modified B319.2 alloys.

helps to strengthen the alloy upon heat treatment; secondly, Mg is also known to have a modifying effect on the eutectic Si particles. Thus, the plots in Figure 5.13(a) appear similar to those of the Sr-modified 319.2 alloy shown in Figure 5.12(b), even when no Sr has been added. However, due to the additional contribution of the strengthening Mg_2Si precipitates, the relationships at all cooling rates are of a more complex nature (*viz.*, power as against linear relations).

When Sr is added to the B319.2 alloy, Figure 5.13(b), the impact energy is further enhanced at all DASs; most significantly at the lowest Fe level and highest cooling rate. In the latter case, however, the impact energy drops very rapidly as the alloy Fe level is increased. Thus, while Sr modification and a high cooling rate can optimize the impact toughness of low Fe-containing B319.2 alloys, maintaining a low Fe concentration is critical if the optimum properties are to be retained. A possible explanation for this could be that, in addition to the Mg_2Si precipitates, other Mg-containing Fe-intermetallics such as Al_5Mg_8FeSi are also formed with the addition of magnesium. These intermetallics being similar in nature to the β-Al_5FeSi iron intermetallics also provide an additional amount of brittle phase particles and crack initiation sites in the microstructure, and hence lower impact energies.

A comparison of Tables 5.4 and 5.5 reveals that alloy B has a higher impact energy than alloy A at all cooling rates and for all iron levels in the unmodified alloys, as well as at the lowest iron level in the Sr-modified alloy. Komatsu *et al.*[72] observed, however, that with an increase in Mg content, the impact energy of Al-6.1%Si-4.5%Cu alloy decreased in both as-cast and solution heat-treated conditions. They attributed the decrease to the

precipitation of Mg-containing intermetallics, and to an increase in the β-Al_5FeSi iron intermetallic size (larger lengths, but smaller thicknesses) with Mg addition.

Samuel *et al.*,[57,96,148] on the other hand, reported that smaller β-iron intermetallic sizes were obtained in Mg-containing B319.2 alloys, as a result of the transformation of the β-Al_5FeSi phase into Al_5Mg_8FeSi. The higher impact energies observed in the unmodified B alloy contradicts what would be expected from the larger β-iron platelet lengths that were reported by Komatsu *et al.*[72] with the addition of magnesium.

Magnesium has also been reported to negate the effect of Sr modification.[148] Thus, in the Sr-modified B alloys, Figure 5.13(b), effectively, less Sr would be available to modify the eutectic Si and β-iron intermetallics. This negative influence of Mg is much more apparent at the larger DASs, but is not that evident at the highest cooling rate where cooling rate and Fe-content are the primary factors controlling the impact behavior. Also, the size of the microconstituents would be small enough such that the amount of Sr available for modification would be sufficient to refine and modify these constituents.

In addition to the above, the influence of both Sr and Mg on the segregation of the $CuAl_2$ phase is expected to increase the severity of the segregation, resulting in the formation of larger amounts of the coarser block-like form of the phase in the B319.2 alloy, thus providing another means for reducing the impact energy in the latter, particularly at low cooling rates.

5.2.2.3 Alloy A356.2 (alloy C)

The impact energy data obtained from the A356.2 alloy is summarized in Table 5.6. The corresponding data distribution with respect to cooling rate and iron content is plotted

in Figure 5.14. It is important to note that the impact energy (y-axis) scale in Figure 5.14 is more than double that of the scales used in Figures 5.12 and 5.13 for the 319 alloys. This difference in energy range should be kept in mind when comparing the three alloys.

Table 5.6. Summary of impact test data for alloy A356.2

Iron Content (%)	Sr Addition	Impact Energy (J)											
		DAS 23 μm (Level 1)			DAS 47 μm (Level 3)			DAS 60 μm (Level 5)			DAS 83 μm (Level 10)		
		E_I	E_P	$\mathbf{E_T}$	E_I	E_P	$\mathbf{E_T}$	E_I	E_P	$\mathbf{E_T}$	E_I	E_P	$\mathbf{E_T}$
0.098	No	22.85	6.03	**28.88**	14.59	2.56	**17.15**	4.48	8.51	**12.99**	4.91	5.66	**10.57**
0.0936	Yes	60.44	20.44	**80.88**	48.86	9.31	**58.17**	40.06	9.13	**49.19**	22.60	6.20	**28.80**
0.429	No	5.55	10.24	**15.79**	5.10	5.57	**10.67**	5.53	1.59	**7.12**	4.40	1.28	**5.68**
0.427	Yes	33.20	3.40	**36.60**	14.69	5.16	**19.85**	7.25	7.93	**15.18**	6.55	2.00	**8.55**
0.62	No	5.63	2.13	**7.76**	1.31	1.66	**2.97**	1.08	1.81	**2.89**	1.14	1.31	**2.45**
0.605	Yes	12.48	11.56	**24.04**	6.34	1.71	**8.05**	5.12	1.86	**6.98**	3.41	1.46	**4.87**

As Figure 5.14(a) shows, for the unmodified A356.2 alloy, the impact energies depict linear relations versus Fe content at all cooling rates. Unlike the more complex 319 alloys, the impact energy in this Al-Si-Mg alloy is determined mainly by the eutectic Si particle characteristics at each cooling rate. However, in comparison to the 319.2 alloy, the corresponding impact energies at each DAS for a particular Fe level are always higher in the A356.2 alloy at every DAS level. At very low Fe levels, of the order of 0.1%, and at 23 μm DAS, the impact energy is ~29 J.

Looking at the Fe contents, the impact energy is most sensitive to the Fe content at the lowest DAS. As the microstructure coarsens, the microconstituents therein also increase in size correspondingly, so that at the coarsest DAS, not much change in impact energy is

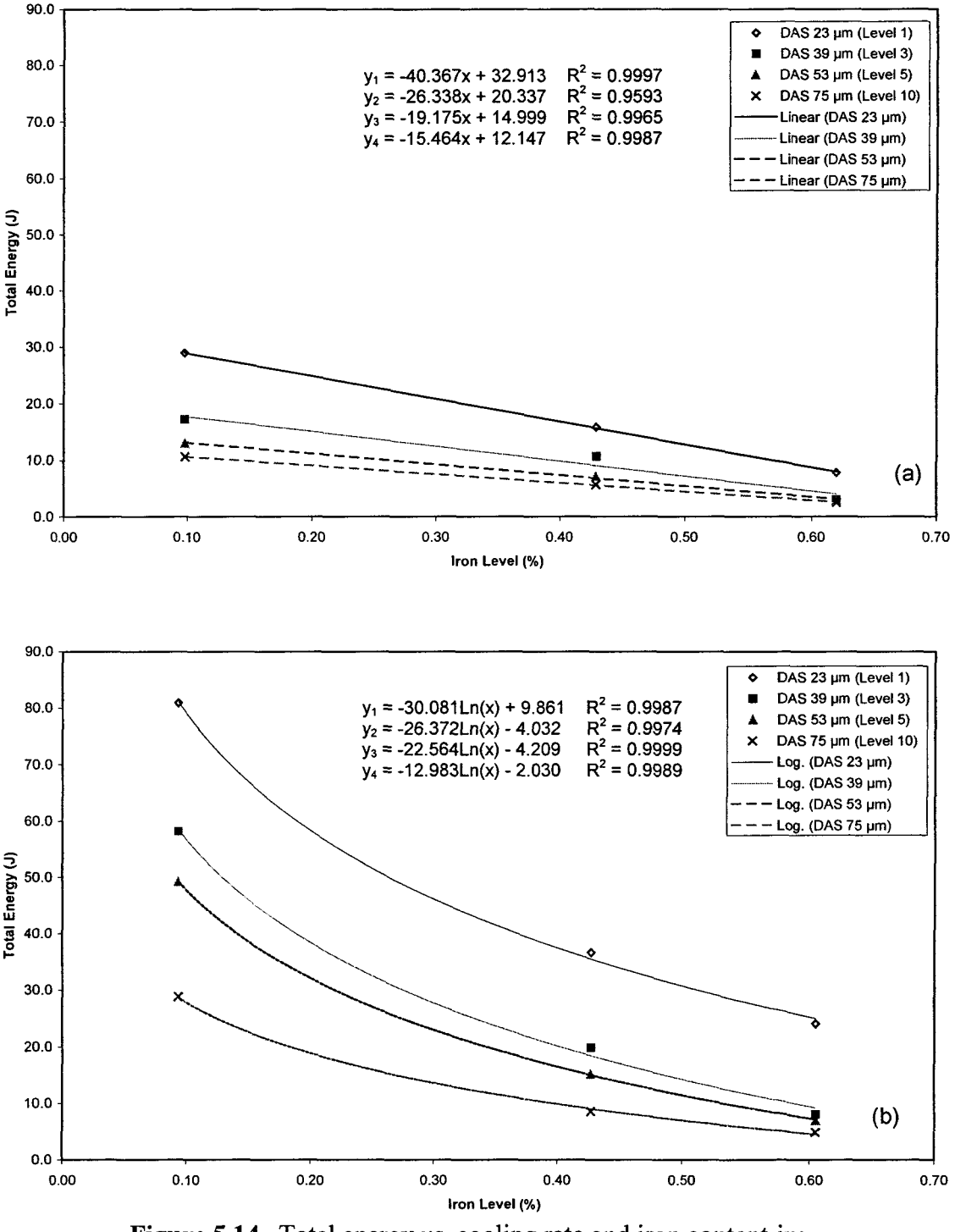

Figure 5.14. Total energy *vs.* cooling rate and iron content in: (a) unmodified and (b) Sr-modified A356.2 alloys.

observed with respect to the Fe level. Apparently, the intermetallics have already attained large enough sizes to lower the impact properties to a minimum. The slightly coarser DASs of the 319 alloys compared to A356.2 alloy would be partially responsible for the lower impact energies observed in Tables 5.4 and 5.6 at DASs > 23 μm.

When the A356.2 alloy is modified with Sr, Figure 5.13(b), vast improvements in impact energy are observed, particularly at the smallest DAS level. At the lowest Fe content, the impact energy is 81 J. In this case, the relationships are logarithmic in nature.

Thus, a high cooling rate and Sr modification can improve the impact energy at high Fe levels considerably, to levels close to those observed in the unmodified alloy at the lowest DAS-lowest Fe level condition. Addition of Sr is also seen to separate the Fe and DAS levels one from another, even at their highest values.

5.2.3 Effect of the Size of β-Iron Intermetallics

As discussed previously in Chapter 4, although the effect of β-Al_5FeSi iron intermetallic size on the impact energy is a representation of the effect of iron, the two are not exactly the same, since the β-platelet size depends not only on the iron content, but also on the cooling rate, Sr modification and any other parameters which may affect its size (this will made evident from a comparison of the figures shown in this section with Figures 5.12 through 5.14). In this regard, the average maximum β-Al_5FeSi platelet length and average area were selected as the parameters best representing the size of the β-platelet for purposes of discussing their effect on the impact energy of the alloys studied.

It is important to mention here that, as these β-platelets are actually three-dimensional entities, it is difficult to estimate correctly the actual volume fraction of the β-Al_5FeSi phase in the microstructure. Optical micrographs only provide a two-dimensional picture from which we can at best estimate the area fraction of the phase by measuring the length and thickness of the needle-like β-platelets observed in such micrographs. Although, for purposes of quantitative metallography, area fractions are taken as equivalent to the volume fractions, the third dimension of these platelets can possibly have a critical effect on the feedability of the liquid metal during solidification, as well as the tortuosity of the crack propagation path during fracture; effects that cannot be incorporated in the property *vs.* β-platelet size plots. This aspect should be kept in mind when analyzing the results.

5.2.3.1 Alloy 319.2 (alloy A)

A decrease in impact energy with respect to the increase in both β-iron intermetallic length and area parameters can be readily observed from Figure 5.15, for both unmodified and Sr-modified alloys. The impact energy follows a power relationship with the β-platelet size. In all the cases, the correlations are quite good, as seen from the R^2 values listed in the figures.

At smaller β-platelet sizes, the impact energy drops very rapidly with an increase in β-platelet size. As the platelet size increases further, the impact energy decreases more gradually until, after a certain size (~140 μm length, or 400 μm^2 area), the impact energy stays the same, at about 3 to 4 J.

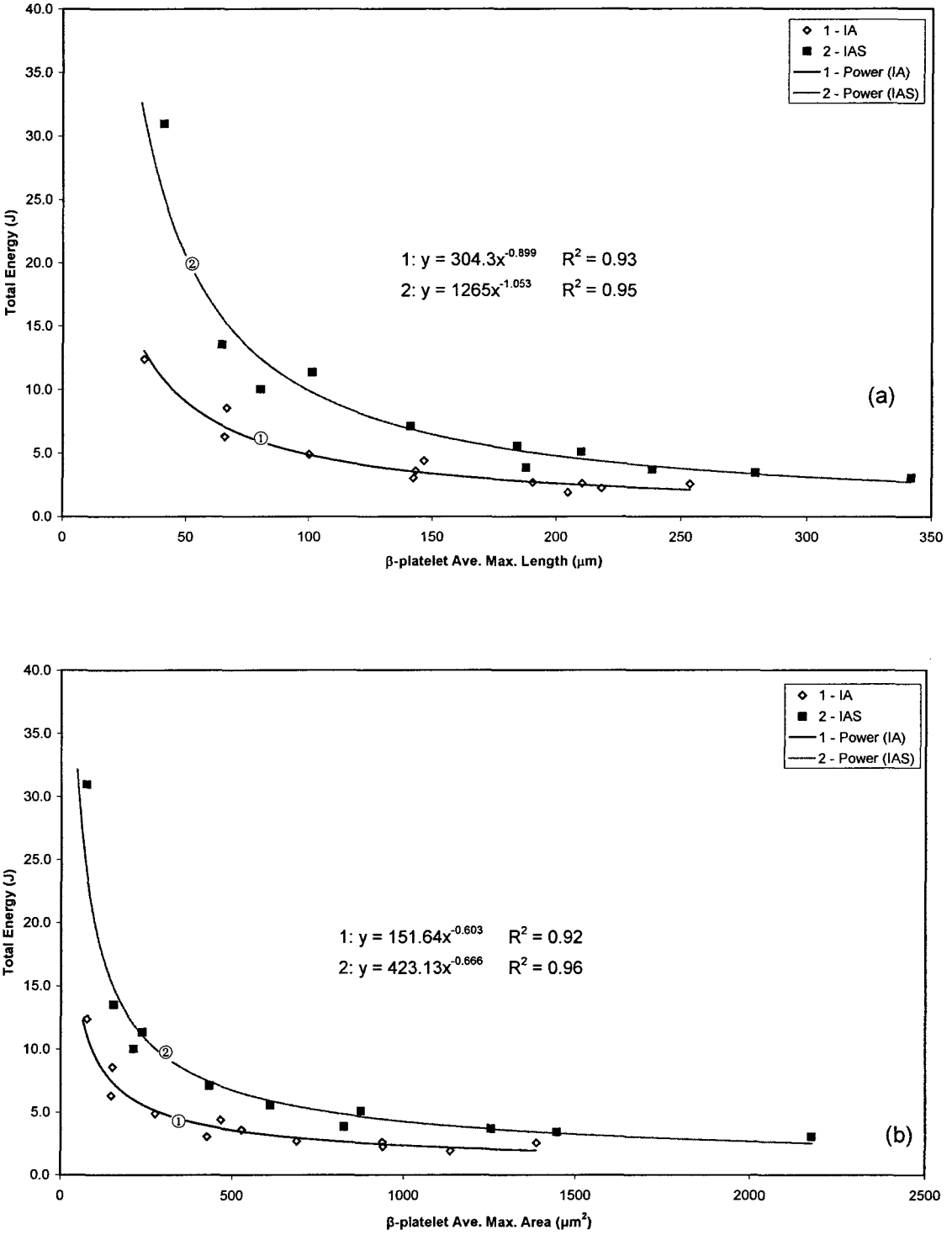

Figure 5.15. Total energy *vs.* β-platelet size in 319.2 alloys:
(a) average maximum length; (b) average maximum area.

Strontium modification improves the impact energy of the unmodified alloy. The improvement is very significant at the smallest β-platelet sizes, but lessens considerably as the platelet size increases. These observations may be explained as follows.

As discussed previously in Chapter 4, with regard to the fracture mechanisms operating in these alloys, when the β-platelet sizes are small, the Si particles control the fracture, and the Sr is mainly used up in the modification of these Si particles. However, any increase in the β-platelet size would decrease the amount of Sr available for this purpose, as some of it would react with the β-platelets, as well. Also, as the β-phase platelets increase in size, the fracture is more and more controlled by these platelets, until, after a specific β-size, the fracture is mainly controlled by the β-phase. In this case, as Figure 5.15 shows, the difference in the impact energies of the modified and unmodified alloys will not be significant.

5.2.3.2 Alloy B319.2 (alloy B)

Due to the absence of data for the B319.2 alloy samples containing 0.6% Fe, the data points in Figure 5.16 are much less than those compared to Figures 5.15 and 5.17. Nevertheless, the decrease in impact energy with the β-platelet size follows power relationships similar to those observed for the other alloys. Of importance to note is that (a) both the unmodified and Sr-modified alloy curves lie close to each other, and that (b) they are shifted towards higher impact energies. Additionally, the β-platelet size after which the impact energy remains the same is also shifted to somewhat higher values (~150 μm length, or ~500 μm^2 area) compared to the 319.2 alloy.

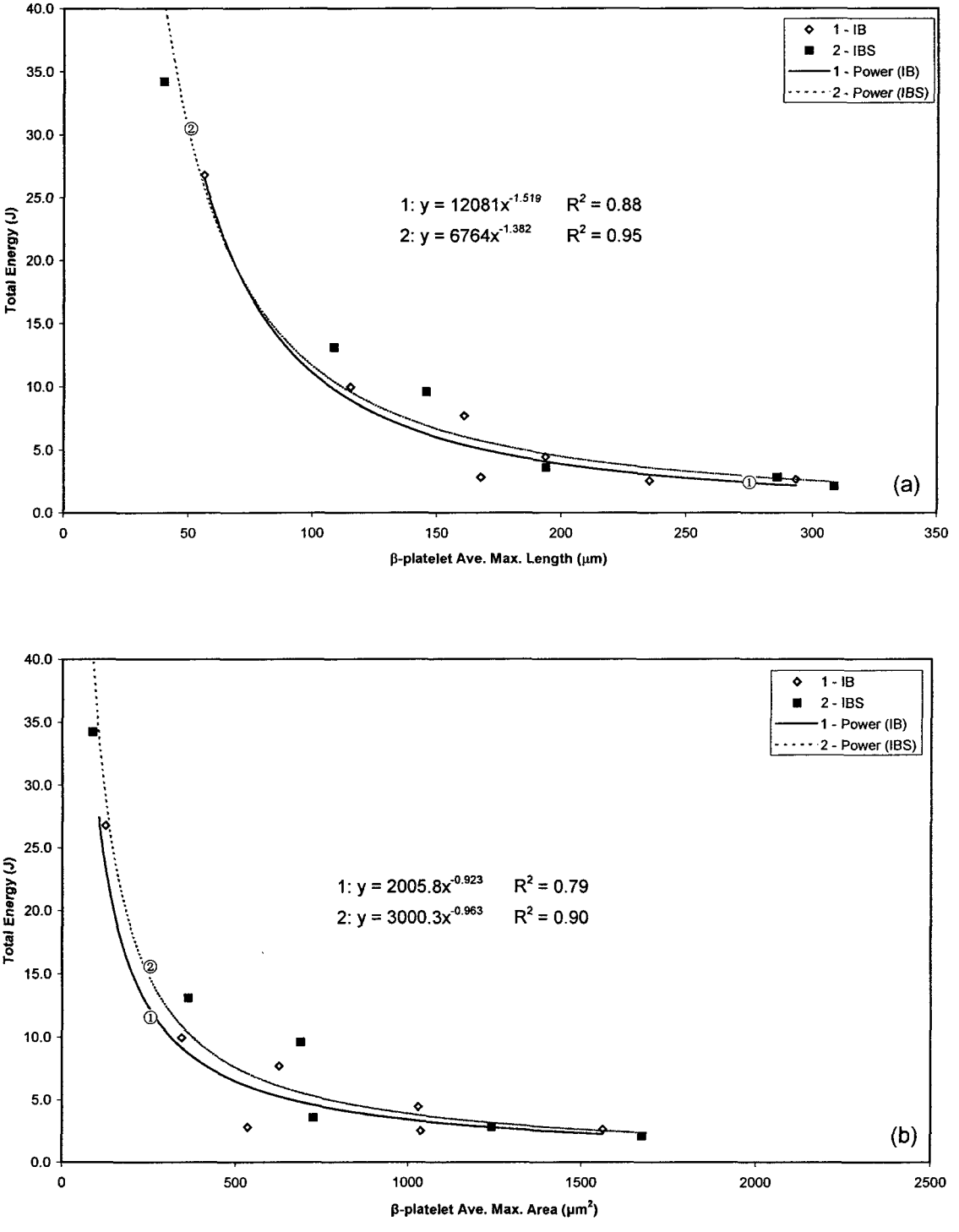

Figure 5.16. Total energy *vs.* β-platelet size in B319.2 alloys: (a) average maximum length; (b) average maximum area.

The β-platelet sizes in the B alloy samples were larger, compared to those observed in the A alloy samples. In addition, the unmodified B alloys, as well as the modified B alloy, containing the lowest Fe level showed higher impact energies than the corresponding A alloys. In the other modified B alloys – intermediate and high Fe levels – the impact energy decreased, instead. These various observations can be explained on the basis of (a) the modification effect of Mg on the eutectic Si, and (b) the Mg-Sr interaction, wherein the presence of Mg would negate the modification effect of Sr. Thus, fracture behavior would be influenced by all of these aspects rather than by the β-iron intermetallic size alone.

5.2.3.3 Alloy A356.2 (alloy C)

The effect of the β-iron intermetallic size on the impact energy in the A356.2 alloy is also similar to that of the 319 alloys, as shown in Figure 5.17. Compared to 319.2 alloy, the impact energy *vs.* β-platelet size curves are also shifted towards the higher impact energies. Compared to the B319.2 alloy, the shift is less apparent in the unmodified alloy, while it is more significant in the modified A356.2 alloy at small β-platelet sizes (50 μm length or 180 μm^2 area). Correspondingly, the curves are shifted to the left, *i.e.*, towards smaller β-platelet sizes, narrowing the β-Al_5FeSi size range covering the impact energies observed. The rapid decrease in impact energy at smaller β-platelet sizes in the A356.2 alloy indicates that even small iron contaminations would deteriorate the impact energy considerably. Thus, in such alloys containing low levels of impurities, only small iron intermetallic sizes can be tolerated if satisfactory impact energy values are to be maintained.

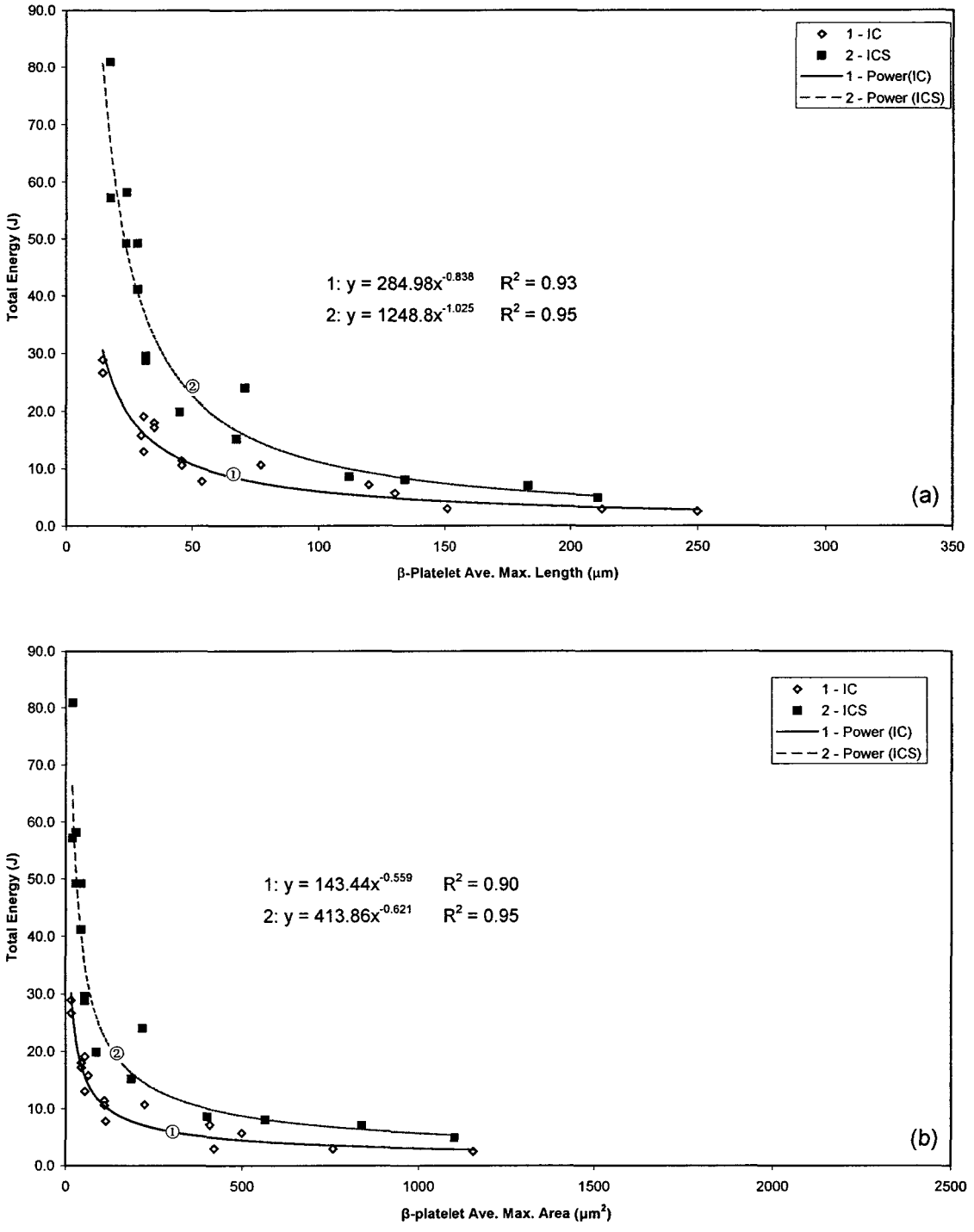

Figure 5.17. Total energy *vs.* β-platelet size in A356.2 alloys: (a) average maximum length; (b) average maximum area.

5.2.4 Effect of Porosity

In Chapter 4, when the correlation between tensile properties and porosity was discussed, only the maximum pore area was employed as the characteristic porosity parameter for the alloy, since the other two parameters – area percentage porosity and maximum pore length yielded less satisfactory results. However, it is interesting to note that in the case of impact energy, a fairly good correlation was obtained between impact energy and all three porosity parameters, although R^2 values of ~0.7 were obtained in some cases, as will be discussed below. Similar to the case of the tensile properties, the effect of porosity on the impact energy of alloy A and alloy C only were studied, representing the 319 and 356 alloys.

Tsukuda *et al.*[164] have observed that the influence of porosity on impact test results is not very significant. The fairly good correlation between impact energy and porosity parameters obtained in our study, coupled with the correlations obtained between impact energy and β-platelet size presented in the previous sections, would appear to support the proposal that iron intermetallics facilitate the formation of porosity, as reported by other researchers.[94,104]

5.2.4.1 Alloy 319.2 (alloy A)

Figure 5.18 depicts the plots of impact energy *vs.* the three porosity parameters for the 319.2 alloy samples. Generally speaking, the impact energy decreases with the increase in area percentage porosity, maximum pore area and maximum pore length. The plots of impact energy *vs.* area percentage porosity and maximum pore area are similar to each

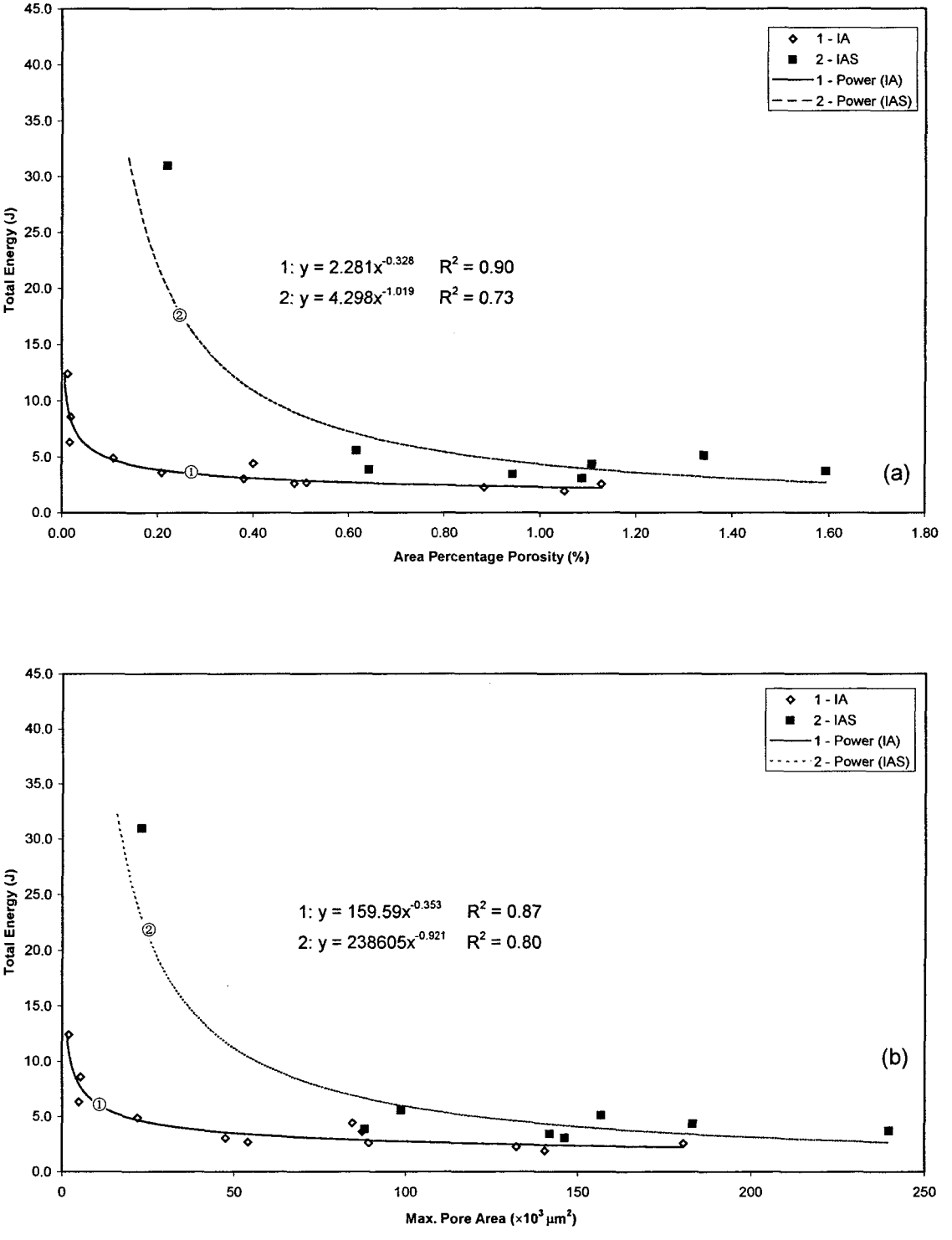

Figure 5.18. Total energy vs. porosity properties in 319.2 alloys: (a) Area percentage porosity, (b) maximum pore area, and (c) maximum pore length.

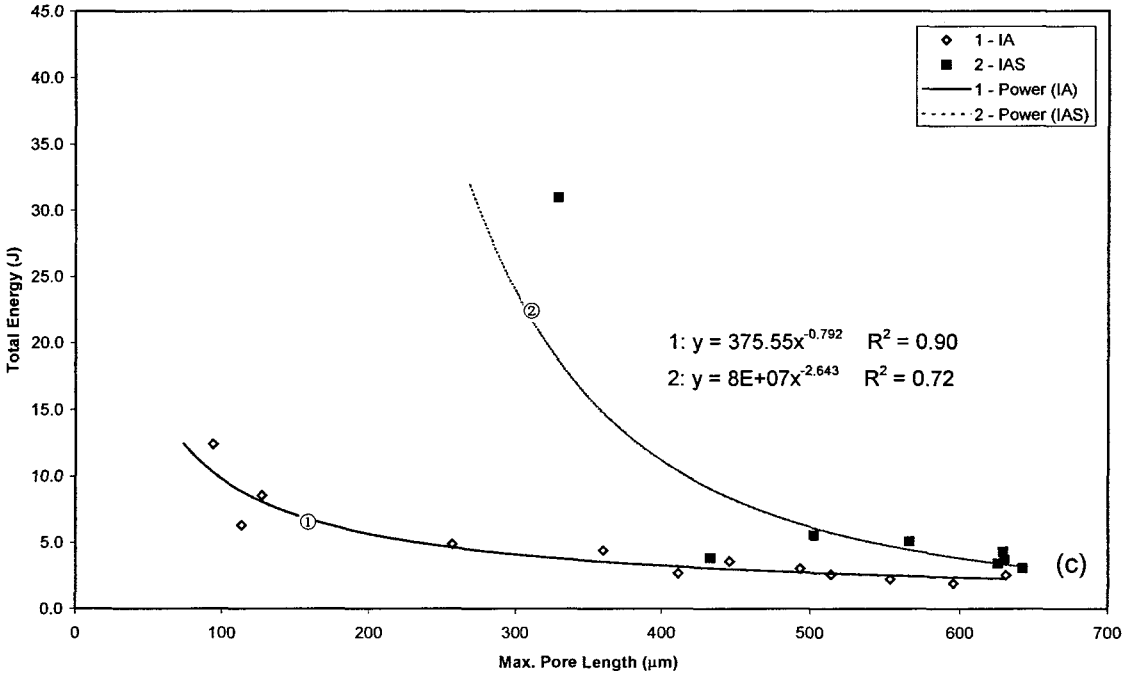

Figure 5.18. Total energy vs. porosity properties in 319.2 alloys: (a) Area percentage porosity, (b) maximum pore area, and (c) maximum pore length.

other (Figures 5.18(a) and 5.18(b)), but differ from that of impact energy *vs.* maximum pore length, Figure 5.18(c). In the unmodified alloy, the impact energy falls rapidly within a narrow range of area percentage porosity or maximum pore area values, *viz.*, 0-0.2% and 0-2×10^4 μm^2 ranges. After that the impact energy remains practically the same, at about 2.5 J, over the entire range of the porosity parameter values observed. This would indicate that the impact energy is extremely sensitive to the presence of porosity in the unmodified alloy and the only means to optimize it is to minimize the porosity as far as possible. This would explain Tsukuda *et al.*'s[164] observation that the influence of porosity on impact energy is not very significant.

With respect to the maximum pore length parameter, the drop in impact energy is more gradual, covering a wider range of values (~80 to 350 μm), before it stabilizes to ~2.5 J.

While it is clear that the feedability-related problems associated with the presence of β-platelets during the process of solidification can result in porosity formation, the similarity of the impact energy *vs.* β-platelet size plots in Figure 5.15 and those shown in Figures 5.18(a) and 5.18(b), indicates a more direct link between the two. In fact, recent studies by Liu *et al.*[170] have shown that the β-Al_5FeSi phase platelets act as pore nucleation sites.

In the Sr-modified alloy, although the plots of impact energy *vs.* porosity parameters also follow power relationships similar to the unmodified alloys, two important differences are observed: (i) higher impact energies are obtained compared to the unmodified alloy at the same porosity content/pore size value, and (ii) the impact energy curve is shifted to the right, *viz.*, high impact energy values are still achieved at larger area percentage porosity and maximum pore area sizes.

For example, at 0.2% porosity, the Sr-modified alloy exhibits an impact energy of about 30 J, whereas the unmodified alloy shows about 3 to 4 J only. This can be attributed to the refinement of the Si particles with the addition of Sr, indicating that the Si particle size is one of the main parameters controlling the alloy toughness. This observation is in good agreement with the published data.[156] The second observation shows that the same levels of impact energy can be obtained with higher porosity contents if the alloy is modified.

It is well established that the addition of Sr increases porosity formation. This is variously demonstrated in Figure 5.18 by the higher minimum values of the three porosity parameters obtained for the Sr-modified alloy compared to the unmodified alloy (*cf.* a maximum pore length of 330 μm *vs.* 94 μm for the unmodified alloy). However, as higher

impact energies are still exhibited by the modified alloy samples, apparently, the beneficial effects of Sr modification on the eutectic Si and β-Al_5FeSi phase outweigh that associated with porosity. Due to the interaction of all three effects, the impact energy *vs.* porosity parameter plots display weaker correlations (R^2 ~0.72 to 0.8) compared to the unmodified alloy.

5.2.4.2 Alloy A356.2 (alloy C)

From Figure 5.19, it is evident that the 356 alloy offers high levels of toughness compared to those obtained from 319 alloys, due to the absence of copper intermetallics such as $CuAl_2$, Al_7FeCu_2 and $Al_5Si_6Mg_8Cu_2$ in this alloy.[17]

As mentioned previously, the addition of Sr allows for higher porosity tolerances in the alloy to maintain the same toughness levels. For example, to achieve an impact energy of ~5 J, the unmodified A356.2 alloy should contain no more than ~0.3% porosity, Figure 5.19(a). In the modified condition, however, this level of energy can be achieved at even ~1% porosity content. The maximum pore area parameter (Figure 5.19(b)) may be the appropriate parameter to characterize the overall porosity effect. Similar observations were reported for fatigue properties. The work of Major[171] on porosity control and fatigue behavior in A356T61 aluminum alloy shows that, the largest pore size has the largest influence on fatigue life.

The plot of the energy data *vs.* the corresponding maximum pore length in Figure 5.19(c) shows a large difference between Sr-modified and unmodified 356 alloys. This

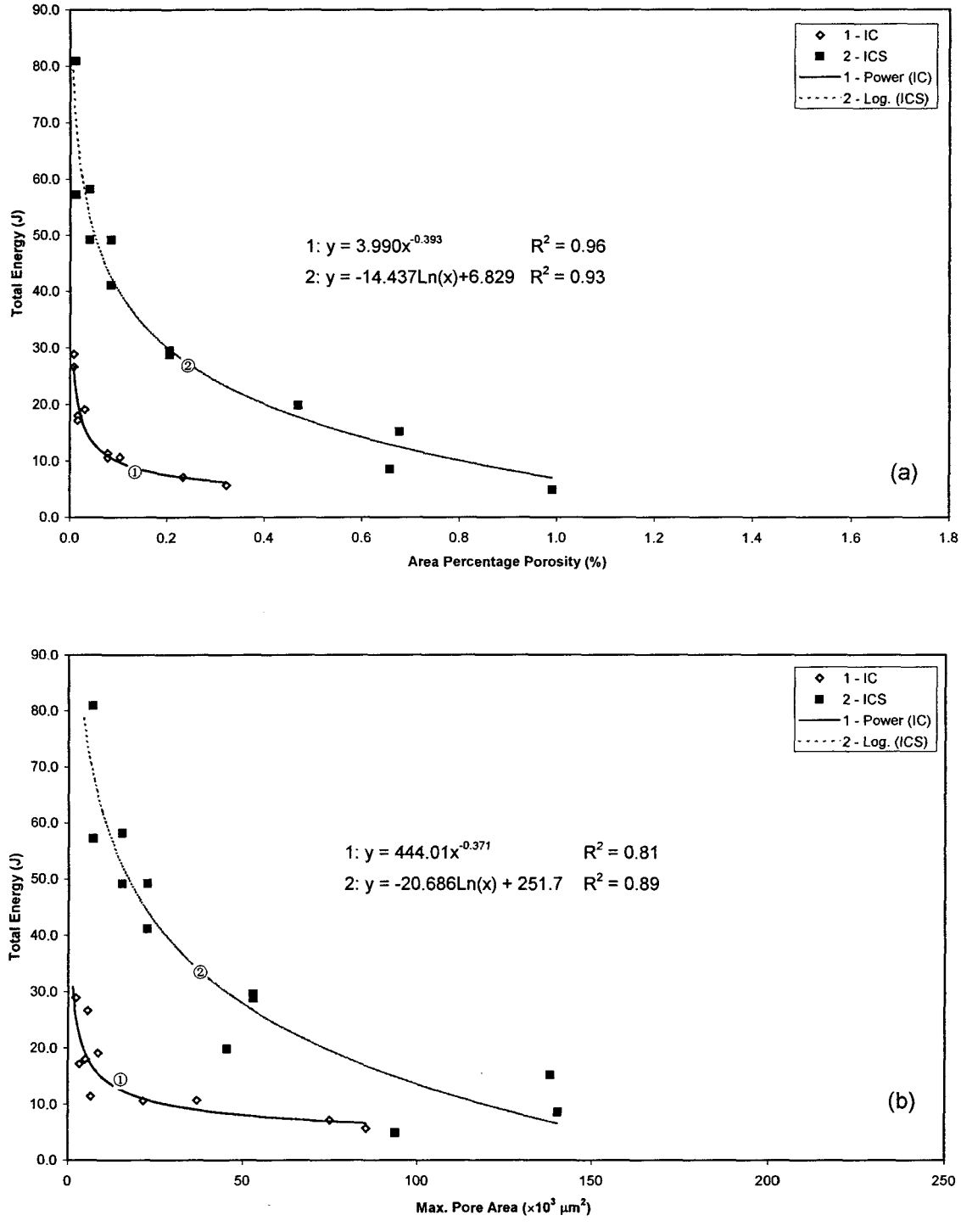

Figure 5.19. Total energy *vs.* porosity parameter plots in A356.2 alloys: (a) area percentage porosity, (b) maximum pore area, and (c) maximum pore length.

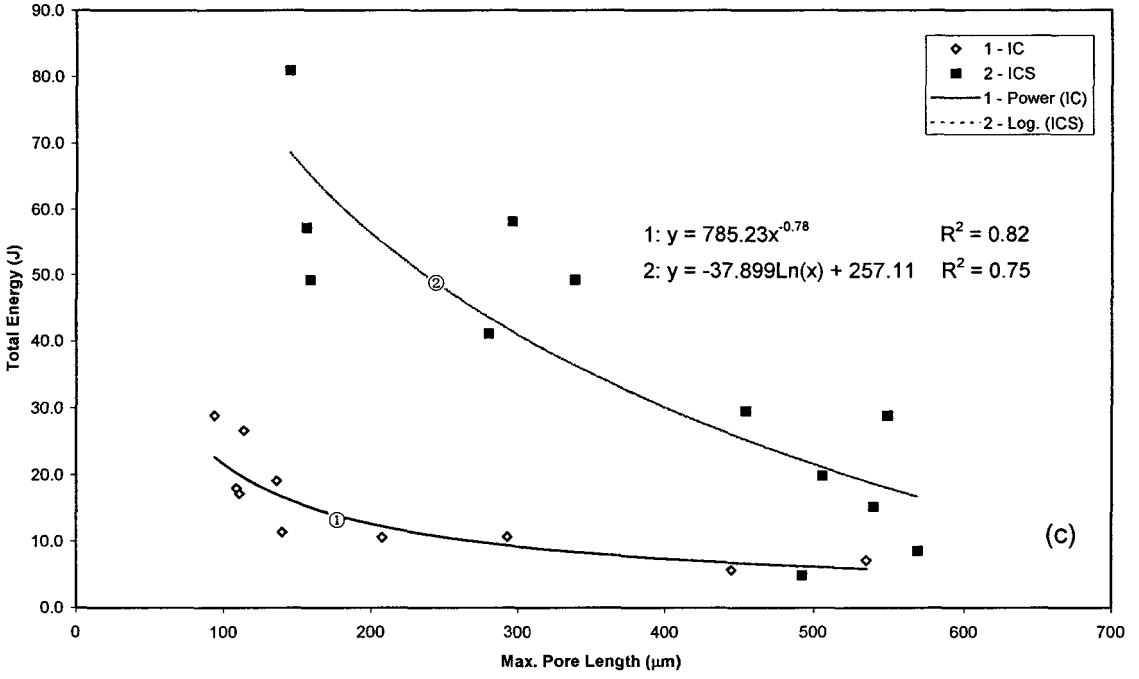

Figure 5.19. Total energy *vs.* porosity parameter plots in A356.2 alloys: (a) area percentage porosity, (b) maximum pore area, and (c) maximum pore length.

observation supports the above proposal that the maximum pore area is the most detrimental porosity factor affecting alloy toughness.

It ought to be mentioned here that the percentage porosity and pore sizes reported for 356 alloys are much less compared to those measured for 319 alloys. This difference is the result of the shorter solidification times for 356 alloys due to the absence of copper intermetallics (which precipitate in the 319 alloys). These factors attributed to the higher impact energies reported in Figure 5.19 for the A356.2 alloy compared to those shown in Figure 5.18 (*cf.* maximum attainable energies of 80 J with 30 J in the Sr-modified A356.2 and 319.2 alloys, respectively). In addition, the R^2 values for the A356.2 alloy plots are superior to those of the 319.2 alloys (under similar working conditions).

5.2.5 Effect of Strontium

The effect of strontium modification on the impact energy has already been incorporated in the previous sections that discussed the effects of other parameters (*i.e.*, iron content and cooling rate), where the unmodified alloys were compared with the modified ones. This section essentially separates the results obtained for the three Sr-modified alloys. These results are discussed in the context of the figures and tables shown in the earlier sections.

5.2.5.1 Alloy 319.2 (alloy A)

From Table 5.4, it can be seen that for all iron levels studied, Sr modification improves the impact energy, even at the higher iron content. Shivkumar *et al.*[159] have found that in 319 alloys, Sr modification is more effective at low cooling rates. Decreasing the cooling rate or increasing the Fe content diminishes the effectiveness of Sr modification on the alloy toughness considerably. These observations can be explained in terms of the roles of the size and distribution of both the eutectic Si particles and β-iron intermetallics.

As described in Section 4.2.4.1, as the Fe content increases, the amount of β-iron platelets increases, reducing the effectiveness of the eutectic Si modification (due to the Sr addition) in enhancing the alloy toughness. As a result, the impact energy is lowered in spite of the modification.

Although Sr "neutralizes" the harmful effect of iron to some extent by altering the acicular β-Al_5FeSi intermetallics in the more compact α-AlFeSi Chinese script form[62,63] or by accelerating the fragmentation and dissolution of the β-AlFeSi phase,[21,32] this does not

always happen. Some very long β-AlFeSi platelets are also persistently observed in Sr-modified alloys. Nevertheless, their impact energies are still higher than those of the unmodified alloy, Figure 5.15.

The difference in energies between the modified and unmodified alloys decreases as the β-platelet size increases. The largest differences in energies are observed at very small β-platelet sizes. The sharp drop in energy thereafter indicates that at small β-platelet sizes, the Si particles control the sample failure, whereas at larger β-platelet sizes, the fracture is increasingly controlled by the latter. When the β-platelet sizes are sufficiently large, no difference in impact energies are observed between the modified and unmodified alloys.

As Figure 5.18 shows, the addition of Sr increases porosity formation. Due to the fact that the alloy failure is mainly controlled by the size and distribution of the eutectic Si particles and the β-iron intermetallics, any increase in the porosity level in the modified alloys will not reflect on the impact energy, provided the size of the β-platelets remain small (low Fe-high cooling rate condition).

5.2.5.2 Alloy B319.2 (alloy B)

Due to the higher magnesium content in this alloy, the effect of strontium is different from that reported for alloy A. This is mainly on account of the Mg-Sr interaction leading to the formation of the $Mg_2Sr(Si_3Al_4)$ compound.[172]

Compared to alloy A, the improvement in impact energy with Sr modification is much less in this case. For the sample representing the best conditions, *i.e.*, lowest Fe-highest cooling rate, the improvement after Sr modification is only 28%, compared to 150% for the

A alloy. An increase in the iron level to ~0.53% reduces the improvement by half (*i.e.* to 15%) at 23 μm DAS, after which the addition of Sr appears to have little or no effect on the impact energy with either an increase in Fe content or an increase in DAS.

It is interesting to note, however, that the highest improvement (44%) in impact energy with Sr addition in the B alloy is obtained for the lowest Fe-lowest cooling rate sample. Surprisingly, the corresponding Sr-modified A alloy sample shows the lowest improvement (20%) under the same conditions. These discrepancies from the general behavior can be attributed to the respective E_I and E_P energy values obtained for the two samples. These, in turn, are determined by the type and characteristics of the microstructural constituents of the samples during the impact testing.

5.2.5.3 Alloy A356.2 (alloy C)

The improvement in impact energy in A356.2 alloy with modification is more pronounced than that observed for the 319 alloys. For the lowest Fe-highest cooling rate sample – an improvement of 180% is noted. As Table 5.6 shows, the improvement in impact energy of the Sr-modified C alloy is not systematic with respect to the cooling rate or Fe content, as the lowest Fe samples at higher DASs (47 μm and 60 μm) display much higher improvements (230% and 279%, respectively). The energy is determined, rather, by how high the crack initiation energy (E_I) is for a particular sample. The E_I value primarily determines the improvement in the impact energy.

The much larger E_I values observed in the A356.2 alloy samples reflect the effectiveness of Sr modification in this alloy (mainly related to the eutectic Si particle

characteristics) compared to the more complex 319 alloys (containing a greater amount of intermetallics). Indirectly, this observation also reveals the sensitivity of the impact properties to the alloy microstructure and to the changes therein. Also, from Figure 5.15 it can be seen that the effectiveness of Sr modification drops with the increase in β-iron intermetallic size, such that for β-platelet lengths of 50 μm (or 200 μm^2 area) and above, the difference in impact energies between the Sr-modified and unmodified alloys is marginal.

5.2.6 Relationship between Impact Energy and Tensile Properties

It has been found that castings that have identical properties when tested in tension or torsion at slow strain rates can show pronounced differences in their tendency for brittle fracture under impact testing.[18] Thus, it should be of interest to study the relation between these two sets of properties in the present work.

The relationships between impact energy *vs.* tensile strength and elongation are shown in Figures 5.20 through 5.22 for the three alloys studied. In all cases, the impact energy *vs.* tensile strength and elongation plots follow exponential and linear relationships, respectively, and the modified alloys displaying more consistent correlations (R^2 values of 0.83 to 0.94) in general, compared to the unmodified alloys where the R^2 values range between 0.69 and 0.98 (except in the impact-elongation plots in 319 alloys, where higher R^2 values in unmodified alloys were noticed). Most of the data points are distributed within impact energy ranges of 2 J to 15 J in the 319 alloys, and within 3 J to 30 J in the 356 alloys.

5.2.6.1 Alloy 319.2 (alloy A)

The relationships between impact energy and tensile strength and impact energy and elongation for the 319.2 alloy are presented in Figures 5.20(a) and 5.20(b), respectively. In Figure 5.20(a), the curves for both unmodified and Sr-modified alloys show exponential correlations. The nature of the curves indicates that the overall effect of alloying and melt processing parameters on tensile strength and impact energy are similar in both cases. However, impact energy is more sensitive to casting parameters than tensile strength, especially in the high tensile strength region. For example, in the unmodified alloy, points A and A' correspond to the samples obtained at 23 μm DAS, but containing 0.4% and 0.8% Fe, respectively. They possess the same tensile strength (~252 and 251 MPa), but very different impact energies (~12.4 J and 6.3 J, respectively). In the modified alloy, the points B and B' (obtained still at 23 μm DAS, but containing 0.4% and 0.6% Fe) depict how rapidly the impact energy can increase (from ~13.5 J to ~31.0 J) within a tensile strength increase of ~25 MPa. The higher and steeper nature of the curve for the modified alloy shows that Sr modification has a more pronounced effect on the impact energy than on the tensile strength.

With respect to ductility, linear correlations are observed for both unmodified and Sr-modified alloys. The two trend lines intersect at ~1.75% El, indicating that when the alloy displays low mechanical properties, the addition of Sr does not do much to improve the properties.

In general, Figure 5.20 shows that the higher the tensile strength, the higher the elongation and the higher the impact energy obtained.

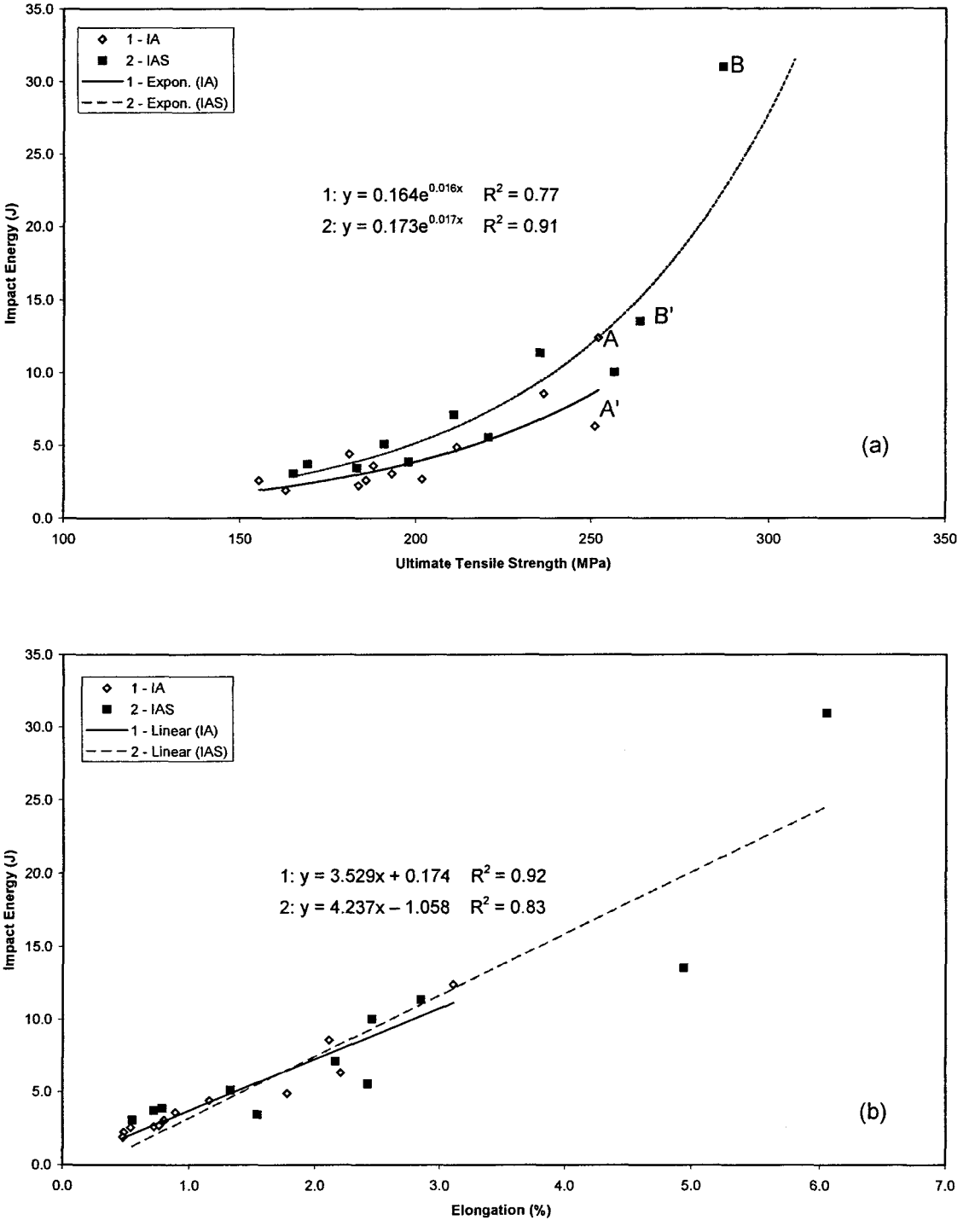

Figure 5.20. Correlation between impact energy and tensile properties in 319.2 alloy.

5.2.6.2 Alloy B319.2 (alloy B)

The relationships between impact energy and tensile strength (Figure 5.21) are more or less similar to those of alloy A, with both unmodified and Sr-modified alloys exhibiting good R^2 values (0.89 and 0.94, respectively). As before, the trend lines indicate that impact energy is more sensitive to casting parameters in the high tensile strength property region, as evidenced by the rapid increase in impact energy (from A to A') over a small increase in strength. Obviously, Sr modification is less effective than 319.2 alloy, due to the Sr-Mg interaction see Figure 5.21(a).

The impact energy vs. elongation relationships for the unmodified and Sr-modified B alloys are linear, Figure 5.21(b), and show the best correlations (R^2 values of 0.98, 0.94, respectively). The points A and A' corresponding to alloy samples with 0.4% Fe and 23 μm DAS revealed the effectiveness of Sr modification in increasing the impact energy from ~27 J to 34 J. However, the cluster of points towards the bottom left in Figure 5.21(b) also indicate that in cases when the alloy has low ductilities, no improvement can be achieved by adding strontium.

5.2.6.3 Alloy A356.2 (alloy C)

Figure 5.22 shows the impact energy *vs.* tensile property relationships for the A356.2 alloy. Although the impact energy *vs.* tensile strength curves for the unmodified and Sr-modified alloys, Figure 5.22(a), exhibit exponential correlations similar to those observed for the 319 alloys, the curves are shifted towards the left, indicating higher impact energies are obtained in the A356.2 alloy even at moderate tensile strengths. It is also important to

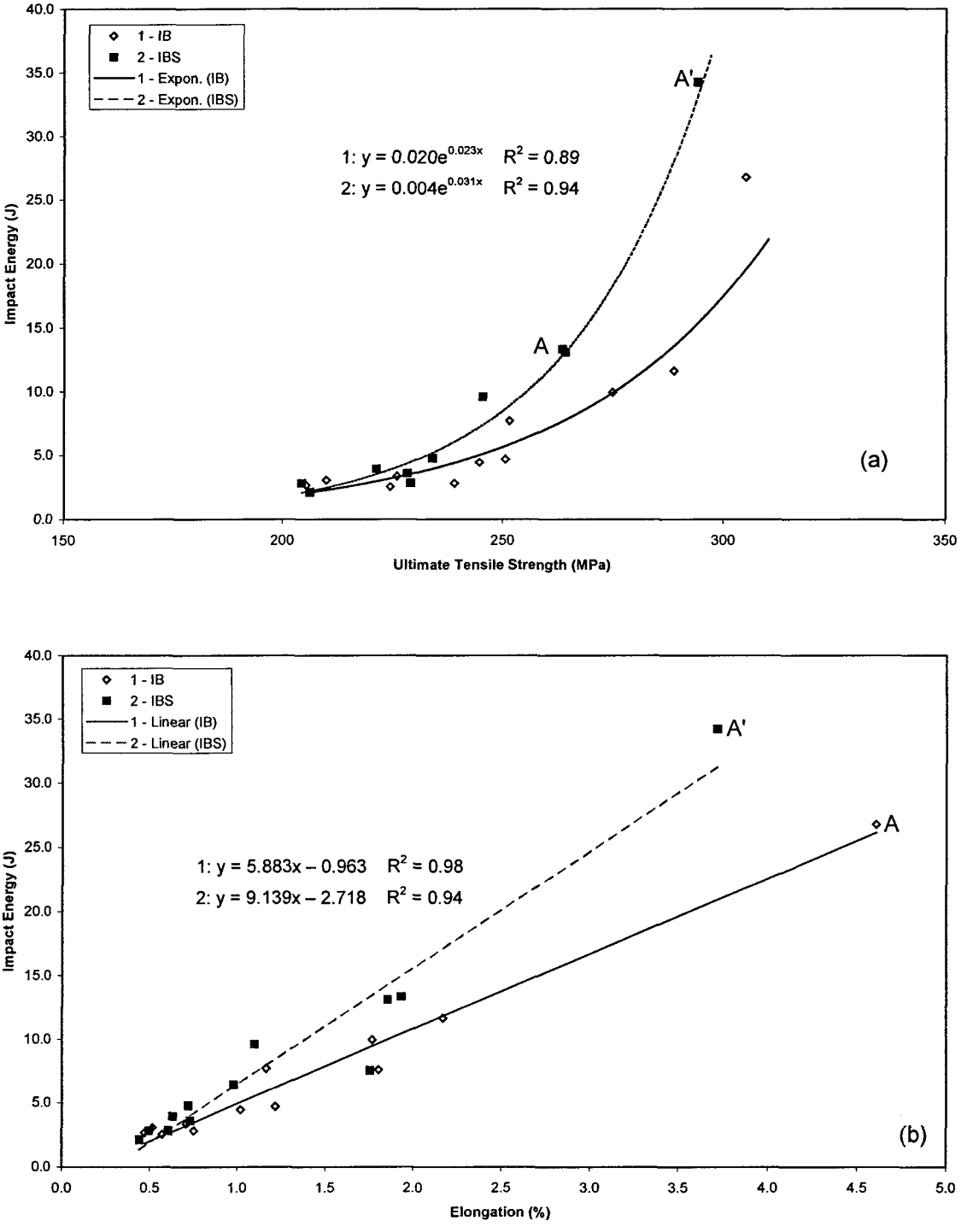

Figure 5.21. Correlation between impact energy and tensile properties in B319.2 alloy.

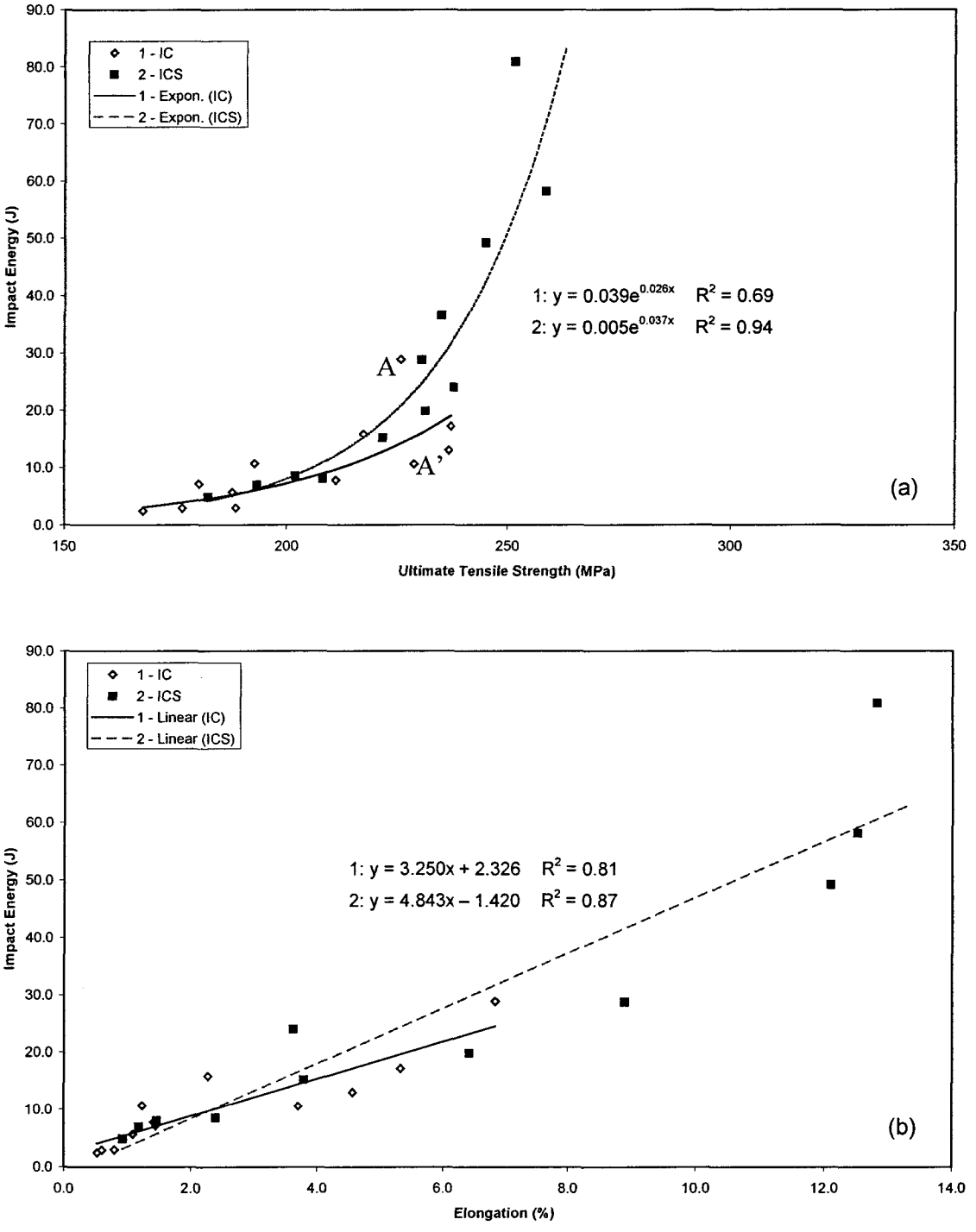

Figure 5.22. Correlation between impact energy and tensile properties in A356.2 alloy.

note that the impact energy scale (y axis) in Figure 5.22 is more than twice that of Figures 5.20 and 5.21. Thus overall, the toughness of the A356.2 alloy is far superior to that of the 319 alloys over the alloying and melt treatment conditions studied. The steeper nature of the curve for the Sr-modified samples in Figure 5.22(a) compared to Figure 5.21(a) indicates that the effectiveness of Sr addition is both faster and greater in the A356.2 alloy. In comparison, the Sr-modified 319.2 alloy, Figure 5.20(a) shows a slower and much more gradual response to improvement in impact toughness.

Summarizing the results for the three alloys, it is found that the impact energy–tensile strength plots display exponential correlations, whereas the impact energy–elongation plots show linear relationships, regardless of the alloy chemical composition. The A356.2 alloy displays far superior impact toughness compared to the 319 alloys, the larger content of intermetallics (both Fe- and Cu-intermetallics) being responsible for the lower impact energies in the latter.

CHAPTER 6

FRACTOGRAPHY

CHAPTER 6

FRACTOGRAPHY

6.1 INTRODUCTION

Fractography is defined as the study and documentation of fracture surfaces.[173] The purpose of fractography is to analyze fracture features and attempt to relate the topography of the fracture surface to the causes and/or basic mechanisms of fracture.[174] The knowledge of fracture behavior is important in upgrading material specifications, improving product design, and analyzing failures for improved reliability.[115]

A study of the characteristics of fracture surfaces is often carried out using optical microscopy (*viz.*, light-microscope fractography), particularly when a low magnification of the fracture surface is adequate. The magnification is usually selected such that a good resolution is obtained, and can range from "macroscopic" or low magnification fields (up to 50 diameters) to "microscopic" or high magnification fields (50 diameters and above).

When very fine details of the fracture surface, *e.g.*, dimples and microvoids are required to be observed, a scanning electron microscope (*viz.*, SEM fractography) is employed instead, where the magnifications can go from about 5 to 240,000 diameters. With a resolution limit of ~100 Å and a depth of field about 300 times that of an optical microscope, the SEM is generally preferred over the latter for the analysis of fracture

surfaces. Further details with regard to the SEM modes of operation employed in the present study are given in Section 6.2.1.

Four major types of fracture (or failure) modes have been discussed in the literature. Briefly, these modes and the sources of their occurrence are as follows:[115]

(1) Dimpled rupture (or microvoid coalescence) caused by ductile fracture or rapid overload fracture;

(2) Cleavage or quasi-cleavage caused by brittle fracture or premature or overload failure by catastrophic rapid fracture;

(3) Intergranular fracture caused by stress corrosion cracking, hydrogen embrittlement, or subcritical growth under sustained load; and

(4) Ductile striations caused by fatigue cracking or subcritical growth under cyclic load.

The first three types are microstructurally dependent. Complications arise in determining failure type when complex microstructures are involved. For example, in aluminum alloys containing extensive intermetallic compounds, the failure may occur by a combination of ductile rupture of the matrix and brittle cleavage of the intermetallic particles. Such intermetallic compounds (> 1 μm) also reduce the alloy toughness. Often, transgranular fracture of the brittle compounds can also occur. Multiple microstructural phases can lead to numerous combinations of microscopic fracture modes.

Al-Si alloys are essentially a combination of the high-strength, brittle silicon phase and the low-strength, ductile aluminum matrix, containing, in addition, other microstructural features such as iron intermetallic phases, porosity, inclusions, *etc.* While it is natural to

assume that the Si particles play an important role in the fracture behavior, the contribution of these other microstructural aspects must also be considered, even if their relative importance is affected by the amount and morphology of the constituents, and the interactive effects between them. Consequently, the alloying and melt processing parameters (*e.g.*, strontium modification, grain refining) and the solidification rates (different dendrite arm spacings) which directly affect the microstructure also come into the picture.

Figure 6.1 shows the two main types of fracture observed in the Al-Si alloy under tensile overloading. Figure 6.1(a) illustrates an example of the simple rupture mode of fracture, where the particles are observed at the bottom of the dimples. These particles are seen to have decohered from the surrounding matrix. In such cases, where decohesion of the particles takes place, the resultant fracture surface attains the dimpled appearance seen in the figure. The alloy is said to have failed by the process of microvoid coalescence. The microvoids nucleate at regions of localized strain discontinuity, such as that associated with second phase constituents, inclusions, grain boundaries or dislocation pileups.[175]

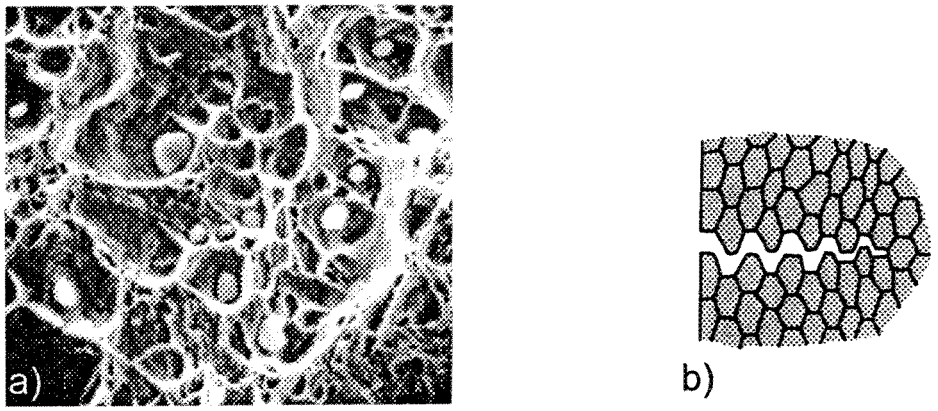

Figure 6.1. Two main types of fracture observed in the Al-Si alloys under tensile overloading. (a) Dimple rupture and (b) cleavage fracture of intermetallics.[175]

Figure 6.1(b) represents an example of the cleavage fracture of intermetallics. Cleavage is a low-energy fracture that propagates along well-defined low-index crystallographic planes known as cleavage planes. Theoretically, a cleavage fracture should have perfectly matching faces and a completely flat and featureless surface. However, as the Al-Si alloys used are polycrystalline and contain grain boundaries, inclusions and dislocations, these imperfections affect the propagating cleavage, and later the perfectly flat characteristics to a certain extent. Sometimes, the microconstituents present in the path of the propagating crack, can result in the alloy sample exhibiting a mixed fracture mode, as was observed in the present study.

In this chapter, the fracture behavior of Al-Si-Cu and Al-Si-Mg cast alloys as reported by other researchers in the literature will be reviewed, to obtain a basic idea about the subject. Based on this, the fracture behavior of selected impact samples tested in the present study will be discussed. Attention will be focused on alloy sample conditions corresponding to optimum or minimum impact energy conditions.

6.1.1 Si Particles

Voigt and Bye[121] studied the fracture behavior of Al-Si-Mg (A356) alloys using tensile samples of different section sizes and under different conditions (as-cast/heat-treated, unmodified/Sr-modified), where *in-situ* observations of the surface crack initiation and propagation using scanning electron microscopy were presented. Cracks were found to initiate with the fracture of Si particles at relatively low strain values. Crack propagation also proceeded by the same mechanism, preferably through the eutectic region of the

microstructure, avoiding the primary Al dendrite cores wherever possible. Continued strain resulted in localized plastic deformation around the fractured Si particles, which eventually led to the formation of microcracks in the eutectic region. Further straining caused selected microcracks to link up with other neighboring microcracks in the same eutectic region to initiate the primary crack, or to link up with the propagating crack front. The overall fracture paths tended to follow the eutectic regions in the microstructure.

Gall *et al.*,[176] described the microstructure of A356 alloys as consisting of primary Al-1 pct Si dendrites and a eutectic with silicon particles (12 pct volume) embedded in the Al-1 pct Si matrix. Room-temperature constant-amplitude fatigue tests revealed that for a low crack-tip driving force, the surface fatigue crack propagated primarily through the Al-1 pct Si dendrite cells. The silicon particles in the eutectic remained intact and served as barriers at low fatigue-crack propagation rates. When the fatigue crack crossed the three-dimensional Al-Si eutectic network, it propagated mainly along the interface between the silicon particles and the Al-1 pct Si matrix. Therefore, nearly all of the silicon particles were progressively debonded by fatigue cracks propagating at low rates, with the exception of elongated particles with a major axis perpendicular to the crack plane, which were fractured. For a high crack-tip driving force, silicon particles ahead of the crack tip were fractured, and the crack subsequently propagated through the weakest distribution of prefractured particles in the Al-Si eutectic. Only small rounded silicon particles were observed to debond at high crack propagation rates. The crack process in the two cases is schematically depicted in Figure 6.2.

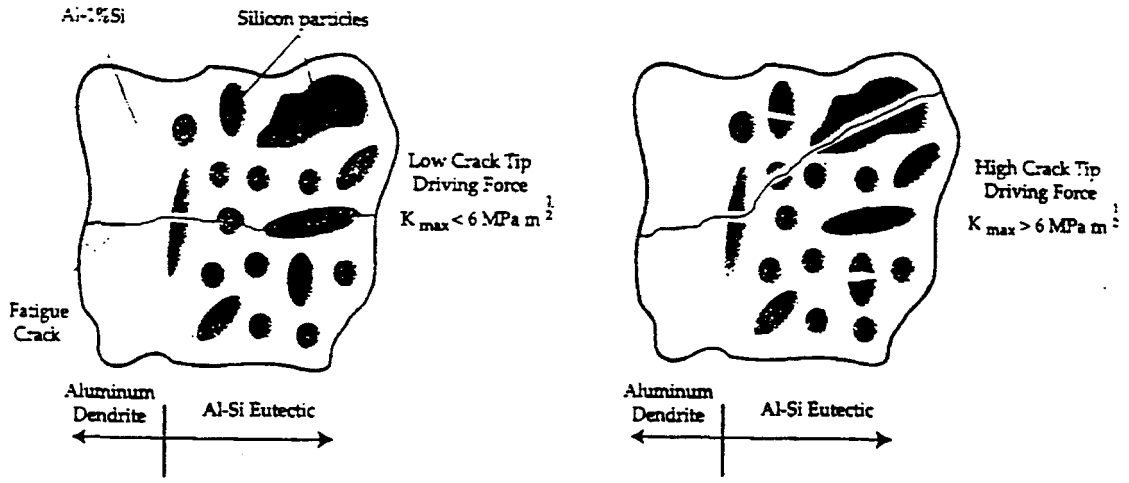

Figure 6.2. Schematic of the fatigue crack process through the silicon particle-rich eutectic regions at low and high crack-tip driving forces.[176]

Hafiz and Kobayashi[119] conducted a study on the microstructure-fracture behavior relations in Al-Si casting alloys using tensile testing. The main focus was on Si particles, where different morphologies of the Si particles were obtained using a variety of solidification rates and different Sr levels. Fracture paths in the mid-sections were examined using optical microscopy, while the features of the fracture surface were examined using scanning electron microscopy. In general, the voids were found to initiate at silicon particles. The individual voids then grew and coalesced, creating microcracks in the eutectic region. These microcracks linked up to form the main crack, resulting in the final fracture.

Lee *et al.*[177] observed that the fatigue crack growth in Al-Si-Mg casting alloys occurs either by the nucleation and linkage of microcracks or voids formed as a result of the decohesion of non-fractured Si particles from the surrounding matrix (such as those encountered in modified alloys), or by cleavage or the cracking of silicon particles (such as

those occurring in unmodified alloys), or both. In alloys containing intermediate Si particle size ranges, a mixed fracture morphology is observed, with both the cleavage fracture of Si particles and particle decohesion taking place.

Thus, the fracture mechanism proceeds as follows:

(i) cracking of the Si particles or their decohesion from the Al matrix at low strain;

(ii) localized plastic deformation with increase in strain, leading to the formation of microcracks in eutectic regions;

(iii) microcrack coalescence followed by crack propagation, leading to final fracture.[123,178]

Figure 6.3 shows a schematic representation of the process.

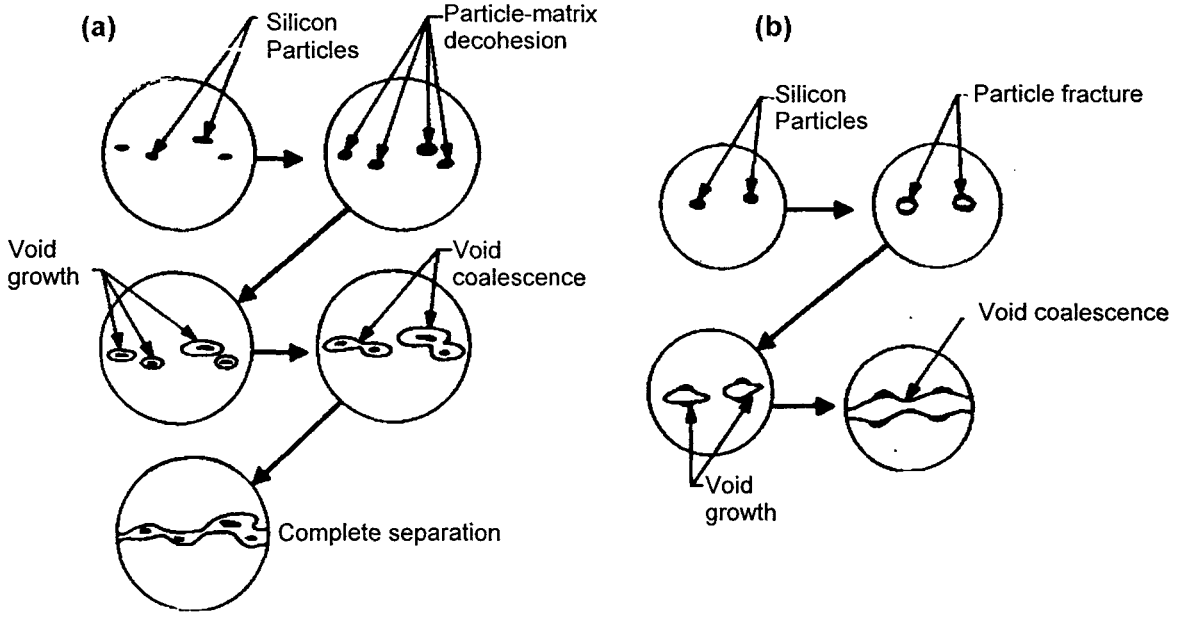

Figure 6.3. Schematic illustration of fracture mechanisms based on Si particles. (a) Initiation by Si particle-Al matrix interface decohesion. (b) Initiation by Si particle fracture.[178]

According to Dighe and Gokhale,[120] in commercial A356 alloy, the fracture path of tensile-tested specimens proceeds mainly through the largest silicon particles, which constitute less than 1% of the overall population of silicon particles in the bulk microstructure. Cáceres and Griffiths[127,128] pointed out that the larger and longer silicon particles are more prone to cracking. In coarser structures, silicon particle cracking occurs at low strains, while in finer structures, the progression of damage is more gradual. They also found that in the former case, broken particles were observed at both cell and grain boundaries, with no evident preference for either, whereas in the case of finer structures, cracking initiated on the grain boundaries. Lee *at al.*[177] also reported that the fatigue behavior of Al-Si-Mg casting alloys depends on the size, orientation, and local distribution of the Si particles.

6.1.2 Strontium Modification

As strontium modification is commonly employed to alter the morphology of the eutectic Si particles in Al-Si alloys, the process is expected to affect the fracture behavior of the alloy. Hafiz *et al.*[166] studied the role of microstructure in relation to the toughness of hypoeutectic Al-Si casting alloys, using U-notched Charpy impact test samples. Additions of 0.017 or 0.03 wt% Sr were employed to modify the alloys. In the unmodified alloy, the fracture followed a path marked by the eutectic Si, circumventing the primary Al dendrites, where Si particles could be seen adhering to the sides of the crack path. Detection of submicroncracks showed that the fracturing of the Si particles corresponded to an early stage of the crack propagation process, *i.e.*, the Si particles tend to fracture ahead of the

main crack. In the modified alloy, the fracture propagated through both the eutectic region and the Al matrix, with sheared aluminum cells being detected in the fracture path, and the submicroncracks observed in the eutectic regions clearly indicating that the interdendritic structure had failed first.

Hafiz and Kobayashi[119] observed that in unmodified Al-8% Si alloy, fracture surface mainly consists of a complicated array, resembling the Si array in the eutectic region containing cleaved Si particles. In addition, broken Si particles could also be detected. In the Sr-modified condition, two main features were observed: dimple colonies which represented the majority of the fracture surface, and a smooth ripple pattern surrounding the dimple colonies, typical of ductile fracture.

According to Voigt and Bye,[121] even though the fracture details are influenced by the Si particle morphology and the Al matrix, the basic fracture sequence is independent of changes in their microstructural characteristics due to the strontium modification. However, the addition of strontium does increase the amount of strain required to initiate and propagate the microcracks, particularly with respect to crack initiation.

6.1.3 Iron Intermetallics

Their brittle nature, lateral or faceted growth mode (which makes them poorly bonded to the Al matrix) and the multiple (001) growth twins (parallel to the growth direction) of the plate-like β-Al_5FeSi iron intermetallic particles make them pro-crack sites. Hrong *et al.*[179] studied the fracture behavior of A356 alloys with different iron contents under resonant vibration. According to them, the cracks were found to initiate and grow along the

eutectic Si and Fe-rich intermetallic phase particles. The crack paths propagated predominantly through the Si particles, and occasionally through the Fe-rich intermetallics. When the iron content was below 0.57 wt%, the iron intermetallics were mainly α-$Al_8Mg_3FeSi_6$ or α-$Al_5Fe_3Si_2$, whereas above that, the Fe-intermetallics occurred mostly as β-Al_5FeSi, which was found to be detrimental to the vibration fracture resistance.

According to Surappa *et al.*,[122] directly after the onset of plastic deformation, Al-7Si-0.3Mg sand-cast alloys display microcracks which are associated with brittle grain boundary cracking and cleavage of plate-shaped iron intermetallics, although the iron content is as low as 0.1 wt%. Intermetallics can be seen only in part of the grain boundaries failed by brittle fracture. In die-cast alloys, microcracks occur due to fracture of small intermetallic particles located at interdendritic boundaries. With the increase in strain, Si particles at grain boundaries begin to fracture, followed by decohesion from the matrix.

Kato[132] examined the microstructure of Al-7.0% Si-1.0% Fe alloys during tensile deformation using optical microscopy and *in-situ* scanning electron microscopy. He found that the needle-like β-iron intermetallics are cracked easily in the earlier stages of deformation, whereas the α-iron Chinese script intermetallics can withstand a higher stress. When the form of the iron intermetallics was changed from Chinese script to needle-like, crack initiation did not occur at the silicon particles but at the iron intermetallics.

Villeneuve and Samuel[133] found that in Al-13%Si-Fe alloy castings, cracks appeared within the β-Al_5FeSi platelets rather than at the β/Al interface. This is due to the brittle nature of the β-phase, whereby the platelets are easily split into two halves.

6.1.4 Solidification Rate

As the solidification rate directly affects the microstructure of an alloy casting, it is expected to affect the fracture behavior as well. The work of Surappa *et al.*[122] on the tensile testing of Al-7Si-0.3Mg alloy showed that, in sand-cast alloys, microcracks are associated with brittle grain boundary cracking and the cleavage of plate-shaped intermetallics and can be observed only in those parts of the grain boundaries that failed by brittle fracture, indicating an intergranular fracture mode. In die-cast alloys, all microcracks observed are due to the fracture of small intermetallic particles and located at interdendritic boundaries, indicating the fracture mode to be the transgranular type.

The work of Cáceres *et al.*[130] on fracture behavior of an Al-7Si-0.4Mg (A356.0) casting alloy shows that under low cooling rate conditions, when coarse structures are observed, the cell boundaries are distinct, the cracked particles are located with equal probability in the cell and grain boundaries, and the fracture mode is of the transgranular type. At high cooling rates (*viz.*, in fine structures), the cracked particles are preferentially located in the grain boundaries, and the fracture mode is of the intergranular type.

In a similar study, Wang *et al.*[131] observed that in large cell-size material, the fracture tends to occur along the dendritic cell boundaries (transgranular fracture), while for smaller cell-size material, the fracture path runs along grain boundaries in an increasing proportion (intergranular fracture). The proportion of intergranular fracture increases from zero at large DAS values to about 60% for small dendrite arm spacings.

The work of Samuel and Samuel[96] on 319.2 alloys using end-chill castings showed that, in general, fracture surfaces of alloys obtained at 5-mm distance from the chill (DAS

~15 μm) displayed a transgranular mode of fracture, typical of ductile materials. At the highest distance from the chill (100 mm, DAS ~95 μm), however, the fracture was of the intergranular type, customarily associated with brittle, low-ductility materials.

6.1.5 Porosity

According to Surappa *et al.*,[122] after the onset of plastic deformation which generates microcracks, intense shear bands commonly form. They are oriented in directions of about 45 degrees with respect to the tensile axis and propagate preferentially along grain boundaries. Microcracks grow and link along these shear bands. The presence of porosity can support shear band formation but does not initiate shear bands in the absence of the intermetallic particles. In certain cases, pores can even act as crack stoppers if located at the tips of sharp cracks.

Estensoro *et al.*[180] studied the fatigue behavior of two cast Al-7% Si alloys, with magnesium contents of 0.3 and 0.45%, respectively, and observed a very strong effect of defects (porosity) on the fatigue life. Fractographic examination showed that the strong scatter in fatigue life was associated with the amount of porosity in the specimen, and determined by the number, size and location of the pores in the fatigue specimens. The dispersion was more significant when the porosity emerged at the specimen surface. They also found that porosity exerts more influence on fatigue life than chemical composition or heat treatment.

In their investigation of the high-cycle fatigue testing of AlSi11 cast aluminum alloy, Stanzl-Tschegg *et al.*[181] also showed that casting voids reduce the fatigue strength and lead

to early fracturing. Crack initiation occurs at these voids, particularly if the porosity acts as a stress concentrator. The crack initiation times are strongly influenced by the position of the porosity, *viz.*, whether it is close to the surface or to the center of the specimen.

Savelli *et al.*[182] also reported that, in cast AlSi7Mg0.3 aluminum alloys, internal pores are responsible for the crack initiation of fatigue cracks. Based on this, a mathematical model was proposed by them to predict the fatigue life using pore dimensions as the main parameter.

6.2 FRACTOGRAPHY RESULTS

Optical and scanning electron microscopy were used to examine the facture surfaces of selected impact-tested samples. In each alloy, samples with the lowest and highest iron levels were taken, obtained at the highest and lowest cooling rates (*i.e.*, at DASs of ~23 μm and ~85 μm). Taking both the unmodified and Sr-modified alloys into account, a total of twenty-four fracture surfaces were examined as follows.

3 alloys × 2 Fe levels × 2 cooling rates × 2 Sr levels = 24 samples

In each case, at least two SEM micrographs were taken, one from the edge, and one from the central region of the fracture surface, to observe the crack initiation and crack propagation characteristics, respectively. In addition, interesting features appearing on the fracture surface were also examined. Optical micrographs from longitudinal sections (perpendicular to the fracture surface) of these samples, particularly those of A356.2 alloy, were also obtained, to further interpret the fracture process.

6.2.1 SEM Fractography

The popular use of a scanning electron microscope for fractography studies is on account of the fact that it allows for a direct examination of the fracture surface without the need for a replica, as in the case of transmission electron microscopy. One of the great advantages of the SEM is its ability to examine specimens at low magnifications of about 50 diameters, then enlarge regions of special interest to very high magnifications.

Both backscattered electron and secondary electron modes of operation are normally employed for fractographic purposes. The secondary electron image (SEI) offers a better resolution, whereas the backscattered electron image (BEI) offers an improved image contrast that is necessary in the case of smooth specimens and at low magnifications. The high image contrast is, however, accompanied by a loss of resolution, inherent with the backscattered mode of operation.

Backscattered electrons are electrons with high energy (equivalent to that provided by the accelerating voltage, which is usually in the range of 20-25 kV). The electrons escape from as deep as 300 Å in the specimen. Because of scatter within the specimen, the resultant source is much larger in diameter than the incident-beam diameter. On the other hand, the secondary electrons that are generated possess energies of about 20-50 eV (maximum), which is no more than is required for the electrons to escape from the top 100 Å layer of the specimen. A zone within 100 Å of the surface, then, constitutes the source of secondary electrons that can be captured by the electron collectors. Secondary electrons generated further within the specimen do not have enough energy to escape. The

difference in the volume of the source for the two types of electrons accounts for the difference in resolution.[183]

Most of the fractographs presented here are backscattered electron images, to bring out the contrast in the various features observed on the fracture surfaces of the samples studied.

6.2.1.1 Alloys 319.2 and B319.2 (Alloys A and B)

The SEM fractographs of the 319.2 alloy sample corresponding to the 0.4% iron level and highest cooling rate are presented in Figures 6.4 and 6.5, taken respectively from the sample edge where the sample was hit during impact testing, and the center of the sample surface.

The features exhibited in Figure 6.4 are typical of cleavage fracture, as is expected to be the case at high deformation rates during impact loading. The fracture plane changes orientation from grain to grain. A certain amount of intergranular cleavage is also observed in the form of secondary cracks. The fracture surface reveals the presence of β-Al_5FeSi iron intermetallic platelets, undissovled $CuAl_2$ or Al_7Cu_2Fe (insoluble phase) particles (since all alloy samples were T6-heat treated), and acicular Si particles surrounding them. The fragmentation of all three particle types indicates that possibly all three could have acted as crack initiation sites. The microstructural constituents of interest in Figure 6.4 and those that follow have been marked in each case.

Figure 6.5, taken from the central region of the fracture surface of the same sample, shows a cracked α-iron script particle, surrounded by brighter Cu-containing phase

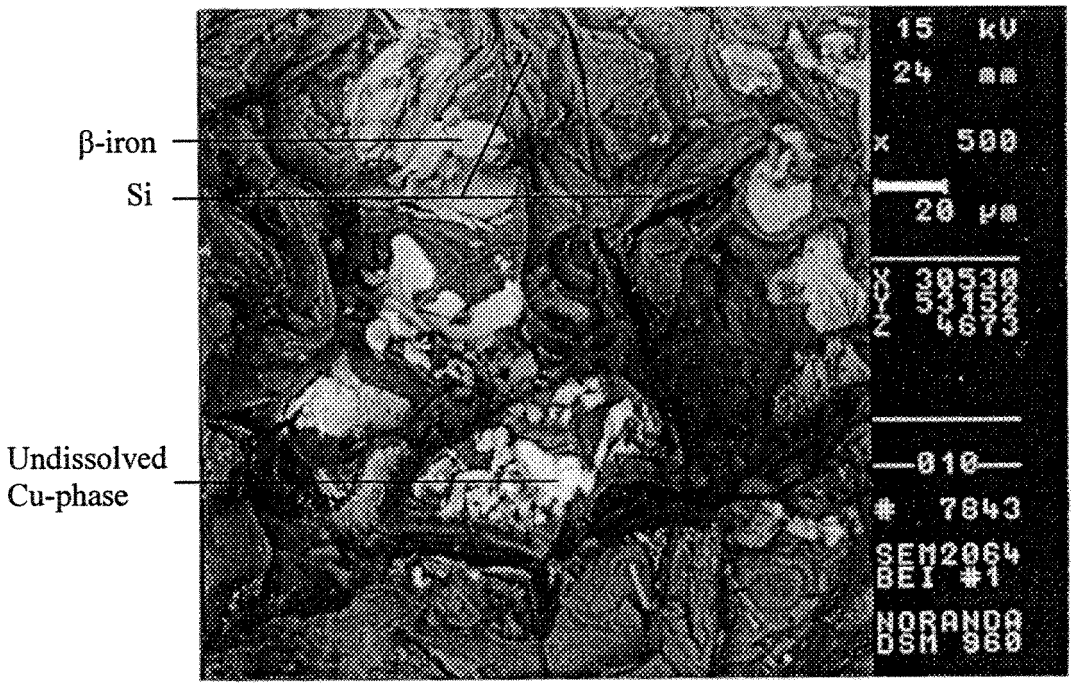

Figure 6.4. SEM micrograph showing fracture surface of alloy 319.2 (0.4% Fe, DAS 23 µm, unmodified, edge).

Figure 6.5. SEM micrograph showing fracture surface of alloy 319.2 (0.4% Fe, DAS 23 µm, unmodified, center).

particles on either side. The presence of cracks within these particles confirms how crack formation is facilitated when such intermetallics are present in the microstructure.

At the highest iron level (0.8%) and lowest cooling rate, the SEM fractograph of Figure 6.6 reveals that crack initiation occurs by massive cleavage of the brittle β-Al_5FeSi phase. A profusion of β-platelets is expected to be observed in the alloy microstructure at such Fe levels and, as can be seen, the crack propagates from one β-platelet across the other, along the direction delineated by the open arrows. In an ordinary two-dimensional optical micrograph, these β-platelets would appear in the form of branched needles. The much larger dimensions of the plate-like β-Al_5FeSi phase would make it more susceptible to crack initiation compared to the Si particles, even if the latter occur in brittle, acicular form in the unmodified alloy.

In cleavage fracture, the fracture path follows a transgranular plane that is usually a well-defined crystallographic plane, as is judged to be the case by the relatively smooth surfaces of the β-platelets seen in Figure 6.6.

The central area of the fracture surface of the same sample, Figure 6.7, shows instances of the Cu-containing (brighter) phase, precipitated on the β-platelets, amplifying the likelihood for crack propagation through these locations. The crack propagates in the direction denoted by the open arrows, along the cleaved intermetallic particles. A number of secondary cracks are also observed in the vicinity.

In keeping with the brittle fracture features observed in Figures 6.6 and 6.7, this sample exhibited a low impact energy of 1.90 J.

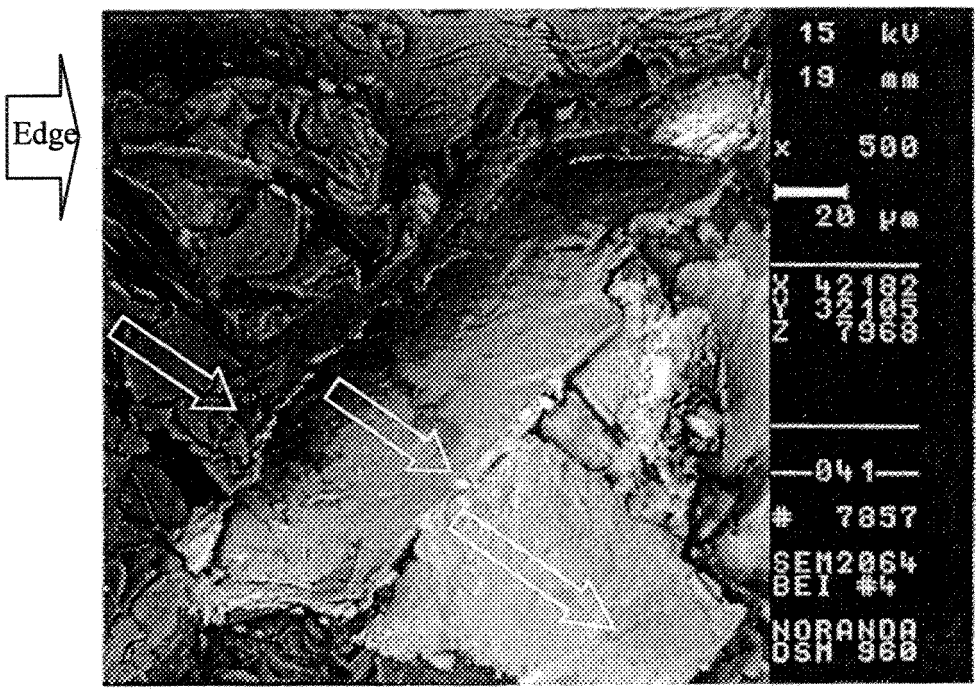

Figure 6.6. SEM micrograph showing fracture surface of alloy 319.2 (0.8% Fe, DAS 83 µm, unmodified, edge).

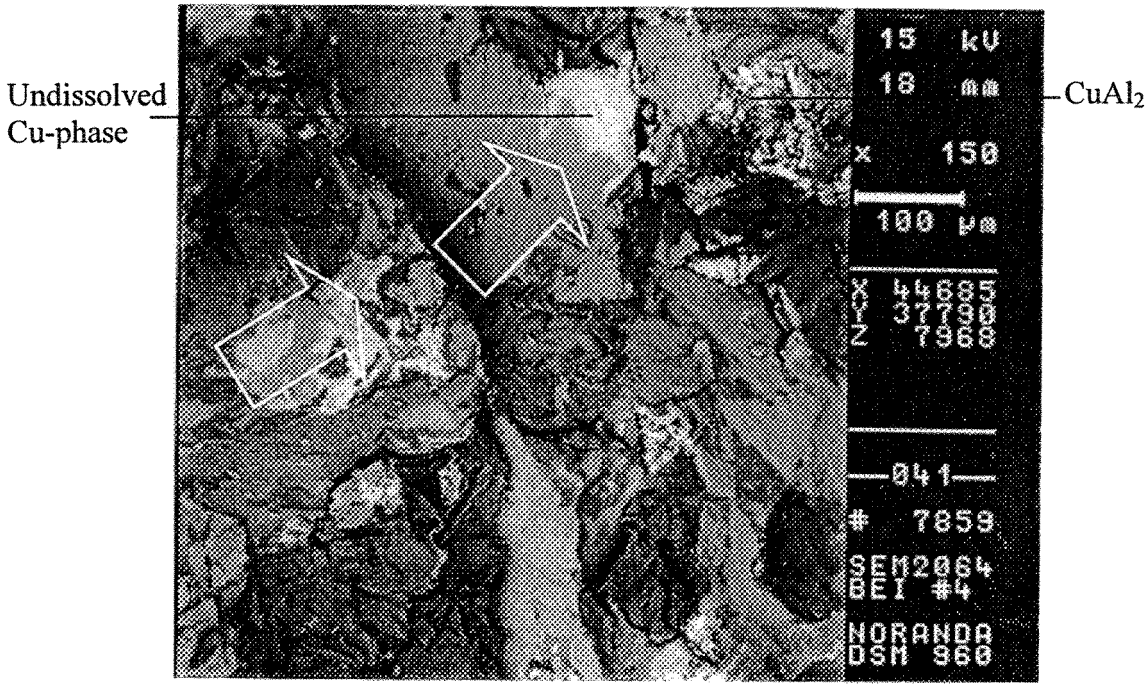

Figure 6.7. SEM micrograph showing fracture surface of alloy 319.2 (0.8% Fe, DAS 83 µm, unmodified, center).

In the case of the modified 319.2 alloy containing 0.4% Fe and obtained at the highest cooling rate, the SEM fractographs, Figures 6.8 and 6.9, revealed considerably different characteristics. Upon application of a high deformation rate during impact loading, Figure 6.8, the β-platelet at the edge of the sample fragmented into several smaller segments, rather than undergoing cleavage as was observed in Figure 6.4 for the unmodified alloy. Keeping in mind the effect of Sr (in the modified alloy) on the dissolution and fragmentation of the β-Al_5FeSi phase, the deterioration of the β-phase caused by Sr addition would more likely result in the fragmentation of the β-platelets rather than their cleavage (as observed in the case of solid β-platelets in the unmodified alloy). Consequently, crack propagation would proceed at a slower rate, leading to a higher impact energy, as indicated by the E_I, E_P and E_T of 16.39, 14.57 and 30.96 J, respectively. In addition, the transformation of the eutectic Si particles from acicular to fibrous form would also result in a more ductile fracture mode.

From the much higher magnification of Figure 6.8 (2000X) compared to that of Figure 6.4 (500X), one can also estimate the much smaller sizes of the β-platelets obtained in the modified alloy.

Figure 6.9 shows fractured α-iron script and Cu-containing phase (bright) particles. Due to the surrounding eutectic structure, the fracture surface is more reminiscent of ductile, rather than brittle, fracture, in spite of the cracks observed in the $CuAl_2$ particles.

In summary, therefore, Sr-modified Fe-containing 319.2 alloys would be expected to exhibit a mixed fracture mode. This is also reflected by their increased ductility, as observed from tensile testing.

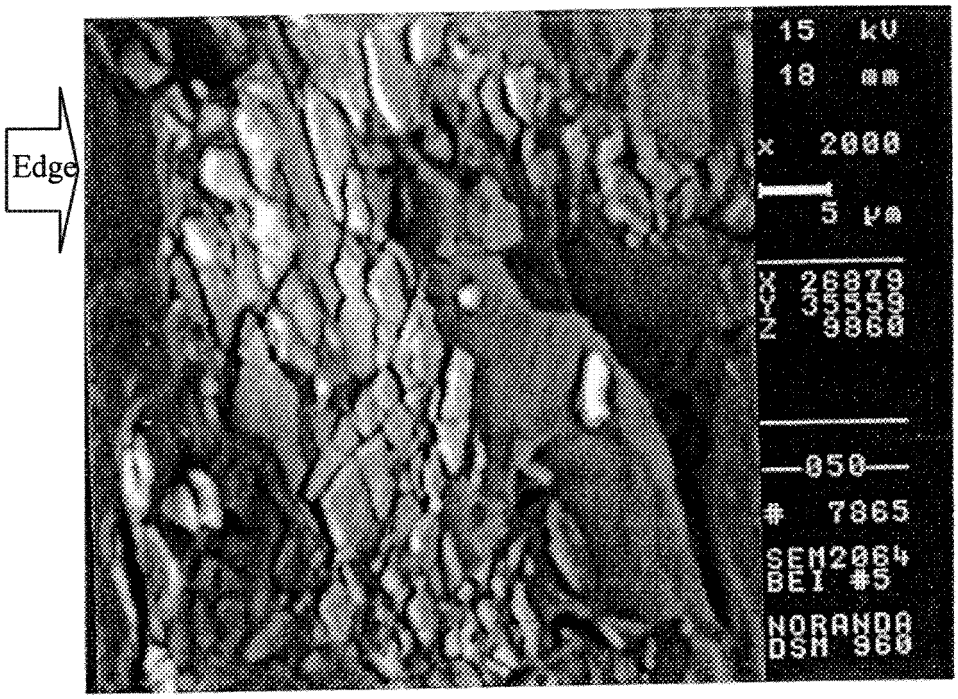

Figure 6.8. SEM micrograph showing fracture surface of alloy 319.2 (0.4% Fe, DAS 23 µm, modified, edge).

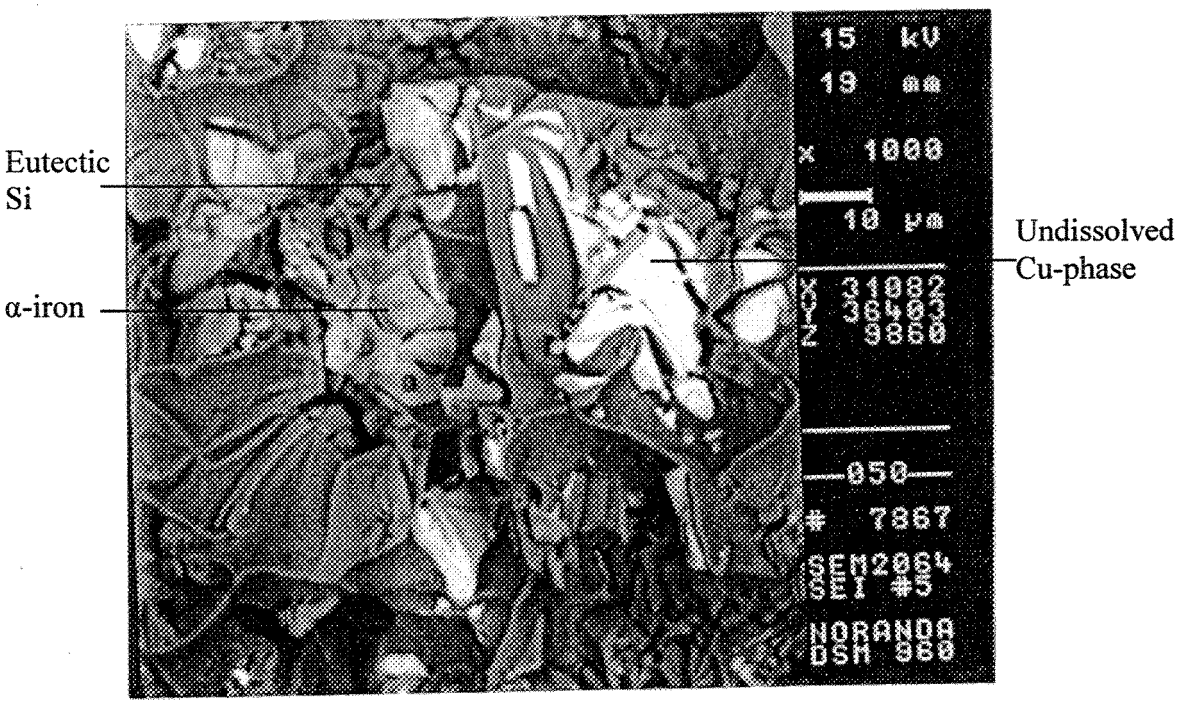

Figure 6.9. SEM micrograph showing fracture surface of alloy 319.2 (0.4% Fe, DAS 23 µm, modified, center).

Figures 6.10 and 6.11 show the SEM fractographs taken from the modified 319.2 alloy sample containing 0.8% Fe and obtained at the lowest cooling rate. Comparing Figure 6.10 with Figure 6.6 corresponding to the same alloy in the unmodified condition, the effect of Sr on the β-Al_5FeSi phase is evident, in the deteriorated appearance of the latter (see medium gray regions all over the fracture surface). The small bright spots in Figure 6.10 correspond to particles of undissolved $CuAl_2$. In Figure 6.11, however, the bright regions (marked C) viewed on top of the β-platelets are Cu-containing phases, most likely Al_7Cu_2Fe. As observed by Li *et al.*,[184] this phase is insoluble even after 100 h solution heat treatment at 500 °C. Compared to the flat surface of the β-platelet marked B, the perforated nature of those marked A is quite clear. Due to the high Fe content of the alloy, the volume fraction of β-Al_5FeSi phase, although considerable, appears distributed as smaller platelets all over the microstructure. It is interesting to note from the smooth surface of the β-platelet at B (and that at C below) that the β-platelets not modified by Sr cracked by cleavage quite easily, whereas elsewhere, the crack passed through other regions (*e.g.*, eutectic Si) as well, as evidenced by the intergranular cracking.

Both cleavage fracture and intergranular fracture are characteristically low-energy mechanisms, and the simultaneous operation of both can occur when the resolved stresses for transgranular cleavage are approximately equal. Also, if the preferred grain boundary fracture path is not continuous and if the cleavage stress is relatively low, the regions that do not fracture intergranularly can fracture by cleavage. Figure 6.11 shows an example of this type of fracture.

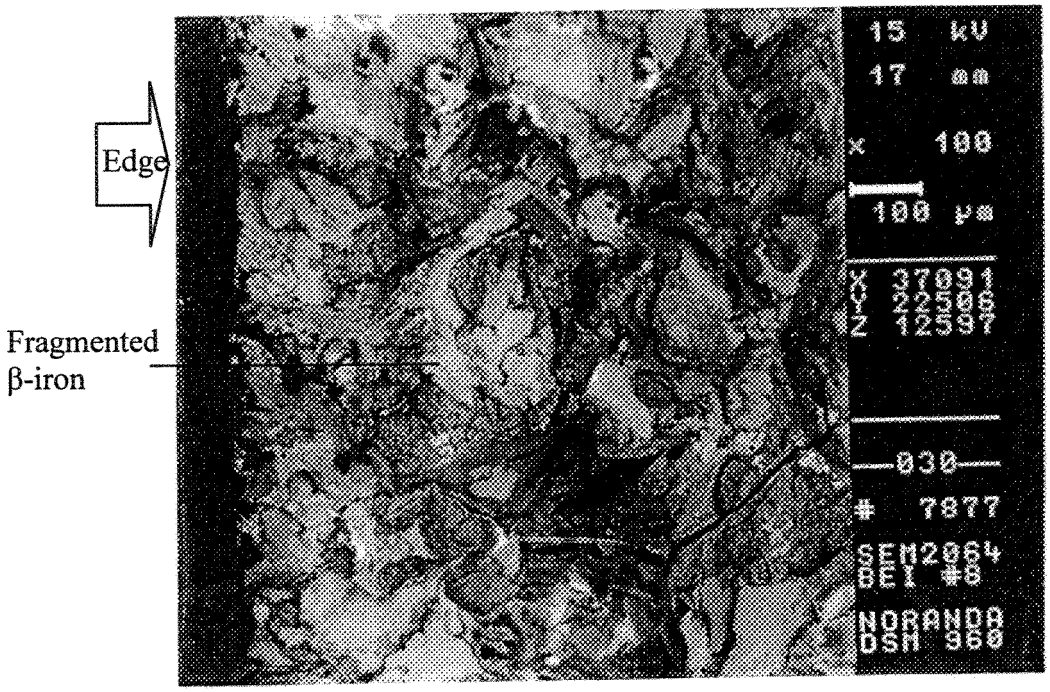

Figure 6.10. SEM micrograph showing fracture surface of alloy 319.2 (0.8% Fe, DAS 83 µm, modified, edge).

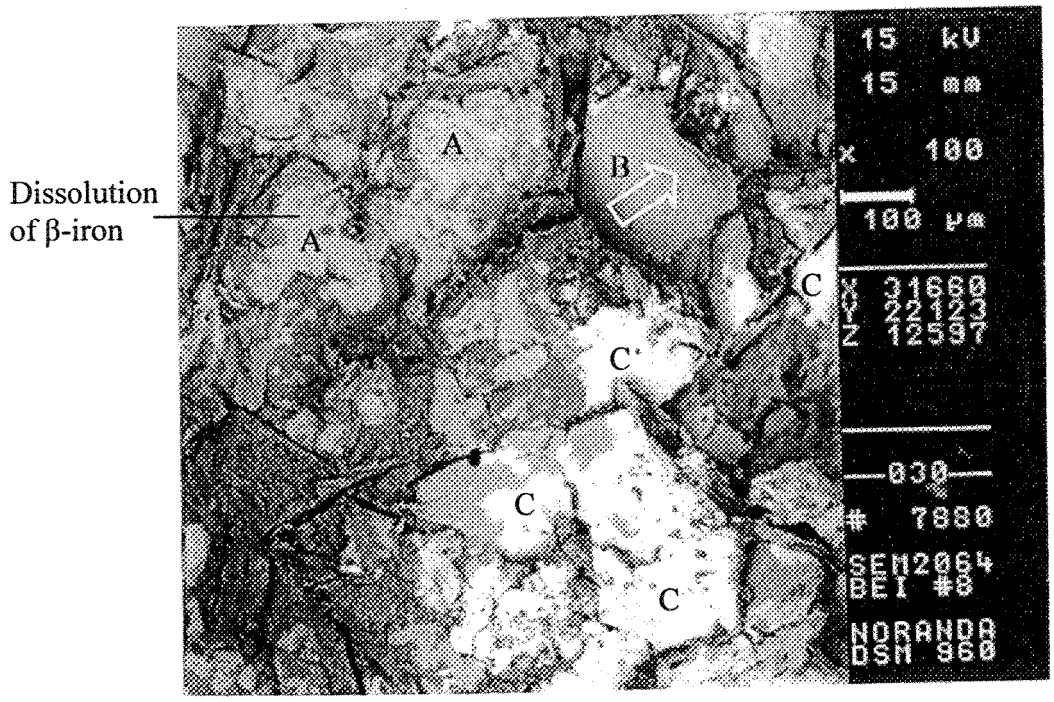

Figure 6.11. SEM micrograph showing fracture surface of alloy 319.2 (0.8% Fe, DAS 83 µm, modified, center).

From the overall mode of fracture observed in Figures 6.10 and 6.11, the modified alloy exhibits more resistance to crack propagation than that offered by the unmodified alloy (*cf.* E_I and E_P of 1.30 and 0.60 J with 1.63 and 1.43 J in the unmodified and modified alloys, respectively) where the brittle fracture/cleave features reflect the ease of crack propagation in that sample.

In what follows, some of the interesting features that were observed in the analysis of the fracture surfaces of various 319.2 alloy samples studied will be shown. These samples were selected to highlight other microstructural aspects such as inclusions or porosity, besides the α- and β-iron intermetallics and Si particles, that could affect the fracture behavior.

The SEM micrograph of Figure 6.12 shows the cleavage fracture of an α-AlFeSi intermetallic particle in the modified 319.2 alloy sample containing 0.8% Fe and obtained at the highest cooling rate. The fracture consists of several cleavage steps that provide an indication of the local direction of crack growth. Further above, the cleavage planes followed by the crack show various alignments, as influenced by the orientations of individual grains.

Another feature of cleavage fracture, the "tongue" appears on cleavage facets as very fine slivers (see arrows marked T) that result from cleavage across microturns formed by plastic deformation at the tip of the main propagating crack.[185] Around the α-AlFeSi particle, the surrounding eutectic Si regions are identified by the small microvoids and dimpled nature of the fracture surface, indicating the mixed fracture mode of the sample. The E_I, E_P and E_T in this case are 8.71, 1.31 and 10.02 J, respectively.

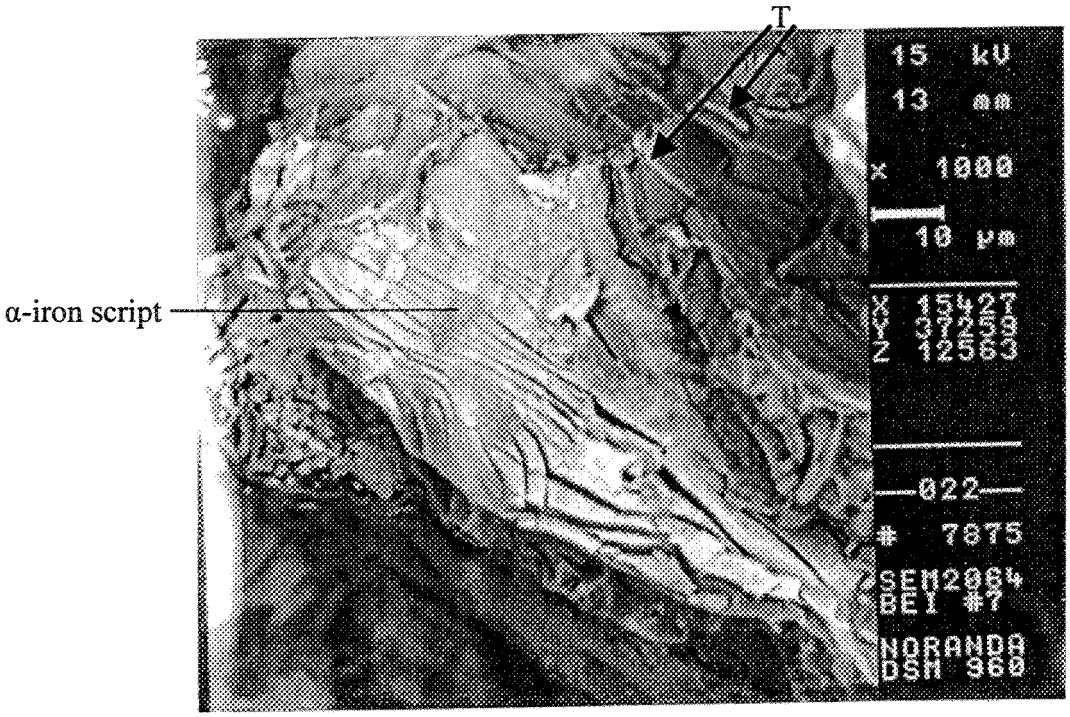

Figure 6.12. SEM micrograph showing fracture of α-AlFeSi intermetallics in alloy 319.2 (0.8% Fe, DAS 23 μm, modified).

It should be mentioned here that the iron intermetallic phases/particles referred to in the different fractographs presented in this chapter were identified using EDX analysis. The flat cleaved surfaces of these iron intermetallics facilitated identification. For the Cu-containing particles, it was difficult to obtain the exact composition of the $CuAl_2$ particles due to their size and the uneven nature of the surrounding fracture surface. In the case of the Al_7Cu_2Fe phase, as it occurred on top of the β-Al_5FeSi phase (the precipitation of the Al_7Cu_2Fe phase follows that of the β-Al_5FeSi phase[184]), its composition could not be verified correctly, as well.

Figure 6.13 shows another fractograph of the same sample, where the fracture surface consists of interlinked β-phase regions that would probably correspond to more than one branched β-platelets. Alpha-Al dendrites appear through parts of the β-phase where

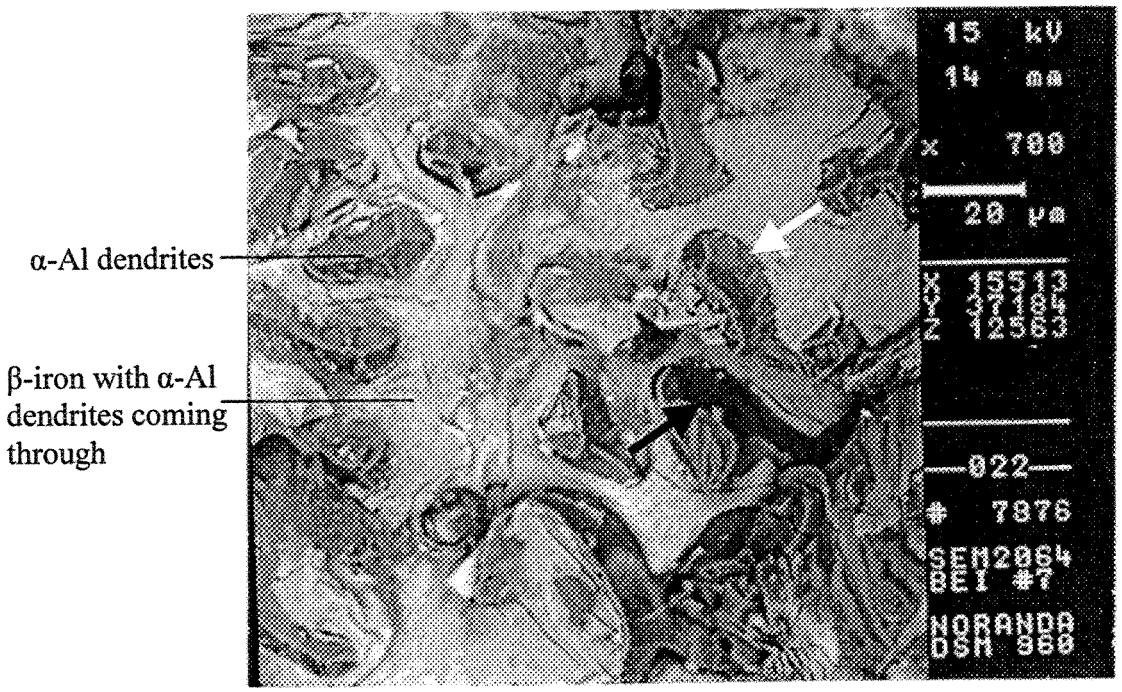

Figure 6.13. SEM micrograph showing fracture of β-AlFeSi intermetallics in alloy 319.2 (0.8% Fe, DAS 23 µm, modified).

dissolution of the platelets has occurred. Dimpled rupture of the eutectic Si regions interspersed in between is also observed. The shallow, depressed nature of the dendrite observed near the white arrow, together with the darker void region below (black arrow) indicate the existence of a pore in this area, which would have facilitated crack propagation. The smooth interface between the β-phase and the α-Al dendrite and the pore linked to them affirms the feedability-related characteristics of the β-platelet phase, aiding in the formation of porosity.

Figure 6.14 shows the fractograph taken from the unmodified B319.2 alloy sample containing 0.8% Fe, obtained at the highest cooling rate. Transgranular fracture of all intermetallics, *viz.*, the α-Fe, β-Fe and Cu-containing phases is observed. In this alloy, containing a higher level of Mg, the Cu-phase would include $Al_5Mg_8Cu_2Si_6$ and

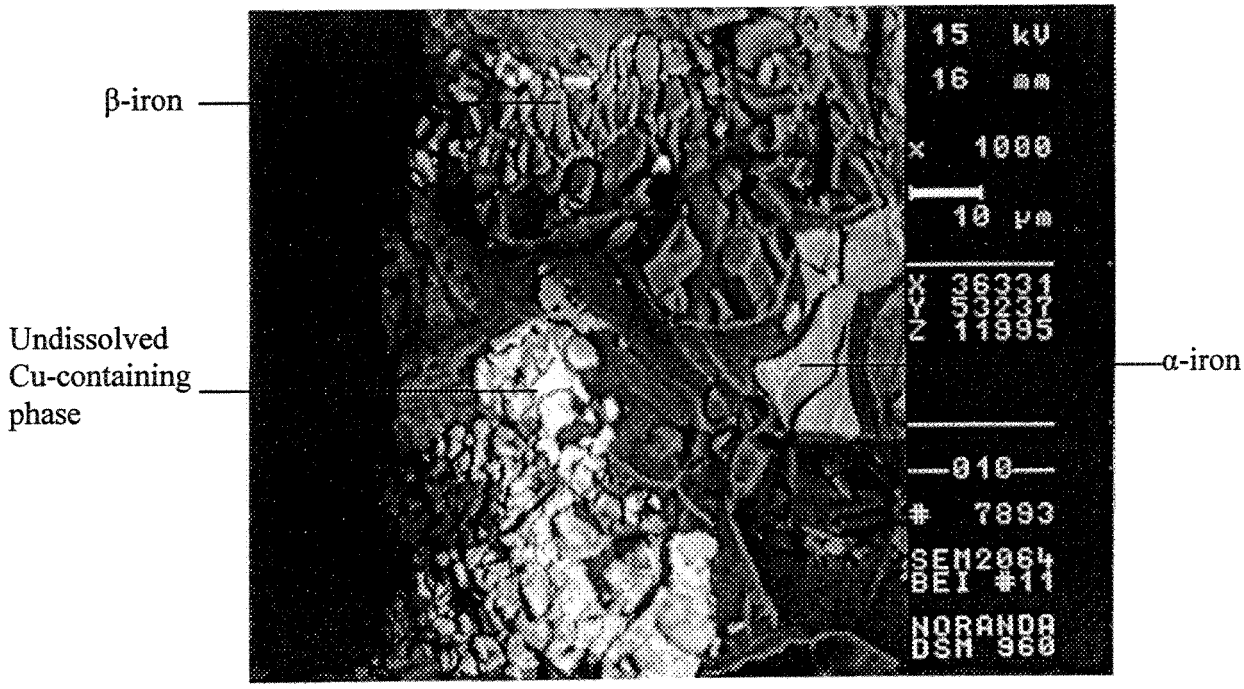

Figure 6.14. SEM micrograph showing fracture of both iron and copper intermetallics in alloy B319.2 (0.8% Fe, DAS 23 μm, unmodified).

$Al_{15}(Mn,Fe,Cu)_3Si_2$, in addition to the $CuAl_2$ phase. The presence of cracked Si particles and associated microvoids are also seen.

A comparison with the fractograph shown in Figure 6.6 (same Fe level, but lowest cooling rate) shows how a high cooling rate is more effective than the Fe content in determining the size of the β-platelets that result and, hence, the nature of the fracture, *i.e.*, fragmentation or cleavage (this point is further brought out in the context of Figure 6.16). The corresponding E_I, E_P and E_T of this sample are 6.18, 1.40 and 7.58 J, respectively. However, as Figure 6.15 shows, the β-platelet can still fracture by cleavage, particularly in regions where several platelets have precipitated together. The smooth surface of the various β layers in the figure clearly indicate that fracture in this part of the specimen

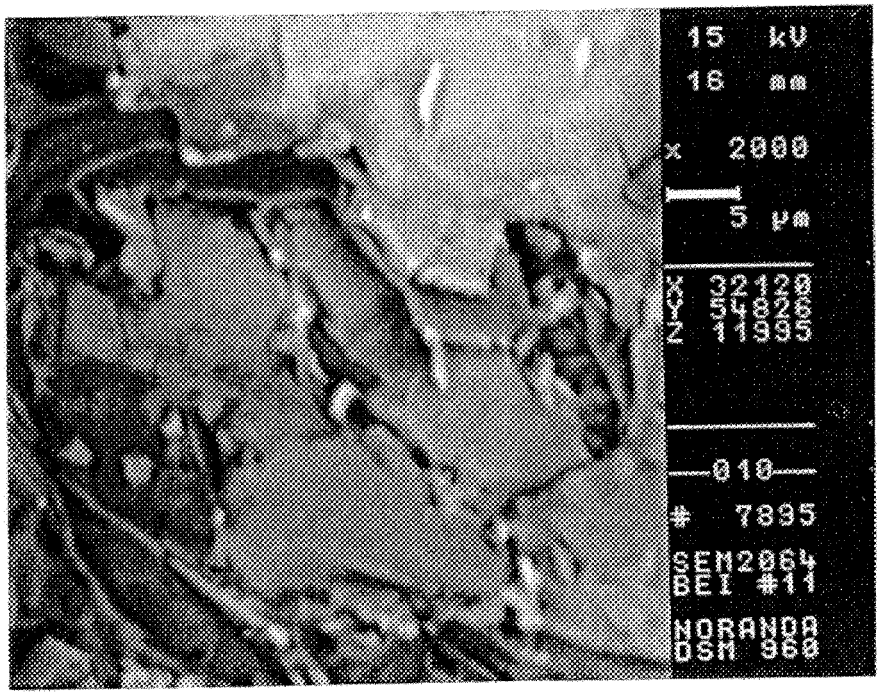

Figure 6.15. SEM micrograph showing fracture of β-platelets in alloy B319.2 (0.8% Fe, DAS 23 µm, unmodified).

occurred by cleavage. It is not hard to imagine the branched appearance of these several platelets in a two-dimensional optical micrograph.

The SEM fractograph, Figure 6.16, of the same 0.8% Fe-containing unmodified B319.2 alloy obtained, however, at the lowest cooling rate shows clearly the massive dimensions that the β-Al_5FeSi platelets can attain at the same 0.8% Fe level, depending upon the solidification conditions. Again, the platelet fractures by cleavage; the open arrow indicating the cleavage direction. Secondary cracks (white arrows) are also observed when the crack propagates through the eutectic Si regions.

Figures 6.17 and 6.18 are SEM fractographs obtained from modified 319.2 and B319.2 alloys, respectively, under the same Fe and solidification conditions (0.8% Fe, lowest cooling rate). The rather large dimensions of the pore observed in Figure 6.17, as evidenced

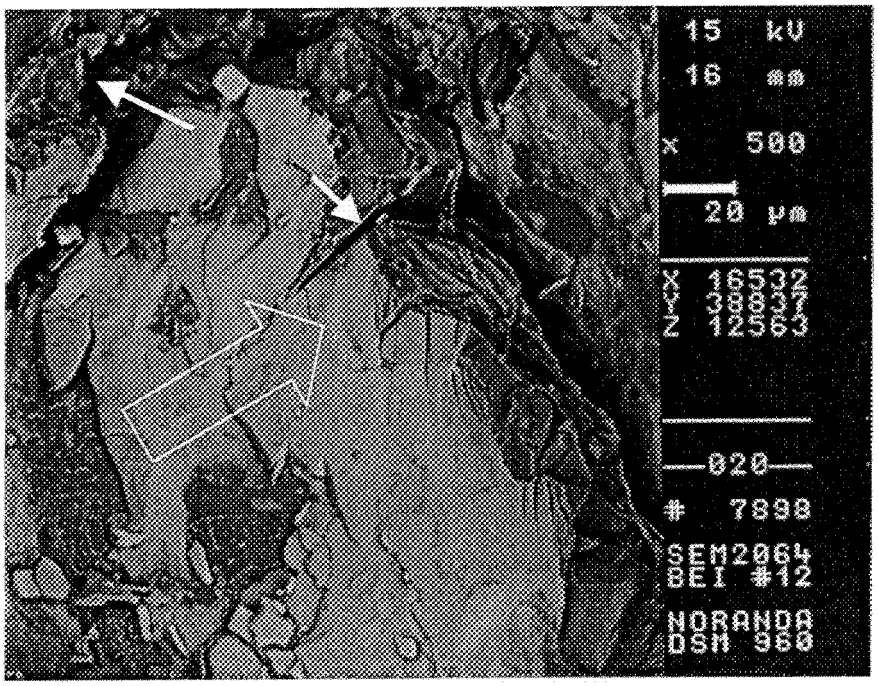

Figure 6.16. SEM micrograph showing fracture of β-AlFeSi intermetallics in alloy B319.2 (0.8% Fe, DAS 83 µm, unmodified).

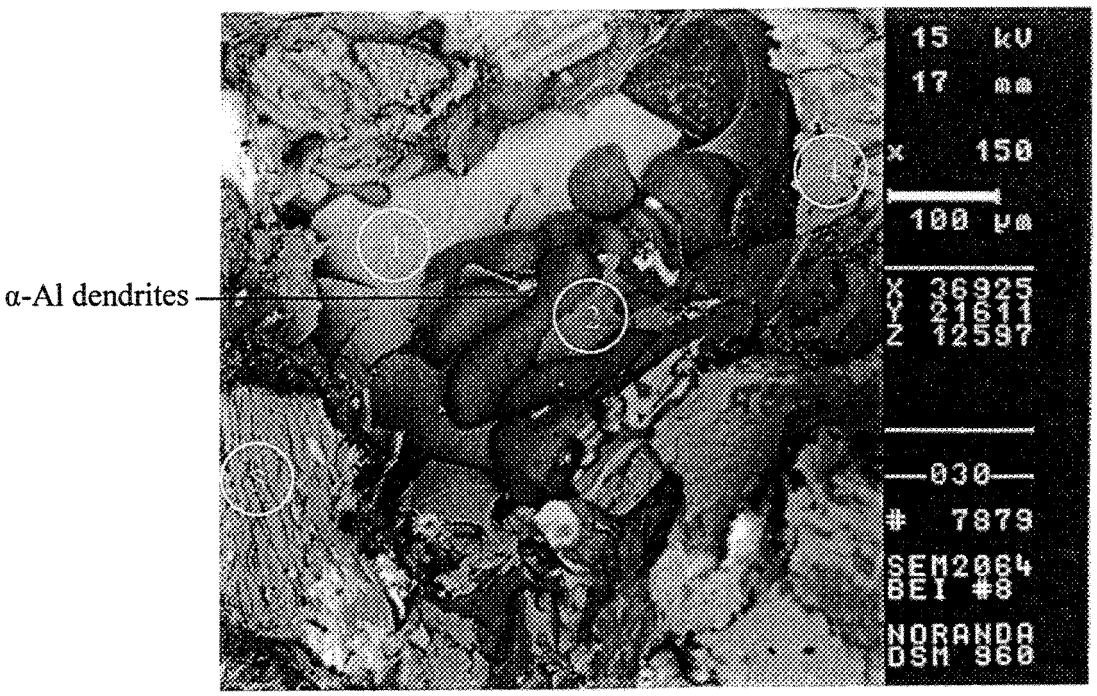

Figure 6.17. SEM micrograph showing the effect of porosity participating in the fracture behavior of alloy 319.2. (0.8% Fe, DAS 83 µm, modified).

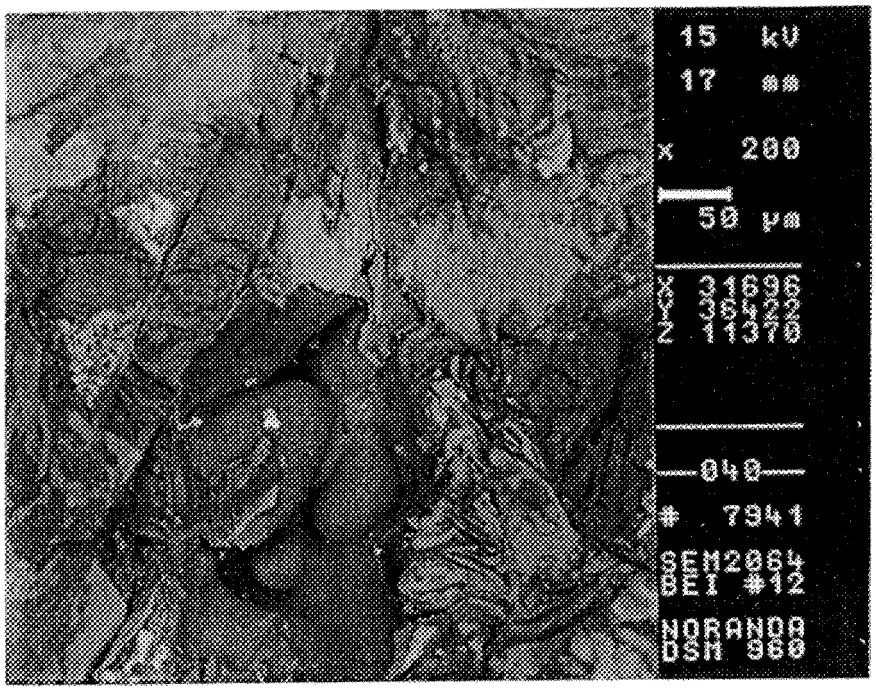

Figure 6.18. SEM micrograph showing the effect of porosity participating in the fracture of alloy B319.2. (0.8% Fe, DAS 83 µm, unmodified)

by the untouched α-Al dendrites sitting inside, show how the µ-phase platelets lodged beside (1) and between (2) the dendrites, restrict the flow of the liquid metal in the surrounding region, and hence lead to the formation of porosity. The presence of the pore facilitates fracture. In contrast to the fractured β-platelets (*e.g.*, 3 and 4) around the pore area, the β-platelets within the pore did not participate in the fracture process and remained quite intact.

Similarly, Figure 6.18 shows an example of a pore observed on the fracture surface of the modified B319.2 alloy. In this instance, the pore appears to be much smaller in dimension and more shallow than the one depicted in Figure 6.17, with fragments of cleaved β-phase platelets on the surrounding fracture surface. The dissolution of the β-platelets due to the effect of Sr is more evident in this fractograph.

6.2.1.2 Alloy A356.2 (Alloy C)

As was done for the 319 alloys, the fractographs of A356.2 alloy samples covering the lowest Fe content - highest cooling rate (optimum property) and highest Fe content - lowest cooling rate (minimum property) conditions have been selected for discussion purposes, to bring out the contrast in their fracture modes and hence comprehend the difference in their impact properties.

As Voigt and Bye[121] have commented, features appearing on the fracture surfaces of Al-Si-Mg casting alloys such as A356 alloys can be very difficult to interpret due to the lack of SEM contrast between the α-Al and the eutectic Si phases appearing on the surface. As Al and Si are close in their atomic numbers, even the use of SEM techniques such as backscattered electron imaging cannot provide additional phase contrast. However, the features observed on the fracture surfaces of A356 alloys can be more clearly interpreted based on a study of the surface crack initiation and propagation process. Usually, by observing the microstructure just below the surface that can be observed inside the crack using SEM techniques, or else by studying longitudinal sections of the fractured samples (perpendicular to the fracture surface) using optical microscopy, additional information can be obtained that is useful in analyzing fracture behavior.

Figures 6.19 and 6.20 are the SEM fractographs taken from the modified A356.2 alloy sample containing 0.1% Fe and obtained at the highest cooling rate. Figure 6.19 shows the fracture to be of the transgranular dimpled rupture type. As mentioned before, the BEI image does not provide a good phase contrast.

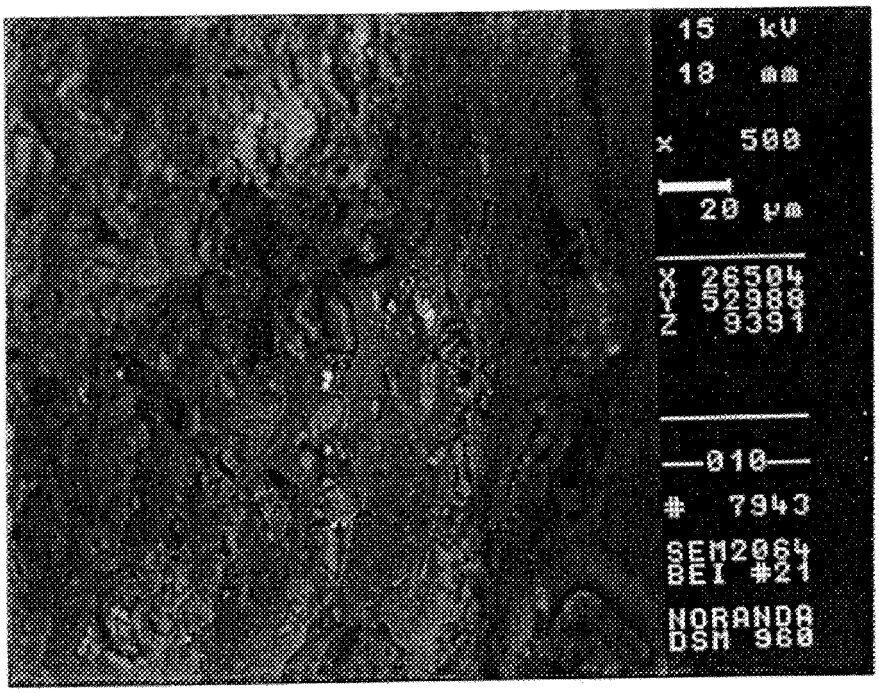

Figure 6.19. SEM micrograph showing fracture surface of alloy A356.2 (0.1% Fe, DAS 23 µm, modified, edge).

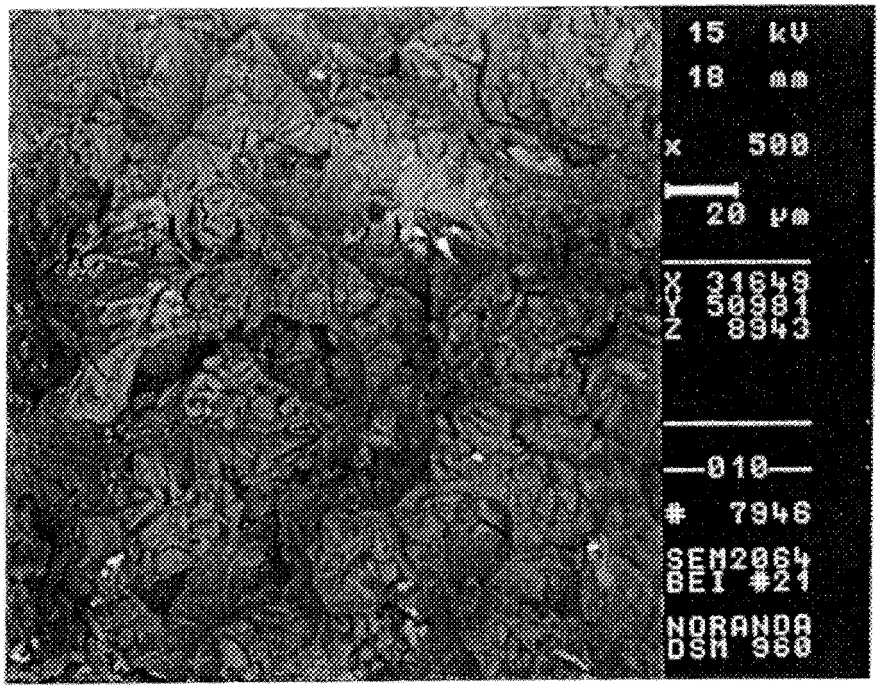

Figure 6.20. SEM micrograph showing fracture surface of alloy A356.2 (0.1% Fe, DAS 23 µm, modified, center).

The fractograph of Figure 6.20 taken from the center of the sample, shows these features more clearly. Note the fine Si particles in the structure. The absence of intermetallics due to the low Fe content, together with the fine Si particles obtained under the optimum alloy conditions of a high cooling rate and Sr modification, result in the sample exhibiting the highest impact energy (80.88 J).

Figures 6.21 and 6.22 depicts the SEM fractographs of the unmodified A356.2 alloy sample containing a high Fe level (0.6%) and obtained at the lowest cooling rate. The presence of massive β-Al_5FeSi platelets in the alloy microstructure under these conditions result in the brittle fracture of the sample. As Figure 6.21 shows, crack initiation takes place by the fragmentation of the β-phase at the edge of the sample and some amount of transgranular fracture, as well, whereas the crack propagates by cleavage fracture, as evidenced by the relatively smooth surfaces of the β-platelets observed in Figure 6.22, as also by intergranular fracture. Accordingly, the impact energy of this sample was 2.45 J.

When the same alloy is modified, crack initiation occurs by fragmentation of the β-Al_5FeSi platelet, followed by cleavage, as seen in Figure 6.23. Modified silicon eutectic regions around the β-platelet can also be distinguished. Figure 6.24 shows that the fracture mode is a mixture of cleavage and intergranular fracture.

The high magnification SEM fractograph of an unmodified A356.2 alloy sample containing 0.1% Fe and obtained at the lowest cooling rate, Figure 6.25, reveals the eutectic Si regions much more clearly, where the fracture is seen to occur by the transgranular brittle fracture of the acicular Si particles (see circled areas).

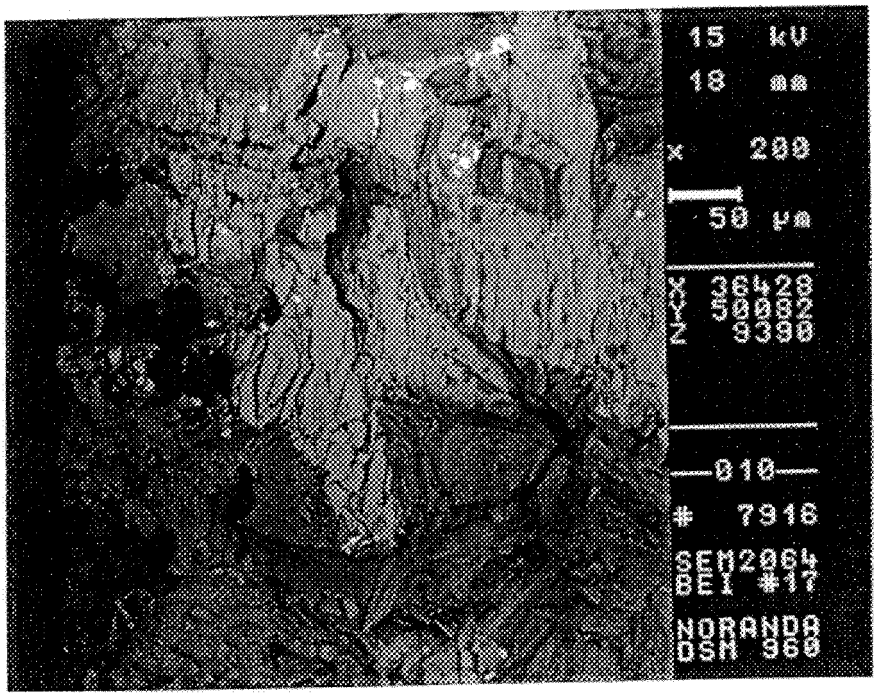

Figure 6.21. SEM micrograph showing the role of β-Al_5FeSi intermetallics in initiating fracture in alloy A356.2 (0.6% Fe, DAS 75 µm, unmodified).

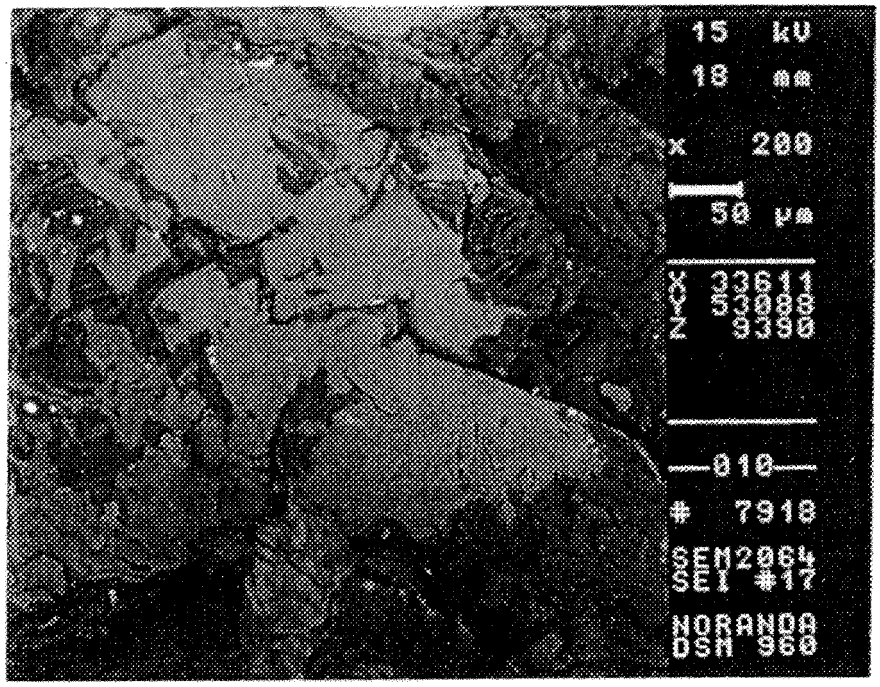

Figure 6.22. SEM micrograph showing crack propagation in alloy A356.2 (0.6% Fe, DAS 75 µm, unmodified).

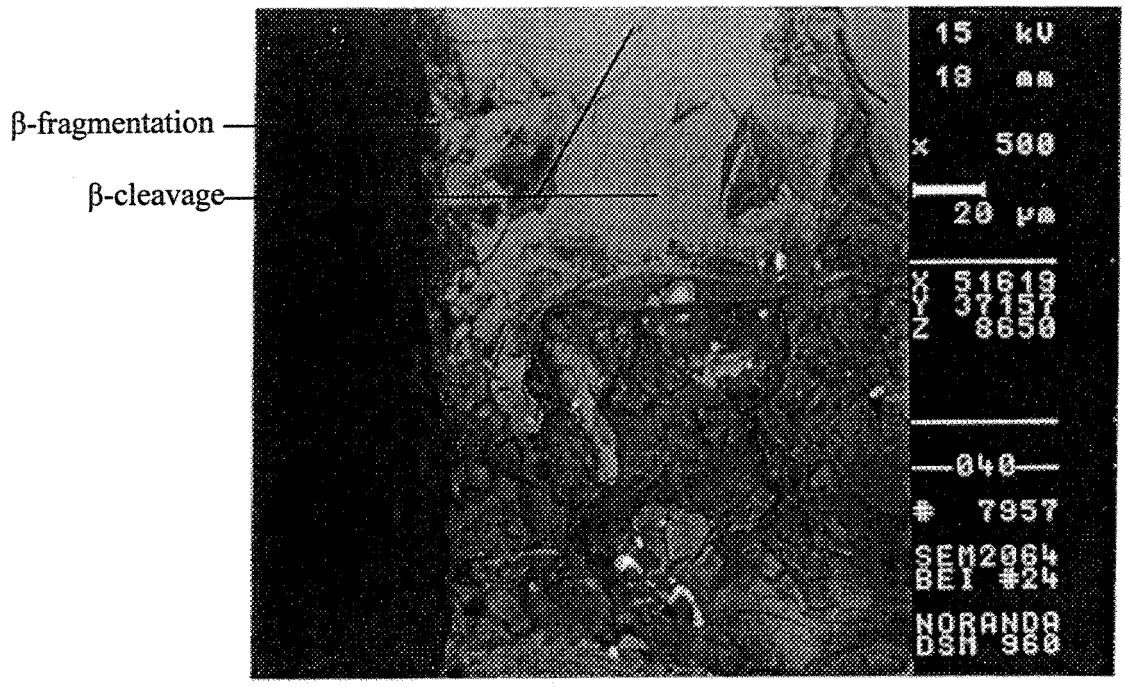

Figure 6.23. SEM micrograph showing fracture surface of alloy A356.2 (0.6% Fe, DAS 75 µm, modified, edge).

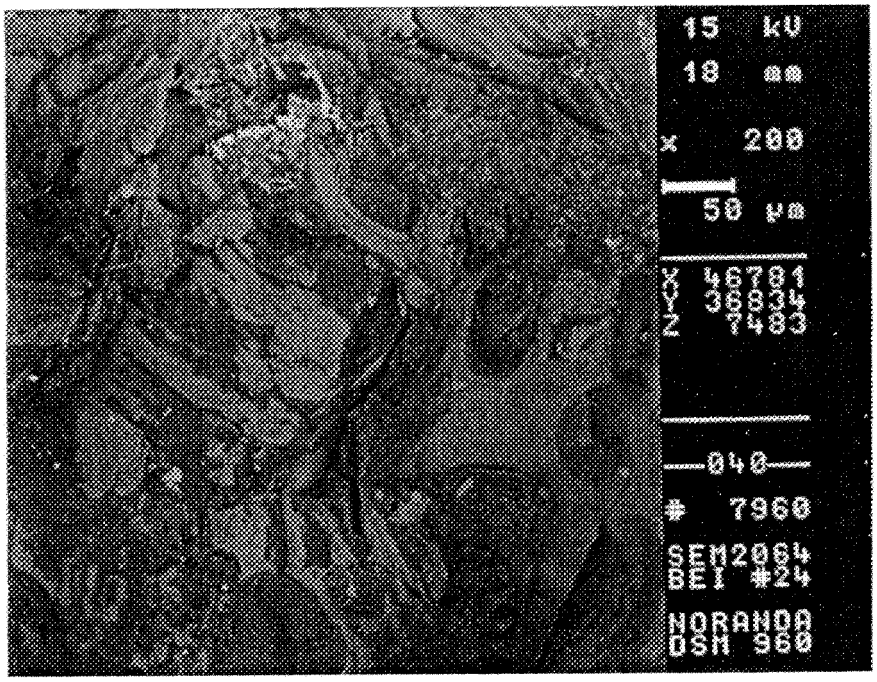

Figure 6.24. SEM micrograph showing fracture surface of alloy A356.2 (0.6% Fe, DAS 75 µm, modified, center).

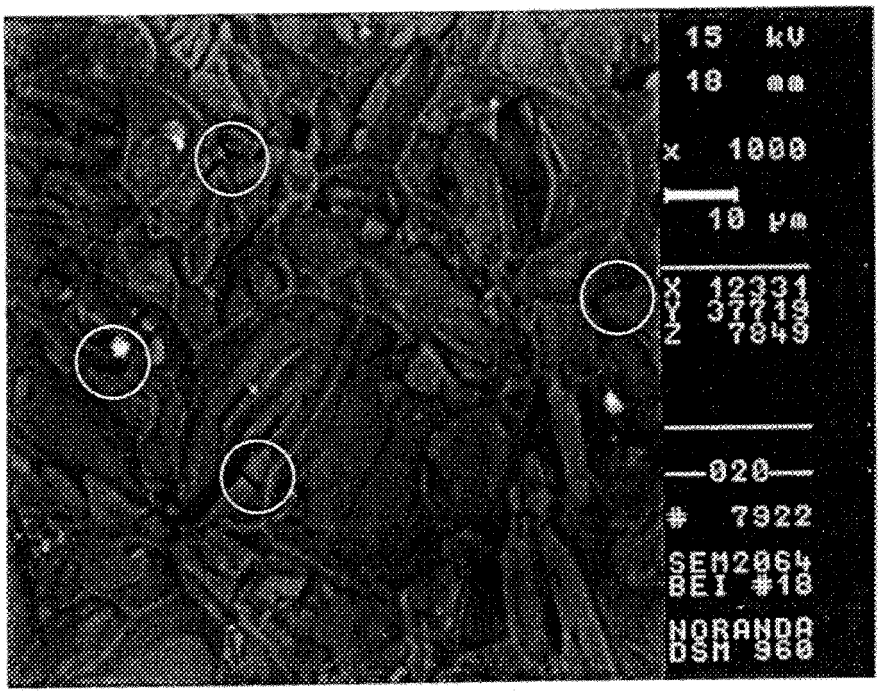

Figure 6.25. SEM micrograph showing fracture of eutectic Si particles in alloy A356.2 (0.1% Fe, DAS 75 µm, unmodified).

6.2.2 Optical Microscope Fractography

Regardless of SEM fractography, it is also quite useful to examine the fracture profile on sections perpendicular to the fracture surface. This can be carried out easily using an optical microscope. In this way, the origin of the fracture can be examined to determine if important microstructural abnormalities are present that either caused or contributed to fracture initiation. It is also possible to determine if the fracture path at the initiation site is transgranular or intergranular and to determine if the fracture path is specific to any phase or constituent present.[186] Some examples of the longitudinal sections of the A356.2 alloy samples are presented in this section with a view to further clarifying the fracture process in these samples as their SEM fractographs, did not display as good a phase contrast as those shown by the 319 alloy samples.

The optical micrographs presented in Figure 6.26 show the polished longitudinal section of the fractured A356.2 unmodified alloy sample containing 0.6% Fe, obtained at the lowest cooling rate. In (a), the edge of the sample on the left shows how crack initiation occurs by the cleavage and/or the transgranular fracture of the Si particles and β-Al_5FeSi platelets. The sample edge corner is relatively straight, indicating that cracking occurred almost immediately, *i.e.*, by brittle fracture mode, and the crack propagated along the direction shown.

A higher magnification micrograph, Figure 6.26(b), of the fracture surface corresponding to the circled area in (a), shows how the crack propagates further along the fracture surface by cleavage of the β-iron intermetallic and coarse Si particles. The persistence of such coarse Si particles, even after solution heat treatment at 540 °C/8h aids in inducing the brittle fracture of the sample. Correspondingly, under such alloy conditions, the sample exhibited the lowest impact energy (2.45 J), see Table 5.6. Figure 6.26 provides a good example of how optical microscopy can aid in providing a clearer interpretation of the crack initiation and propagation in A356 type Al-Si-Mg alloys.

The optical micrograph of Figure 6.27, taken from an A356.2 unmodified alloy sample containing 0.4% Fe and obtained at the highest cooling rate, shows the propagation of a secondary crack (see white arrow) that splits a β-Al_5FeSi platelet right through the middle. The crack propagates to the end of the platelet, till it reaches the aluminum matrix which, being ductile, allows for stress relaxation at the crack tip by local plastic flow.

Compared to the micrographs shown in Figure 6.26, those obtained from the A356.2 alloy sample corresponding to optimum energy conditions (*viz.*, 0.1% Fe, lowest cooling

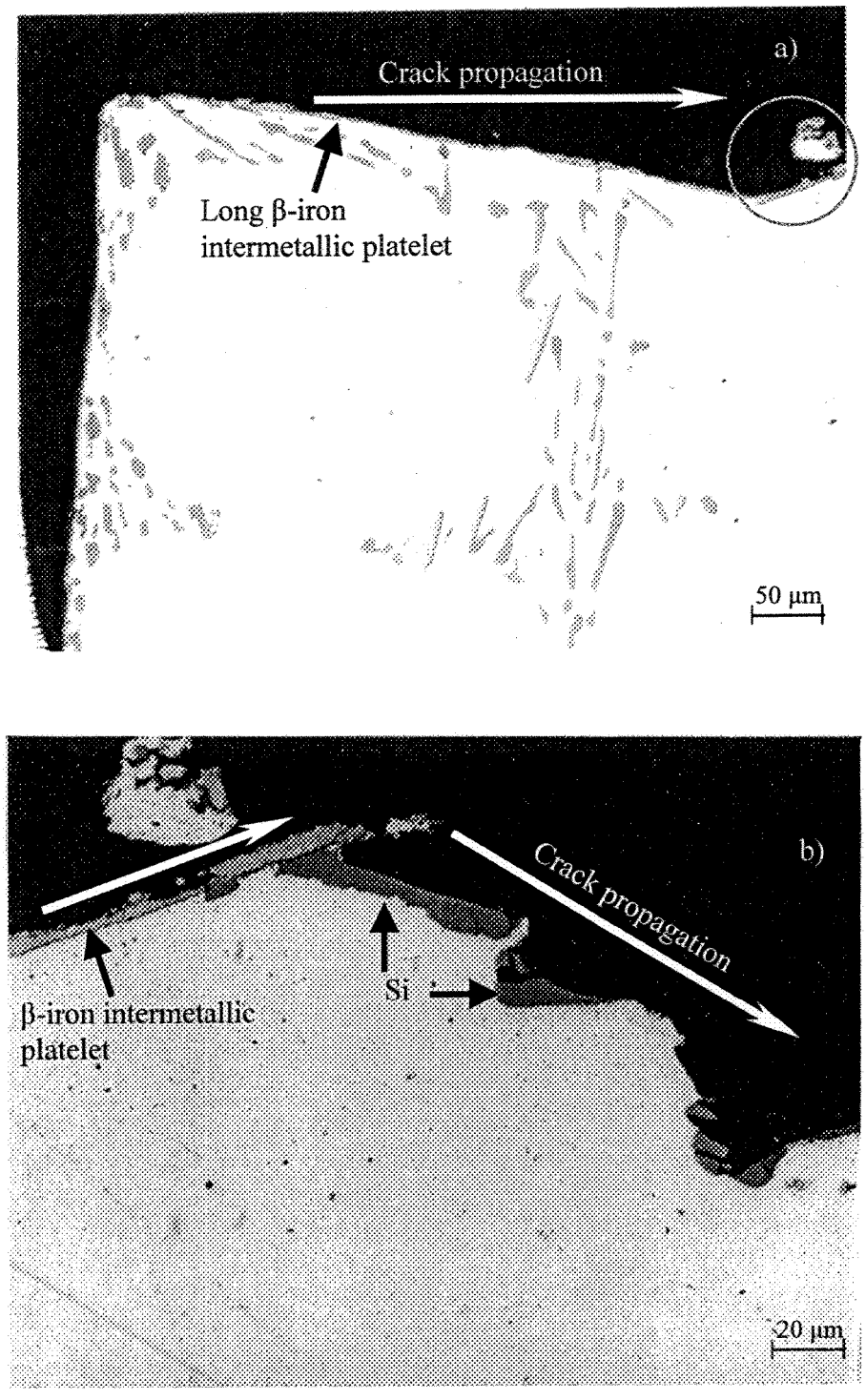

Figure 6.26. Optical microstructures showing fracture behavior of alloy A356.2 (0.6% Fe, DAS 75 μm, unmodified, edge). A high magnification micrograph of the circled area in (a) is shown in (b).

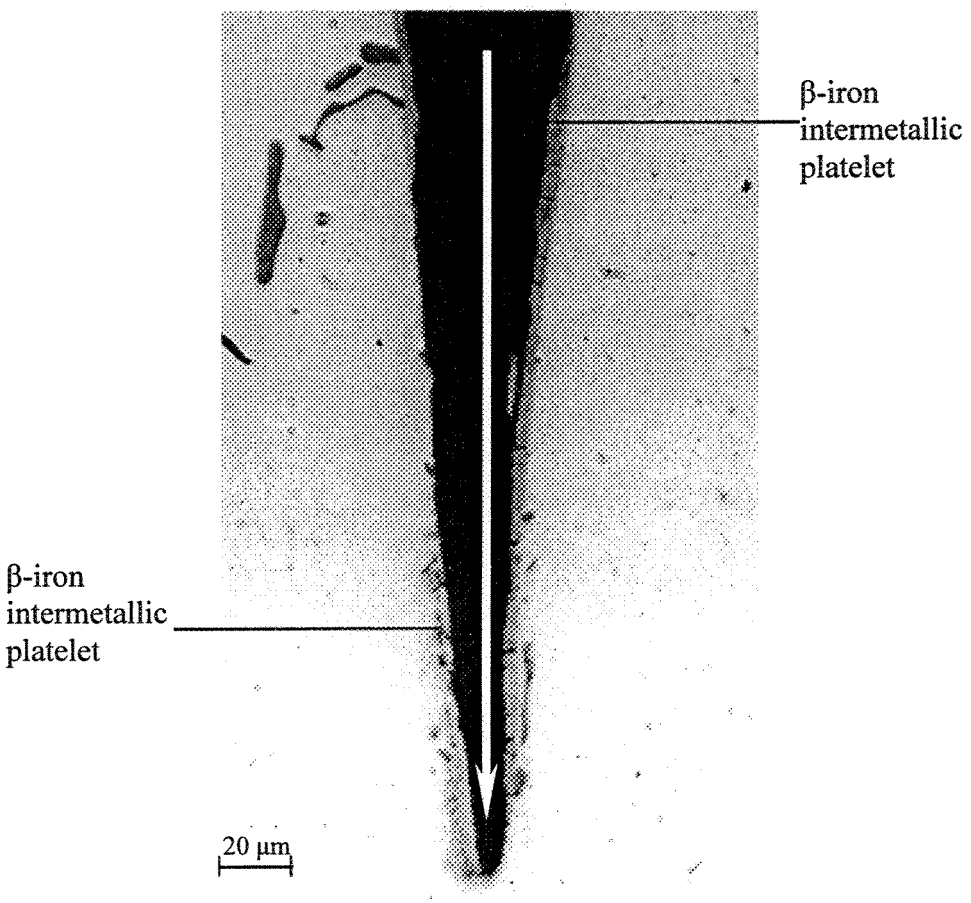

Figure 6.27. Optical micrograph showing fracture behavior of alloy A356.2 (0.4% Fe, DAS 23 μm, unmodified, edge, 500×).

rate, Sr-modified alloy), Figure 6.28, shows how the sample edge is more curved or rounded (Figure 6.28(a)), rather than flat as was observed in the case of the unmodified alloy sample of Figure 6.26. The curvature of the fracture surface, also clearly observed in Figure 6.28(b) indicates a ductile mode of rupture as the crack propagates through the well-modified Si eutectic regions. The E_I, E_P and E_T in this case are of 60.44, 20.44 and 80.88 J, respectively, compared to those of 1.41. 1.31 and 2.45 J in the case of Figure 6.26.

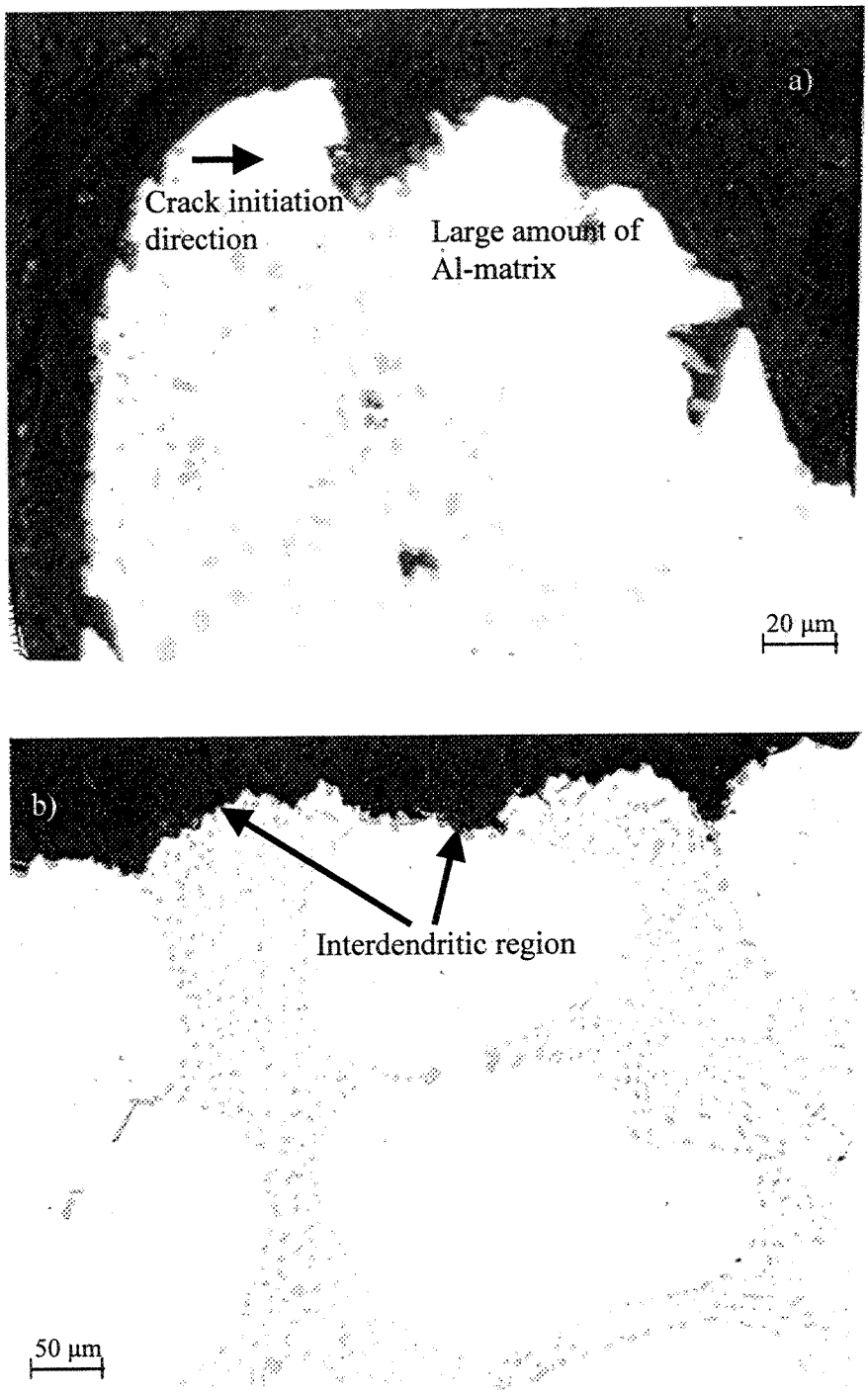

Figure 6.28. Optical micrographs showing fracture behavior of alloy A356.2 (0.1% Fe, DAS 23 µm, Sr-modified, edge).

However, when the alloy Fe level is increased and the cooling rate decreased to its lowest value, even in the Sr-modified alloy, the fracture still occurs mainly by cleavage of the brittle β-Al_5FeSi platelets, Figure 6.29(a). Note the sharp edge of the sample fracture surface in this case, compared to Figure 6.28. Figure 6.29(b) shows these features much more clearly at high magnification. In instances when the crack propagates through the more ductile Al-Si regions, the fracture surface is more rounded than sharp. The corresponding E_I, E_P and E_T are 3.41, 1.46 and 4.87 J, respectively.

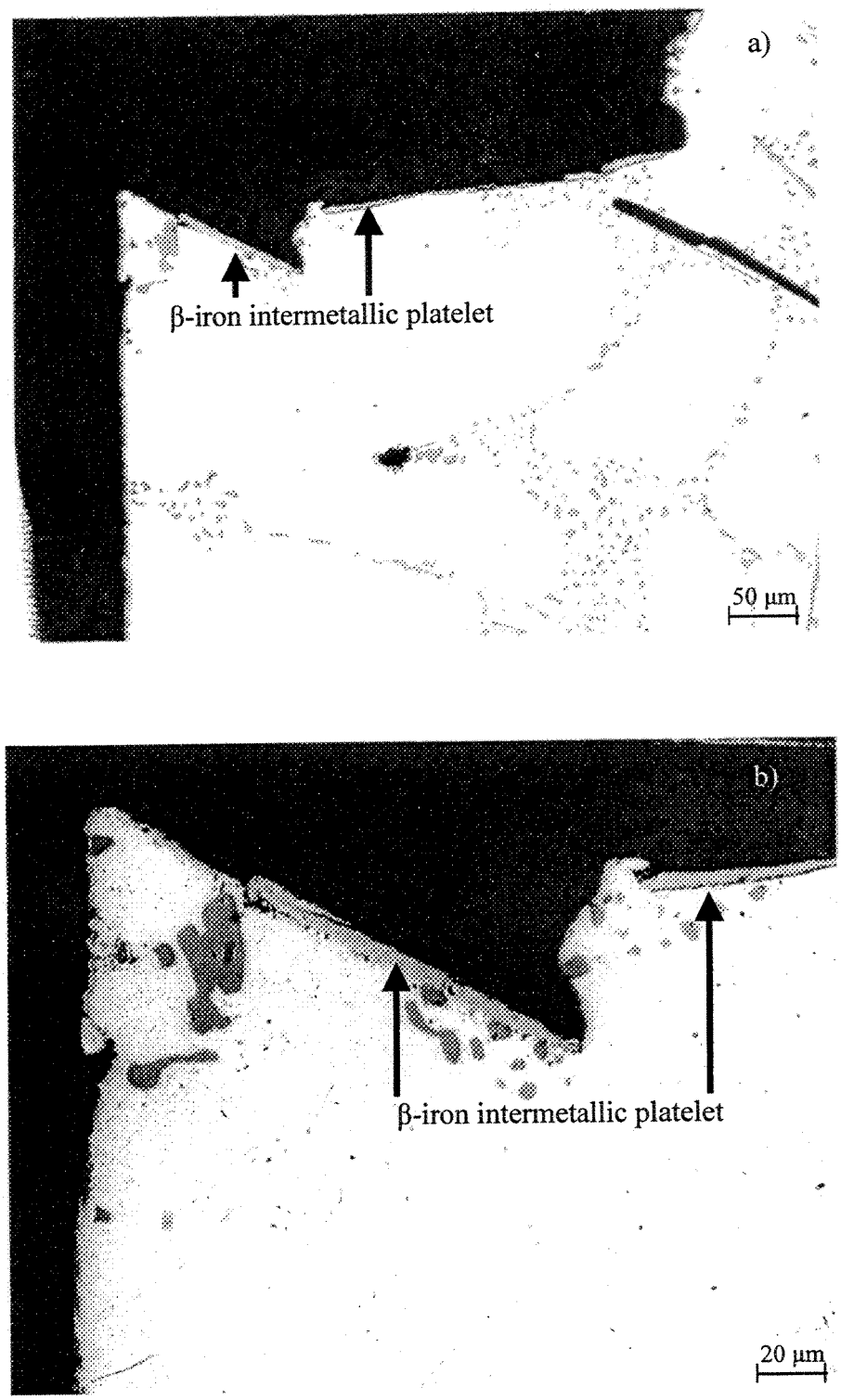

Figure 6.29. Optical micrographs showing fracture behavior of alloy A356.2 (0.6% Fe, DAS 75 μm, Sr-modified, edge).

CONCLUSIONS

CONCLUSIONS

The present work was carried out to investigate the effect of iron intermetallics and porosity on the performance of Al-Si-Cu (319) and Al-Si-Mg (356) cast alloys, using castings obtained under directional solidification conditions, followed by T6 temper treatment. Both experimental and industrial alloys were employed in the study, to obtain an overall estimation of the scatter in properties that could be expected when using industrial alloys. The cooling rate, iron content, and Sr modification conditions were varied in order to emphasize their influence on alloy tensile and impact properties. As well, the fracture mechanism of impact-tested samples was established. From the analysis and discussion of the results presented in Chapters 4, 5 and 6, the following may be concluded.

Microstructure

1. For the range of cooling rates covered in the present study (corresponding to dendrite arm spacings of 23-83 μm), the highest cooling rate (23 μm DAS) is the more significant parameter in controlling the size and distribution of the β-Al_5FeSi intermetallic phase and porosity in the unmodified 319 and 356 alloys.
2. The effect of strontium addition on the fragmentation of the β-Al_5FeSi intermetallic phase (*i.e.*, in decreasing its size) at high DASs in the 319.2 alloy is effective at lower

iron levels, *viz.*, below 0.6 wt% Fe. For the B319.2 (high Mg version of 319 alloy) and A356.2 alloys, the effect is more evident at low DASs.

3. Both porosity volume fraction (area percentage porosity) and pore size (maximum pore length and maximum pore area) increase significantly with strontium addition. This observation is consistent with the published data.

4. With the addition of magnesium, the β-iron intermetallic size (measured by the average maximum β-platelet length) is found to decrease, due to its partial transformation to the $Al_8FeMg_3Si_6$ phase in the unmodified alloy. This phase appears in the form of compacted particles (spherical Chinese-script) that are less harmful to the alloy mechanical properties compared to the β-Al_5FeSi platelets.

5. In Sr-modified alloys, an increase in the β-Al_5FeSi platelet maximum length is still observed at some cooling rates, in spite of the Sr-Mg interaction that results in the formation of $Mg_2Sr(Si_3Al_4)$ compound. Porosity volume fraction and pore size also decrease with Mg addition.

Tensile Properties

6. A simultaneous increase in cooling rate and decrease in iron content are effective in improving alloy ductility. This may be attributed to the corresponding reduction in the size and volume fraction of both β-Al_5FeSi platelets and porosity.

7. In the unmodified experimental 319.2 alloys, containing a very low amount of impurities or tramp elements, and at an iron level of 0.2-0.4 wt%, only a high cooling rate can significantly enhance alloy ductility. The unmodified industrial 319.2 alloys,

however, show no such improvement with the increase in cooling rate at iron contents beyond 0.4%, for DASs of up to 47 μm. In both alloys, in the Sr-modified condition, increasing the cooling rate further improves alloy ductility. Ductility in the B319.2 alloy is lower than that in the 319.2 alloy due to (i) the precipitation of Mg_2Si, (ii) partial transformation of β-Al_5FeSi into $Al_8FeMg_3Si_6$ phase, and (iii) a Sr-Mg interaction that diminishes the effectiveness of Sr modification. Due to the absence of the $CuAl_2$ intermetallic phase in its microstructure, A356.2 alloy displays much higher ductilities compared to the 319 alloys for the same iron level.

8. Iron has a detrimental effect on the ultimate tensile strength (UTS) in unmodified experimental and modified industrial 319.2 alloys, as well as in B319.2 and A356.2 alloys. A second-degree polynomial correlation between UTS and iron content is obtained for the 319.2 and A356.2 alloys for all cooling rates, with R^2 values in the range of ~0.6-1 (most of them > 0.8). For the modified experimental and unmodified industrial 319.2 alloys, although second-degree polynomial correlations were still maintained between UTS and iron contents (at all the cooling rates), most of the R^2 values are less than 0.5, indicating a considerable dispersion in the effect of iron content on UTS. Increasing the cooling rate, or adding Sr, or both, is essential in minimizing the harmful effects of iron, except in the experimental 319.2 alloys, where a reduction in UTS values with Sr modification was observed.

9. The correlation between yield strength (YS) and the cooling rate or iron content is more complex than that observed for UTS, as it is also a function of other factors such as the alloy system, chemical composition, Sr modification, trace elements, *etc.* In

general, in the 319.2 alloys YS increases as both the cooling rate and iron content increase, except in the case of the unmodified experimental alloy. In other words, the presence of iron can harden the alloy to some extent. For all the cooling rates studied, a second-degree polynomial correlation between YS and iron content is obtained, with regression coefficients $R^2 > 0.8$.

10. The effect of the cooling rate on YS is not very apparent in B319.2 alloys. Iron increases YS in the experimental alloys, but decreases the YS in the industrial alloys, due, most likely, to stricter limitations on the impurity content in the experimental alloys. In the A356.2 alloys, YS values are distributed within a narrow band, as opposed to a linear relationship, that shows a decreasing trend in the unmodified alloys and an increasing trend in the modified alloys (due to the fragmentation effect of Sr).
11. The β-Al_5FeSi platelet size (average maximum length and average area) is deleterious to alloy ductility and tensile strength. After a certain β-platelet size (~100 μm length or 400 μm^2 area for the 319 alloys, and ~70 μm length or 300 μm^2 area for A356.2 alloys), further deterioration in properties with an increase in the β-platelet size is less noticeable. This behavior is well illustrated by the power or logarithmic correlations obtained between ductility or tensile strength and β-iron intermetallic size, with R^2 values of more than 0.8 in most cases.
12. While the percent elongation is primarily controlled by the size of the β-iron intermetallics in the 319 alloys, the presence of tramp elements in the industrial 319.2 alloys are also expected to influence ductility. In the A356.2 alloy, only small variations in β-iron intermetallic platelet sizes can be tolerated, to maintain satisfactory

ductility requirements. The decrease in tensile strength (UTS) as a function of the β-iron intermetallic size is less sharp in the B319.2 and A356.2 alloys than in the 319.2 alloys. No definite relation between β-platelet size and yield strength could be established.

13. Modification with strontium increases both ductility and tensile strength in the industrial 319.2 and A356.2 alloys, but does not affect elongation in the experimental 319.2 alloys which, due to their purity, already possess high ductilities compared to their industrial counterpart. Strontium slightly increases elongation in the experimental B319.2 alloy, whereas the UTS is decreased in both the experimental and industrial B319.2 alloys. In general, modification with Sr is useful in maintaining a consistent UTS level in 319 alloys, in that much less dispersion of UTS values is observed in the Sr-modified alloys, regardless of their source. No apparent effect on YS is observed with the addition of strontium.

14. Porosity is always harmful to alloy ductility and tensile strength. While the maximum pore area is the parameter that best characterizes the porosity-tensile property relationships, the regression coefficients obtained indicate that it is not the primary factor controlling ductility and tensile strength. No definite correlation between YS and porosity was established.

15. Despite the poor relationships between UTS and iron content in 319.2 alloys, fairly good correlations between log (UTS) and log (%El) were obtained for all the alloys studied – experimental or industrial – *under all conditions*. A linear correlation was obtained in all conditions, with R^2 values in the range of ~0.6-0.93 (mostly > 0.8). This

indicates that the log UTS – log %El correlation is fairly consistent, regardless of the alloy condition. Thus, rather than using the quality index UTS *vs.* log %El plots proposed by Drouzy *et al.*,[136] the use of Log UTS – log %El plots is recommended, as they can be applied to both Al-Si-Cu and Al-Si-Mg alloys, whereas the quality index concept is suitable only for Al-Si-Mg alloys. Such plots provide an alternate means of interpreting tensile properties in a more global manner, with respect to alloying and melt processing and casting parameters (under the same heat treatment conditions).

Impact Properties

16. An increase in the cooling rate and decrease in iron content are beneficial to the impact properties. Linear correlations are obtained at all cooling rates in the unmodified 319.2 and A356.2 alloys. The modified 319.2 alloys show linear correlations at low cooling rates (*viz.*, at 60 and 83 μm DAS) and power correlations at high cooling rates (23 and 47 μm DAS). While power correlations are obtained at all cooling rates in both the unmodified and Sr-modified B319.2 alloy. Logarithmic correlations were obtained at all cooling rates in modified A356.2 alloy. In all cases, the correlations were quite good, with $R^2 > 0.95$. The highest cooling rate provides impact energies far superior to those obtained at other cooling rates (*e.g.* 12.40 J at 23 μm DAS compared to 4.88 J at 85 μm DAS in the unmodified 319.2 alloy at 0.4% Fe level, and 30.96 J versus to 11.35 J in the Sr-modified case).
17. The β-iron intermetallics deteriorate the impact properties significantly. The effect is most apparent within the ranges of 30 to 150 μm β-platelet lengths in the 319 alloys

and 10-50 μm β-platelet lengths in the A356.2 alloy, as illustrated by the power correlations between impact energy and β-platelet length/area obtained in all the alloys (with $R^2 > 0.95$). Porosity has a detrimental effect on impact energy. Fairly good correlations are obtained between impact properties and percentage porosity, and maximum pore length/area parameters. In the presence of magnesium, an increase in impact energy was observed for unmodified 319 alloys, particularly at low iron content (0.4%) and high cooling rates (23-47 μm DASs). This beneficial effect of Mg is reduced with an increase in iron content and decrease in the cooling rate.

18. Strontium modification is effective in improving the impact energy, even at high iron levels. The improvement is less apparent in B319.2 alloys. In the 319.2 alloys, the effect is very sensitive to the change in cooling rate: the higher the cooling rate, the greater the improvement. For example, the impact energy increases by 150, 133, 61 and 20% at DASs of 23, 47, 60 and 83 μm, when Sr is added to 319.2 alloy containing 0.4% Fe. In the case of the A356.2 alloy, the improvement rates at the lowest and highest iron contents (0.1% and 0.6%) are higher than that at moderate iron content (0.4%).

19. The impact energy of Sr-modified A356.2 alloys is twice that of the 319 alloys under the same conditions, whereas the tensile strength is almost half that of the 319 alloys, due to the absence of $CuAl_2$ phase in the 356.2 alloys.

20. The average crack speed of impact-tested samples shows a good inverse relation with impact energy: the highest crack speeds are normally obtained for the unmodified samples corresponding to the highest iron contents and lowest cooling rates. Crack

speed can thus provide a qualitative estimation of the impact energy expected for special alloy conditions.

21. Impact testing is more sensitive to variations in microstructure or casting defects than tensile testing. The impact energy – ultimate tensile strength plots display exponential relationships, while the impact energy – percent elongation plots display linear relationships in all three alloy, in both unmodified and Sr-modified cases, and regardless of alloy composition.

Fracture Mechanism

22. At low iron levels and high cooling rates (0.4% Fe, 23 μm DAS), and in the unmodified condition, 319 alloys undergo crack initiation through the fragmentation of Si particles, β-iron intermetallics, and $CuAl_2$ particles. Crack propagation is through the linking of the fragmented particles. A dimpled structure is observed for the Sr-modified alloys, indicating ductile fracture.

23. At high iron levels and low cooling rates (0.8% Fe, 83 μm DAS), in the unmodified condition, crack initiation and propagation occurs through the cleavage of β-Al_5FeSi platelets (rather than by the decohesion of the β-platelets from the matrix). The morphology of β-iron intermetallic platelets (individual or branched) is important in determining the direction of crack propagation. Cracks also propagate through the fracture of undissolved $CuAl_2$ or other Cu-intermetallics such as Al_7Cu_2Fe, as well as through fragmented Si particles. In the Sr-modified alloys, cracks are initiated mostly with the fragmentation or cleavage of perforated β-phase platelets. A small amount of

initiation can also take place through the fragmentation of coarse Si particles (that have not fully undergone spheroidization) or undissolved Cu-intermetallics. Thus, all microstructural constituents contribute to the fracture process.

24. In the A356.2 alloys, in samples obtained under optimum conditions (0.1% Fe, 23 μm DAS, Sr-modified), cracks initiate mainly through the fracture of Si particles or the debonding of the Si particles from the Al matrix. In the unmodified condition, cracks mainly propagate through the coalescence of fractured Si particles, except where β-iron intermetallics are present, in which case the latter takes priority in fracture propagation. In the Sr-modified condition, more of the Al matrix is involved when cracks propagate through the linkage of fractured/debonded Si particles, as well as fragmented β-iron intermetallics. For samples characterized by low impact energies, crack initiation and propagation occurs mainly through the cleavage of β-iron intermetallics.

SUGGESTIONS FOR FURTHER WORK

The results of the present study have highlighted the role of some important metallurgical parameters such as cooling rate, iron content, magnesium level, strontium modification, grain refining, porosity level and heat treatment on the performance of two popular Al-Si automotive alloys, *viz.*, 356 and 319 alloys. The work could be further elaborated by extending the mechanical property and microstructural aspects by incorporating the following.

1. Fatigue testing, using (a) a rotation-bending technique, employing curved samples, and (b) fatigue crack growth (FCG) analysis using compacted tension (CT) samples, at different stress intensity factors, in particular, near the threshold value.

2. Fracture toughness testing under plain strain conditions (K_{IC}).

3. Examining the log(UTS) – log(%El) correlation under different heat treatment conditions (T6 *vs.* T7).

4. A detailed study of the effects of Sr, Mg and tramp elements on Fe to investigate the possibility of effectively "lowering" the iron levels in the industrial alloys by their presence and subsequent interactions with other alloying elements.

REFERENCES

1. J. E. Gruzleski and B. M. Closset, *The Treatment of Liquid Aluminum-Silicon Alloys*, American Foundrymen's Society, Inc., Des Plaines, Illinois, U.S.A., 1990.

2. Q. T. Fang and D. A. Granger, "Porosity Formation in Modified and Unmodified A356 Alloy Castings," *AFS Transactions*, Vol. 97, 1989, pp. 989-1000.

3. A. Milosavljevic, V. Sijacki-Zeravcic, P. Smiljanic, A. Markovic, and Z. Stamenic, "Fracture Characteristic of Casting Alloys of AlSi11Cu3 Type, Reliability and Structural Integrity of Advanced Materials," *ECF9 Proceedings*, Vol. 1, 1992, pp. 587-590.

4. D. Emadi and J. E. Gruzleski, "Effects of Castings and Melt Variables on Porosity in Directionally-Solidified Al-Si Alloys," *AFS Transactions*, Vol. 102, 1994, pp. 307-312.

5. G. V. Kutumba Rao and V. Panchanathan, "End Chills Influence on Solidification Soundness of Al-Cu-Si (LM4) Alloy Castings," *AFS Cast Metals Research Journal*, 1973, pp. 133-138.

6. M. C. Flemings, *Solidification Processing*, McGraw-Hill, Montreal, 1974.

7. I. Minkoff, *Solidification and Cast Structure*, John Wiley & Sons, Toronto, 1986.

8. D. E. J. Talbot, "Effects of Hydrogen in Aluminum, Magnesium, Copper and Their Alloys," *International Metallurgical Reviews*, Vol. 20, 1975, pp. 166-184.

9. O. Madelaine-Dupuich and J. Stolarz, "Fatigue of Eutectic Al-Si Alloys," *Materials Science Forum*, Vols. 217-222, 1996, pp. 1343-1348.

10. L. A. Narayanan, *Crystallization and Dissolution Studies of Iron Intermetallics in Al-Si Alloys*, Ph. D. Thesis, McGill University, Montréal, 1994.

11. F. Palazzo, "The Future of Aluminum in the Automotive Industry," *Alluminio*, Vol. 46, No. 9, Sept. 1977, pp. 323-334.

12. G. L. Armstrong, "Alloy Selection for Automotive Aluminum Castings," *SAE Technical Paper*, No. 780249, Society of Automotive Engineers, 1978, 7 pages.

13. *Registration Record of Aluminum Association Alloy Designation and Chemical Composition Limits for Aluminum Alloys in the Form of Castings and Ingot*, The Aluminum Association, Washington, DC, Aug. 1982.

14. H. E. Boyer and T. L. Gall (Eds.), *Metals Handbook, Desk Edition,* American Society for Metals, Metals Park, Ohio, USA, 1985.

15. K. R. Van Horn (Ed.), *Aluminum. Vol. I. Properties, Physical Metallurgy and Phase Diagrams*, American Society for Metals, Metals Park, Ohio, USA, 1967.

16. J. E. Davis (Ed.), *Aluminum and Aluminum Alloys*, ASM Specialty Handbook®, ASM International, Materials Park, Ohio, USA, 1993.

17. J. E. Hatch (Ed.), *Aluminum: Properties and Physical Metallurgy*, American Society for Metals, Metals Park, Ohio, USA, 1984.

18. G. E. Dieter, Jr., *Mechanical Metallurgy*, 2nd edition, Metallurgy and Metallurgical Engineering Series, McGraw-Hill, New York, 1976.

19. S. Murali, A. Trivedi, K. S. Shamanna, and K. S. S. Murthy, "Effect of Iron and Combined Iron and Beryllium Addition on the Fracture Toughness and Microstructures of Squeeze-Cast Al-7Si-0.3Mg Alloy," *Journal of Materials Engineering and Performance*, Vol. 5(4), 1996, pp. 462-468.

20. P. N. Crepeau, "Effect of Iron in Al-Si Casting Alloys: A Critical Review," *AFS Transactions*, Vol. 103, 1995, pp. 361-366.

21. A. M. Samuel, F. H. Samuel, and H. W. Doty, "Observations on the Formation of β-AlFeSi Phase in 319 Type Al-Si Alloys," *Journal of Materials Science*, Vol. 31, 1996, pp. 5529-5539.

22. W. B. Pearson, *Handbook of Lattice Spacing and Structures of Metals and Alloys,* Oxford, Pergamon Press, Vol. 2, New York, 1967.

23. L. F. Mondolfo, *Aluminum Alloys: Structure and Properties*, Butterworths, London, 1976.

24. D. Munson, "Clarification of the Phases Occurring in Aluminum-rich Aluminum-Iron-Silicon Alloys, with Particular Reference to Ternary Phase α-AlFeSi," *Journal of the Institute of Metals*, Vol. 95, 1967, pp. 217-219.

25. J. N Pratt and G. V. Raynor, "The Intermetallic Compounds in the Alloy of Aluminum and Silicon with Cr, Mn, Fe, Co, Ni," *Journal of the Institute of Metals*, Vol. 79, 1951, pp. 211-232.

26. A. L. Dons, "AlFeSi-Particles in Commercial Pure Aluminum," *Zeitschrift für Metallkunde*, Vol. 75, 1984, pp. 170-174.

27. G. Gustafsson, T. Thorvaldsson, and G. L. Dunlop, "The Influence of Fe and Cr on the Microstructure of Cast Al-Si-Mg Alloys," *Metallurgical Transactions A*, Vol. 17A, 1986, pp. 45-52.

28. M. R. Ghomashchi, "Intermetallic Compounds in an Al-Si Alloy Used in High Pressure Die-Casting," *Zeitschrift für Metallkunde*, Vol. 78, 1987, pp. 784-787.

29. J. Gobrecht, "Ségrégations par gravité du fer, du manganèse et du chrome dans les alliages aluminium-silicium de fonderie," *Fonderie*, No. 367, Mai 1977, pp. 171-173.

30. J. G. Barlock and L. F. Mondolfo, "Structure of Some Aluminum-Iron-Magnesium-Manganese-Silicon Alloys," *Zeitschrift für Metallkunde*, Vol. 66 (10), 1975, pp. 605-611.

31. S. Yaneva, N. Stoichev, Z. Kamenova, and S. Budurov, "Quaternary Iron-containing Phases in Al-Si Cast Alloys," *Zeitschrift für Metallkunde*, Vol. 75, 1984, pp. 395-398.

32. G. Phragmen, "On the Phases Occurring in Alloys of Aluminum with Copper, Magnesium, Manganese, Iron and Silicon," *Journal of the Institute of Metals*, Vol. 77, 1950, pp. 498-553.

33. J. E. Gruzleski, F. Paray, S. G. Shabestari, and M. H. Mulazimoglu, "Applications of Strontium in Cast and Wrought Aluminum Alloys," *AL13 – le magazine de l'aluminium,* Vol. 2, No. 1, 1996, pp. 23-33.

34. L. Bäckerud, G. Chai, and J. Tamminen, *Solidification Characteristics of Aluminum Alloys, Vol. 2: Foundry Alloys*, AFS/SKANALUMINIUM, Des Plaines, IL, USA, 1990.

35. J. Iglessis, C. Frantz, and M. Gantois, "La croissance par propagation de plans de macle des composés eutectiques dans le système ternaire Al-Fe-Si," *Mémoires scientifiques de la revue de métallurgie*, Fév. 1978, pp. 93-100.

36. A. Griger, V. Stefanniay, A. Lendvai, and T. Turmezy, "Possible Modification of Cast Structure by Continuous Casting Technology in AlFeSi Alloys, Part III: Intermetallic Phases," *Aluminium*, Vol. 65, No. 10, 1989, pp. 1049-1056.

37. L. F. Mondolfo and J. G. Barlock, "Effect of Superheating on the Structures of Some Aluminum Alloys," *Metallurgical Transactions B*, Vol. 6B, 1974, pp. 565-572.

38. H. Iwahori, H. Takamiya, K. Yonekura, Y. Yamamoto, and M. Nakamura, *Casting* (in Japanese), Vol. 60, No. 9,1988, pp. 590-595.

39. A. Franek, J. Pazdernik, and A. K. Hanna, "On the Morphology of the Eutectic and Phases in Aluminium-Silicon 12-Iron and Aluminuium-Silicon 20-Iron Alloys," *Praktische Metallographie,* Vol. 10, No. 10, Oct. 1973, pp. 582-587.

40. J. D. Evensen and T. B. Pedersen, "Microstructural Aspects of the Fracture Behavior of AlSiMg(Mg) Casting Alloys," *Proc. Conf. of the 7th International Light Metals Congress*, Loeben/Vienna, June 22-26, Aluminium-Verlag GmbH, 1981, pp. 77-79.

41. A. M. Samuel, F. H. Samuel, C. Villeneuve, H. W. Doty, and S. Valtierra, "Effect of Trace Elements on β-Al_5FeSi Characteristics, Porosity and Tensile Properties of Al-Si-Cu (319) Cast Alloys," *International Journal of Casting Metals Research*, Vol. 14, 2001,pp. 97-120.

42. L. F. Mondolfo, *Manganese in Aluminum Alloys*, The Manganese Centre, France, 1990.

43. A. Couture, "Iron in Aluminum Casting Alloys – A Literature Survey," *AFS International Cast Metals Journal*, Vol. 6, No. 4, Dec. 1984, pp. 9-17.

44. J. Iglessis, C. Frantz and M. Gantois, "Conditions de formation des phases de fer dans les alliages Al-Si de pureté commerciale," *Mémoires scientifiques de la revue de métallurgie,* vol. 73, no. 4, 1977, p. 237-242.

45. ASM International Handbook Committee (Ed.), *ASM Handbook, Volume 2: Properties and Selection: Nonferrous Alloys and Special Purpose Materials,* ASM International, Materials Park, Ohio, USA, 1990.

46. D. L. Colwell and R. J. Kissling, "Die and Permanent Mold Casting Aluminum Alloy Minor Elements," *AFS Transactions*, Vol. 69, 1961, pp. 610-616.

47. C. Mascré, "Influence du fer et du manganèse sur les alliages du type de l'A-S13 (Alpax)," *Fonderie*, Vol. 108, Jan. 1955, pp. 4330-4336.

48. Y. Komiyama, K. Uchida, and M. Gunshi, "Effect of Fe, Mn, Zn and Ti on Mechanical Properties and Microstructures of Al-Si-Cu-Mg Casting Alloy," *Journal of the Japan Institute of Light Metals* (in Japanese), Vol. 26, No. 7, 1976, pp. 311-319.

49. L. A. Narayanan, F. H. Samuel, and J. E. Gruzleski, "Crystallization Behavior of Iron-Containing Intermetallics Compounds in 319 Aluminum Alloy," *Metallurgical and Materials Transactions A*, Vol. 25A, 1994, pp. 1761-1773.

50. D. A. Granger, "Investigation of a Star-like Intermetallic Phase Occuring in Alloy 339," *AFS Transactions*, Vol. 99, 1991, pp. 379-383.

51. J. L. Jorstad, "Understanding 'Sludge'," *Die Casting Engineer*, Nov.-Dec. 1986, pp. 30-36.

52. G. Farhadi, *Effects of Trace Elements on the Characteristics of 6XXX Type Automotive Alloys*, M. Eng. Thesis, Université du Québec à Chicoutimi, Chicoutimi, Québec, October 1999.

53. K. G. Wikle, "Improving Aluminum Castings with Beryllium," *AFS Transactions*, Vol. 86, 1978, pp. 513-518.

54. W. A. Bailey, "Beryllium Effect on Strength and Mechanical Properties of 356 Variant-T6 Aluminum Alloys," *Modern Casting*, Aug. 1964, pp. 443-454.

55. S. Murali, K. S. Raman, and K. S. S. Murthy, "Effect of Trace Additions on the Mechanical Properties and Fracture Toughness of Fe-Containing Al-7Si-0.3Mg Alloy," *Cast Metals*, Vol. 6, No. 4, 1994, pp. 189-198.

56. S. Murali, K. S. Raman, and K. S. S. Murthy, "The Formation of β-$FeSiAl_5$ and Be-Fe Phases in Al-7Si-0.3Mg Alloy Containing Be," *Materials Science and Engineering A*, Vol. 190A, 1995, pp. 165-172.

57. A. M. Samuel, P. Ouellet, F. H. Samuel, and H. W. Doty, "Microstructural Interpretation of Thermal Analysis of Commercial 319 Aluminum Alloy with Magnesium and Strontium Additions," *AFS Transactions*, Vol. 105, 1997, pp. 951-962.

58. H. de la Sablonnière and F. H. Samuel, "Solution Heat Treatment of 319 Aluminum Alloy Containing ~0.5wt% Mg: Part I – Solidification and Tensile Properties," *International Journal of Cast Metals Research*, Vol. 9 (4), 1996, pp. 195-211.

59. R. DasGupta, C. C. Brown, and S. Marek, "Effect of Increased Magnesium Content on the Mechanical Properties of Sand-Cast 319 Aluminum Alloy," *AFS Transactions*, Vol. 97, 1989, pp. 245-254.

60. D. Apelian, G. K. Sigworth, and K. R. Whaler, Assessment of Grain Refinement and Modification of Al-Si Foundry Alloys by Thermal Analysis," *AFS Transactions,* Vol. 92, 1984, pp. 297-307.

61. R. DasGupta, C. G. Brown, and S. Marek, "Analysis of Overmodified 356 Aluminum Alloy," *AFS Transactions*, Vol. 96, 1988, pp. 297-310.

62. L. R. Morris and F. B. Miners, "Aluminum Alloys," U.S. Patent No. 3,926,690, Dec. 16, 1975.

63. M. H. Mulazimoglu, B. Closset, and J. E. Gruzleski, "Evaluation of the Metallurgical Effects of Strotium on Cast 6000 Series Aluminium Alloys," *Aluminium*, Vol. 68, No. 6, 1992, pp. 489-493.

64. B. Kulunk and D. J. Zuliani, "Applications for the Strontium Treatment of Wrought and Die-Cast Al," *JOM,* Oct. 1996, pp. 60-63.

65. S. G. Shabestari, *Formation of Iron-bearing Intermetallics in Aluminum-Silicon Casting Alloys,* Ph. D. Thesis, McGill University, Montreal, 1994.

66 Y. Shimizu, Y. Awano, and M. Kakamura, "A New Heat Treatment to Improve Toughness of Aluminum Cast Alloys," *Alutopia* (in Japanese), Vol. 19, 1989, pp. 9-17.

67 L. A. Narayanan, F. H. Samuel, and J. E. Gruzleski, "Dissolution of Iron Intermetallics in Al-Si Alloys through Nonequilibrium Heat Treatment," *Metallurgical and Materials Transactions A*, Vol. 26A, Aug. 1995, pp. 2161-2174.

68. L. Grand, "Influence of Some Impurities on the Quality of Aluminum Alloys," *Fonderie*, Vol. 217, Mar. 1964, pp. 95-100.

69. G. M. Vorob'ev, R. M. Gol'shtein, and I. I. Maurits, "Effect of Impurities on the Main Properties of Silumin," *Metallurgical Abstracts*, Vol. 32, 1964, pp. 960-961.

70. W. Bonsack, "Discussion on the Effect of Minor Alloying Elements on Aluminum Casting Alloys," *ASTM Bulletin 117*, 1942, pp. 45-51.

71. S. Hajas, "Effect of Iron Contamination on the Mechanical Properties of Aluminium Casting Alloys" *Chemical Abstracts*, Vol. 73, No. 133571, 1970.

72. N. Komatsu, M. Nakamura, and Y. Yamamoto, "Metallurgical Structure and Impact Strength of Al-Si Alloys," *Technical Report of Toyota R&D Center*, TR-11, 1975. 3, pp. 1-46 (in Japanese).

73. S. Nishi, T. Shinoda, and E. Kato, "Effect of Iron Contents, Beryllium Addition and Cooling Velocity on Mechanical Properties of Al-Si-Mg-Zn Cast Alloys," *Journal of the Japan Institute of Light Metals* (in Japanese), Vol. 18, No. 12, 1968, pp. 627-635.

74. N. Beck and O. Veda, "Selections of Limit of Iron Content and Heat Treating Conditions in Al-Si-Mg Alloy (AC4C) Castings," *Journal of the Japan Institute of Light Metals* (in Japanese), Vol. 27, No. 4, 1977, pp. 189-192.

75. E. F. Bishop and W. S. Pellini, "The Contribution of Risers and Chill-Edge Effects to Soundness of Cast Steel Plates," *AFS Transactions*, Vol. 58, 1950, pp. 185-197.

76. E. T. Myskowski, H. F. Bishop, and W. S. Pellini, "Applications of Chills to Increase the Feeding Range of Risers," *AFS Transactions*, Vol. 60, 1952, pp. 389-400.

77. W. D. Walther, C. M. Adams, and W. S. Pellini, "Mechanism for Pore Formation in Solidifying Metals," *AFS Transactions*, Vol. 64, 1956, pp. 658-664.

78. A. M. Samuel and F. H. Samuel, "Porosity Factor in Quality Aluminum Castings," *AFS Transactions*, Vol. 100, 1992, pp. 657-666.

79. J. Charbonnier, "Gaz dans les alliages d'alumimium de fonderie," *Techniques de l'Ingénieur, traité Métallurgie*, 1991, pp. M218-1–M218-14.

80. H. Fredriksson and I. Svensson, "On the Mechanism of Pore Formation in Metals," *Metallurgical Transactions B*, Vol. 7B, 1976, pp. 599-606.

81. F. Weinberg and D. A. Hirschfeld, "Porosity in Cast and Directionally Solidified Al and Al-Cu Alloys," *Metal Science*, Vol. 13, No. 6, June 1979, pp. 335-340.

82. T. S. Piwonka and M. C. Flemings, "Pore Formation in Solidification," *Transactions of the Metallurgical Society of AIME*, Vol. 236, Aug. 1966, pp. 1157-1165.

83. P. M. Thomas and J. E. Gruzleski, "Threshold Hydrogen for Pore Formation During the Solidification of Aluminum Alloys," *Metallurgical Transactions B*, Vol. 9B, 1978, pp. 139-141.

84. H. Iwahori, K. Yonekura, Y. Yamamoto, and M. Nakamura, "Occurring Behavior of Porosity and Feeding Capacities of Sodium- and Strontium-Modified Al-Si Alloys," *AFS Transactions*, Vol. 98, 1990, pp. 167-173.

85. J. Zou, K. Tynelius, S. Shivkumar, and D. Apelian, "Microporosity Formation in A356.2 Castings," *Production, Refining, Fabrication and Recycling of Light Metals*, Pergamon Press, New York, 1990, pp. 323-332.

86. S. Shivkumar, D. Apelian, and J. Zou, "Modeling of Microstructure Evolution and Microporosity Formation in Cast Aluminum Alloys," *AFS Transactions*, Vol. 98, 1990, pp. 897-904.

87. D. R. Poirier, K. Yeum, and A. L. Maples, "A Thermodynamic Prediction for Microporosity Formation in Aluminum-Rich-Al-Cu Alloys," *Metallurgical Transactions A*, Vol. 18A, 1981, pp. 1979-2000.

88. R. D. Pehlke, "Foundry Processes – Their Chemistry and Physics," *General Motors Research Laboratories*, Warren, MI, 1987, pp. 427-445.

89. K. Kubo and R. D. Pehlke, "Mathematical Modeling of Porosity Formation in Solidification," *Metallurgical Transactions B*, Vol. 16B, 1985, pp. 359-366.

90. H. Iwahori, K. Yonekura, Y. Sugiyama, Y. Yamamoto, and M. Nakamura, "Behavior of Shrinkage Porosity Defects and Limiting Solid Fraction of Feeding on Al-Si Alloys," *AFS Transactions*, Vol. 93, 1985, pp. 443-452.

91. X.-G. Chen and S. Engler, "Hydrogen and Porosity in Aluminum-Silicon and Aluminum-Magnesium Alloys, Part 1. Aluminum-Silicon Alloys," *Metall*, Vol. 45, No. 10, 1991, pp. 995-1000.

92. X.-G. Chen and S. Engler, "Hydrogen and Porosity in Aluminum-Silicon and Aluminum-Magnesium Alloys, Part 2. Aluminum-Magnesium Alloys and Discussion on Pore Formation," *Metall*, Vol. 45, No. 12, 1991, pp. 1225-1231.

93. G. A. Edwards, G. K. Sigworth, C. H. Cáceres, D. H. StJohn, and J. Barresi, "Microporosity Formation in Al-Si-Cu-Mg Casting Alloys," *AFS Transactions*, Vol. 105, 1997, pp. 809-818.

94. N. Roy, A. M. Samuel, and F. H. Samuel, "Porosity Formation in Al-9 Wt Pct Si-3 Wt Pct Cu Alloy Systems: Metallographic Observations," *Metallurgical and Materials Transactions A*, Vol. 27A, 1996, pp. 415-429.

95. G. K. Sigworth, C. Wang, H. Huang, and J. T. Berry, "Porosity Formation in Modified and Unmodified Al-Si Alloy Castings," *AFS Transactions*, Vol. 102, 1994, pp. 245-261.

96. A. M. Samuel and F. H. Samuel, "A Metallographic Study of Porosity and Fracture Behavior in Relation to Tensile Properties in 319.2 End Chill Castings," *Metallurgical and Materials Transactions*, Vol. 26A, 1995, pp. 2539-2372.

97. D. Emadi, J. E. Gruzleski, and J. M. Toguri, "The Effect of Na and Sr Modification on Surface Tension and Volumetric Shrinkage of A356 Alloy and Their Influence on Porosity Formation," *Metallurgical Transactions B*, Vol. 24B, Dec. 1993, pp. 1-9.

98. D. Argo and J. E. Gruzleski, "Porosity in Modified Aluminum Alloy Castings," *AFS Transactions*, Vol. 96, 1988, pp. 65-74.

99. M. D. Hanna, S. Lu, and A. Hellawell, "Modification in the Aluminum Silicon System," *Metallurgical Transactions A*, Vol. 15A, 1984, pp. 459-469.

100. G. K. Sigworth, "A Scientific Basis for the Degassing of Aluminum," *AFS Transactions*, Vol. 95, 1987, pp. 73-78.

101. G. K. Sigworth, "Fundamentals of Grain Refining in Aluminum Alloy Castings," *Proc. of International AFS/CMI Conf. on Molten Aluminum Processing,* City of Industry, California, USA, 1986, pp. 75-99.

102. N. Roy, L. Zhang, P. R. Louchez, and F. H. Samuel, "Porosity Formation in Al-9 wt% Si-3 wt% Cu- X Alloy Systems: Measurements of Porosity," *Journal of Materials Science*, Vol. 31, 1996, pp. 1243-1254.

103. K. E. Tynelius, *A Parametric Study of the Evolution of Microporosity in Al-Si Foundry Alloys*, Ph. D. Thesis, Drexel University, Philadelphia, PA, 1992.

104. J. A. Taylor, G. B. Schaffer, and D. H. StJohn, "The Role of Iron in the Formation of Porosity in Al-Si-Cu Based Casting Alloys: Part I. Initial Experimental Observations," *Metallurgical and Materials Transactions A*, Vol. 30A, June 1999, pp. 1643-1650.

105. S. Shivkumar, L. Wang, and R. Lavigne, "Quantitative Evaluation of Pore Characteristics in Cast Al Alloys," *Light Metals 1993*, S.K. Das (Ed.), The Minerals, Metals & Materials Society, Warrendale, PA, 1993, pp. 829-838.

106. J. A. Eady and D. M. Smith, "The Effect of Porosity on the Tensile Properties of Aluminum Castings," *Materials Forum*, Vol. 9, No. 4, 1986, pp. 217-223.

107. D. L. McLellan, "Tensile Properties of A357-T6 Aluminum Castings," *Journal of Testing & Evaluation*, Vol. 8, No. 4, July 1980, pp. 170-176.

108. F. O. Traenkner, "A Checklist for the Mechanical Properties of Aluminum Castings," *Modern Casting*, Vol. 70, No. 10, Oct. 1982, pp. 36-37.

109. A. Herrera and V. Kondic, "The Efect of Porosity on Tensile Properties of Two Al-Si Alloys," *Proc. Int. Conf. on Solidification and Cast Metals*, The Metals Society, Sheffield, UK, 1977, pp. 460-465.

110. M. K. Surappa, E. W. Blank, and J. C. Jaquet. "Effect of Macro-Porosity on the Strength and Ductility of Cast Al-7Si-0.3Mg Alloy," *Scripta Metallurgica*, Vol. 20, 1986, pp. 1281-1286.

111. K. Radhakrishna, S. Seshan, and M. R. Seshadri, "Effect of Porosity on Mechanical Properties of Aluminum Alloy Castings," *Transactions of the Indian Institute of Metals*, Vol. 34, No.2, Apr. 1981, pp. 169-171.

112. E. N. Pan, C. S. Lin, and C. R. Loper, Jr., "Effects of Solidification Parameters on the Feeding Efficiency of A356 Aluminum Alloy," *AFS Transactions*, Vol. 98, 1990, pp. 735-746.

113. C. M. Cáceres and B. I. Selling, "Casting Defects and the Tensile Properties of an Al-Si-Mg Alloy," *Materials Science and Engineering A*, Vol. A220, No. 1, 1996, pp. 109-116.

114. A. M. Samuel, H. W. Doty, and F. H. Samuel, "Influence of Melt Treatment and Solidification Parameters on the Quality of 319.2 Endchill Aluminum Castings," *Proceedings of 4th International Conference on Molten Aluminum Processing*, Sheraton World Resort, Orlando, Florida, Nov. 12-14, 1995, pp. 261-294.

115. W. W. Gerberich, "Microstructure and Fracture," *Metals Handbook, 9th Edition, Vol. 8: Mechanical Testing*, American Society for Metals, Metals Park, OH, 1985, pp. 476-491.

116. J. Gurland and J. Plateau, "The Mechanism of Ductile Rupture of Metals Containing Inclusions," *Transactions of Metallurgical Society of AIME*, Vol. 56, 1963, pp.442-.454.

117. A. Gangulee and J. Gurland, "On the Fracture of Silicon Particles in Aluminum-Silicon Alloys," *Transactions of Metallurgical Society of AIME*, Vol. 239, 1967, pp. 269-

118. S. F. Frederick and W. A. Bailey, "The Relation of Ductility to Dendrite Cell Size in a Cast Al-Si-Mg Alloy," *Transactions of Metallurgical Society of AIME*, Vol. 242, Oct. 1968, pp. 2063-2067.

119. M. F. Hafiz and T. Kobayashi, "A Study on the Microstructure – Fracture Behavior Relations in Al-Si Casting Alloys," *Scripta Metallurgica et Materialia*, Vol. 30, 1994, pp. 475-480.

120. M. D. Dighe and A. M. Gokhale, "Relationship Between Microstructural Extremum and Fracture Path in a Cast Al-Si-Mg Alloy," *Scripta Materialia*, Vol. 37, No. 9, 1997, pp. 1435-1440.

121. R. C. Voigt and D. R. Bye, "Microstructural Aspects of Fracture in A356," *AFS Transactions*, Vol. 99, 1991, pp. 33-50.

122. M. K. Surappa, E. W. Blank, and J. C. Jaquet, "Microstructural Approach to Deformation and Fracture of Cast Al-7Si-0.3Mg," *3rd International Conference on Solidification Processing*, Sheffield, UK, 1987, pp. 424-427.

123. Q. G. Wang and C. H. Cáceres, "The Fracture Mode in Al-Si-Mg Casting Alloys," *Materials Science and Engineering A*, Vol. A241, 1998, pp. 72-82.

124. N. Fat-Halla, "Structure, Mechanical Properties and Fracture of Aluminium Alloy A-356 Modified with Al-5Sr Master Alloy," *Journal of Materials Science*, Vol. 22(3), 1987, pp. 1013-1018.

125. R. W. Coade, S. M. Nugent, D. S. Saunders, J. R. Griffiths, B. A. Parker, "The Relationship Between Crack Propagation and Microstructure in an Aluminum Casting Alloy," *Prof. of the 30th Annual Conference of the Australasian Institute of Metals*, Melbourne, 1977, pp. 6B1-6B2.

126. K. Okabayshi, M. Kawamoto, A. Ikenaga, M. Tsujikawa, and K. Nomura, "Relationship Between Fracture Properties and Microstructure of Hyper-Eutectic Al-Si Alloy Castings," *Imono (Journal of the Japan Foundrymen's Society)*, Vo. 57, No. 2, 1985, pp. 108-112.

127. C. H. Cáceres and J. R. Griffiths, "Damage by the Cracking of Silicon Particles in an Al-7Si-0.4Mg Casting Alloy," *Acta Metallurgica*, Vol. 44, No. 1, 1996, pp. 25-33.

128. C. H. Cáceres and J. R. Griffiths, "Fracture Micromechanisms in an Al-Si-Mg Casting Alloy," *Strength of Materials*, ICSMA 10, The Japan Institute of Metals, Sendai, Japan, Aug. 1994, pp. 22-26.

129. A. Saigal and J. T. Berry, "Study of the Effects of Volume Fraction, Size and Shape of Silicon Particles on Mechanical Properties in Al-Si Alloys Using Finite Element Method," *AFS Transactions*, Vo. 93, 1985, pp. 699-704.\

130. C. H. Cáceres, C. J. Davidson, and J. R. Griffiths, "The Deformation and Fracture Behavior of an Al-Si-Mg Casting Alloy," *Materials Science and Engineering A*, Vol. A197, 1995, pp. 171-179.

131. Q. G. Wang, C. H. Cáceres, and J. R. Griffiths, "Transgranular and Intergranular Fracture in Al-Si-Mg Casting Alloys," *Advances in Fracture Research – International Conference on Fracture*, Vol. 5, 1997, pp. 2511-2518.

132. E. Kato, "Relationship Between Fracture Process of Al-Si Alloy Castings and Shape of Iron Compounds," *Journal of Japan Institute of Light Metals* (in Japanese), Vol. 45, No. 1, 1995, pp. 9-14.

133. C. Villeneuve and F. H. Samuel, "Fragmentation and Dissolution of β-Al_5FeSi Phase During Solution Heat Treatment of Al-13%Si-Fe Alloys," *International Journal of Cast Metals Research*, Vol. 12, 1999, pp. 145-160.

134. S. Holeček, P. Řezníček, K, Štětina, and M. Ruda, "Influence of Iron Content on the Embrittlement of AlSiFe Alloys," *Aluminium* (English Edition), Vol. 59, No. 8, August 1983, pp. E227-E229.

135. ASTM Designation: E23-94b, "Standard Test Methods for Notched Bar Impact Testing for Metallic Materials," ASTM Standards, Vol. 03.01, pp. 137-157.

136. M. Drouzy, S. Jacob, and M. Richard, "Interpretation of Tensile Results by Means of Quality Index and Probable Yield Strength," *AFS International Cast Metals Journal*, June 1980, pp. 43-50.

137. C. H. Cáceres, "A Rationale for the Quality Index of Al-Si-Mg Casting Alloys," *Cast Metals*, No. 193, pp. 1-7.

138. C. H. Cáceres, T. Din, A. K. M. B. Rashid, and J. Campbell, "On the Quality Index of Al-Cu Casting Alloys," *Materials Science & Technology A*, in press (1999).

139. C. H. Cáceres, "Materials Properties and Quality Index in Al-Si-Mg Casting Alloys," *AFS Transactions*, Vol. 106, 1998, pp 601-604.

140. C. H. Cáceres, "Microstructural Effects on the Strength-Ductility Relationship of Al-7Si-Mg Casting Alloys," *Materials Science Forum*, Vol. 331-337, 2000, pp. 223-228.

141. P. N. Anyalebechi, T. N. Rouns, and R. E. Sanders, Jr., "Effect of Cooling Rate and Grain Refining on Constituent Phase Particle Size in As-cast 3004 Alloy," *Light Metals 1991*, E. L. Rooy (Ed.), The Minerals, Metals & Materials Society, Warrendale, PA, 1990, pp. 821-850.

142. M. C. Flemings, T. Z. Kattamis, and B. P. Bardes, "Dendrite Arm Spacing in Aluminum Alloys," *AFS Transactions*, Vol. 99, 1991, pp. 501-506.

143. O. Vorren, J. E. Evensen, and T. B. Pedersen, "Microstructure and Mechanical Properties of AlSi(Mg) Casting Alloys," *AFS Transactions*, Vol. 92, 1984, pp. 459-466.

144. J. M. Boileau, P. C. Collins, and J. E. Allison, "The Effect of Solidification Time and Heat Treatment on the Tensile and Fatigue Properties of a Cast 319 Aluminum Alloy," *5th International AFS Conference on Molten Aluminum Processing*, Nov 8-10, 1998, Orlando, FL, pp. 158-172.

145. E. Nava Vazquez, A. Manzano Ramirez, J. Torres Torres, and M. Mendez Nonell, "Influence of Solidification Rates on Casting Soundness, Segregation Level and Tensile Properties of Aluminium Alloy 319," *Archives of Metallurgy*, Vol. 41, Issue 1, 1996, pp. 43-59.

146. P. Meyer, D. Massinon, and P. Guerin, "Influence of Microstructure on the Static and Thermal Fatigue Properties of 319 Alloys," *SAE Paper #970705*, SAE International, Warrendale, PA, 1997.

147. H. W. Doty, "The Effects of Strontium Addition on the Solidification of Near-eutectic Aluminum-Silicon Alloys," Private communication.

148. F. H. Samuel, P. Ouellet, A. M. Samuel, and H. W. Doty, "Effect of Mg and Sr Additions on the Formation of Intermetallics in Al-6 Wt Pct Si-3.5 Wt Pct Cu-(0.45) to (0.8) Wt Pct Fe 319-Type Alloys," *Metallurgical and Materials Transactions A*, Vol. 29A, No. 12, Dec. 1998, pp. 2871-2884.

149. I. Alfaro, J. Martinez, and C. Hernaiz, *Chemical Abstracts*, Vol. 71, No. 6152, 1969.

150. R. S. Archer and L. W. Kempf, "Modification and Properties of Sand-cast Aluminum-Silicon Alloys," *AIME Transactions*, Vol. 73, 1926, pp. 581-621.

151. M. Drouzy and S. Jacob, "Mechanical Properties of Die Cast AS10U4 Alloy – Influence of Iron Content," *Fonderie*, Vol. 240, Feb. 1966, pp. 50-54.

152. M. Moustafa, F. H. Samuel, H. W. Doty, and S. Valtierra, "Effect of Mg and Cu Additions on the Microstructural Characteristics and Tensile Properties of Sr-modified Al-Si Eutectic Alloys," To be published for *International Journal of Cast Metals Research.*

153. J. M. Boileau, J. W. Zindel, and J. E. Allison, "The Effect of Solidification Time on the Mechanical Properties in a Cast A356-T6 Aluminum Alloy," *5th International AFS Conference on Molten Aluminum Processing*, Nov 8-10, 1998, Orlando, FL, pp. 63-74.

154. K. Tynelius, J.F. Major, and D. Apelian, "A Parametric Study of Microporosity in the A356 Casting Alloy System," *AFS Transactions*, Vol. 101, 1993, pp. 401-413.

155. R. A. Wullaert, "Application of the Instrumented Charpy Impact Test," *Impact Testing of Metals, ASTM STP 466*, American Society for Testing and Materials, 1970, pp. 148-164.

156. F. Paray, B. Kulunk, and J. E. Gruzleski, "Impact Properties of Al-Si Foundry Alloys," *International Journal of Cast Metals Research,* Vol. 13, 2000, Issue. 1, pp. 17-37.

157. M. Tsukuda, S. Koike, and M. Harada, "The Heat Treatment of Al-7%Si-0.3Mg Alloy," *Journal of Japan Institute of Light Metals* (in Japanese), Vol. 28, No. 1, pp. 8-14.

158. M. Richard, "La résilience des alliages d'aluminium moulés," *Fonderie*, Vol. 404, Dec. 1980, pp. 397-400.

159. S. Shivkumar, L. Wang, and C. Keller, "Impact Properties of Al-Si-Cu Alloys," *Zeitschrift für Metallkunde*, Vol. 85, No. 6, 1994, pp. 394-399.

160. S. Shivkumar, L. Wang, and C. Keller, "Impact Properties of A356-T6 Alloys," *Journal of Materials Engineering and Performance*, Vol. 3, Feb. 1994, pp. 83-90.

161. S. Hotta, K. Saruki, and M. Nakamura, "Effects of T6 Heat Treatment on the Impact Strength of AC4C and AC2B Aluminum Alloy Castings Solidified for a Long Time," *Journal of Japan Institute of Light Metals* (in Japanese), Vol. 37, No. 7, July 1987, pp. 478-482.

162. M. Hafiz and T. Kobayashi, "Mechanical Properties of Modified and Nonmodified Eutectic Al-Si Alloys," *Journal of Japan Institute of Light Metals*, Vol. 44, No. 1, Jan. 1994, pp. 28-34.

163. R. Elliott, "Growth Kinetics of Silicon Crystal Flake, Strontium, Antimony and Chill Modified Al-Si Eutectic Alloys," *Proceedings of the 2nd Internatioanl Conference on Molten Aluminum Processing*, Orlando, Florida, Nov. 6-7, 1989, American Foundrymen's Society, Des Plaines, IL, 1989.

164. M. Tsukuda, T. Suzuki, I. Fukui, and M. Harada, "Problems on Modification of Al-7%Si-0.8%Mg Alloy by Sb," *Journal of Japan Institute of Light Metals*, Vol. 30, No. 2, 1980, pp. 65-71.

165. S. Kamado, M. Tsukuda, I. Tokutomi, and K. Hirose, "Effect of Solidification Conditions on Mechanical Properties of Directionally Solidified 356 Aluminum Alloy," *Journal of Japan Institute of Light Metals*, Vol. 37, No. 4, 1987, pp. 268-276.

166. M. F. Hafiz, T. Kobayashi, and N. Fat-Halla, "Role of Microstructure in Relation to the Toughness of Hypoeutectic Al-Si Casting Alloy," *Cast Metals*, Vol. 7, No. 2, pp. 103-111.

167. M. Tsukuda, M. Harada, T. Suzuki, and S. Koike, "The Effect of Si, Mg, Fe on the Mechanical Properties of Al-Si-Mg Alloys for Casting," *Journal of Japan Institute of Light Metals* (in Japanese), Vol. 28, No. 3, 1978, pp. 109-115.

168. S. Nishi and T. Kobayashi, "A Study on the Toughness of Aluminum Alloy Castings," *Journal of the Japan Foundrymen's Society* (in Japanese), Vol. 46, No. 10, Oct. 1974, pp. 905-912.

169. E. Kato, Y. Ueda, and A. Matumoto, "Effect of Various Modification Elements on Fatigue and Impact Properties of Al-Si System Casting Alloys," *Journal of the Japan Foundrymen's Society* (in Japanese), Vol. 63, No. 4, 1990, pp. 283-288.

170. L. Liu, A. M. Samuel, F. H. Samuel, H. W. Doty, and S. Valtierra, unpublished data (2002).

171. J. F. Major, "Porosity Control and Fatigue Behaviour in A356T61 Aluminum Alloy," Private communication.

172. A. T. Joenoes and J. E. Gruzleski, "Magnesium Effects on the Microstructure of Unmodified and Modified Al-Si Alloys," *Cast Metals*, Vol. 4, No. 2, 1991, pp. 62-71.

173. B. L. Gabriel, *SEM: A User's Manual for Materials Science*, American Society for Metals, Metals Park, OH, 1985, p. 97.

174. J. L. McCall, "Failure Analysis by Scanning Electron Microscopy", *MIMC Report*, Metals and Ceramics Information Center, Dec. 1972.

175. V. Kerlins, A. Phillips, "Modes of Fracture," *Metals Handbook, 9th Edition. Vol. 12: Fractography*, American Society for Metals, Metals Park, OH, 1987, pp. 12-71.

176. K. Gall, N. Yang, M. Horstemeyer, D. L. McDowell, and J. Fan, "The Debonding and Fracture of Si Particles during the Fatigue of a Cast Al-Si Alloy", *Metallurgical and Materials Transactions A*, Vol. 30A, Dec. 1990, pp. 3079-3088.

177. F. T. Lee, J. F. Major, and F. H. Samuel, "Effect of Silicon Particles on the Fatigue Crack Growth Characteristics of Al-12 Wt Pct Si-0.35 Wt Pct Mg-(0 to 0.02) Wt Pct Sr Casting Alloys", Metallurgical and Materials Transactions A, Vol. 26 A, June 1995, pp. 1553-1570.

178. C. R. Brooks and A. Choudhury, *Metallurgical Failure Analysis*, McGraw-Hill, Inc., New York, 1993.

179. J. H. Horng, D. S, Jiang, T. S. Lui, and L. H. Chen, "The Fracture Behaviour of A356 Alloys with Different Iron Contents under Resonant Vibration", *International Journal of Cast Metals Research*, Vol. 13, 2000, pp. 215-222.

180. F. J. Estensoro, A. Pelayo, and A. M. Insarri, "Fatigue Behavior of Two Cast Aluminum-Silicon Alloys," *ECF 11 – Mechanisms and Mechanics of Damage and Failure*, Poiers-Futuroscope, France, 1996, pp. 1045-1050.

181. S. E. Stanzl-Tschegg, H. R. Mayer, E. K. Tschegg, and A. Beste, "In-service Loading of AlSi11 Aluminum Cast Alloy in the Very High Cycle Regime," *International Journal of Fatigue*, Vol. 15, No. 4, 1993, pp. 311-316.

182. S. Savelli, J.-Y. Buffière, and R. Fougères, "Pore Characterization in a Model Cast Aluminum Alloy and its Quantitative Relation to Fatigue Life Studied by Synchrotron X-Ray Microtomography," *Materials Science Forum*, Vols. 331-337, 2000, pp. 197-202.

183. The ASM Committee on Fractography by Electron Microscopy, "The Scanning Electron Microscope and Its Application to Fractography," *Metals handbook, 8th Edition, Vol. 9: Fracrography and Atlas of Fractographs*, American Society for Metals, Metals Park, OH, 1978, pp. 49-53.

184. Z. Li, A. M. Samuel, F. H. Samuel, C. Ravindran, and S. Valtierra, "Effect of Alloying Elements on the Segregation and Dissolution of $CuAl_2$ Phase in Al-Si-Cu 319 Alloys," to be published.

185. The ASM Committee on Fractography by Electron Microscopy, "The Interpretation of Scanning-Electron-Microscope Fractographs," *Metals handbook, 8th Edition, Vol. 9: Fracrography and Atlas of Fractographs*, American Society for Metals, Metals Park, OH, 1978, pp. 64-78.

186. G. F. Van der Voort, "Visual Examination and Light Microscopy", *Metals Handbook, 9th Edition, Vol. 12: Fractography*, American Society for Metals, Metals Park, OH, 1987, pp. 91-165.